

Low-Energy Spin Dynamics in geometrically frustrated 3d-Magnets and Single-Ion Spin Systems

μ^+ SR studies on $\text{BaTi}_{0.5}\text{Mn}_{0.5}\text{O}_3$ and $\text{NaCaCo}_2\text{F}_7$ and ^{57}Fe -Mössbauer
spectroscopy on Fe-diluted $\text{Li}_2(\text{Li}_{1-x}\text{Fe}_x)\text{N}$

DISSERTATION

Doctor rerum naturalium

(Dr. rer. nat.)

vorgelegt

dem Bereich Mathematik und Naturwissenschaften
der Technischen Universität Dresden

von

Diplom-Physiker Sascha Albert Bräuninger
geboren am 05.11.1985 in Lüdenscheid

Datum der Disputation: 27.01.2020

1. Gutachter: Prof. Dr. H.-H. Klauß
2. Gutachter: Prof. Dr. J. Wosnitza

Abstract

In this work, I present nuclear probe spectroscopy studies, in detail, μ^+ SR and ^{57}Fe -Mössbauer spectroscopy on solid-state systems with localized magnetic moments of $3d$ transition-metal ions supported by density functional theory calculations. Local probes are able to extract local quantities, e.g. the spin dynamics of the ^{57}Fe site or the local, mostly interstitial μ^+ site to distinguish between different magnetic phases. The density functional theory calculations help to identify the muon site position from which the local quantity depends. My μ^+ SR studies on frustrated $3d$ magnets with quenched disorder concern the physics of phase transitions, avoided order-by-disorder, quantum fluctuations or the appearance of spin-liquid-by-disorder. μ^+ SR is able to identify quantum spin-liquid-like ground states without symmetry breaking or static magnetic order by the magnetic field at the muon site.

$\text{BaTi}_{0.5}\text{Mn}_{0.5}\text{O}_3$ is a magnetically highly-frustrated double perovskite with quenched disorder. It shows no freezing temperature or no frequency dependence of χ' as expected for a spin glass. Microscopically, it is proposed that local interactions between magnetic orphan spins, dimers, and magnetic trimers of Mn^{4+} play an important role. The μ^+ SR experiment on $\text{BaTi}_{0.5}\text{Mn}_{0.5}\text{O}_3$ shows an increase of the dynamical muon spin relaxation rate below 3K which saturates down to 0.019K coexisting with residual short-range magnetic order ($< 20\%$ of the signal). A clear difference is observed in comparison with the classical cluster-spin glass $\text{SrTi}_{0.5}\text{Mn}_{0.5}\text{O}_3$ which shows a peak of the zero-field muon spin relaxation rate: a persistent low-energy spin dynamics is present in $\text{BaTi}_{0.5}\text{Mn}_{0.5}\text{O}_3$ down to 20mK. My DFT calculations propose a positive muon site insight the Ba plane close to O atoms. Here, a slight preference of the muon site close to Mn^{4+} is possible which could put the muon close the orphan spins, dimers, and magnetic trimers, respectively, avoiding the nonmagnetic Ti^{4+} face-sharing octahedra. Theoretically, a specific ground state of $\text{BaTi}_{0.5}\text{Mn}_{0.5}\text{O}_3$ is not proposed. A clear discrimination between a quantum spin liquid ground state and a mimicry state with the appearance of spin-liquid-by-disorder is not possible from the existing data.

I present a μ^+ SR study on the bond-disordered magnetically highly frustrated pyrochlore fluoride $\text{NaCaCo}_2\text{F}_7$. Neutron spectroscopy studies on $\text{NaCaCo}_2\text{F}_7$ revealed static short-range order consistent with a continuous manifold of cluster-like states being a superposition of noncoplanar $\psi_2(m_{3z^2-r^2})$ and coplanar $\psi_3(m_{x^2-y^2})$ states with a correlation length of around 16 Å. No evidence for static magnetic long-range order is found in $\text{NaCaCo}_2\text{F}_7$ probed by μ^+ SR confirming the absence of an order-by-disorder mechanism. The experimental results are not consistent with a classical local-planar XY cluster-spin glassiness.

In these μ SR experiments, two muon sites are observed. The relative occupancy of both muon sites is nearly temperature independent. Muon site **I** is a collinear diamagnetic F- μ^+ -F bound state pulling two F^- close towards the muon revealed by the muon spin time evolution. To investigate the pure

F- μ^+ -F bound state in a broad temperature range I have performed an additional μ^+ SR study on CaF₂. This study solved open questions of muon diffusion around 290 K which was observed in NaCaCo₂F₇ as well. The F- μ^+ -F spin relaxation indicates the slowing down of the magnetic Co²⁺ spin fluctuations upon cooling towards the NMR spin freezing temperature $T_f \approx 2.4$ K. The relaxation rate saturates below 800 mK and remains constant down to 20 mK. The dominant part of the magnetic short-range relaxation signal is a dynamical relaxation as probed by longitudinal magnetic-field experiments.

Muon site **II** exhibits a strong dynamical relaxation rate at 290 K and below and shows persistent μ^+ spin dynamics down to 20 mK. Qualitatively, muon site **II** shows persistent μ^+ spin dynamics with one order of magnitude higher dynamical relaxation rates compared to muon site **I**.

DFT calculations of a comparison of the unperturbed unit cells of NaCaCo₂F₇ and NaCaNi₂F₇, which has shown just one muon site experimentally, are consistent with a decrease of the energy differences of energy minima and support the experimentally observed muon site ambivalence. In summary, the μ^+ SR studies propose NaCaCo₂F₇ as a quantum cluster-spin glass candidate.

I present a systematic ⁵⁷Fe-Mössbauer study on highly diluted Fe centers in Li₂(Li_{1-x}Fe_x)N as a function of temperature and magnetic field applied transverse and longitudinal with respect to the single-ion anisotropy axis. Here, Fe is embedded in an α -Li₃N matrix. The oxidation state of Fe and possible ferromagnetic nature are in controversial discussions in the literature. Below 30 K the Fe centers exhibit a giant magnetic hyperfine field of $\bar{B}_A = 70.25(2)$ T parallel to the axis of strongest electric field gradient $\bar{V}_{zz} = -154.0(1)$ V/Å². This observation is consistent with a Fe¹⁺ d^7 charge state with unquenched orbital moment and $J = 7/2$. Fluctuations of the magnetic hyperfine field are observed between 50 K and 300 K and described by the Blume two-level relaxation model consistent with single-atomic magnetism as proven by the invariance of Blume relaxation parameters for the concentration tuning $x \leq 0.025$ excluding a ferromagnetic nature. From the temperature dependence of the fluctuation rate an Orbach spin-lattice relaxation process is deduced. An Arrhenius analysis yields a single thermal-activation barrier of $\bar{E}_A = 570(6)$ K and an attempt frequency $\bar{\nu}_0 = 309(10)$ GHz.

Mössbauer spectroscopy studies with applied transverse magnetic fields up to 5 T reveal a large increase of the fluctuation rate by two orders of magnitude. In longitudinal magnetic fields a splitting of the fluctuation rate into two branches is observed.

The experimental observations are qualitatively reproduced by a single-ion spin Hamiltonian analysis. It demonstrates that for dominant magnetic quantum tunneling relaxation processes a weak axial single-ion anisotropy D of the order of a few Kelvin can cause a two orders of magnitude larger energy barrier for longitudinal spin fluctuations.

Contents

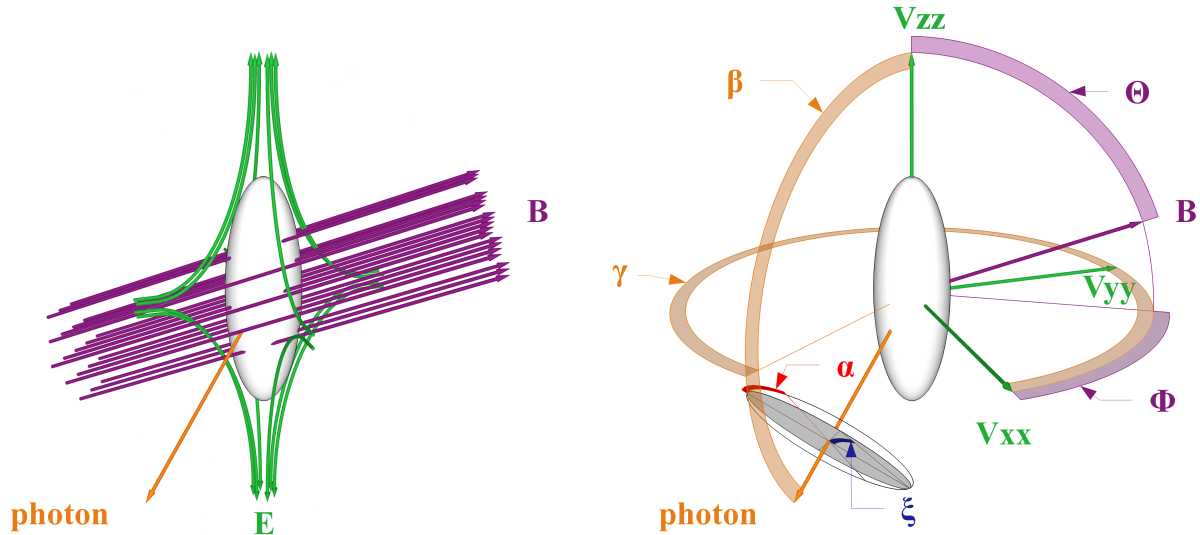
Acronyms and Symbols	9
1 Preface	13
1.1 Personal remarks	13
1.2 The main projects and methods	13
1.3 Outline of the thesis	15
1.4 Style of the document	17
2 Methods	19
2.1 μ^+ spin spectroscopy	19
2.1.1 The positive muon: μ^+	20
2.1.2 μ^+ SR technique	21
2.1.3 Muon interactions and local magnetic fields	24
2.1.4 Muon-spin polarization functions: Overview	27
2.1.5 Simple cosine	28
2.1.6 Gaussian Kubo-Toyabe	29
2.1.7 Exponential	30
2.1.8 Stretched exponential	33
2.1.9 Pure Gaussian	35
2.1.10 Quantum approach	35
2.2 ^{57}Fe -Mössbauer spectroscopy	38
2.2.1 The Mössbauer effect: Intuitive overview	38
2.2.2 ^{57}Fe -Mössbauer technique	40
2.2.3 Lamb-Mössbauer factor	41
2.2.4 Hyperfine interactions and limits	43
2.3 Density functional theory	45
2.3.1 Kohn-Sham equations	45
2.3.2 Coulomb potential and Elk	46
2.3.3 Units	47
2.3.4 Disorder and Approximations	48
2.3.5 Performed calculations	49
3 Role of Disorder: Overview	51
3.1 Types, spin glassiness and order-by-disorder	51
3.2 Appearance of spin-liquid-by-disorder	53

3.3	Quantum fluctuations in rare-earth pyrochlore oxides	54
4	Pyrochlore Fluoride NaCaCo₂F₇	57
4.1	Frustration in fluorides and NaCaCo ₂ F ₇	57
4.2	Order-by-disorder and XY cluster-spin glassiness	62
4.3	Previous experimental studies on NaCaCo ₂ F ₇	64
4.3.1	Spin glass-like freezing, bond-disorder and XY cluster-spin glassiness	65
4.3.2	XY planar anisotropy versus isotropy in NaCaCo ₂ F ₇	69
5	Persistent μ^+ Spin Dynamics in BaTi_{0.5}Mn_{0.5}O₃	73
5.1	Motivation	73
5.2	Properties	75
5.3	μ^+ SR study on BaTi _{0.5} Mn _{0.5} O ₃	77
5.4	DFT of BaTi _{0.5} Mn _{0.5} O ₃	77
5.5	Discussion	81
5.6	Conclusion	82
6	μ^+SR Study on CaF₂ and the F-μ^+-F state	85
6.1	Structure and DFT calculations	85
6.2	Experimental details	88
6.3	μ SR Results of CaF ₂ and the F- μ -F state	89
6.4	Discussion of CaF ₂	91
6.5	Conclusions of CaF ₂	94
7	Persistent μ^+ Spin Dynamics in NaCaCo₂F₇	95
7.1	Experimental description	95
7.2	μ^+ SR results of NaCaCo ₂ F ₇	96
7.2.1	Muon sites	96
7.2.2	Temperature-independent model of the muon-site occupancy	98
7.2.3	LF experiments above T_f	98
7.2.4	Low-temperature decoupling $T < T_f$ and persistent μ^+ spin dynamics	99
7.2.5	DFT calculations	100
7.3	Discussion	103
7.3.1	Muon site I	103
7.3.2	DFT treatment	105
7.3.3	Muon site II	107
7.3.4	Persistent μ^+ spin dynamics	108
7.4	Conclusions	109
7.5	Outlook	110
7.5.1	NaCaCo ₂ F ₇	110
7.5.2	Highly frustrated pyrochlore FeF ₃	111
7.5.3	Mixed-metal β -pyrochlore RbFe ²⁺ Fe ³⁺ F ₆	111

8	^{57}Fe-Mössbauer spectroscopy on $\text{Li}_2(\text{Li}_{1-x}\text{Fe}_x)\text{N}$ ($x \ll 1$)	113
8.1	Introduction	113
8.1.1	Single-molecule and single-atomic magnets	113
8.1.2	The host crystal $\alpha\text{-Li}_3\text{N}$	114
8.1.3	$\text{Li}_2(\text{Li}_{1-x}\text{Fe}_x)\text{N}$	116
8.1.4	Motivation	117
8.2	Results	119
8.2.1	Doping concentrations and magnetization studies of $\text{Li}_2(\text{Li}_{1-x}\text{Fe}_x)\text{N}$ with $x \ll 1$	119
8.2.2	Experimental description: ^{57}Fe Mössbauer Spectroscopy	119
8.2.3	Low temperature ^{57}Fe -Mössbauer spectroscopy at base temperature T_B	120
8.2.4	Zero field ^{57}Fe -Mössbauer spectroscopy for $T_B < T < 300\text{ K}$	124
8.2.5	^{57}Fe -Mössbauer spectroscopy in transverse magnetic fields B_T	126
8.2.6	Mössbauer spectroscopy in longitudinal magnetic fields B_L	127
8.2.7	Single-ion spin Hamiltonian calculation of spin dynamics	131
8.3	Discussion	136
8.3.1	Magnetization steps in the hysteresis loop	136
8.3.2	Mössbauer sites and sample homogeneity	137
8.3.3	Oxidation and spin state of Fe ions in $\text{Li}_2(\text{Li}_{1-x}\text{Fe}_x)\text{N}$	138
8.3.4	Energy barrier and spin dynamics	140
8.4	Conclusions	142
8.5	Outlook	143
8.5.1	Advantages of $\text{Li}_2(\text{Li}_{1-x}\text{Fe}_x)\text{N}$	143
8.5.2	μSR on Fe-diluted $\text{Li}_2(\text{Li}_{1-x}\text{Fe}_x)\text{N}$	143
8.5.3	NMR	144
8.5.4	Bridge up to $x = 0.30$	145
9	Summary	147
	Bibliography	149
A	Appendix	163
A.1	$\text{NaCaCo}_2\text{F}_7$	163
A.1.1	$\mu^+\text{SR}$ spectra in 30 G at 290 K	163
A.1.2	LTF data of λ_f	163
A.1.3	Low-field SQUID measurements of $\text{NaCaCo}_2\text{F}_7$	163
A.2	$\text{Li}_2(\text{Li}_{1-x}\text{Fe}_x)\text{N}$	165
A.2.1	Mass absorption coefficients	165
A.2.2	Magnetization hysteresis loops	165
A.2.3	Debye-fit for Θ_D	166
A.2.4	Discussion of the ^{57}Co -source splitting in longitudinal magnet fields B_L	166
A.3	Additional DFT results	167
A.3.1	DFT results of $\text{Fe}_4\text{Si}_2\text{Sn}_7\text{O}_{16}$	167

A.3.2	DFT results of $\text{Fe}_3\text{PO}_4\text{O}_3$	167
-------	---	-----

Acronyms and Symbols



(a) Imagination of the nucleus in a dominant electric field (green) applying a magnetic field \mathbf{B} (purple) with respect to the γ -beam (orange). (b) Often used parameter labeled for the static crystal Hamiltonian model.

Figure 0.1: Orientation of the nucleus (white) in the magnetic field \mathbf{B} (purple) and the EFG (electric field gradient) principle axes (green). To describe the emission/absorption of a photon (orange) in the static Hamiltonian approach, one needs seven angles: Θ and Φ describing the orientation of magnetic field relative to the EFG, β and γ describing the photon flight direction relative to the EFG and α , φ , and ξ describing the polarization state of the photon. Both figures are taken from S. Kamusella *et al.* [1, 2] and the corresponding Moessfit manual [3].

a.c.	alternating current
ALC	avoided level crossing
α	azimuthal tilting angle as labeled in figure 0.1 (b)
a_0	$= \frac{4\pi\epsilon_0\hbar^2}{m_e e^2}$, Bohr radius, the values of the DFT input file are defined in atomic units
AFM	antiferromagnet(ic)
ARPES	angle-resolved photoemission spectroscopy
$A(t)$	Asymmetry of the muon spin polarisation, also denoted as $A(t) = A_0 P_Z(t)$
β	polar angle between EFG z-axis and gamma beam, see figure 0.1 (b); or: exponent in a stretched exponential muon spin polarization function $P_Z(t) = ae^{-(\lambda t)^\beta} + b$
\mathbf{B}_{con}	Fermi contact field

B_{dem}	demagnetization field
B_{dia}	Fermi contact field
B_{dip}	total dipole field
B_{ext}	external magnetic field
B_L	Lorentz field
B_{loc}	local magnetic field (of the muon), total magnetic field
B_{RKKY}	Rudermann-Kittel-Kasuya-Yoshida field
B_{trans}	transferred hyperfine field
χ^2	goodness of fit, $\chi^2 := \sum_i \left(\frac{y_i - m(x_i, \mathbf{p})}{\Delta_i} \right)^2$ with the model function m with model parameters \mathbf{p} and data (x_i, y_i) and measurement error Δ_i
<i>CS</i>	centre shift, describes the shift of the centre of a Mössbauer spectra due to isomer shift and quadratic Doppler effect, means relative to the ^{57}Co -source
Cu K-α	Transition from the L to the K-shell of Copper leading to the emitted K- α X-ray which is often used in X-ray instruments in the laboratory, the energy is ≈ 8.04 keV
d.c.	direct current
δ	small change of an a parameter, or: isomer shift
DFT	density functional theory
e$_{\gamma}$	direction of the gamma beam
E_h	Hartree energy, $E_h = \frac{m_e e^4}{4\epsilon_0^2 \hbar^2} \approx 4.35974465 \cdot 10^{-18} \text{ J} \approx 27.2 \text{ eV}$
ESR	electron spin resonance (spectroscopy)
ev_{zz}	direction of the EFG z-axis
E_{γ}	Mössbauer transition energy, ≈ 14.4 keV for ^{57}Fe
EDX	energy dispersive X-ray spectroscopy
EFG	electric field gradient
FC	Field Cooled (magnetic field cooled), applying the magnetic at high temperature T above the spin freezing $T \gg T_f$
FM	ferromagnet(ic)
f_r	resonant fraction
f	frustration index, $f = \frac{\Theta_W}{T_f}$
γ	azimuthal angle between EFG z-axis and gamma beam, see figure 0.1 (b), or muon gyromagnetic ratio, $\gamma = 2\pi\gamma_{\mu}$
γ_{μ}	$= \frac{\gamma}{2\pi} \approx 0.0135538817 \text{ MHz/G}$
Γ	full Mössbauer line width
GGA	generalized gradient approximation
GPS	“General Purpose Spectrometer”, μSR spectrometer of the Paul-Scherrer-Institute in Switzerland, which was used for the measurements in this thesis
GUI	graphical user interface
I	nuclear spin quantum number
ICP	long: ICP-OES, means inductively-coupled-plasma optical-emission-spectroscopy
$I(v)$	intensity of the Mössbauer radiation, theoretical Mössbauer spectrum, corresponds to experimental transmission

I_∞	baseline of the Mössbauer spectrum, intensity without absorption, $I(v \rightarrow \pm\infty)$
k_B	Boltzmann constant
λ	relaxation rate
LAPW	linearized augmented plane wave
LF	longitudinal field with respect to muon beam/gamma beam
LRO	long-range order
LTF	“Low Temperature facility”, μ SR spectrometer of the Paul-Scherrer-Institute in Switzerland, which was used for the measurements in this thesis
mbs	file extension in a Moessfit model file
Mo K-α	Transition from the L to the K-shell of Molybdenum leading to the emitted K- α X-ray which is often used in X-ray instruments in the laboratory, the energy is ≈ 17.45 keV
MPMS	Magnetic Property Measurement System, MPMS 3 SQUID magnetometer
μ SR	muon spin rotation/relaxation/resonance
η	asymmetry of the EFG
NMR	nuclear magnetic resonance
$\mathbf{P}(t)$	muon spin polarisation, e.g. longitudinal part $P_Z(t)$
Φ	azimuthal angle between EFG z-axis and \mathbf{B} , see figure 0.1 (b)
PSD	persistent (muon, μ^+) spin dynamics
PXRD	Powder X-ray diffraction
$T(v)$	transmission integral
Θ	polar angle between EFG z-axis and \mathbf{B} , see figure 0.1 (b)
QCP	quantum critical point
Q	quadrupole moment, 0.16(1) eb for ^{57}Fe
RT	room temperature, typically 295 K
SAM	single-atomic magnet
SMM	single-molecule magnet
SRO	short-range order
SXRD	Single crystal X-ray diffraction
σ	standard deviation, in μ SR the corresponding relaxation for a Gaussian distribution of fields
t_a	effective thickness, $\sigma_0 n_a f d$
T_f	freezing temperature, magnetic moments starts to freeze like in a spin glass
Θ_W	Curie-Weiß temperature
TF	transverse field with respect to muon beam/gamma beam
T_N	Neél temperature, transition temperature of an antiferromagnet
ω_{abs}	absorber line width
V_{zz}	principal or main component of the EFG tensor
XRD	X-ray diffraction
XY	planar XY states perpendicular to the local [111]-axis in pyrochlores
ZF	Zero Field (zero magnetic field)
ZFC	Zero Field Cooled

1 Preface

1.1 Personal remarks

The scientific work described in this thesis was performed between June 2015 and July 2019. The final writing process started in January 2018. I have joined the *Nuclear probe* spectroscopy group of Prof. Dr. Hans-Henning Klauss in 2015, for details see figure 1.1. The reason is I like it very much to look microscopically *into* something to get a deeper understanding. Fortunately and unfortunately, fortunately because one can improve the knowledge based on bulk measurements, unfortunately because the experimental effort and the deep data analysis often require a considerable amount of time. In general, NMR and Mössbauer spectroscopy have the advantage to provide a detailed knowledge of the probed nuclei and it's particular site in the lattice. Muon spin rotation/resonance/relaxation spectroscopy (μ^+ SR) is here sometimes tricky because of the lack of knowledge of the mostly interstitial position of the positive muon.

The title

Low-Energy Spin Dynamics in geometrically frustrated 3d-Magnets and Single-Ion Spin Systems

is rather broadly formulated because of the broad topics which are covered emphasized by the subtitle

μ^+ SR studies on $\text{BaTi}_{0.5}\text{Mn}_{0.5}\text{O}_3$ and $\text{NaCaCo}_2\text{F}_7$ and ^{57}Fe -Mössbauer spectroscopy on Fe-diluted $\text{Li}_2(\text{Li}_{1-x}\text{Fe}_x)\text{N}$.

Two main μ^+ SR studies are presented, my CaF_2 study and my density functional theory (DFT) calculations are not mentioned in the title. $\text{NaCaCo}_2\text{F}_7$ and $\text{BaTi}_{0.5}\text{Mn}_{0.5}\text{O}_3$ are intrinsically disordered compounds and show persistent μ^+ spin dynamics (PSD). The nonmagnetic CaF_2 provides a direct introduction into the F- μ^+ -F physics as observed in $\text{NaCaCo}_2\text{F}_7$. In the following, I give an overview of the topics and methods used in this thesis.

1.2 The main projects and methods

The investigation of the enhanced low-energy spin dynamics of diluted or strongly frustrated transition metal compounds is the shared topic of my studies.

$\text{NaCaCo}_2\text{F}_7$ and $\text{NaSrCo}_2\text{F}_7$ are magnetically frustrated pyrochlore fluorides with bond disorder located at the boundary between spin glassiness and long-range order forming a cluster spin glass¹. Initially, $\text{NaCaCo}_2\text{F}_7$ was proposed as order-by-disorder candidate to solve open questions regarding

¹For detailed information and references see main text. The preface is the only chapter which does not contain references with full attention.

the understanding of the quantum-order-by-disorder candidate $\text{Er}_2\text{Ti}_2\text{O}_7$. $\text{NaSrCo}_2\text{F}_7$ is not mentioned in the title and was investigated as well. The suppression of $\text{NaSrCo}_2\text{F}_7$ in the title and in the following discussions is readability since qualitatively there is no difference between $\text{NaCaCo}_2\text{F}_7$ and $\text{NaSrCo}_2\text{F}_7$ observed.

Fe-diluted $\text{Li}_2(\text{Li}_{1-x}\text{Fe}_x)\text{N}$ behaves like a single-atomic magnet as probed by ^{57}Fe -Mössbauer spectroscopy. This shows the diversity of topics and techniques used and performed by the author in this thesis including my DFT calculations. Started by my own, we have supplemented our studies by

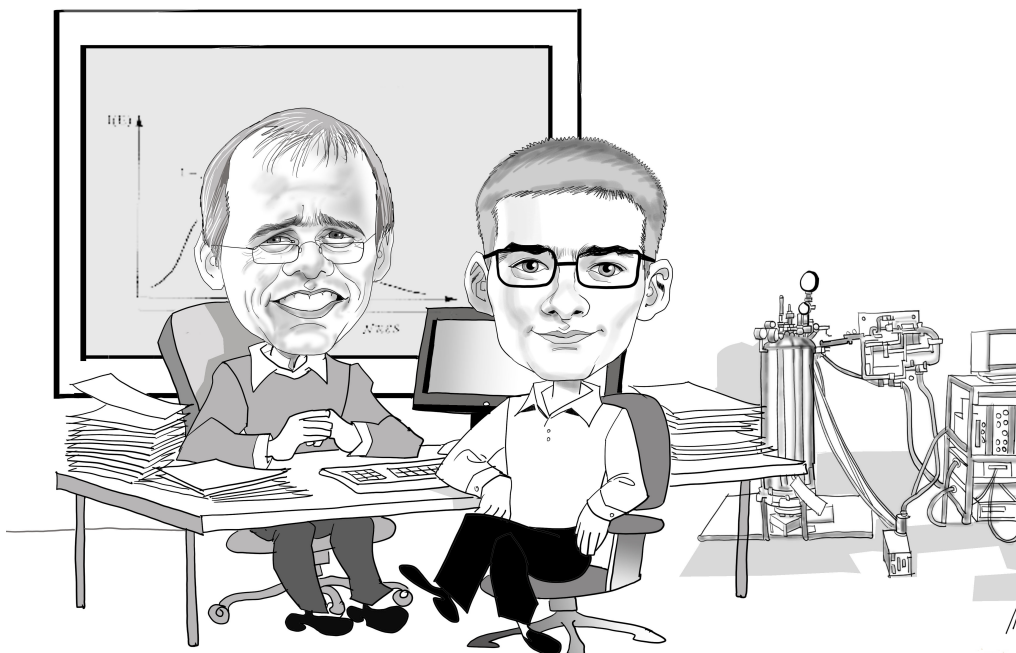


Figure 1.1: Caricature of Hans-Henning Klauss (left) and the author of this thesis (right) sitting in his bureau with the small ^{57}Fe -Mössbauer cryostat in the background in the right corner.

pulsed-high-field magnetization studies on single crystals of $\text{NaCaCo}_2\text{F}_7$ measured during a granted magnet time in Dresden-Rossendorf². Additionally, I have motivated ESR studies by our IFW colleagues and shown how important networking is to solve open question, however, this issue is also not the main content of this work and has led to another topic for a PhD student.

I have initiated and performed DFT calculations by myself and introduced it into our group. The aim of the DFT calculations is to study possible positive muon sites and to calculate electrostatic parameters, e.g., the electric field gradient (EFG) to compare it with NMR results. Detailed magnetic DFT treatments are a challenge and an own topic.

The pyrochlore antiferromagnet $\text{NaCaCo}_2\text{F}_7$ is a highly frustrated correlated electron systems. $\text{NaCaCo}_2\text{F}_7$ is one of the most interesting $\mu^+\text{SR}$ studies so far done on magnetic pyrochlore systems because of the muon site unambiguity and the possibility to quantify the distortion, i.e. the lattice displacement induced by the muon. This is my personal opinion.

²Nicely supported by the Rossendorf team, see below.

In contrast, $\text{Li}_2(\text{Li}_{1-x}\text{Fe}_x)\text{N}$ is for low Fe-concentration, means $x \ll 1$, a single-atomic magnet, as we will discuss below, which mimics magnetism. Here, the relaxation time of the electronic system is huge because of a magnetic energy barrier given by the anisotropy of the crystal structure leading to a huge static magnetic hyperfine field probed by ^{57}Fe -Mössbauer spectroscopy at low temperature $T < 50\text{ K}$. Since $\text{NaCaCo}_2\text{F}_7$ and $\text{NaSrCo}_2\text{F}_7$ are proposed as XY antiferromagnets, a local magnetic anisotropy is here present as well sharing this topic. So, an alternative title of this work could be

Low-Energy Spin Dynamics in selected 3d-Systems with a local magnetic Anisotropy.

Mössbauer and μ^+ SR spectroscopy are complementary, not only regarding the time window sensitivity. μ^+ SR is a particle-accelerator based technique dealing with the challenge to measure everything in a very limited time slot. On the other hand, Mössbauer spectroscopy is in the framework of this work used as a laboratory technique and not as synchrotron Mössbauer spectroscopy.

The scientific projects $\text{NaCaCo}_2\text{F}_7$ and $\text{Li}_2(\text{Li}_{1-x}\text{Fe}_x)\text{N}$ are contrasting for other reasons as well. The pyrochlore fluoride project is a project to investigate a possible order-by-disorder mechanism which is located full inside the SFB (Sonderforschungsbereich) 1143 *From Frustration to Topology*³ and the crystals were ready in a high quality. Frustrated systems are able to form (quantum) spin liquids because of the competition of magnetic interactions for which the Landau theory is not sufficient because those can not be described by broken symmetries and order parameters. There is a gap between proposed theoretical models and the confirmation by the experimental possibilities, means quantities. The closing of this gap is an important driving force for this work.

On the other hand, the $\text{Li}_2(\text{Li}_{1-x}\text{Fe}_x)\text{N}$ is an independent project. The synthesis of the large single crystals and the sample preparation in the group of Dr. Anton Jesche at the University of Augsburg was a challenge and the study contains a broad series of various concentrations. We have measured eleven samples in total. $\text{Li}_2(\text{Li}_{1-x}\text{Fe}_x)\text{N}$ is a very nice example for a project in which we got a very deep understanding to explain the magnetic field sensitivity together with theory colleagues.

1.3 Outline of the thesis

I would like to mention two investigated compounds additionally and parallel to the main studies, CaF_2 and $\text{BaTi}_{0.5}\text{Mn}_{0.5}\text{O}_3$, because these systems are very close to the main study on $\text{NaCaCo}_2\text{F}_7$. Figure 1.2 shows the connection of topics and the discussed projects in this PhD thesis. In detail:

- $\text{BaTi}_{0.5}\text{Mn}_{0.5}\text{O}_3$ is a double perovskite probed by μ^+ SR which is close to the $\text{NaCaCo}_2\text{F}_7$ project because of the intrinsic disorder. It shows the general contrast of μ^+ SR studies of oxides and fluorides. It helps from a didactic point of view and supplements to an overall picture of my studies of quenched disorder. The $\text{Li}_2(\text{Li}_{1-x}\text{Fe}_x)\text{N}$ project contains disorder as well, especially important for higher concentration of $x > 0.1$. So, disorder and the prove of the absence of clusters in Fe-diluted $\text{Li}_2(\text{Li}_{1-x}\text{Fe}_x)\text{N}$ is an issue which is shared. Additionally, $\text{NaCaCo}_2\text{F}_7$ and $\text{BaTi}_{0.5}\text{Mn}_{0.5}\text{O}_3$ show PSD which is a very important point concerning the spin dynamics.

³which is the case for $\text{BaTi}_{0.5}\text{Mn}_{0.5}\text{O}_3$ as well.

- CaF_2 is a nonmagnetic ionic fluoride. In fluorides, the positive muon is able to form a bound state, the so-called F- μ -F state which is in the focus of this discussion. An observed anomaly of $\text{NaCaCo}_2\text{F}_7$ around room temperature is not understood and the CaF_2 results helps to obtain a deeper understanding and a comparison to a nonmagnetic example. A study of CaF_2 decades ago is set in a new light.

Therefore, the thesis contains two main projects and two side projects. The chapters of the side projects are shorter. This thesis is split into the following chapters:

1. Preface

The preface emphasizes the connection of topics, cross relations, and compounds in this thesis.

2. Methods

This chapter explains the used methods in this thesis. The longest chapter is the μ^+ SR part because it is the most frequently used technique. The Mössbauer section is rather short because the hyperfine interactions and the corresponding Hamiltonians are explained in the main part of the $\text{Li}_2(\text{Li}_{1-x}\text{Fe}_x)\text{N}$ study. The DFT part is short, discussing only core ideas because this is an experimental work.

3. Role of Disorder: Overview

This chapter provides a brief overview about different research topics nowadays focusing frustrated magnets, e.g., the *order-by-disorder* and *appearance of spin-liquid-by-disorder* phenomena. This is an excursion and no introduction in concepts.

4. Pyrochlore Fluoride $\text{NaCaCo}_2\text{F}_7$

The first main part the thesis contains the $\text{NaCaCo}_2\text{F}_7$ project. This chapter introduces the phenomena of magnetic geometrical frustration in fluorides, the structure of $\text{NaCaCo}_2\text{F}_7$ and previous studies showing the relation to other topics.

5. Quenched Disorder and persistent μ^+ Spin Dynamics in $\text{BaTi}_{0.5}\text{Mn}_{0.5}\text{O}_3$

Here, $\text{BaTi}_{0.5}\text{Mn}_{0.5}\text{O}_3$ is discussed and the consequence of the intrinsic disorder for the μ^+ SR spectra of this frustrated oxide⁴. The effect of PSD is discussed and compared to other frustrated compounds providing an indirect introduction to the main study on $\text{NaCaCo}_2\text{F}_7$.

6. μ^+ SR study on CaF_2 and the F- μ^+ -F state

This chapter has an introductory nature containing F- μ -F state physics although the parent compound is not so close to $\text{NaCaCo}_2\text{F}_7$ but conclusively related. The CaF_2 study shows the formations of the F- μ -F state in a nonmagnetic compound and at least, the $\text{NaCaCo}_2\text{F}_7$ combines everything above: The F- μ -F state, magnetic disorder, and PSD as discussed in $\text{BaTi}_{0.5}\text{Mn}_{0.5}\text{O}_3$.

7. Persistent μ^+ spin dynamics, F- μ^+ -F state relaxation and local μ^+ -induced lattice distortion in $\text{NaCaCo}_2\text{F}_7$

⁴Magnetically, there is another difference to $\text{NaCaCo}_2\text{F}_7$. $\text{NaCaCo}_2\text{F}_7$ contains only randomness of nonmagnetic ions of Na^+ and Ca^{2+} .

This and the next chapters contain the main issues of this report. The main chapter of $\text{NaCaCo}_2\text{F}_7$ discusses the observed dynamical muon spin relaxation down to 20 mK and the two muon sites. A DFT estimation supplements the experimental findings.

8. Magnetic field tuning of low-energy spin dynamics in the single-atomic magnet $\text{Li}_2(\text{Li}_{1-x}\text{Fe}_x)\text{N}$ probed by ^{57}Fe -Mössbauer spectroscopy

The $\text{Li}_2(\text{Li}_{1-x}\text{Fe}_x)\text{N}$ project is discussed in this part. Once again, figure 1.2 shows the cross relations. The introduction of $\text{Li}_2(\text{Li}_{1-x}\text{Fe}_x)\text{N}$ discusses the structure of the α - Li_3N matrix and performed experimental and theoretical studies of the $\text{Li}_2(\text{Li}_{1-x}\text{Fe}_x)\text{N}$ compounds for $x < 0.31$. Experimentally, the prove of the absence of clusters and homogenous Fe-site dilution is playing one important role for low x . In addition, the temperature-dependent observed low-energy spin dynamics is presented probed Mössbauer spectroscopy together with transverse and longitudinal magnetic field experiments which are supplemented by a single-ion spin Hamiltonian analysis by Prof. Andre Zvyagin.

1.4 Style of the document

To the style of this document, the style is at some point a bit unusual to support convenience and traceability.

Selected chapters and sections start with a short explanation and description by the author. This personal remarks are set out-of-line and containing information why the part is put there connecting different parts of the document improving the readability to follow the outline of the author and remembering on figure 1.2. This helps to get a better understanding of the entire work and the intention of the section.

Footnotes have a comparable function since those are much more local emphasizing experimental circumstances, restrictions of statements or in rare cases opinions.

A figure containing different figures showing, e.g., a unit cell in different directions without important physical changes is counted as one entire figure, means the figure is not split into subfigures⁵.

The appendix contains selected contributions to supplement my work. Outlooks are added below the discussion of the two main projects. Quoted sentences are *cursive ending with the reference [...]*. It is quiet unusual in physics to cite sentences, figures are more frequently cited, however, it is on the other hand a high quality scientific practice and there is no reason to reinvent the wheel. From my side, it is on top of this an appreciation of scientists which have done a great job.

Sascha Albert Bräuning

September, 2019

⁵For sure, one can discuss this critically. At least it is the artistic license of the author and corresponding freedom of art and writing.

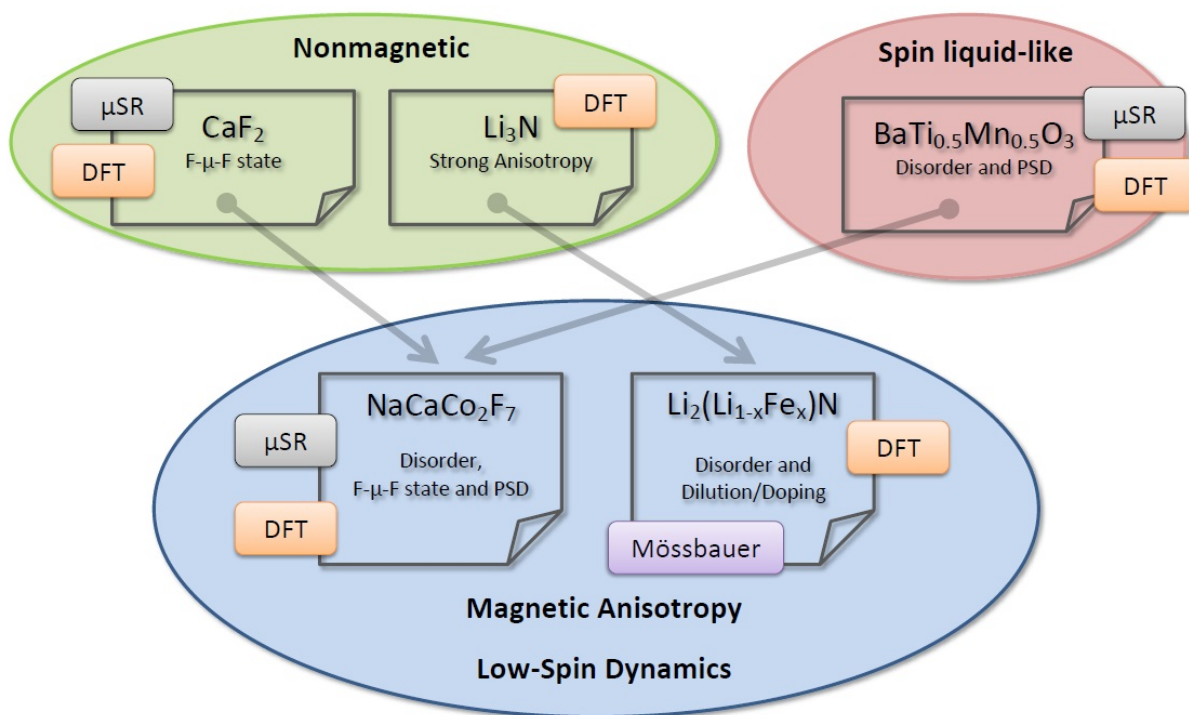


Figure 1.2: Overview of connected topics of compounds discussed in this thesis represented by project squares. The nuclear probe investigation of spin dynamics is the purpose of this work and disorder and magnetic anisotropy are the microscopic commonality of the main compounds (blue background). The $\text{NaCaCo}_2\text{F}_7$ project combines the 50%: 50%-disorder of one crystallographic site and PSD as in $\text{BaTi}_{0.5}\text{Mn}_{0.5}\text{O}_3$ and the observed F- μ -F state in CaF_2 as probed by $\mu^+\text{SR}$. Both projects $\text{BaTi}_{0.5}\text{Mn}_{0.5}\text{O}_3$ and CaF_2 are considered as secondary $\mu^+\text{SR}$ studies for this report. The orange squares visualize the broad application of the used DFT code supplementing the experimental studies.

2 Methods

2.1 μ^+ spin spectroscopy

This section describes the basics of μ^+ spin spectroscopy. μ^+ spin spectroscopy is often called muon spin rotation/relaxation/resonance and, therefore, written as μ^+ SR or μ SR¹. In this work, the relaxation of the muon spin plays the important role for the investigation. The purpose of this section is to give an introduction and an overview about the basics and used relaxation models used in my thesis. My intention is not to reinvent the wheel writing a detailed introductory text which does already exist. Two books are mentioned for the interested reader which I have used:

- *Muon Spin Rotation, Relaxation, and Resonance: Applications to Condensed Matter* by A. Yaouanc and P. Dalmas de Réotier [4].

This textbook is very compact and rather complete since it covers the most known relaxation models and even muonium spectroscopy and quantum approaches. The density of information is quiet high.

- *Muon spin rotation spectroscopy* by A. Schenck [5].

It is an older textbook (1985), however, it gives a nice overview in a short amount of time focusing the core issues and models.

Basic statements contained in conventional textbooks are not further cited in the following, only in rare exceptions. There are existing useful review-like introductions which I have used as well:

- *Spin-polarized muons in condensed matter physics* by S. Blundell [6].

This freely available short review is a very nice starting point discussing the main principles and it is very useful.

- *Muon spin rotation and relaxation in magnetic materials* by P. Dalmas de Réotier and A. Yaouanc [7].

This review can be regarded as a selected part of the main text book by the same authors discussing different topics of magnetic materials sharing the same quality as the main text book.

- *Muon spin spectroscopy: magnetism, soft matter and the bridge between the two* by L. Nuccio, L. Schulz and A. J. Drew [8].

This work covers soft matter, e.g., polymers, organic semiconductors, molecular magnets and magnetism as well. The first topics are not important directly in this

¹For sure, μ SR could include the negative muon as well. In the following μ SR is the positive μ^+ SR spin spectroscopy.

work probed by μ SR, however, it gives a nice overview. Tangentially, I have discussed the possibility of μ^+ SR on Fe-diluted $\text{Li}_2(\text{Li}_{1-x}\text{Fe}_x)\text{N}$ to measure the spin dynamics by the positive muon in the outlook which behaves like a single-atomic magnet. Therefore, the topics are not so far away as expected.

2.1.1 The positive muon: μ^+

It is important to discuss the basic properties of the positive muon μ^+ to perform μ^+ SR experiments. The most important points are the nature of the character as light proton and the asymmetric decay preferring the emission direction of the muon spin direction for the emitted positron e^+ . This last point is making this experiment possible.

Interestingly, this work deals with two things which are strongly correlated with two evidences of the special theory of relativity proposed by A. Einstein. The second-order Doppler shift of Mössbauer spectroscopy is the direct evidence of the time dilatation as discussed in the main part of the $\text{Li}_2(\text{Li}_{1-x}\text{Fe}_x)\text{N}$ results. On the other hand, historically, it was a wonder that a particle with a rest lifetime of $\tau_\mu = 2.19703(4) \mu\text{s}$ is able to survive much longer arriving at the surface of the Earth: The muon. The reason is the high velocity close to the speed of light leading to the time dilatation of special relativity. This subsection discusses the basic properties of the positive muon and the asymmetric spatial decay.

Table 2.1 shows the basic properties of the positive muon μ^+ . The muon has only around 10% of the proton mass m_p and is, therefore, considered as light proton carrying the same charge $+e$. The positive muon prefers mostly interstitial positions insight a crystal because of the character as a small nucleus. The positive muon is a fermion with a spin $I = \frac{1}{2}$ and has, therefore, no electric quadrupole moment. This is in contrast to the ^{57}Fe -Mössbauer spectroscopy which probes the quadrupole interaction because of the excitation of the ^{57}Fe nucleus into the $\frac{3}{2}$ -state as we will discuss later². The spin precession frequency of the muon in an applied magnetic field B is given by the gyromagnetic ratio γ_μ :

$$\omega_\mu = 2\pi\nu = \gamma_\mu B, \quad (2.1)$$

where

$$\gamma_\mu = g \frac{e}{2m_\mu} \quad (2.2)$$

is the mentioned gyromagnetic ratio for the positive muon. Table 2.2 shows the comparison of the rounded values of the magnetic moment and the gyromagnetic ratio of the electron, muon, and proton. The gyromagnetic ratio of the muon is located between the values of the electron and the proton. The gyromagnetic ratio of the muon is small compared to the ratio of the electron, in detail more than two orders of magnitude smaller. Electronic spin resonance (ESR) uses microwave frequencies ($\nu > 3 \cdot 10^9 \text{ Hz}$) and uses the electron as probe³. NMR (Nuclear magnetic resonance) uses radio frequencies $\nu < 10^9 \text{ Hz}$, e.g. for a 12-15 T magnet the 500-650 MHz range and the nucleus as probe.

²The ^{57}Fe ground state of the nucleus is $I = \frac{1}{2}$ and has therefore no quadrupole interactions.

³According to the fundamental equation $h\nu = g_e(657\mu_p)B$ with the Planck constant h in the magnetic field B with the electronic g-factor g_e for the free electron.

Quantity	Values
Mass m_μ	$216.76835(11)m_e \approx 0.1126096m_p$
Electric charge	$+e \approx 1.60219 \cdot 10^{-19} \text{ C}$
Spin I	$\frac{1}{2}\hbar$
Gyromagnetic ratio $\gamma_\mu/2\pi$	$13.553879(0.2 \text{ ppm}) \text{ kHz/G}$
Magnetic moment μ_μ	$3.1833455(5) \mu_p$
Direction of μ_μ	$+ \gamma_\mu I$
Lifetime τ_μ	$2.19703(4) \mu\text{s}$

Table 2.1: Properties of the positive muon μ^+ . Here, m_e is the electron mass, m_p the proton mass and μ_p the proton magnetic moment. The values are taken from A. Schenck [5].

Particle	Spin	Magnetic moment [μ_p]	$ \gamma/2\pi $ [kHz/G]
Electron e^-	1/2	$657\mu_p$	≈ 2800
Muon μ^+	1/2	$3.18\mu_p$	13.6
Proton p^+	1/2	μ_p	4.3

Table 2.2: Comparison of the values of the magnetic moments and the gyromagnetic ratios of the electron, muon, and proton [6]. μ_p is the magnetic moment of the proton.

For instance, the gyromagnetic ratio of the proton differs from the gyromagnetic ratio of the muon by a factor of four. Figure 2.1 shows a comparison of different techniques and the time windows of relaxation processes and μSR is located between the NMR and Mössbauer time window.

The important point to have the possibility to use the muon as probe is the asymmetric decay of the muon. The muon decays with a probability proportional to e^{-t/τ_μ} after the time t , where τ_μ is the mentioned lifetime of the muon. The muon decays in three particle, one positron and two neutrinos:

$$\mu^+ \rightarrow e^+ + \nu_e + \bar{\nu}_\mu, \quad (2.3)$$

and the positron e^+ is the particle to detect [9]. The preferred direction of the emission of the positron is the muon spin direction at the time of the muon decay. The decay needs the weak interaction and the decay does not conserve parity⁴.

2.1.2 $\mu^+\text{SR}$ technique

This subsection discusses general experimental issues, e.g., advantages and disadvantages of the μSR technique. The time windows of different relaxation techniques are compared, e.g., the muon is a stronger probe for weak magnetic relaxation processes than Mössbauer spectroscopy. The experimental geometries of the μSR setups are presented and the measured and extracted physical observables.

Figure 2.1 shows a comparison of different techniques and the time windows of relaxation processes. $\mu^+\text{SR}$ is a technique which enables the investigate relaxation processes between 10^{-4} s and 10^{-10} s. The μSR technique has important advantages:

⁴For details, see arbitrary introductory books about particle physics, e.g. *Particles and Nuclei* by B. Povh *et al.* [10].

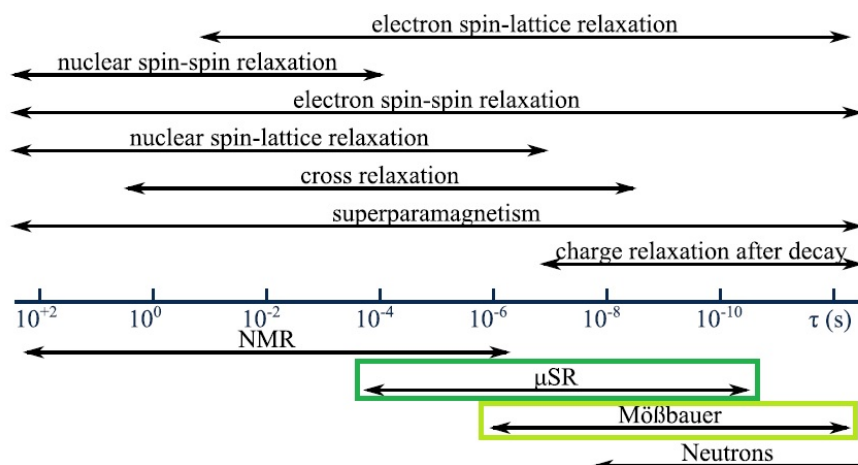


Figure 2.1: Comparison of time windows of different techniques taken from S. Kamusella *et al.* [2].

1. The restriction of a local probe in the sample, e.g., a ^{57}Fe -nucleus, is not needed. Theoretically, therefore, μSR can be done on every solid sample⁵.
2. μSR can be done in zero magnetic field, e.g., in contrast to NMR or ESR.
3. The positive muon can act as proton-like impurity, e.g., in semiconductors.
4. A stimulation/resonance excitation is not needed, e.g., which can change superconductor transition temperatures. The muons are spin polarized outside the sample before implantation.
5. The muon is a probe for very small magnetic field of fractions of a Gauss.

Therefore, the perturbation of the system of interest by applied magnetic fields or radio-frequency fields can be avoided. The often known disadvantages are:

1. The knowledge of the muon site is necessary for quantitative treatments. Here, DFT calculations are helpful or other possibilities to restrict the muon site. For instance, this is given in $\text{NaCaCo}_2\text{F}_7$ by characteristic F- μ -F state oscillations.
2. Since the muon can mimic hydrogen atoms the distortion caused by the muon is often discussed. As we will discuss, the minimal local lattice displacement distortion in $\text{NaCaCo}_2\text{F}_7$ is around 12%.
3. The muon has an upper limitation for measurements in strong magnetic fields of up to a few Tesla.
4. The muon is an exotic particle which needs a muon facility and, therefore, *beamtime* and is not available in every laboratory. However, this is no real disadvantage, more an experimental inconvenience.

⁵The question of a reasonable μSR study on Fe-diluted $\text{Li}_2(\text{Li}_{1-x}\text{Fe}_x)\text{N}$ is discussed in the *Outlook* of the corresponding $\text{Li}_2(\text{Li}_{1-x}\text{Fe}_x)\text{N}$ chapter.

To use the muon of the atmosphere one needs a long stepladder, however, the muon-beam intensity is unsatisfactory since the muons are spin unpolarized. Therefore, positive muons are produced in proton accelerators. The first step is to fire the proton into a graphite target for proton collision,

$$p + p \rightarrow \pi^+ + p + n, \quad (2.4)$$

where n is a neutron. The produced pion π^+ decays into a muon and a muon-neutrino:

$$\pi^+ \rightarrow \mu^+ + \nu_\mu. \quad (2.5)$$

To perform μ SR experiments the muon beam has to be spin polarized. The pion has spin $I = 0$. To conserve the momentum the muon and the muon-neutrino are emitted in opposite directions. In fact, the muons are longitudinal spin polarized which means momentum and spin are parallel but opposite. Experimentally, the spin orientation can be changed by a polarizer and the beam is focussed by a series of magnets.

The simplest detector arrangement for the emitted positrons contains one forward (F) and one backward (B) detector with the normal vectors of the detector faces parallel to the muon-beam direction. The counted events as a function of time is given by

$$N_{B/F} = b_{B/F} + N_{B/F}^0 e^{-t/\tau_\mu} [1 \pm A_0 P(t)]. \quad (2.6)$$

Here, N_i^0 is the initial number of events and b_i a background. This background is coming from events of cosmic muons, electronic noise and muons which have passed the sample. For small backgrounds the so-called experimental asymmetry,

$$A(t) = \frac{N_B(t) - \alpha N_F(t)}{N_B(t) + \alpha N_F(t)}, \quad (2.7)$$

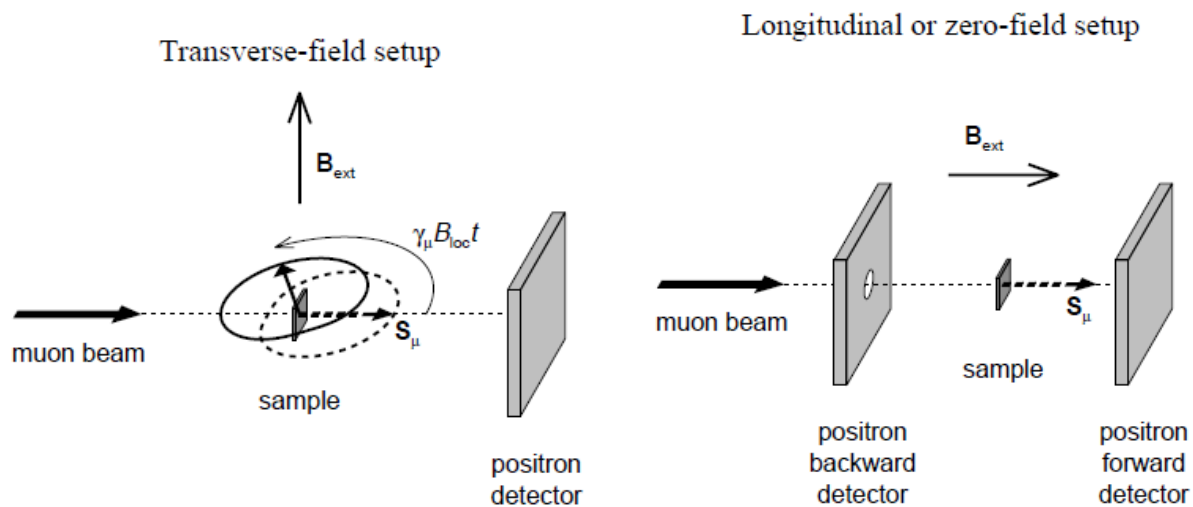
is plotted. This is a normalized difference taking into account the decay and experimental conditions. Here, α is an experimental value which depends especially on the

- detector efficiency,
- detector geometry,
- sample position, and
- sample amount.

Therefore, one can extract α and the initial asymmetry A_0 of the muon spin polarization function $P(t)$ as a function of time by a calibration run:

$$A(t) = A_0 P(t). \quad (2.8)$$

Experimentally, figure 2.2 (a) and (b) show the used experimental geometries of the muon beam with respect to the applied magnetic field. The muons are close to be 100% polarized parallel to the beam



(a) Transverse magnetic field setup, e.g., used to determine the α -value and initial total asymmetry A_0 . (b) Longitudinal magnetic field setup, e.g., to decouple the static from the dynamic relaxation contribution.

Figure 2.2: Visualization of the experimental geometries with respect to the applied magnetic field B_{ext} , taken from P. Dalmas de Réotier and A. Yaouanc [7].

direction. In contrast to the figures, one should keep in mind that muon spin and momentum are opposite in reality. Figure 2.2 (a) shows the transverse geometry with the applied magnetic field perpendicular to the beam leading to a spin precession. This geometry is used for the calibration runs getting α and initial A_0 in the paramagnetic phase. Figure 2.2 (b) shows the longitudinal setup in which the magnetic field is parallel to the muon beam. Here, it is possible to distinguish between static and dynamic local fields at the muon site when the static local fields do not exceed the applied field by orders of magnitude. Often there are more detectors installed in left (L) and right (R) directions allowing alternative and complementary treatments. The side detectors are in the following not further considered.

2.1.3 Muon interactions and local magnetic fields

It is a very important question how the muon interacts with the sample. The important quantity which is probed is the local magnetic field. The local magnetic field is the sum of different contributions. The origin of the measured magnetic field is the key of the understanding.

The muon starts to enter the sample with an energy in the order of mega electron volts. The muon interacts with the sample and loses the kinetic energy in the order of nanoseconds. It is assumed that the thermalization process involves only electrostatic interactions which conserves the muon spin polarization. It is always assumed that the muon finds the lowest energy minimum by a Bloch picture: The muon reaches a few electron volts after the main (electric) energy-loss processes and is then given by a Bloch function and still delocalized similar to electrons in a metal which are quasi free. Additional energy losses lead to a localization of the muon in the energy minimum and the

muon loses the possible description of the plane wave modulated by the periodicity of the lattice. As mentioned above, the muon does not carry a quadrupole moment and is, therefore, blind for electric quadrupole interactions.

The local magnetic field at the muon site is given by eight contributions:

$$\mathbf{B}_{\text{loc}} = \mathbf{B}_{\text{con}} + \mathbf{B}_{\text{RKKY}} + \mathbf{B}_{\text{trans}} + \mathbf{B}'_{\text{dip}} + \mathbf{B}_{\text{L}} + \mathbf{B}_{\text{dem}} + \mathbf{B}_{\text{dia}} + \mathbf{B}_{\text{ext}}, \quad (2.9)$$

see below. The contributions \mathbf{B}'_{dip} , \mathbf{B}_{L} , and \mathbf{B}_{dem} are parts of the total dipole interaction field,

$$\mathbf{B}_{\text{dip}} = \mathbf{B}'_{\text{dip}} + \mathbf{B}_{\text{L}} + \mathbf{B}_{\text{dem}}. \quad (2.10)$$

Even when some contributions are not important in the following, it shall be discussed for completeness because the magnetic field is what the muon probes and therefore the heart of μSR . The total dipole interaction is given by

$$\mathbf{B}_{\text{dip}} = \frac{\mu_0}{4\pi} \sum_{i=1}^N (-g_i \mu_B) \left[-\frac{\mathbf{J}_i}{r_i^3} + \frac{3(\mathbf{J}_i \cdot \mathbf{r}_i)\mathbf{r}_i}{r_i^5} \right]. \quad (2.11)$$

Here, the magnetic moment $\mathbf{m}_i = -g_i \mu_B \mathbf{J}_i$ is given by the total angular momentum \mathbf{J}_i and the atomic splitting factor g_i at site i . This expression can be formulated by the three mentioned contributions $\mathbf{B}'_{\text{dip}} + \mathbf{B}_{\text{L}} + \mathbf{B}_{\text{dem}}$ which should not be developed here in detail. The terms and physical meaning of the local magnetic field are the following:

- Contact hyperfine field \mathbf{B}_{con}

It is known, dipole-dipole interactions between the nucleus and the s -electrons with $l = 0$ are zero, because of the spherical shape is the average $\langle B_s \rangle = 0$. However, s -electrons have a non-zero probability $|\psi(0)|^2$ of the wavefunction ψ at the nucleus. Spins with the same polarization feeling an attractive force, e.g., equally polarized s - and d -electrons, and a higher opposite spin density is remained at the nucleus resulting in an effective core polarization. This is a direct interaction of s - and valence electrons between the magnetic moments called Fermi contact interaction⁶.

In μSR , the contact hyperfine field \mathbf{B}_{con} is a result of the spin density of electrons at the muon site by the presence of polarized conduction electrons. Here, the electron leads to a polarization of the muon because the electron is partially at the muon position and, therefore, this interaction scales with the spin density $\rho_e(0)$ at the muon site. This contribution plays, therefore, only a role in metals because then $\rho_e(0) \neq 0$ (delocalization). Effectively, the electrons form a cloud around the muon.

- RKKY field \mathbf{B}_{RKKY}

The Rudermann-Kittel-Kasuya-Yoshida (RKKY) field \mathbf{B}_{RKKY} is a contribution in metals reflecting the so-called indirect RKKY interaction. The reason is that conduction electrons are

⁶This interaction will appear again in Mössbauer spectroscopy and the $\text{Li}_2(\text{Li}_{1-x}\text{Fe}_x)\text{N}$ study. For this reason it is explained starting from the atomic picture.

polarized by localized magnetic moments. This is an indirect process mediated by Fermi contact interaction. The spins of the conduction electrons are coupled to the localized spins and contact interaction leads to a contribution to the local magnetic field of the muon. An often mentioned particle picture is that the electron moves, couples to the local moment, adapts the polarization of the localized moment and transfers this moving to the muon.

- Transferred hyperfine field $\mathbf{B}_{\text{trans}}$

The possibility of the overlap of the wavefunction of the muon and electrons is given and can be important in insulators depending on the muon site. This contribution is called transferred hyperfine field and sometimes included in \mathbf{B}_{RKKY} because of the comparable form of the term:

$$\mathbf{B}_{\text{trans}} = \frac{\mu_0}{4\pi} \sum_{i=1}^N \frac{(-g_i \mu_B) H_{r_i}}{v_c} \mathbf{J}_i, \quad (2.12)$$

see P. Dalmas de Réotier *et al.* [4]. Here, N sums over nearest neighbors and H_{r_i} are hyperfine constants, v_c the the unitless dipole tensor and g_i the spectroscopic splitting factor⁷. $\mathbf{B}_{\text{trans}}$ and \mathbf{B}_{RKKY} are called together hyperfine field \mathbf{B}_{hyp} ⁸.

- Dipole field \mathbf{B}'_{dip}

Analytically, the total dipole field \mathbf{B}_{dip} can expressed by a Lorentz sphere assumed to be smaller than a typical domain size separating the dipole interaction in three parts according to P. Dalmas de Réotier and A. Yaouanc [7] and therein. Typically, a few thousands moments insight the Lorentz sphere leads to a high accuracy to take into account a magnetic polarization. \mathbf{B}'_{dip} is the term which restricts the dipole sum over the lattice to the Lorentz sphere. \mathbf{B}'_{dip} depends on the symmetry of the muon site and can be even canceled in antiferromagnets. The rest of \mathbf{B}_{dip} is given by the following two contributions \mathbf{B}_{L} and \mathbf{B}_{dem} outside the Lorentz sphere:

- Lorentz field \mathbf{B}_{L}

This contribution can be expressed by $\mathbf{B}_{\text{L}} = \mu_0 \mathbf{M}_{\text{sat}}/3$. \mathbf{M}_{sat} is the saturation magnetization and given by the vector sum of moments on the surface of the sphere.

- Demagnetization field \mathbf{B}_{dem}

For this contribution one obtains $\mathbf{B}_{\text{dem}} = -(\mu_0/3)\mathbf{N} \cdot \mathbf{M}_{\text{bulk}}$ for an ellipsoidal sample. Here, \mathbf{M}_{bulk} is the bulk magnetization and \mathbf{N} the demagnetization tensor which depends on the shape of the sample. For instance, for a sphere $\mathbf{N} = 1/3$ is reduced to a scalar. This term describes the macroscopic bulk magnetization which can be strongly anisotropic and in powder samples leads to the so-called powder broadening in transverse field measurement, e.g., see H.-H. Klaus [11].

- Diamagnetic field \mathbf{B}_{dia}

The diamagnetic field plays a role in superconductors which are not a topic of this thesis. \mathbf{B}_{dia} is negligible in magnets.

⁷Constants like μ_0 are explained in *Acronyms and Symbols*.

⁸One should clearly distinguish between the Mössbauer magnetic hyperfine field which includes more contributions as I will point out later.

- External field \mathbf{B}_{ext}

\mathbf{B}_{ext} is the applied magnetic field. In our case, the transverse or longitudinal magnetic field with respect to the muon-beam direction as visualized in the previous subsection. For paramagnets and superconductors there is usually a frequency shift observed and \mathbf{B}_{loc} is different from the external field but $\mathbf{B}_{\text{ext}} \gg |\mathbf{B}_{\text{loc}} - \mathbf{B}_{\text{ext}}|$. The ratio K , with

$$K = \frac{\mathbf{B}_{\text{ext}} \cdot (\mathbf{B}_{\text{con}} + \mathbf{B}_{\text{trans}} + \mathbf{B}'_{\text{dip}})}{B_{\text{ext}}^2}, \quad (2.13)$$

is called Knight shift related to the paramagnetic and diamagnetic susceptibility.

For an antiferromagnet in zero field (ZF) $\mathbf{B}_{\text{dem}} = \mathbf{B}_{\text{L}} = 0$. In a paramagnet or a saturated magnet $\mathbf{B}_{\text{dem}} = -\mathbf{B}_{\text{L}}$ and for this reason $\mathbf{B}'_{\text{dip}} = \mathbf{B}_{\text{dip}}$. It is emphasized that \mathbf{B}'_{dip} depends strongly on the muon site.

2.1.4 Muon-spin polarization functions: Overview

The muon-spin polarization function $P_{\alpha}(t) = A(t)/A_0$ describes the time-dependence of the muon-spin polarization. Therefore, basic aspects and the used polarization function are discussed. Every polarization function and the physical interpretation is emphasized.

In the following, the used muon-spin polarizations are discussed including their general and physical understanding. The development of the polarization function can fill books and is here partially skipped. The starting point of the calculation of the polarization function $P_{\alpha}(t)$ as a function of time is the field-distribution function $D(\mathbf{B}_{\text{loc}})$ and

$$P_{\alpha}(t) = \int \hat{S}_{\mu,\alpha}(t, \mathbf{B}_{\text{loc}}) D(\mathbf{B}_{\text{loc}}) d^3\mathbf{B}_{\text{loc}}. \quad (2.14)$$

Here, $\alpha = \{X, Y, Z\}$ is the polarization function in the three spatial directions. The Z -axis is parallel to the muon-beam measured by the forward and backward detector, respectively. Here, the function $P_Z(t)$ is of main interest. The field-distribution function $D(\mathbf{B}_{\text{loc}})$ is often split into the product of the three coordinates and their magnetic-field projections B_{loc}^X to

$$D(\mathbf{B}_{\text{loc}}) = D_c(B_{\text{loc}}^X) D_c(B_{\text{loc}}^Y) D_c(B_{\text{loc}}^Z), \quad (2.15)$$

when possible. Table 2.3 shows the list of muon spin polarizations or parts of polarization functions important in this thesis which are explained and summarized in the following subsections. The total muon-spin polarization can be constructed out of this functions.

In general, the entire muon spin polarization function can be a product and sum of the different here presented polarization functions:

$$A_0 P_Z(t) = A_0 \sum_{i=1}^N \prod_{j=1}^{M_i} P_{Z,i,j}(t). \quad (2.16)$$

Name	Formula	Physical understanding
Simple cosine	$\frac{1}{3} + \frac{2}{3} \cos(\gamma_\mu B t)$ $= \frac{1}{3} + \frac{2}{3} \cos(\omega_\mu t)$	single static magnetic field (powder)
Kubo-Toyabe	$\frac{1}{3} + \frac{2}{3} e^{-\Delta^2 t^2 / 2} (1 - \Delta^2 t^2)$	Static Gaussian isotropic field distribution in ZF
Exponential	$e^{-\lambda t}$	Motional-narrowing limit of the relaxation
Stretched exponential	$e^{-(\lambda t)^\beta}$ ($0.9 > \beta > 0.4$)	Distribution of relaxation rates, e.g., bond-disordered systems
Gaussian	$e^{-(\sigma t)^2}$	Gaussian field distribution often given by nuclear moments
Brewer	$G(t)$	Time evolution of quantum state by dipole interaction (here: F- μ^+ -F state)

Table 2.3: Full or fractional muon spin polarization functions $P_{Z,i}(t)$ which are important in this thesis. The used symbols are explained in detail in the following and in the case of $G(t)$ in the main text. The background of the spectra is not included. A possible part between 0 and 1/3 is not mentioned in the Gaussian and stretched model which can be taken into account.

One should keep in mind the adequate using of possible static 1/3-parts (powder) and the introduction of a fractionalization of this part in this formula. Since a static relaxation/rotation contains a 1/3-part in a powder, this part varies between 0 (no magnetic field component parallel to the polarization) and 1 (full local magnetic field parallel to the polarization) in a crystal. An additional independent muon site is given by an additional summand and, therefore, N muon sites. The background is explained in the part of the stretched exponential.

2.1.5 Simple cosine

This muon-spin polarization function reflects a homogenous static magnetic field B_{loc} at the muon site leading to a muon- spin precession with a frequency $\omega_\mu = \gamma_\mu B_{\text{loc}}$. This polarization function plays a very important role during the calibration runs.

In a sample in which all muons probe the same local magnetic field tilted by an angle θ with respect to the initial muon spin polarization \mathbf{S}_μ (antiparallel to the beam) the muon-spin precession is given by

$$P_\alpha(t) = \cos^2 \theta + \sin^2 \theta \cos(\omega_\mu t). \quad (2.17)$$

For instance, for $\theta = 0$ one would not see any time-dependence. On the other hand, for $\theta = \pi/2$ all muon spins precess in the circle perpendicular to the magnetic field in plane. Formally, the field distribution is given by a Dirac delta function. The muon-spin polarization has a time dependence although the magnetic field is static. In a powder average one obtains

$$P_Z(t) = \frac{1}{3} + \frac{2}{3} \cos(\omega_\mu t) \quad (2.18)$$

for the longitudinal field setup because one third of the spins (or exactly spin projections) are parallel to the field. Therefore, a homogenous local magnetic field at the muon site leads to an oscillation with a frequency ω_μ . The 1/3-part is also called tail because it is the preserved part of the polarization function for $t \rightarrow \infty$ and disappears for dynamical local fields at the muon site, see below.

2.1.6 Gaussian Kubo-Toyabe

The Kubo-Toyabe function is the result of the assumed (quasi) static-field distribution probed by the muon. Here, one distinguishes between the Gaussian and Lorentzian Kubo-Toyabe function assuming the initial magnetic-field distribution is Gaussian or Lorentzian, respectively. The field distribution is assumed to be isotropic in all three Cartesian components and centered around zero. The Kubo-Toyabe function is used in the NaCaCo₂F₇ chapter to exclude a relaxation by a static magnetic field.

The static Gaussian Kubo-Toyabe function is the result of Gaussian field distributions. Here,

$$D_c(B_{\text{loc}}^\alpha) = \frac{1}{\sqrt{2\pi}\Delta_G} \exp\left[-\frac{(B_{\text{loc}}^\alpha)^2}{2\Delta_G^2}\right], \quad (2.19)$$

in which Δ_G is the variance of the Gaussian distribution. The result is

$$P_Z(t) = \frac{1}{3} + \frac{2}{3}(1 - \gamma_\mu^2 \Delta_G^2 t^2) \exp\left(-\frac{\gamma_\mu^2 \Delta_G^2 t^2}{2}\right) \quad (2.20)$$

and the ZF Kubo-Toyabe function. $P_Z(t)$ has a dip at

$$t_d = \frac{\sqrt{3}}{\gamma_\mu \Delta_G}, \quad (2.21)$$

with $P(t_d) = 0.03583$. $P_Z(t)$ goes to 1/3 for $t \rightarrow \infty$ and for small times $P_Z(t)$ can be approximated by

$$P_Z(t) = 1 - \gamma_\mu^2 \Delta_G^2 t^2. \quad (2.22)$$

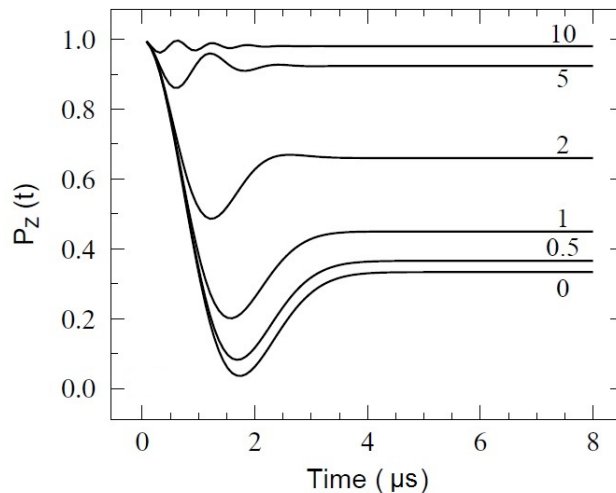


Figure 2.3: Decoupling: Dependence of the longitudinal polarization function for various applied longitudinal magnetic fields (units of Δ_G) derived for a static isotropic Gaussian field distribution after [7]. The value of $B_L = 0$ corresponds to the Gaussian Kubo-Toyabe function in ZF. The polarization function quenches for large fields $B_L > 5\Delta_G$.

The Gaussian Kubo-Toyabe function can be extended to applied longitudinal magnetic fields B_L . For large applied longitudinal fields ($B_L \approx 10\Delta_G$) it leads to a quenching of the depolarization and $P_Z(t, B_L) \approx 1$. This is often called decoupling and used to distinguish between static and fluctuating magnetic fields at the muon site. Figure 2.3 shows a simulated decoupling for various longitudinal depolarization functions depending on the magnetic field. The physical origin of the Gaussian field distribution can be given by dense electronic or nuclear moments.

It is mentioned for completeness: A Lorentzian magnetic field distribution with a half-width maximum Δ_L leads to

$$P_Z(t) = \frac{1}{3} + \frac{2}{3}(1 - \gamma_\mu \Delta_L t) \exp(-\gamma_\mu \Delta_L t). \quad (2.23)$$

For small times the polarization function is exponential-like and not Gaussian as in the Kubo-Toyabe case. This field distribution is observed in systems with diluted magnetic impurities which are uncorrelated.

2.1.7 Exponential

The exponential shape of the polarization function is a consequence of the motional-narrowing limit well known from NMR. Here, the effective field distribution of the muon is narrowed and reduced by dynamics. The correlation time τ_c is introduced together with the autocorrelation function below.

The exponential shape of the relaxation by dynamical local magnetic fields of the muon site can be obtained by different polarization functions in the so called motional-narrowing limit.

In the following we are starting from the model of a spin-reversal process because it is a very intuitive

and simple model⁹. Let us assume that the spins associated with a magnetic field $\mathbf{B}_f = \pm B_f \hat{e}_X$ flip from parallel to antiparallel to the X-axis and reverse with a frequency ν_c .

There are two possibilities to proceed which are called the strong- and weak-collision model. In the strong-collision model the muon probes a sudden change in \mathbf{B}_{loc} . The weak-collision model uses a gradual change such as in the Gaussian-Markov approach. In the strong-collision model, the Laplace transformation¹⁰ of the function

$$P_Z(s) = \frac{s + \nu_c}{s^2 + \nu_c s + \gamma_\mu B_f^2} \quad (2.24)$$

is the polarization function $P(t)$. The four regimes are:

- Strong field $\nu_c < 2\gamma_\mu B_f$.

The definitions

$$\omega_{\text{eff}} = \sqrt{\gamma_\mu^2 B_f^2 - \frac{\nu_c^2}{4}} \quad (2.25)$$

and

$$\tan \phi = \frac{\nu_c}{2\omega_{\text{eff}}} \quad (2.26)$$

lead to

$$P_Z(t) = \frac{1}{\cos \phi} \exp\left(-\frac{\nu_c t}{2}\right) \cos(\omega_{\text{eff}} t - \phi). \quad (2.27)$$

Therefore, $P_Z(t)$ is an exponentially damped oscillation with a reduced frequency shifted by a phase ϕ .

- $\nu_c = 2\gamma_\mu B_f$.

Here, the time dependence is given by

$$P_Z(t) = \left(1 + \frac{\nu_c t}{2}\right) \exp\left(-\frac{\nu_c t}{2}\right), \quad (2.28)$$

which is an exponential.

- Weak field $\nu_c > 2\gamma_\mu B_f$.

The introduction of

$$\nu_{\text{eff}} = \sqrt{-\gamma_\mu B_f^2 + \frac{\nu_c^2}{4}} \quad (2.29)$$

yields

$$P_Z(t) = \left(-\frac{\nu_c t}{2}\right) \left[\cosh(\nu_{\text{eff}} t) + \frac{\nu_c}{2\nu_{\text{eff}}} \sinh(\nu_{\text{eff}} t) \right]. \quad (2.30)$$

The important limit of this formula is the motional-narrowing limit.

⁹It helps to waste not to much time on formalism and equations which are not needed in the following. However, for the interested reader an introduction in Redfield theory is proposed.

¹⁰Per definition, the Laplace transform $f(s)$ of a function $f(t)$ is given by $f(s) = \int_0^\infty f(t) \exp(-st) dt$, see an arbitrary introduction in mathematical physics.

- Motional narrowing limit $\nu_c \gg 2\gamma_\mu B_f$.

The limit of the upper equation is

$$P_Z(t) = \exp\left(-\frac{\gamma_\mu^2 B_f^2}{\nu_c} t\right). \quad (2.31)$$

The exponential relaxation can be obtained by field-distribution models in the same way, however, the analytical effort is higher and the relaxation is described by terms representing the corresponding distribution. For instance, an isotropic Gaussian distribution in the extreme motional-narrowing limit results in

$$P_Z(t) = \exp(-\lambda_Z t), \quad (2.32)$$

with

$$\lambda_Z = \frac{2\gamma_\mu^2 \Delta_G^2}{\nu_c} = 2\gamma_\mu^2 \Delta_G^2 \tau_c, \quad (2.33)$$

in which τ_c is the so-called correlation time and Δ_G is the introduced width of the Gaussian distribution used in the Gaussian Kubo-Toyabe subsection. Interestingly, the result of the Gaussian field distribution replaces $B_f \mapsto \sqrt{2}\Delta_G$ of the spin-reversal calculation. τ_c is a measure of the exponential decay of the autocorrelation function of the fluctuating magnetic field:

$$\langle B_i(t)B_i(t+\tau) \rangle_t = \langle B_i^2 \rangle \exp\left(-\frac{|\tau|}{\tau_c}\right). \quad (2.34)$$

Quantitatively, it gives a statement how much the value $B_i(t)$ at time t deviates after the time τ leading to the value $B_i(t+\tau)$ and describes the correlation of the magnetic field with itself. One should emphasize:

- Obviously, for $\tau = 0$ it yields $\langle B_i(t)B_i(t+\tau) \rangle_t = \langle B_i^2 \rangle$.
- $\langle B_i(t)B_i(t+\tau) \rangle_t$ decreases for long times ($\tau \rightarrow \infty$) which means the correlation function and, therefore, the correlation with the start value $B_i(t)$ decreases more and more with time. Finally, $\langle B_i(t)B_i(t+\tau) \rangle_t$ goes to zero and has nothing to do with the initial value.
- $\langle B_i(t)B_i(t+\tau) \rangle_t$ goes for a fixed τ for $\tau_c \rightarrow \infty$ to $\langle B_i(t)B_i(t+\tau) \rangle_t = \langle B_i^2 \rangle$ and is consistent with the $\tau = 0$ case. In other words, the magnetic field is highly correlated in time.
- $\langle B_i(t)B_i(t+\tau) \rangle_t$ goes for a fixed τ for $\tau_c \rightarrow 0$ to zero and the magnetic field is fully uncorrelated in time. In other words, the initial field value at time t does not influence the next magnetic field value at time $t+\tau$. The magnetic field changes too strongly.

A set of phenomenological equations is given by the so-called Bloch equations. These equations describe the time evolution of the magnetization relaxing back to the equilibrium state after switching off an external perturbation (or excitation in NMR). These equations are

$$\frac{dP_Z(t)}{dt} = -\lambda_Z P_Z(t), \quad (2.35)$$

$$\frac{dP_X(t)}{dt} = -\lambda_X P_X(t) + \gamma_\mu B_{\text{loc}} P_Y(t), \quad (2.36)$$

$$\frac{dP_Y(t)}{dt} = -\lambda_X P_Y(t) - \gamma_\mu B_{\text{loc}} P_X(t), \quad (2.37)$$

assuming a static field B_{loc} to the Z-axis. Here, $\lambda_Z = 1/T_1$ is the so-called longitudinal or (μ SR) spin-lattice relaxation rate. The name arises from the dynamical origin and the needed energy transfer of the muon and the crystal lattice. $\lambda_X = 1/T_2$ is called transverse or spin-spin relaxation rate. It arises from the interaction of the muon spin with the surrounded spins and corresponding field distribution. This analogy to NMR is mentioned to avoid confusion because of the sometimes used name (μ SR) spin-lattice relaxation rate. The Bloch equations lead to exponentially damped relaxation functions

$$P_Z(t) = P_Z(t=0) \exp(-\lambda_Z t), \quad (2.38)$$

$$P_X(t) = P_X(t=0) \exp(-\lambda_X t) \cos(\gamma_\mu B_{\text{loc}} t), \quad (2.39)$$

$$P_Y(t) = -P_X(t=0) \exp(-\lambda_X t) \sin(\gamma_\mu B_{\text{loc}} t). \quad (2.40)$$

For details, see A. Yaouanc and P. Dalmas de Réotier [4]. A rather compact discussion of the fluctuation regimes according to the Redfield and a comparison of extended calculations by Hayano *et al.* [12] is presented by H.-H. Klauss [11] led to four different τ_c regimes. The full solution by Hayano *et al.* is given by

$$\frac{1}{T_1} = \frac{1}{2} M_2 \tau_c \left[\frac{1}{1 + (\omega_0 - \omega_J)^2 \tau_c^2} + \frac{3}{1 + \omega_0^2 \tau_c^2} + \frac{6}{1 + (\omega_0 + \omega_J)^2 \tau_c^2} \right] \quad (2.41)$$

and

$$\frac{1}{T_2} = \frac{1}{4} M_2 \tau_c \left[4 + \frac{6}{1 + \omega_J^2 \tau_c^2} \right] + \frac{1}{2} \frac{1}{T_1}. \quad (2.42)$$

Here, J is the quantum number of the total moment of the paramagnetic ion with the Larmor frequency $\omega_J = \gamma_J B_{\text{ext}}$, $\omega_0 = \gamma_\mu B_{\text{ext}}$ and M_2 is the so called second moment in the Van Vleck limit. However, in the motional narrowing limit ($\tau_c \ll \omega_J^{-1} \ll \omega_0^{-1}$) this yields

$$\frac{1}{T_1} = \frac{1}{T_2} = 5M_2 \tau_c \quad (2.43)$$

and the longitudinal and transverse relaxation rates are identical, which is not the case in general.

2.1.8 Stretched exponential

The stretched exponential is the used polarization function for the double perovskite $\text{BaTi}_{0.5}\text{Mn}_{0.5}\text{O}_3$. The stretched exponential is a more general polarization function often observed in disordered compounds reflecting a distribution of different local relaxation rates.

The polarization function is described by a stretched exponential¹¹,

$$P_Z(t) = a \exp \left[-(\lambda t)^\beta \right] + b = a e^{-(\lambda t)^\beta} + b. \quad (2.44)$$

Here, λ is the μ^+ relaxation rate of the muon-spin polarization, which can be a static or dynamical relaxation, and the positive β is the so-called stretched exponent. This behavior is known as Kohlrausch law. In general, in some books and papers the letter λ means only a dynamical relaxation which is much more precise, however, one should keep in mind this accuracy in the literature.

b is the fraction of muons not stopping in the sample, e.g., in the silver plate, depending on the spectrometer and a is the fraction of muons stopping in the sample. In detail, the second term is given by $b \exp(\lambda_b t)$ including a possible relaxation of the background material. In many cases it is set to

$$b \exp(-\lambda_b t) \approx b, \quad (2.45)$$

because of practical reasons, quantitatively $\lambda_b \ll \lambda$. In studies where the changes of the relaxation rates are in the same order of λ_b this can not be neglected, e.g., in selected superconductors concerning time reversal symmetry-breaking studies. The stretched exponential model reflects for $\beta \approx \frac{1}{2}$ a huge amount of relaxation channels and has a phenomenological nature:

$$P_Z(t) = a \exp \left[-\sqrt{(\lambda t)} \right]. \quad (2.46)$$

A similar model is sometimes taken for the depolarization of the population difference of the nuclei in NMR [13]. The relaxation-channel distribution or frequency distribution is a consequence of the intrinsic disorder reflecting the microscopic magnetic disorder, e.g., because of structural disorder which is magnetoelastically coupled, e.g., because of the Ti^{4+} and Mn^{4+} randomness in $\text{BaTi}_{0.5}\text{Mn}_{0.5}\text{O}_3$. A mathematical model assumes the mentioned stretched exponential as sum of pure exponential decays with a defined probability per exponential. This assumes the motional-narrowing limit, one can write

$$e^{-(\lambda t)^\beta} = \int_0^\infty P(s, \beta) e^{-s\lambda t} ds \quad (2.47)$$

where $P(s, \beta)$ is the distribution function of relaxation rates with the Laplace transformation parameter s . $P(s, \beta)$ can be computed by the expansion

$$P(s, \beta) = -\frac{1}{\pi s} \sum_{k=0}^{\infty} \frac{(-1)^k}{k!} \sin(\pi \beta k) \Gamma(\beta k + 1) s^{-\beta k} \quad (2.48)$$

for $\beta < 1$, where $\Gamma(x)$ is the well-known gamma function, for details see M. N. Berberan-Santos *et al.* [14]. For positive integer n one gets $\Gamma(n) = (n-1)!$. For $\beta = \frac{1}{2}$ one obtains

$$P(s, \beta = \frac{1}{2}) = \frac{1}{2s\sqrt{\pi}} \sqrt{s} e^{(-\frac{s}{4})}. \quad (2.49)$$

¹¹For compactness, $\exp(\dots)$ is written as $e^{(\dots)}$ insight the integral and in longer formula.

Here, the distribution arises from an ensemble of independent relaxation channels in the motional-narrowing limit. Experimentally, a convergence of β close to $\beta = \frac{1}{2}$ is often observed in disordered compounds down to low temperatures. One should keep in mind, the mean value $\langle \frac{1}{\lambda} \rangle$ of relaxation rates is given by

$$\langle \frac{1}{\lambda} \rangle \equiv \int_0^\infty e^{-(\lambda t)^\beta} dt = \frac{1}{\lambda\beta} \Gamma\left(\frac{1}{\beta}\right). \quad (2.50)$$

So, λ can only be understood for $\beta = 1$ as one channel rate with $\langle \frac{1}{\lambda} \rangle = \frac{1}{\lambda}$.

2.1.9 Pure Gaussian

The Gaussian-like relaxation by nuclear moments for small times is mentioned in the CaF₂ and NaCaCo₂F₇ chapter for the purpose of comparison of the spectra. Therefore, it is discussed here for completeness.

For $\beta = 2$ of the stretched exponential one obtains the Gaussian polarization function often written as

$$P_Z(t) = \exp(-\sigma^2 t^2), \quad (2.51)$$

instead of λ^2 reflecting a (quasi) static field. Such a behavior is often observed at high temperatures because of the field distribution of nuclear moments at early times $t < 1 \mu s^{-1}$. Since $P_Z(t \rightarrow \infty) = 0$ this term is often used as product with other polarization functions describing this time part and a possible the 2/3(...) + 1/3-fractionalization is not considered. However, the full description is given by the (dynamical) Kubo-Toyabe function.

Obviously, for $\beta = 1$ of the stretched exponential model one ends up in the conventional single exponential. Therefore, the stretched-exponential is a very general model as starting point of the data analysis (motional-narrowing limit).

2.1.10 Quantum approach

The quantum approach of the polarization function plays a very important role to understand and to describe a so called F- μ^+ -F state polarization function observed in fluorides such as CaF₂ and NaCaCo₂F₇. Therefore, it is a key polarization function of this work. Here, the analytical solution is presented of the interaction of the muon with one single nucleus with spin I . For fluorine $I = \frac{1}{2}$ and it exists just one isotope ¹⁹F in nature. The extension to two noninteracting nuclei with the muon located in the middle of the two nuclei is discussed in the CaF₂ chapter.

The polarization function treatments discussed so far are classical and based on the magnetic-field distribution. Quantenmechanically, the polarization of interest can be calculated by

$$P_Z(t) = \frac{1}{2} \text{Tr}\{\rho_{\text{tot}} \sigma^Z \sigma^Z(t)\} \quad (2.52)$$

and

$$P_X(t) = \frac{1}{2} \text{Tr}\{\rho_{\text{tot}} \sigma^X \sigma^X(t)\}, \quad (2.53)$$

with

$$\sigma^\alpha(t) = \exp\left(i\frac{\hat{\mathcal{H}}_{\text{tot}}t}{\hbar}\right)\sigma^\alpha\exp\left(-i\frac{\hat{\mathcal{H}}_{\text{tot}}t}{\hbar}\right). \quad (2.54)$$

Here, ρ_{tot} is the density matrix of the total system, σ^α the Pauli operator of the muon spin and $\hat{\mathcal{H}}_{\text{tot}}$ the time-independent Hamiltonian of the muon-spin-system ensemble.

The entanglement of states and large dimension of the Hilbert space allows only in rare cases an analytical solution. The dimension of the Hilbert space of N spins with spins I is equivalent to $2 \times (2I + 1)^N$, which is even for few nuclei quiet huge.

An analytical solution is possible for one arbitrary spin I interacting with the muon. This solution is important to describe a so called F- μ^+ state. The main axis of the axial electric-field distribution should be parallel to the Z-axis leading to the Hamiltonian

$$\hat{\mathcal{H}}_{\text{tot}} = \hbar \left[-\frac{\omega_\mu}{2}\sigma^Z - \omega_I I^Z + \hat{\mathcal{H}}_q + \frac{\omega_{I,d}}{2}(\sigma \cdot \mathbf{I} - 3I^Z\sigma^Z) \right], \quad (2.55)$$

with the quadrupole term

$$\hat{\mathcal{H}}_q = 3\omega_E \left[(I^Z)^2 - \frac{I(I+1)}{3} \right], \quad (2.56)$$

which considers a muon-induced quadrupole interaction influencing a neighbor spin $I > 1/2$. Here, $\omega_\mu = \gamma_\mu B_{\text{ext}}$, $\omega_I = \gamma_I B_{\text{ext}}$ with the external magnetic field B_{ext} along the Z-axis and the quadrupole frequency is given by

$$\omega_E = \frac{eqQ}{4\hbar I(2I-1)}, \quad (2.57)$$

with the quadrupole moment Q and the charge number q . The frequency

$$\omega_{I,d} = \frac{\mu_0}{4\pi} \frac{\gamma_\mu \gamma_I \hbar}{r_I^3} \quad (2.58)$$

is the dipole frequency which will play an important role. This yields the analytical solution of the longitudinal polarization function

$$P_Z(t) = \frac{1}{2I+1} \sum_m \frac{S_m^2 + R_m^2 \cos\left(\sqrt{S_m^2 + R_m^2}t\right)}{S_m^2 + R_m^2}, \quad (2.59)$$

with the introduced notations

$$R_m = \frac{\omega_{I,d}}{2} \sqrt{I(I+1) - m(m-1)} \quad (2.60)$$

and

$$S_m = (2m-1) \left(3\omega_E + \frac{\omega_{I,d}}{2} \right) - \omega_I + \omega_\mu, \quad (2.61)$$

according to A. Yaouanc and P. Dalmas de Réotier [4] and therein.

$P_z(t)$ is a sum of cos functions. Qualitatively, the muon probes a superposition of oscillations and time dependencies of the total wavefunction. This upper equations play a role for the further discussed F- μ state involving the spin-1/2-muon and the spin-1/2- ^{19}F nucleus to construct the F- μ -F state and

the corresponding polarization function $G(t)$. This is discussed below.

For a considerable number of nuclei the local-magnetic-field (LMF) approximation can be used leading to the Hamiltonian

$$\hat{\mathcal{H}}_{\text{LMF}} = \gamma_{\mu} S \cdot \langle B \rangle \quad (2.62)$$

and to the Kubo-Toyabe function probing random localized Gaussian fields. The most important difference is that the quantum approach leads to oscillations for $t \rightarrow \infty$ in contrast to the Kubo-Toyabe case. The given dipole-interaction at the muon site can be associated with a static nuclear magnetic field. However, there is a time dependence of the wavefunction because of the fact that the eigenstate is not necessarily an eigenstate of the Hamiltonian [15]. This leads to the time dependence and a slow dynamical relaxation as shown by the missing 1/3 part in the microscopic quantum picture.

2.2 ^{57}Fe -Mössbauer spectroscopy

This section describes the basics of ^{57}Fe -Mössbauer spectroscopy and the Mössbauer effect in general. ^{57}Fe -Mössbauer spectroscopy is needed for the second part of this work of the Fe-diluted $\text{Li}_2(\text{Li}_{1-x}\text{Fe}_x)\text{N}$ study. The details of the hyperfine interactions, the transition probabilities and the two-level Blume model are discussed in the main text of the $\text{Li}_2(\text{Li}_{1-x}\text{Fe}_x)\text{N}$ results for convenience. The data fit was done by Moessfit [3]. This section contains basic knowledge which can be found in

- *Mössbauer Effect in Lattice Dynamics: Experimental Techniques and Applications* by Y.-L. Cheng and D.-P. Yang [16] and
- *Mössbauer Spectroscopy and Transition Metal Chemistry - Fundamentals and Applications* by P. Gütlich, E. Bill, A. X. Trautwein [17].

Basic statements contained in conventional Mössbauer textbooks are not further cited in the following.

2.2.1 The Mössbauer effect: Intuitive overview

The Mössbauer effect, the recoil-energy-free nuclear-resonance absorption, allows to perform Mössbauer spectroscopy which is a nuclear spectroscopy avoiding the huge recoil energy which is expected for a nuclear-resonance transitions. The Mössbauer effect is intuitively discussed and the nuclear transitions of the decays of ^{57}Co and ^{57}Fe are important for ^{57}Fe -Mössbauer spectroscopy.

In the year 1961 Rodolf L. Mössbauer has received the Nobel prize in physics for the observation of the recoil-energy-free nuclear resonance absorption.

Historically, one had asked for the possibility to have a spectroscopy method in the energy range of keV similar to the optical spectroscopy. For this purpose, the conventional recoil energies are compared in atomic and nuclear physics in the following which shows the fundamental difference in spectroscopy.

An atom gets a recoil after the emission or absorption of an electromagnetic quantum of the energy getting $\hbar\omega$. To excite the atom by the energy $\hbar\omega_0$, the energy must be corrected by the recoil energy E_R to

$$\hbar\omega = \hbar\omega_0 + E_R, \quad (2.63)$$

where

$$E_R = \frac{(\hbar\mathbf{k})^2}{2M} = \frac{(\hbar\omega)^2}{2Mc^2}. \quad (2.64)$$

Here, the transferred kinetic energy is called given by the momentum $\hbar\mathbf{k}$, c the speed of light and the atomic mass M . Equation (2.64) is a non-relativistic approximation. This yields an energy difference

$$\Delta E = \frac{(\hbar\omega)^2}{Mc^2} \approx \frac{(\hbar\omega_0)^2}{Mc^2} \quad (2.65)$$

after the emission in total, this is only valid for $E_R \ll \hbar\omega_0$. The distribution of the intensity is given by the Breit-Wigner-formula

$$I(E) = \frac{\frac{\Gamma}{2\pi}}{(E - \hbar\omega_0)^2 + (\frac{\Gamma}{2})^2}, \quad (2.66)$$

which shows that the distribution is given by a Lorentz profile. Γ is called natural line width and reflects the width at half of the energy maximum. Classically, one obtains equation (2.66) with assuming the model of the electronic-nuclear system as damped harmonic oscillator. Here, the intensity distribution is the square of the amplitude function which is the Fourier transform of the displacement function. The energy-time uncertainty is

$$\Delta E \cdot \Delta t \geq \hbar, \quad (2.67)$$

according to Heisenberg. Weisskopf and Wigner have shown that the mean life time τ of an excited state with the natural line width corresponds to

$$\Gamma \cdot \tau = \hbar. \quad (2.68)$$

It is important to emphasize the equality compared the equation (2.67) which is a more restricted statement. This means the groundstate has no energy uncertainty because of the infinitely long lifetime of the ground state. The Lorentz line form is experimentally observed for a thin absorber. For example, yellow sodium-D-line with a wave length of $\lambda \approx 589\text{ nm}$ represents the transition $3P_{1/2} \rightarrow 3S_{1/2}$ which has a lifetime of $\tau \approx 16\text{ ns}$ and yields according to (2.68) a natural line width of

$$\Gamma = \frac{\hbar}{\tau} \approx 4 \cdot 10^{-8} \text{ eV} \gg \frac{(\hbar\omega)^2}{Mc^2} \approx 20,6 \cdot 10^{-11} \text{ eV} \quad (2.69)$$

with $M \approx 23$ atomic mass units. This means the natural line width is much larger than the recoil energy which is negligible. To illustrate, although the existence of recoil energies $\frac{(\hbar\omega)^2}{2Mc^2}$, the Lorentz distributions overlap for absorption and emission in the optical spectroscopy and it comes with a considerable high probability to an absorption.

Figure 2.4 (a) shows the term scheme of the radioactive decay of ^{57}Co to ^{57}Fe . ^{57}Co decays with a probability of 99.84% by an electron capture of the K-shell to the excited nuclear $I = \frac{5}{2}^-$ state of the ^{57}Fe -nucleus and with a probability of 0.16% by an electron capture of a non-K-shell electron because of a very small overlap of the wave function of the non-K-shells with the nucleus¹². $S = 0.87\% \pm 1.7\%$ is the probability of the following decay into the state $I = \frac{3}{2}$. The important nuclear transition of ^{57}Fe is the magnetic dipole transition of 14.4 keV. The γ -decay appears in competition with the internal conversion which transfers the energy of the nucleus to a shell electron to leave the atom. The ratio of the probability of internal conversion and γ -decay is called conversions coefficient α and is

$$\alpha = \frac{c_T}{c_\gamma} = 8.17\% \pm 3.1\%, \quad (2.70)$$

¹²One should mention, historically, the notation was changed from Fe^{57} to ^{57}Fe .

according to W. Robinson *et al.* [18] measured by coincidence spectroscopy. However, the value vary slightly in the literature and are often higher, quantitatively the γ -decay dominates. The lifetime of the $\frac{3}{2}$ state is around $1.43 \cdot 10^{-7}$ s of the γ -decay. This yields

$$\Gamma = \frac{\hbar}{\tau} \approx 4.6 \cdot 10^{-9} \text{ eV} \ll \frac{(\hbar\omega)^2}{Mc^2} \approx 10^{-3} \text{ eV}. \quad (2.71)$$

Therefore, compared to the optical spectroscopy value, the photon loses a big part of its energy because of the considerable recoil energy of nuclear transitions. The probability for a self-resonance absorption is negligible.

An atom in a crystal or in a tight bond may show the *Mössbauer effect* which means that the recoil energy disappears for a part of the atoms according to a temperature defined probability. Classically, one identifies the mass M in equation (2.64) with the mass of the entire crystal lattice getting recoilless. Quantum-mechanically, it is a zero-phonon process which means during the nuclear transition there is no phonon created or annihilated. Interestingly, equation (2.64) is consistent with the quantum-mechanical expectation value.

2.2.2 ^{57}Fe -Mössbauer technique

This subsection discusses the advantages and disadvantages of ^{57}Fe -Mössbauer spectroscopy, some basics of the experimental setup and the velocity spectra.

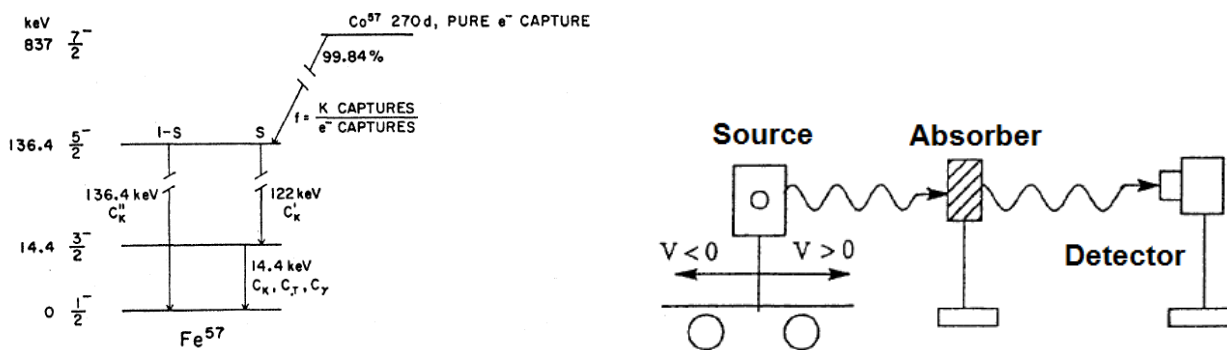
^{57}Fe -Mössbauer has a number of advantages compared to other techniques:

1. Mössbauer spectroscopy works even for low concentrations of the Mössbauer element as we will see in the case of ^{57}Fe -Mössbauer spectroscopy on Fe-diluted $\text{Li}_2(\text{Li}_{1-x}\text{Fe}_x)\text{N}$.
2. Mössbauer spectroscopy can be done in zero magnetic field and in high magnetic field of the Tesla regime.
3. ^{57}Fe -Mössbauer spectroscopy gives information about the electric quadrupole interaction of ^{57}Fe , e.g., NMR is only performed in the ground state with $I = \frac{1}{2}$ and does not provide this information.
4. The excitation (γ -ray) does not significantly heat up the sample.
5. Experimentally, spectra of powder samples are very easy to handle and the results are often less meaningful compared to crystals¹³.

An important disadvantage is the limitation to one element depending on the radioactive source since synchrotron Mössbauer spectroscopy has broader possibilities. Here, the electric monopole interaction is not accessible and the γ -collimator/prism are important experimental challenges.

Figure 2.4 (b) shows the scheme of the modulation of the velocity between source and absorber by the drive unit. To use the Mössbauer effect as spectroscopy method, one moves the ^{57}Co -source on

¹³One exception is the here presented study on Fe-diluted $\text{Li}_2(\text{Li}_{1-x}\text{Fe}_x)\text{N}$. Here, the microscopic understanding is improved by the vanished Mössbauer transitions compared to a powder study.



(a) Decay scheme of Co^{57} , c_K , c_T , c_γ is the probability for K-capture, for the total electron catching and for the γ -decay, respectively, taken from W. Robinson *et al.* [18].

(b) Scheme of the modulation of the velocity between source and absorber by the drive unit taken from V. Schünemann *et al.* [19]. Therefore, the Mössbauer energy unit is mms^{-1} .

Figure 2.4: Basics of ^{57}Fe -Mössbauer spectroscopy: Decay scheme and setup principle.

a drive unit with a velocity $\pm v$ forward and backward to tune the wave length in the order of neV. Therefore, the Mössbauer energy unit is mms^{-1} . This is called *first-order Doppler shift*. Experimentally, the absorber is the sample which is investigated.

The velocity range of ^{57}Fe -Mössbauer spectroscopy is calibrated according to α -iron at room temperature. Figure 2.5 (a) shows the unit cell of α -iron. α -Fe, sometimes called ferrite, has a bcc (body-centered cubic) crystal structure with a lattice constant around $a = 2.856 \text{ \AA}^{14}$. α -Fe has a Curie point of $T_C \approx 1043 \text{ K}$ and is a ferromagnetic soft metal with a magnetic moment of around $2.22 \mu_B$. Figure 2.5 (b) shows the ^{57}Fe -Mössbauer measurement of α -iron which has per definition an energy shift (isomer) shift of $\delta = 0$. The velocity shift of the presented measurement is relative to the ^{57}Co -source, the so called Center shift $\delta C = -0.111(5) \text{ mms}^{-1}$. The measurement shows six nuclear transition reflecting a magnetic hyperfine field of $33.20(5) \text{ T}$ fitted by the static crystal Hamiltonian described in the main text of the $\text{Li}_2(\text{Li}_{1-x}\text{Fe}_x)\text{N}$ results.

2.2.3 Lamb-Mössbauer factor

The Lamb-Mössbauer factor f describes the fraction of resonance transitions for which the Mössbauer effect statistically occurs. This fraction has a temperature dependence and is Fe-species dependent and, therefore, varies with the oxidation and spin state. The ratio of site fractions of two Fe sites must be obtained at a temperature $T \rightarrow 0$ between the areas of intensity of the observed sites.¹⁵ For instance, f is close to zero in proteins at room temperature, however $f \approx 0.7$ in α -iron at room temperature.

The Debye-Waller is called Lamb-Mössbauer factor in Mössbauer spectroscopy describing the fraction of the nuclei for which a energy-recoil-free nuclear resonance-absorption takes place. The Hamilton operator of the entire system can be separated into different parts, e.g., one crystal-lattice part, after

¹⁴see *Precision Measurements of Lattice Constants of Twelve common Metals* by Davey in 1925 [20].

¹⁵Experimentally, He temperature is very close to that because of the negligible occupation of phonon states at 4 K.

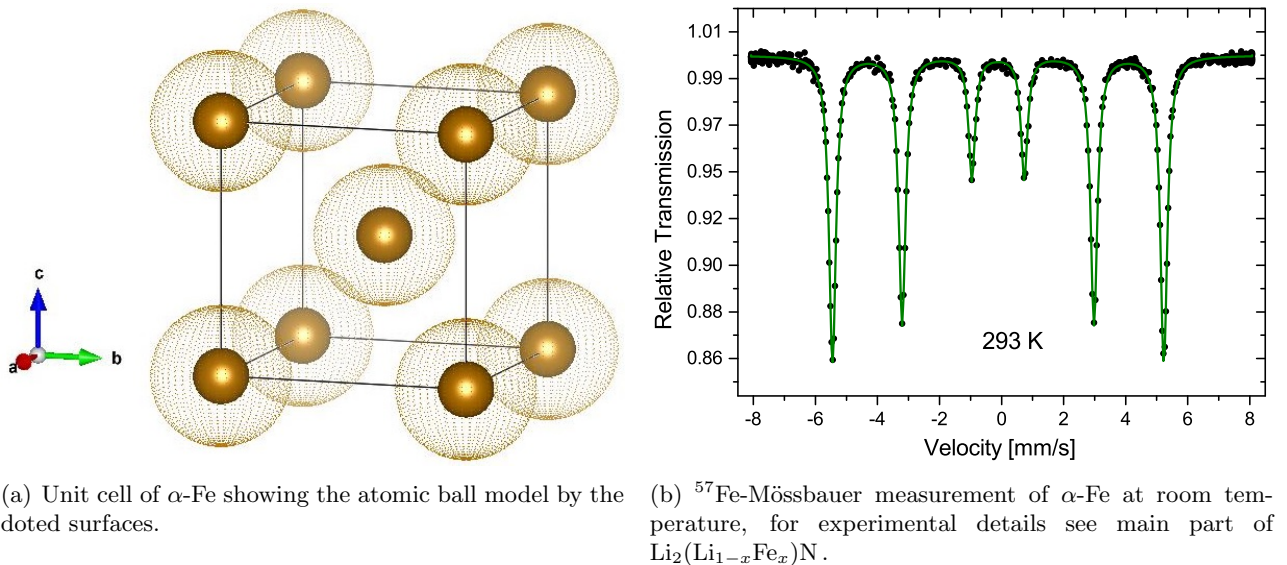


Figure 2.5: α -iron calibration taken for the measurements presented in this work and the corresponding unit cell.

the transformation into the center system of the nucleus. Therefore, the entire state can be described by a product state and the transition matrix element of the lattice,

$$f = |\langle\langle G_j | e^{-ik\hat{x}} | G_j \rangle\rangle_T|^2, \quad (2.72)$$

and can be treated separately. Here, $|G_j\rangle$ is a phonon state of the lattice with wave number $k = \frac{2\pi}{\lambda}$ and $\langle\dots\rangle_T$ the thermal average. Initial and end state are equivalent because only transitions are taking into account for which no photon is created or annihilated, this are the so called zero-phonon processes. Interestingly, a very elegant way to calculate the transition matrix element is the transformation to coherent states of equation (2.72) as presented by D. S. Bateman *et al.* [21]. The coherent states

$$|\alpha\rangle = e^{-\frac{|\alpha|^2}{2}} \sum_{n=0}^{\infty} \frac{\alpha^n}{\sqrt{n!}} |n\rangle \quad (2.73)$$

have minimal uncertainty and play a very important role in quantum optics as well. α is complex and

$$|n\rangle = \frac{(\hat{a}^\dagger)^n}{\sqrt{n!}} |0\rangle \quad (2.74)$$

are the eigenstates of the harmonic oscillator which can be constructed by the ground state $|0\rangle$ by the creation operator \hat{a}^\dagger which is the ad-junction of the annihilation operator \hat{a} . To remember: The harmonic oscillator $\hat{\mathcal{H}} = \frac{\hat{p}^2}{2m} + \frac{m\omega^2}{2}\hat{x}^2$ can be formulated by the creation operator $\hat{a}^\dagger = \sqrt{\frac{m\omega}{2\hbar}}(\hat{x} + \frac{i}{m\omega}\hat{p})$ and the annihilation operator $\hat{a} = \sqrt{\frac{m\omega}{2\hbar}}(\hat{x} - \frac{i}{m\omega}\hat{p})$ yielding $\hat{\mathcal{H}} = \hbar\omega(\hat{a}^\dagger\hat{a} + \frac{1}{2})$. The application of the occupation operator $\hat{n} = \hat{a}^\dagger\hat{a}$ to the eigenstates yields the quantum number: $\hat{n}|n\rangle = n|n\rangle$.

To get an expression, one expresses the displacement of the nuclei by the normal modes and formulates

$e^{ik\hat{x}}$ with creation and annihilation operator taking into account every normal mode introducing coherent product states. The result is

$$f = e^{-k^2\langle x^2 \rangle}, \quad (2.75)$$

in which f depends on the wave number $k = \frac{2\pi}{\lambda}$ and the mean value of the square of the displacement of the nucleus in the direction of the emitted or absorbed quantum. $\langle x^2 \rangle$ depends on the strength of the chemical bond to the (quasi) lattice. For tight bonds the Lamb-Mössbauer factor can be very small or even vanish, e.g., for proteins at room temperature. α -iron has a Lamb-Mössbauer factor of $f \approx 0,7$ reflecting the strong bond. To calculate the temperature dependence of f , one needs a model of the density of phonon states. A restriction to acoustic branches is reasonable for low temperatures which is known as Debye model. The density of states of the Debye model is given by

$$g(\omega) = \frac{3\omega^2}{\omega_D^3}, \quad (2.76)$$

which depends on the square of the phonon frequency ω for values of $\omega < \omega_D$. Here, ω_D is called Debye frequency. One gets

$$f = \exp \left\{ -\frac{3E_R}{2k_B\Theta_D} \left[1 + 4 \left(\frac{T}{\Theta_D} \right)^2 \int_0^{\Theta_D/T} \frac{x dx}{e^x - 1} \right] \right\}, \quad (2.77)$$

with $x = \frac{\hbar\omega}{k_B T}$ and the Debye temperature $\Theta_D = \frac{\hbar\omega_D}{k_B}$. This is an often used and cited approximation. It should be emphasized:

- f increases with decreasing transition energies E_γ . In this work only ^{57}Fe -Mössbauer spectroscopy plays a role ($E_\gamma \approx 14.4 \text{ keV}$),
- f increases with decreasing temperature,
- f decreases with increasing Debye temperature Θ_D .

2.2.4 Hyperfine interactions and limits

The hyperfine interactions are the heart of Mössbauer spectroscopy because these are the probed interactions and extracted quantities since the mentioned area ratios between sites is more of chemical interest. The detailed discussion is shifted to the main text because of the importance and strong correlation with the obtained spectra of $\text{Li}_2(\text{Li}_{1-x}\text{Fe}_x)\text{N}$. The limit of strong and weak magnetic fields compared to the quadrupole splitting energy is briefly discussed.

The 14.4 keV-energy levels of the ^{57}Fe nucleus are influenced by the electric-charge distribution of the electrons and the magnetic dipole interaction. The consequences are shifts and possible splittings of the energy levels. These interactions are called hyperfine interactions. In detail, the important hyperfine interaction are

- the electric monopole interaction ($e0$),

- the electric quadrupole interaction ($e2$),
- and the magnetic dipole interaction ($m1$).

The full static crystal Hamiltonian is explained in the main text of the $\text{Li}_2(\text{Li}_{1-x}\text{Fe}_x)\text{N}$ study. Once again, Figure 2.5 (b) shows the ^{57}Fe -Mössbauer measurement of α -iron. The resonances are the observed nuclear transitions. There are only six transition allowed because of the dipole transition rules $\Delta m_I = 1, 0$. There are two important limits depending on the strength of magnetic dipole and electric quadrupole interaction:

- Limit of strong magnetic hyperfine field B : $g_N\mu_N B \gg \frac{eQV_{zz}}{2}$. Here, e is the elemental charge, the nuclear quadrupole moment $Q = 0.16(1)\text{eb}$ and the main component of the electric field gradient tensor V_{zz} . g_N is the nuclear Landé factor and μ_N is the nuclear magneton. This approximation is valid in the case of the shown α -iron measurement, just a very weak asymmetric shape is possible.
- Limit of weak magnetic field: $g_N\mu_N B \ll \frac{eQV_{zz}}{2}$. Here, the electric dipole interaction dominates the splitting. One resonance splits into a doublet, the other one splits into a quadruplet. The distance of the main resonances corresponds to the quadrupole splitting ΔE_Q .

The limit of strong magnetic hyperfine field is the important limit in $\text{Li}_2(\text{Li}_{1-x}\text{Fe}_x)\text{N}$ as it is the case for α -iron for $T \rightarrow 0$.

2.3 Density functional theory

This section describes the density functional theory (DFT) calculation introduced in our group. The purpose of this section is to explain the used DFT code briefly. Discussed are the core principles and the used functionals. The idea was to get a visualization of possible muon sites and to calculate the electrostatic potential or charge density. Quantitatively, point charge models are often not sufficient to estimate the EFG tensor since DFT treatments take better into account the spatial expansion and, therefore, the electronic charge distribution. I have used the all-electron full-potential linearized augmented-plane wave (FP-LAPW) code Elk 4.3.6 which uses the Spacegroup package as well to obtain the crystal data file based on the crystal structure.

It should be mentioned that a mathematical precise and strict discussion of the theory is not the purpose of this section and can not be covered in an experimental work. Nowadays, the used Nobel-prize lecture

- *Self-Consistent Equations Including Exchange and Correlation Effects* by W. Kohn and L. J. Sham [22]

is not more up to date because of the restriction to non degenerated ground states. However, it is still a fruitful source for an experimental physicist to get an introduction to the basis of the DFT.

2.3.1 Kohn-Sham equations

This subsection discusses the formulation of the Kohn-Sham orbitals and corresponding equations. The main problem of the solution of the many-body problem is transferred to the so-called exchange-correlation term.

The density functional theory (DFT) is based on the Hohenberg-Kohn theorem which are in fact two theorems. Walter Kohn has gotten the Nobel-prize in chemistry in 1998 for his entire work. The first theorem demonstrated the reduction of a many-body particle system with N electrons and therefore $3N$ coordinates to a system given by the charge density $\rho(\mathbf{r})$ determined by 3 spatial coordinates. The second Hohenberg-Kohn theorem considers the ground state of an interacting electron gas in an external potential v_{ext} [23]. This potential v_{ext} is system dependent and describes the electrons moving in the potential of the nuclei of the unit cell. Hohenberg and Kohn have proven the existence of an universal functional $F[\rho(\mathbf{r})]$ of the electron density $\rho(\mathbf{r})$ independent of v_{ext} . The expression

$$E \equiv \int v_{\text{ext}}\rho(\mathbf{r})d\mathbf{r} + F[\rho(\mathbf{r})] \quad (2.78)$$

is a $\rho(\mathbf{r})$ -dependent energy functional. The energy minimum is the ground state energy regarding $\rho(\mathbf{r})$ of the system [23]. This means, the ground state electronic density function $\rho(\mathbf{r})$ is well defined, the potential $V(\mathbf{r})$ and the ground state wave function as well. Strictly, the last formulation is only correct for a non-degenerated ground state. DFT uses the Born-Oppenheimer approximation which assumes that the positions of nuclei are fixed as the basis of the introduction of the external potential

v_{ext} .

The original publication *Self-Consistent Equations Including Exchange and Correlation Effects* by W. Kohn and L. J. Sham is free to read and part of the Nobel-prize focus: *Chemistry by Computer* [22]. For the calculation a fictitious electronic system of non-interacting particles is introduced, the so called Kohn-Sham system. This system generates the same electronic density $\rho(\mathbf{r})$ as the analog interacting system. The Kohn-Sham system is defined by an effective local potential v_{eff} . The Kohn-Sham system describes non-interacting fermions given by Kohn-Sham orbitals $\psi_i(\mathbf{r})$ which are the solution of the Schrödinger-like equation

$$\left(-\frac{\hbar^2}{2m}\Delta + v_{\text{eff}}(\mathbf{r})\right)\psi_i(\mathbf{r}) = \epsilon_i\psi_i(\mathbf{r}), \quad (2.79)$$

with the energy ϵ_i of the corresponding Kohn-Sham orbital $\psi_i(\mathbf{r})$. The density of the N-particle system at position \mathbf{r} is given by

$$\rho(\mathbf{r}) = \sum_{i=1}^N |\psi_i(\mathbf{r})|^2 \quad (2.80)$$

. The total energy is given by

$$E[\rho] = T[\rho] + \int v_{\text{ext}}\rho(\mathbf{r})d\mathbf{r} + E_H[\rho] + E_{\text{xc}}[\rho]. \quad (2.81)$$

Here,

$$T[\rho] = \sum_{i=1}^N \int \psi_i^*(\mathbf{r}) \left(-\frac{\hbar^2}{2m}\Delta\right) \psi_i(\mathbf{r})d\mathbf{r} \quad (2.82)$$

is the Kohn-Sham kinetic energy and v_{ext} the external potential, means here the electron-nuclei interaction. The term

$$E_H[\rho] = \frac{e^2}{2} \int \int \frac{\rho(\mathbf{r})\rho(\mathbf{r}')}{|\mathbf{r} - \mathbf{r}'|} d\mathbf{r}d\mathbf{r}' \quad (2.83)$$

is the Hartree energy describing the electron-electron Coulomb repulsion. E_{xc} is the exchange-correlation energy. The total energy expression is varied and minimized to obtain the Kohn-Sham potential

$$v_{\text{eff}} = v_{\text{ext}} + e^2 \int \frac{\rho(\mathbf{r}')}{|\mathbf{r} - \mathbf{r}'|} d\mathbf{r}' + \frac{\delta E_{\text{xc}}[\rho]}{\delta \rho(\mathbf{r})}, \quad (2.84)$$

with the exchange-correlation potential

$$v_{\text{xc}} \equiv \frac{\delta E_{\text{xc}}[\rho]}{\delta \rho(\mathbf{r})}. \quad (2.85)$$

2.3.2 Coulomb potential and Elk

This part discusses the used main idea of LAPW and mentions the functionals used by Elk.

The problem of solving the Kohn-Sham equations can be done in a self-consistent (iterative) way. One starts with an initial $\rho_1(\mathbf{r}')$ to calculate v_{xc} and to solve the Kohn-Sham equations. One can

Atomic Unit/Quantity	Relation to other constants	Value [SI]
Bohr radius a_0	$a_0 = \frac{4\pi\epsilon_0\hbar^2}{m_e e^2}$	$0.52917721067 \cdot 10^{-10} \text{m}$
Hartree energy E_h	$E_h = \frac{m_e e^4}{4\epsilon_0^2 \hbar^2}$	$4.35974465 \cdot 10^{-18} \text{J}$
	2Ry	$\approx 27.2 \text{eV}$
Magnetic field (cgs)	$\frac{e}{a_0^2 c}$	1715.2554659T
Electric field	$\frac{E_h}{ea_0}$	$5.142206707 \cdot 10^{11} \text{V/m}$
Electric field gradient (EFG)	$\frac{E_h}{ea_0^2}$	$9.717362369 \cdot 10^{21} \text{V/m}^2$

Table 2.4: Atomic units taken from NIST Reference (CODATA value), relations to constants and the SI units. For instance, one atomic unit of the EFG is $\approx 9.72 \cdot 10^{21} \text{V/m}^2$. The value of the magnetic field is based on cgs units since the SI unit would be $2.35 \cdot 10^5 \text{T}$.

continue calculating a new density $\rho_2(\mathbf{r}')$ and proceed until a wished convergence threshold is reached. For example, in the case of CaF_2 the required energy difference was $< 5 \cdot 10^{-5} E_h$ in the last loop of the iteration. The main problem is the exchange term v_{xc} which must be obtained. Elk combines the Hartree energy E_H , the electron-nuclear E_{en} and nuclear-nuclear energy E_{ee} to the Coulomb potential energy

$$E_C = E_H + E_{\text{en}} + E_{\text{ee}} \quad (2.86)$$

with

$$V_C = \int v_C \rho(\mathbf{r}) d\mathbf{r} \quad (2.87)$$

to obtain the Coulomb-potential plots. The calculations presented here have used Broyden mixing [24] and Perdew-Burke-Ernzerhof-GGA (generalized gradient approximation) functionals [25].

Elk is an all-electron full-potential linearized augmented-plane wave (FP-LAPW) code. In a FP-LAPW code a partitioning of the space is introduced into a muffin-tin sphere and an interstitial region. The muffin-tin sphere uses a radial sphere wave-functions expansion which is consistent with an atomic-like treatment. The interstitial region is approximated by plane-wave expansions.

In general, for details see the Elk manual [26] or introductions like R. G. Parr *et al.* [27].

2.3.3 Units

Elk uses atomic units. The input-quantities must be converted in atomic units (e.g., the length of the unit cell in Bohr radii a_0) and the output-quantities are given in atomic unit (e.g., the energy in Hartree energy E_h). A table is presented including the relation to other constants.

All units of extracted experimental quantities are SI Units in this work. The DFT calculations require and generate output results in atomic units. The units of Elk are atomic units with the elementary charge $e = 1$, the length unit is the Bohr radius $a_0 = 1$ and the electron mass $m = 1$. The energy is given in Hartree energy E_h , for details see table 2.4. The electron charge is positive and the core (nucleus) charge is negative.

2.3.4 Disorder and Approximations

The performed calculations contain some approximations to estimate the muon site. On the other hand, disorder is contained in $\text{BaTi}_{0.5}\text{Mn}_{0.5}\text{O}_3$ and $\text{NaCaCo}_2\text{F}_7$. Therefore, the discussion of the concept of disorder realized in DFT calculation is constructive.

There exist different possibilities to proceed with disordered compounds by DFT. This can be disorder or doping, respectively, corresponding to the chemical element ratio.

1. The general case is the construction of a supercell to obey the charge neutrality of the entire supercell. This is important when the disorder or doping leads to hole or electron doping. One special case is to assume one kind of periodicity of the unit cell. This is possible when the unit cell obeys the ratio of chemical ratios directly by the ratio of the atoms per unit cell. This is the case for $\text{BaTi}_{0.5}\text{Mn}_{0.5}\text{O}_3$ in which I have taken one Mn and one Ti per primitive unit cell. I have chosen eight Na and eight Ca to satisfy the element ratio in $\text{NaCaCo}_2\text{F}_7$ of the unit cell.

2. Virtual Crystal Approximation (VCA)

The solution is to generate and introduce virtual atoms with mixed core charges and masses at the disordered sites. In the case of $\text{BaTi}_{0.5}\text{Mn}_{0.5}\text{O}_3$ one would take a non-integer nuclear charge of $Z = (22 + 25)/2 = 23.5$.

3. Coherent Potential Approximation (CPA)

This is another method to find the Green's function of an effective medium replacing the disordered system through a homogenous system. A variational implementation of the muffin-tin approximation to crystalline solids was suggested by Korringa, Kohn, and Rostoker, and is often referred to as the KKR method.

VCA and CPA lead to effective treatments which are very efficient to calculate bulk quantities. In our case, the local physics is playing the important role. Possible muon sites estimated by the electrostatic potential and EFGs are local quantities. For this reason the first option is chosen.

Therefore, the following approximations are used in the DFT calculations presented in this work:

1. Calculated is the unperturbed unit cell. This means the self charge of the muon and a possible local influence is not considered.
2. All shown calculations are spin unpolarized. This means the approximation that the charge density $\rho(\mathbf{r})$ of the spin-unpolarized state and the spin-polarized state is comparable is assumed:

$$\rho(\mathbf{r}) \approx \rho_{\uparrow}(\mathbf{r}) + \rho_{\downarrow}(\mathbf{r}). \quad (2.88)$$

Here, $\rho_{\uparrow}(\mathbf{r})$ and $\rho_{\downarrow}(\mathbf{r})$ are the charge densities of spin-up and spin-down contributions. This approximation is exact in the nonmagnetic case, e.g., for CaF_2 . This approximation includes that a spin polarization leads to a change of occupation of the spin channels since the entire sum of charge density stays constant.

3. The disorder is assumed to be realized by the statistical most expected configuration. This ignores arbitrary ion permutations leading to another muon-preferred electrostatic configuration. This means the total-energy minimum of a supercell containing randomness may be located close to another and special configuration of the disordered ions. The crystallographic position of the energy minimum is mostly unaffected.
4. The taken crystal data are assumed to be temperature independent below 300 K.
5. Other approximations are given by used functionals and DFT routine, e.g., GGA.

All these points suggest that the calculated isosurface of the electrostatic potential φ can be regarded as a rough estimation for the muon site. However, as larger the volume of the isosurface is chosen the better this statement is.

2.3.5 Performed calculations

This is an overview of selected DFT calculations I performed. The plots of $\text{Fe}_3\text{PO}_4\text{O}_3$ and $\text{Fe}_4\text{Si}_2\text{Sn}_7\text{O}_{16}$ are shifted to the *Appendix*. They are not further discussed in the main text and are performed for other purposes and showing the broad application.

The following DFT calculations (selection) are performed:

- $\text{BaTi}_{0.5}\text{Mn}_{0.5}\text{O}_3$ (chapter 5)
- CaF_2 (chapter 6)
- $\text{NaCaCo}_2\text{F}_7$ and $\text{NaCaNi}_2\text{F}_7$ (chapter 7)
- $\alpha\text{-Li}_3\text{N}$ (chapter 8)
- $\text{Li}_2(\text{Li}_{1-x}\text{Fe}_x)\text{N}$ (chapter 8)
- $\text{Fe}_3\text{PO}_4\text{O}_3$ (see *Appendix*)
- $\text{Fe}_4\text{Si}_2\text{Sn}_7\text{O}_{16}$ (see *Appendix*)

The $\text{Li}_2(\text{Li}_{1-x}\text{Fe}_x)\text{N}$ calculation was performed using a supercell approach¹⁶.

¹⁶Special thanks to PD Dr. Manuel Richter (IFW, Dresden) for general discussions of my DFT calculations.

3 Role of Disorder: Overview

In this chapter, I present an overview on the topic of disorder which is present in the materials on $\text{BaTi}_{0.5}\text{Mn}_{0.5}\text{O}_3$ and $\text{NaCaCo}_2\text{F}_7$. The character is comparable with a short expedition through the jungle to give a brief overview about selected ordered states, (quantum) spin liquids and the interplay with structural disorder discussing the core research interests. The definitions of key issues, e.g., frustration and spin liquids follow in the following chapters. The exception is spin glassiness. Therefore, this chapter requires the knowledge of basis concepts. $\text{Li}_2(\text{Li}_{1-x}\text{Fe}_x)\text{N}$ is a single-atomic magnet for low Fe concentration since the compound shows for $x = 0.3$ spin-glass properties. Disorder crawls like a snake through the entire work and can be toxic in wrong situations as unplanned impurities. The discussed examples below should be understood as a personal selection by the author without entitlement to completeness. Theoretical treatments of $\text{BaTi}_{0.5}\text{Mn}_{0.5}\text{O}_3$ and $\text{NaCaCo}_2\text{F}_7$ are discussed in the following chapters in detail. For this reason, this chapter provides supplementary information getting an impression of the role of disorder in frustrated systems. An overview of cross relations and commonalities of projects of this work is presented in figure 1.2.

3.1 Types, spin glassiness and order-by-disorder

Disorder can arise from different sources. Disorder is called quenched or frozen disorder when the variables describing this disorder do not evolve with time, e.g., structural disorder. There are two types of structural disorder important in this thesis which are defects and randomness of sites, the last one leads often to bond-disorder or bond-randomness.

$\text{Li}_2(\text{Li}_{1-x}\text{Fe}_x)\text{N}$ contains for high Fe-dilution single magnetic defects in the $\alpha\text{-Li}_3\text{N}$ matrix.

$\text{BaTi}_{0.5}\text{Mn}_{0.5}\text{O}_3$ and $\text{NaCaCo}_2\text{F}_7$ are bond-disordered systems in which the Ti and Mn sites or Na and Ca sites, respectively, are distributed randomly about the entire crystal restricted by the occupied crystallographic site [28, 29].

In general, structure disorder may lead to magnetic disorder because of magnetoelastic coupling. For instance, structural disorder close to a superexchange path can lead to a variation of the bond-angle and therefore magnetic exchange energy of the involved atoms according to the Goodenough-Kanamori rules. The entropy of the mixing of one crystallographic site is

$$S = k_B \log (\text{number of possible configurations}), \quad (3.1)$$

with the Boltzmann constant k_B . In glasses there is a residual structure entropy persistent for $T \rightarrow 0$ because glasses are disordered like liquids and rigid like crystals. For *spin glassiness* caused by bond-

disorder the magnetic entropy is the analog quantity. Classical spin glasses are systems of broken ergodicity violating the fluctuation dissipation theorem. The spins start to freeze at the so-called freezing or glass temperature T_f into a random pattern. The spins are not arranged in a regular pattern and no magnetic LRO (long-range order) is observed. Qualitatively, there is a huge number of frozen states which is distinct by tiny energies. Experimentally, there are different signatures of classical/conventional spin glasses¹:

- d.c. magnetic susceptibility shows a difference, a divergence, between field-cooled and zero field cooled measurements below T_f
- a.c. magnetic susceptibility shows a strong frequency dependence of χ' and χ'' below T_f
- A linear T dependence of the electronic contribution to the heat capacity at low temperatures
- A sharp decrease of the spin-fluctuation rate observed by μ SR, NMR, and inelastic neutron scattering below T_f
- Absence of magnetic LRO as seen, for instance, in neutron spectroscopy

Two other sources of disorder are thermal or quantum fluctuations. Structural disorder, thermal and quantum fluctuations are able to exist in competition leading to the selection of different magnetic states depending on the system and the strength of the disorder type. The effect of *order-by-disorder* means that a magnetic long-range ordered state is selected by disorder. There is still strong effort to identify *order-by-disorder* candidates to improve the understanding of this mechanism.

For instance, the anisotropic XY pyrochlore² antiferromagnet $\text{Er}_2\text{Ti}_2\text{O}_7$ prefers the stabilization of the so-called coplanar state $\psi_3(m_{x^2-y^2})$ in the presence of nonmagnetic disorder [31]. The pure compound $\text{Er}_2\text{Ti}_2\text{O}_7$ is a *quantum-order-by-disorder* candidate which is stabilized in the noncoplanar ground state $\psi_2(m_{3z^2-r^2})$ and proposed to be driven by quantum fluctuations [32, 33, 34].

Disorder plays a very important role in the investigation of the stability of (quantum) spin liquids violating the Ginzburg-Landau theory because of the lack of any symmetry breaking and order parameter. The main aim is to find a generalized theory of phase transitions. Disorder can lead to a manifold of (magnetic) states depending on the crystal structure, microscopic conditions and the strength of the variation of the exchange interaction.

It is well known that thermal fluctuations suppress magnetic order of a ferromagnet above the Curie temperature, e.g., in α -Fe above 1043 K. Nowadays, the assumption that every kind of bond-disorder should lift the ground-state degeneracy of a frustrated magnet leading to a (cluster) spin-glass phase or a long-range order is dropped. As we will see, $\text{NaCaCo}_2\text{F}_7$ falls into the category of quantum cluster spin glass, although the XY cluster spin glassiness described by a short-range superposition of the states $\psi_2(m_{3z^2-r^2})$ and $\psi_3(m_{x^2-y^2})$ is rather exotic [35, 36]. The not observed *order-by-disorder* mechanism in $\text{NaCaCo}_2\text{F}_7$ has led at the beginning to misunderstanding or theoretical confusion.

¹For details, see e.g. J. E. Greedan [30]. Spin glassiness has been a huge research field in the past to understand the observations which is covered in own books and is exceeding the range of this work.

²For details about $\psi_2(m_{3z^2-r^2})$, $\psi_3(m_{x^2-y^2})$ see below, e.g., figure 4.4. However, figure 3.3 shows the ordered states $\psi_2(m_{3z^2-r^2})$ and $\psi_3(m_{x^2-y^2})$ illustrated at the top of the figure specified by the spin configuration in a single tetrahedron.

However, a general theory of the interplay between disorder, (quantum) spin-liquid physics and the extension of the Ginzburg-Landau theory to a general theory of phase transition including the developments in topological physics is the final goal.

3.2 Appearance of spin-liquid-by-disorder

The investigation of disorder-induced spin-liquid-like states is a part of the puzzle of the understanding of the physics of phase transitions³. The prefix *appearance* or *mimicry* of *spin-liquid-by-disorder* is important because such systems are not necessarily strict (quantum) spin liquids from a theoretical point of view⁴.

As we will see, $\text{BaTi}_{0.5}\text{Mn}_{0.5}\text{O}_3$ shows no phase transition to a magnetic ordered state, a.c. magnetic susceptibility shows no frequency dependence of χ' and χ'' as expected for a spin glass and it is a candidate for a spin liquid ground state down to 20 mK [37]. Briefly, I present in the following two theoretical and two experimental examples of the appearance of spin-liquid-by-disorder. In principle, I should present here a general theory to explain which mechanism lead to spin-liquid-by-disorder. This is not possible because a general understanding is missing.

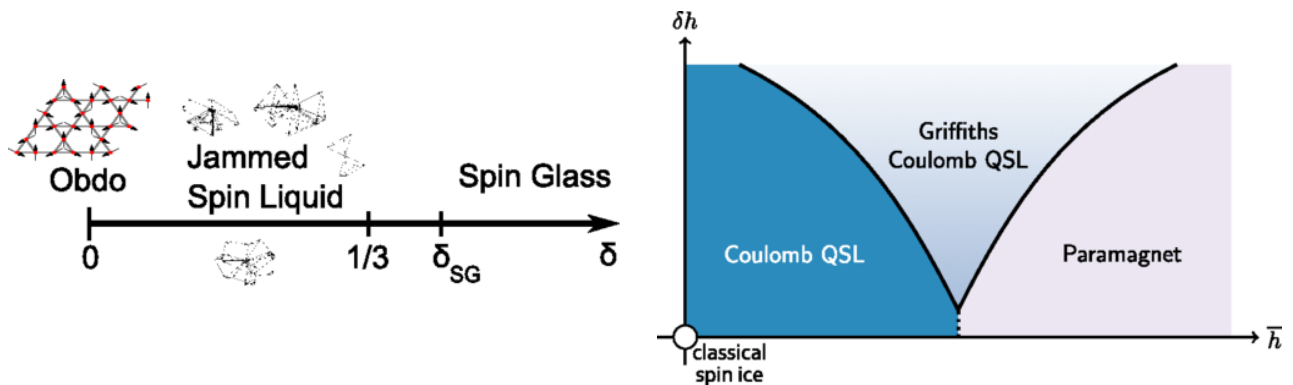
Figure 3.1 (a) shows a 1D phase diagram of the jammed spin liquid in the bond-disordered kagome Heisenberg antiferromagnet as a function of an introduced disorder strength⁵ δ . $\delta = 0$ represents the clean system which is the archetypal frustrated magnet exhibiting order-by-disorder in the form of coplanar state with so-called weak translational symmetry breaking [38]. For $0 < \delta < 1/3$, a jammed spin liquid is predicted. Like in the clean system the ground-state spin configurations minimize energy for every triangle, however, they remain disconnected exhibiting nontrivial zero-energy modes. The phenomenon of jamming remembers on granular media and structural glasses. For $\delta > 1/3$, a spin-glass state develops. This is one example of a 2D spin liquid induced by a critical value of weak disorder strength.

Figure 3.1 (b) shows the phase diagram of an example in 3D, the disorder-induced quantum spin liquid in spin-ice pyrochlores discussed by L. Savary *et al.* [39]. They have proposed that for a class of non-Kramer spin ice systems disorder induces quantum entanglement, here, quantum superpositions of spins and combined with fractionalized excitations. \bar{h} is the mean disorder strength and δh is a parameter of XY-like random fields perpendicular to the local [111]-axis and, therefore, perpendicular to the Ising-like direction known in spin-ice systems. The white circle shows the clean spin-ice system with $\bar{h} = \delta h = 0$. The dotted line indicates a first-order transition and the solid lines represent second-order transitions or the crossover between the so called Coulomb quantum spin liquid and Griffiths Coulomb quantum spin liquid. Using the disordered boson description, the paramagnet phase is a superfluid Higgs phase, the Griffiths phase is a Mott glass, and the Coulomb quantum spin liquid is a Mott insulator [39]. This is one example in 3D on the pyrochlore lattice which shows how disorder tunes a quantum spin liquid.

³I have called the title of this section *Appearance of spin-liquid-by-disorder* to emphasize the exotic and unexpected observation of disorder-induced spin-liquid-like ground states. However, it is not a conventional description in the literature. This field is just to young for this development.

⁴Special thanks to Prof. M. Vojta for discussions and the proper description.

⁵For details, see T. Bilitewski *et al.* [38].



(a) Phase diagram of the jammed spin liquid in the bond-disordered kagome antiferromagnet as a function of disorder strength. The jammed spin liquid appears for $0 < \delta < 1/3$ taken after T. Bilitewski *et al.* [38]. $\delta = 0$ is the clean system showing order-by-disorder (Obdo).

(b) Phase diagram of the disorder-induced quantum spin liquid in non-Kramer spin-ice pyrochlores. Here, \bar{h} is the mean disorder strength and δh is a parameter of XY-like random fields perpendicular to the local [111]-axis, for details see text and L. Savary *et al.* [39].

Figure 3.1: Theoretical phase diagrams in 2D and 3D of two different disorder-induced spin liquids.

Experimentally, it is confirmed that in $\text{Pr}_2\text{Zr}_2\text{O}_7$ disorder induces a quantum spin liquid [40]. Furthermore, it was shown that quenched random crystal fields or disorder can play a crucial role in preventing magnetic LRO at low temperatures and induces a strongly fluctuating Coulomb spin liquid with defect-induced frozen magnetic degrees of freedom in $\text{Tb}_2\text{Hf}_2\text{O}_7$ [41].

These examples of the last years show the new perspective and that the effect of order-by-disorder has got a counterpart. The possibility of the existence of a (quantum) spin liquid in the bond-disordered double perovskite $\text{BaTi}_{0.5}\text{Mn}_{0.5}\text{O}_3$ seems encouraged as I will discuss below.

3.3 Quantum fluctuations in rare-earth pyrochlore oxides

Quantum fluctuations are able to play a role when the spin leaves the classical limit. The spins are classical for the angular momentum $J \rightarrow \infty$, means the spin operators are replaced by classical spins [42]. The spin system is for $J = 1/2$ most quantum while it depends on the size of the moments as well, e.g., $\text{Er}_2\text{Ti}_2\text{O}_7$ and $\text{Yb}_2\text{Ti}_2\text{O}_7$ are pseudo- $S = 1/2$ Kramers systems and XY pyrochlores with a planar magnetic anisotropy perpendicular to the local [111]-axis.

The theory of multiple-phase competition in pyrochlore magnets with anisotropic exchange was applied to $\text{Yb}_2\text{Ti}_2\text{O}_7$, $\text{Er}_2\text{Ti}_2\text{O}_7$ and $\text{Er}_2\text{Sn}_2\text{O}_7$ by H. Yan *et al.* [43]. Here, the starting point is the classical nearest-neighbor Hamiltonian compatible with symmetries of the pyrochlore lattice. Figure 3.2 (a) shows the calculated classical ground-state phase diagram with an anisotropic exchange interaction. The axes are given by ratios of exchange interactions J_i . J_i are often used exchange constants on the pyrochlore lattice which are roughly identified as

1. J_1 : The exchange constant of the XY plane perpendicular to the local [111]-axis;
2. J_2 : The exchange constant of the Ising part parallel to the local [111]-axis;
3. J_3 : Symmetric off-diagonal exchange constant;

4. J_4 : Dzyaloshinskii-Moriya interaction.

This four exchange constants describe the exchange interaction in one single tetrahedron. This model includes a rich manifold of phases, e.g., the exchange-based spin ice for

$$J_1 = -J_2 = J_3 = J_4 < 0, \quad (3.2)$$

or the Heisenberg antiferromagnet on the pyrochlore lattice for

$$J_1 = -J_2 > 0, J_3 = J_4 = 0, \quad (3.3)$$

which are proposed spin liquids. The phase diagram is calculated for vanishing Dzyaloshinskii-Moriya interaction, $J_4 = 0$ and symmetric off-diagonal exchange $J_3 < 0$ as observed in $\text{Yb}_2\text{Ti}_2\text{O}_7$, $\text{Er}_2\text{Ti}_2\text{O}_7$ and $\text{Er}_2\text{Sn}_2\text{O}_7$. The points of $\text{Yb}_2\text{Ti}_2\text{O}_7$, $\text{Er}_2\text{Ti}_2\text{O}_7$ and $\text{Er}_2\text{Sn}_2\text{O}_7$ correspond to the estimated parameters by experiments⁶.

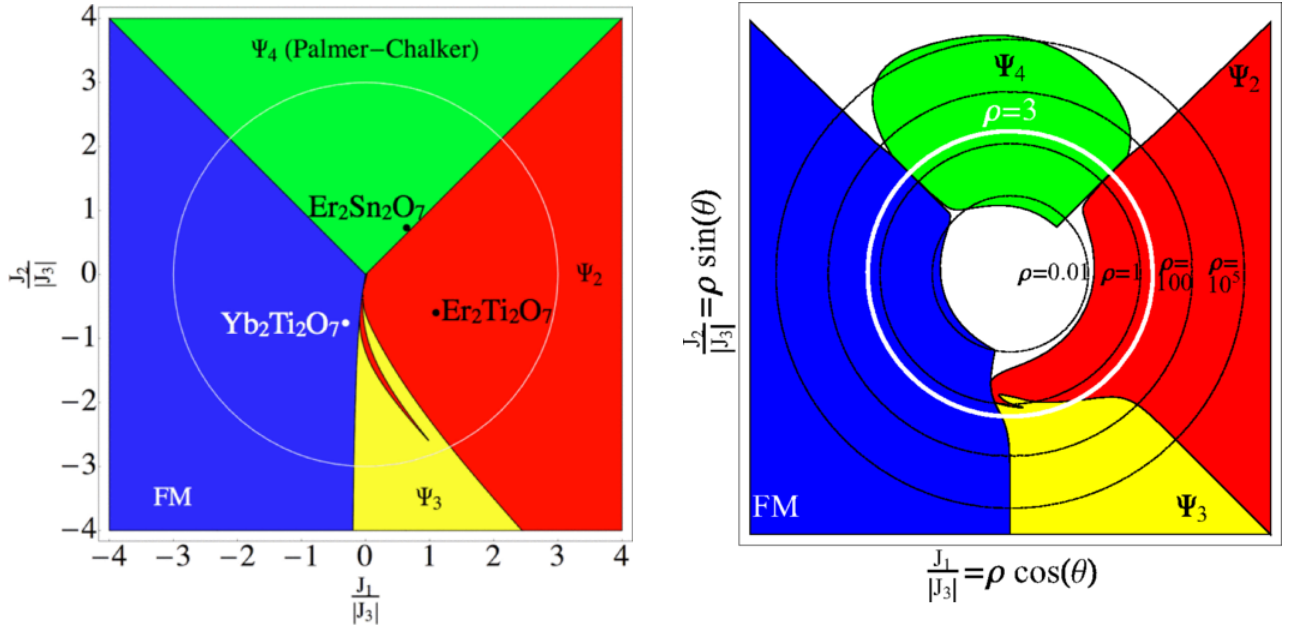
There are the four distinct magnetic ordered phases of the classical case assuming a linear spin wave theory. The four ordered phases are illustrated at the top by the tetrahedron configuration in figure 3.3: Palmer-Chalker state ψ_4 , non-collinear ferromagnetic phase FM, non-coplanar antiferromagnetic phase ψ_2 and coplanar antiferromagnetic phase ψ_3 which are all six-fold degenerate with zero crystal momentum⁷. The white circle of the parameter space selection with $J_1 = |J_3| \cos \theta$ and $J_2 = |J_3| \sin \theta$ is the x -axis in figure 3.3 which is the finite-temperature classical phase diagram for a pyrochlore magnet with anisotropic exchange interactions normalized to $|J_3|$. $T_c/|J_3|$ shows various values depending on θ . Naively, $T_c/|J_3|$ shows a maximum when the competition to another magnetic phase is minimized.

Figure 3.2 (b) shows the non-classical phase diagram of the calculated suppression by quantum fluctuations. There are the four distinct ordered phases of the classical case and white regions in which magnetic LRO is suppressed, e.g., spin-glass-like phases. The introduced quantum fluctuations lead to an effective deformation of the classical phase diagram. The mentioned parameter selection is once again illustrated in white.

The phase diagram of the proposed XY pyrochlore $\text{NaCaCo}_2\text{F}_7$ with and without quantum fluctuations is shown in the next chapter. Based on my μSR studies, $\text{NaCaCo}_2\text{F}_7$ is proposed to be a quantum cluster-spin-glass candidate.

⁶For the general consistency of theory and experiment, especially of $\text{Er}_2\text{Ti}_2\text{O}_7$ see next chapter.

⁷To avoid confusion concerning the notation: I will continue with small ψ_i describing these states, but $\psi_i \equiv \Psi_i$ and, e.g., $\psi_2 = \psi_2(m_{3z^2-r^2})$.



(a) Phase diagram of the calculated classical ground-states with an anisotropic exchange interaction taken from H. Yan *et al.* [43]. Here, $J_4 = 0$ and symmetric off-diagonal exchange $J_3 < 0$. There are four distinct ordered phases which are illustrated in the insets of figure 3.3. The white circle of the parameter space selection with $J_1 = |J_3| \cos \theta$ and $J_2 = |J_3| \sin \theta$ is one axis in figure 3.3.

(b) Phase diagram of the calculated suppression of the classical ground states by quantum fluctuations taken from H. Yan *et al.* [43]. There are the four distinct ordered phases of the classical case and white regions in which magnetic LRO is suppressed. The axes $J_1/|J_3| = \rho \cos \theta$ and $J_2/|J_3| = \rho \sin \theta$ are in logarithmic-polar scale with $0 < \rho < 10^6$. The white circle corresponds to the parameter selection in figure 3.2 (a) and figure 3.3.

Figure 3.2: Calculated difference between the classical phase diagram (left) of pyrochlores with anisotropic exchange interaction and the non-classical case including quantum fluctuations (right) which illustrates the deformation of the phase diagram and additional phases in white.

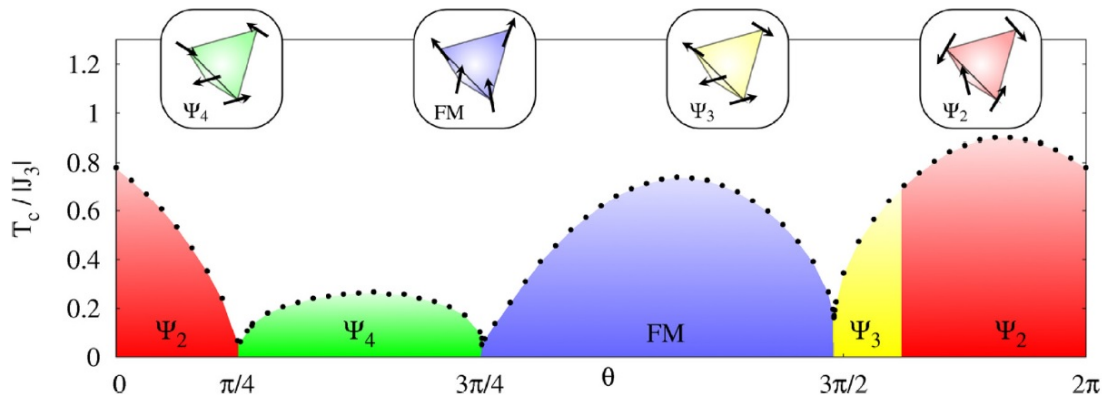


Figure 3.3: The finite-temperature phase diagram for a pyrochlore magnet with anisotropic exchange interactions normalized to $|J_3|$ taken from H. Yan *et al.* [43]. Here, the selection for $J_4 = 0$, symmetric off-diagonal exchange $J_3 < 0$, $J_1 = |J_3| \cos \theta$ and $J_2 = |J_3| \sin \theta$ is shown. The four ordered phases are illustrated at the top by the tetrahedron configuration: Palmer-Chalker state ψ_4 , non-collinear ferromagnetic phase FM, non-coplanar antiferromagnetic phase ψ_2 and coplanar antiferromagnetic phase ψ_3 which are six-fold degenerate.

4 Pyrochlore Fluoride $\text{NaCaCo}_2\text{F}_7$

4.1 Frustration in fluorides and $\text{NaCaCo}_2\text{F}_7$

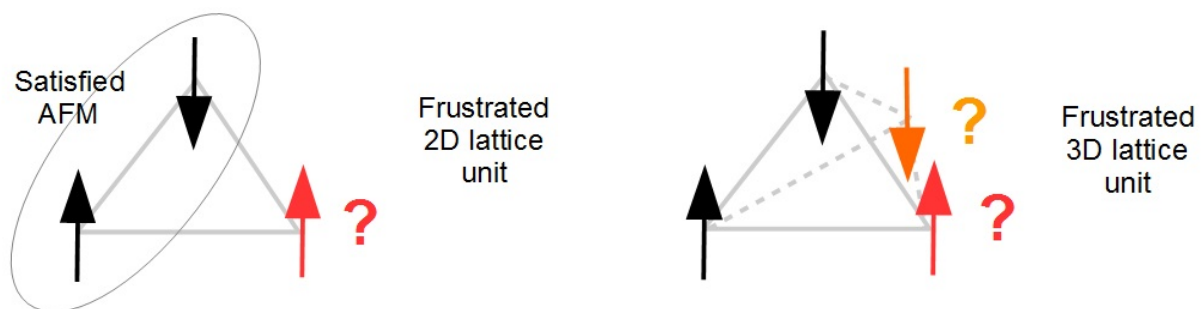
I was fighting with myself if I should write a subsection about pyrochlore oxides or not. On the one hand, it is a sign for completeness, on the other it is nowadays such a broad topic which is impossible to cover in deepness which is needed. I am starting here with the frustration in fluorides to come as soon as possible to the one central topic of my work. Connections to the physics of XY pyrochlore oxides are mentioned and discussed, e.g., to $\text{Er}_2\text{Ti}_2\text{O}_7$. The glass of pyrochlore oxides is for sure not almost empty, on the other hand the glass of pyrochlore fluorides is less touched and, therefore, unexpected full and pyrochlore fluorides are rarely investigated by μSR . After the introduction to frustration it follows the chapter of $\text{BaTi}_{0.5}\text{Mn}_{0.5}\text{O}_3$ to show one example of a disordered frustrated compound probed by μSR showing PSD (persistent μ^+ spin dynamics). CaF_2 probed by μSR exhibits a F- μ^+ -F state and the final chapter of the first main part of this work combines all: Bond-disorder, F- μ^+ -F state physics and PSD in $\text{NaCaCo}_2\text{F}_7$, see figure 1.2. All three studies are supplemented by DFT calculations.

Let me start with a citation taken from L. Balents: *Sometimes, a little frustration can make life interesting* [44]. Historically, the term of magnetic frustration was introduced to explain the behavior of spin-glass systems [45, 46]. In a magnetic geometrically frustrated system it is not possible to minimize the energy of all spins simultaneously due to the constraints of magnetic interaction. A general model for magnetic interaction is given by the Heisenberg two-spin coupling exchange Hamiltonian,

$$\hat{\mathcal{H}} = - \sum_{i < j} J_{ij} \mathbf{S}_i \cdot \mathbf{S}_j, \quad (4.1)$$

with the convention $J_{ij} < 0$ for antiferromagnetic and $J_{ij} > 0$ for ferromagnetic interaction in which the spins \mathbf{S}_i are able to have a classical or quantum nature. A fully non-frustrated system has a collinear or antiparallel (e.g., Néel state) spin structure¹. Figure 4.1 (a) and (b) show two examples of classically frustrated spin arrangements in 2D and 3D, respectively. For the triangle, it is not possible to satisfy and, therefore, energy minimize all AFM paths (grey lines) simultaneously, the lattice is frustrated. In 3D, the tetrahedron contains four faces of triangles leading to a higher degeneracy by frustration. The tetrahedron is the basic brick of magnetic pyrochlore antiferromagnets

¹For sure, there exist non-collinear structures apart from the Hamiltonian $\hat{\mathcal{H}}$, e.g. Dzyaloshinskii-Moriya interaction (antisymmetric exchange) can lead to a spin canting and can stabilize helical order [47]. Only the Hamiltonian $\hat{\mathcal{H}}$ is considered in the following.



(a) Visualization of classical spins arranged in a triangle with antiferromagnetic (AFM) interactions in 2D. It is possible to satisfy one exchange path (grey line in ellipsoid) since the third spin (red) is confused or frustrated.

(b) Visualization of classical spins arranged on a 3D lattice unit as it is the case in AFM pyrochlore structures with the fourth spin (orange) out of plane. Classically, one energy-minimized AFM exchange path lead to two confused spins (red and orange).

Figure 4.1: Classical spin arrangements visualized on 2D and 3D triangular units to explain classically frustration.

containing corner-sharing tetrahedra as discussed below. Firstly, for an elementary square plaquette P , the frustration function

$$\phi = \prod_P \text{sgn}(J_{ij}) \quad (4.2)$$

was introduced [45]. For $\phi = -1$ it is not possible to satisfy all interaction and the square unit is frustrated. An enhanced concept to quantify magnetic frustration and the instability to satisfy all interactions is the deviation from the collinearity or anticollinearity indicated by the ground-state energy [46, 30]. Here, the possibility to rank geometric frustration is the constraint function

$$F_c = -\frac{E}{E_b} = -\frac{\sum_{i,j} J_{ij} \mathbf{S}_i \cdot \mathbf{S}_j}{\sum_{i,j} |J_{ij}| |\mathbf{S}_i| |\mathbf{S}_j|}, \quad (4.3)$$

in which E is the solution of the Hamiltonian $\hat{\mathcal{H}} = -\sum_{i,j} J_{ij} \mathbf{S}_i \cdot \mathbf{S}_j$ of the frustrated lattice normalized to the basis energy $E_b = \sum_{i,j} |J_{ij}| |\mathbf{S}_i| |\mathbf{S}_j|$ on the same lattice assuming collinearity. A non-frustrated system has $F_c = -1$ and a fully frustrated one $F_c = 1$. F_c increases when the lattice interactions are more frustrated. To imagine, one can introduce a mean angle θ_c representing the departure from collinearity by $\theta_c = \cos^{-1}(-F_c)$, which means $\theta_c = 0$ for the non-frustrated case. Table 4.1 shows selected examples for more or less magnetically frustrated fluorides. The discussed frustrated square with

$$\phi = \prod_P \text{sgn}(J_{ij}) = (-1)(-1)(-1)(+1) = -1 \quad (4.4)$$

leads to $F_c = -0.707$ and $\theta_c = 45^\circ$. FeF_3 is polymorph and the most frustrated structure is the cubic pyrochlore [48, 49, 50]. The short formula of the cubic pyrochlore FeF_3 arises from the missing occupancy of the crystallographic $16d$ - and $8a$ -sites. Figure 4.2 shows the unit cell of FeF_3 visualized

Compound and Structure	F_c	θ_c (deg)
K ₂ NiF ₄ , collinear AFM	-1	0
FeF ₃ rhombohedral, collinear AFM	-1	0
Ba ₂ Ni ₃ F ₁₀	-0.967	14.8
KCrF ₄ columns	-0.800	36.9
FeF ₃ hexagonal tungsten-bronze	-0.667	48.2
MnFeF ₅ ·2H ₂ O	-0.500	60
FeF ₃ pyrochlore	-0.333	70.5
Interaction Cr-Cr in KCrF ₄	+0.292	107
Interaction Ni-Ni in Ba ₂ Ni ₃ F ₁₀	+1	180
Saturated AFM in high magnetic fields	+1	180

Table 4.1: Calculated F_c and θ_c values with Monte-Carlo simulations of selected fluorides assuming equal antiferromagnetic next-nearest-neighbor interactions taken from P. Lacorre [46].

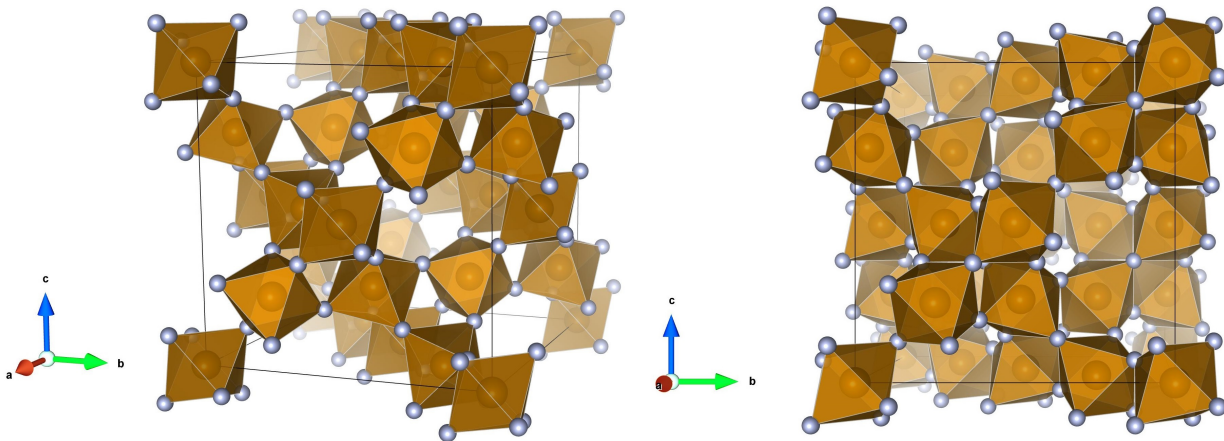


Figure 4.2: Slightly enhanced unit cell of the cubic pyrochlore FeF₃ with Fe in brown and F in grey. The structure parameters with the unit cell length of $a = 10.325(2)$ Å are taken from R. De Pape *et al.* [48].

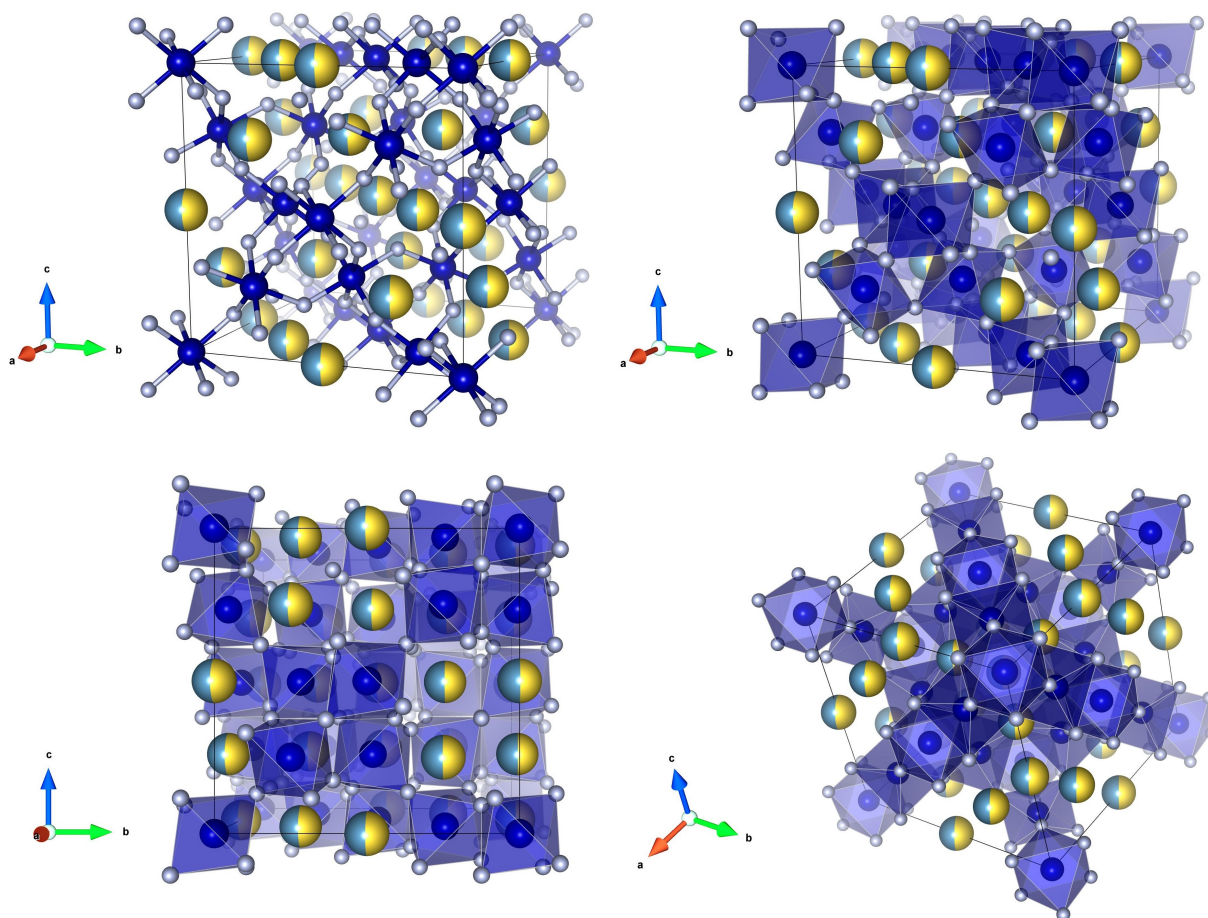


Figure 4.3: Various representations of an enhanced unit cell of the cubic pyrochlore NaCaCo₂F₇ using the ball-stick and polyhedral model: Co²⁺ blue, F⁻ grey balls, disordered Na⁺ and Ca²⁺ aquamarine and yellow, respectively, reflecting the random A-site occupancy of 50% : 50% of Na⁺ and Ca²⁺. The crystal-structure data are taken from J. W. Krizan *et al.* [28].

by VESTA by the ionic radii². The octahedron around Fe emphasizes the octahedral crystal field coordination.

Experimentally, magnetic frustration is more commonly quantified and more accessible by the so-called frustration index

$$f = \frac{|\Theta_{CW}|}{T_N}. \quad (4.5)$$

Here, Θ_{CW} is the Curie-Weiss temperature and a measure of the strength of exchange interactions and T_N is the ordering temperature. T_N is later also equivalent to the freezing temperature T_f , because NaCaCo₂F₇ shows spin-glass-like bulk properties³. Based on mean-field theory one can show that

$$\Theta_{CW} = \frac{2S(S+1)}{3k_B} \sum_{n=1}^N z_n J_n, \quad (4.6)$$

²This compound is not only shown for the purpose of a structural comparison to NaCaCo₂F₇, FeF₃ will play a role in the outlook for the discussion of further proposed studies probed by μ SR.

³The prefix *like* is here important.

Pyrochlore fluoride	Θ_{CW} [K]	T_f [K]	f	Ref.
NaCaCo ₂ F ₇	-139	2.4	56	[28]
NaCaNi ₂ F ₇	-129	3	43	[56]
NaSrCo ₂ F ₇	-127	3	42	[55]
NaSrMn ₂ F ₇	-90	2.5	36	[57]
NaSrFe ₂ F ₇	-98	3.7	27	[57]
NaCaFe ₂ F ₇	-73	3.9	19	[57]

Table 4.2: Synthesized series of bond-disordered cubic pyrochlore fluorides in 2014-2017 (space group $Fd-3m$) with the rounded Curie-Weiss temperature Θ_{CW} , the spin-freezing temperature T_f and the rounded frustration index $f = -\Theta_{CW}/T_f$.

where k_B is the Boltzmann constant, n is the n th neighbor with number z_n , S the spin and J_n the corresponding exchange constant and, therefore, Θ_{CW} is the algebraic sum of exchange interactions [46]. If $f > 5$, the compound is called frustrated. Formally, for $f = \infty$ the ground state has magnetic SRO (short-range order). A highly correlated magnetic system with fluctuating spins and the absence of magnetic LRO at $T_N \ll |\Theta_{CW}|$ is often called a spin liquid⁴.

Magnetic systems containing antiferromagnetic correlated spins situated at corner-sharing tetrahedra are expected to be magnetically highly frustrated which means the ground state is highly degenerated. Therefore, the pyrochlore lattice is one of the best realizations of magnetic frustration [46]. So far, frustrated pyrochlore oxides $A_2^{3+}B_2^{4+}O_7^{2-}$ where A is a rare-earth ion and B is a transition metal have exhibited exotic quantum states and excitations like quantum spin liquids or magnetic monopoles [52, 53]. Cubic pyrochlores crystallize when the ratio of the radii of the A and B site, $r_A : r_B$, lie between 1.2 and 1.5 with $r_B > 0.62 \text{ \AA}$ neglecting the exceptions Pr₂Ru₂O₇ and Pr₂Mo₂O₇ [52]. These values can be applied to cubic pyrochlore fluorides because of the similar radii of O²⁻ and F⁻ [54].

NaCaCo₂F₇ is part of a group of pyrochlore fluorides which were expected to show a rich manifold of exotic phases [28, 54, 55, 56, 57]. This assumption is confirmed by recent neutron-scattering results [35, 58]. Table 4.2 shows the series of cubic pyrochlore fluorides synthesized in 2014-2017 by R. Cava *et al.*. NaCaCo₂F₇ has the highest frustration index reflecting the strong competition of magnetic interactions. Figure 4.3 shows the structural unit cell of NaCaCo₂F₇ using the ball-stick model and the polyhedral model in different directions. The unit cell of cubic pyrochlores is quite large containing 119 atoms and 60 bonds. NaCaCo₂F₇ has a cubic crystal system with the space group $Fd-3m$ (227, origin 2) and a length of the unit cell of $a = 10.4189(9) \text{ \AA}$. This yields a unit-cell volume of $1131.0(3) \text{ \AA}^3$. The formula weight is 313.923 g/mol. Table 4.3 shows the crystallographic data of atom positions obtained at 293 K taken from Krizan *et al.* [28]. The visualizations and estimations in this work are based on these values. In Na⁺Ca²⁺Co₂²⁺F₇⁻, the A sub-lattice contains disordered nonmagnetic Na⁺ and Ca²⁺ ions to remain the charge neutrality, and the B site of the pyrochlore lattice hosts high spin Co²⁺ in CoF₆ octahedra compressed along the local [111]-direction [28]. Na⁺ and Ca²⁺ ions are randomly distributed on the A site in the lattice, and give rise to weak bond disorder via magnetoelastic coupling. In a frustrated magnetic system, the presence of weak bond-

⁴For precise definitions and extensive discussions, e.g., see the review by M. Vojta *Frustration and quantum criticality* [51].

Element	Site	x	y	z	Occupancy
Na	16d	0.5	0.5	0.5	0.5
Ca	16d	0.5	0.5	0.5	0.5
Co	16c	0	0	0	1
F(1)	8b	0.375	0.375	0.375	1
F(2)	48f	0.33289(14)	0.125	0.125	1

Table 4.3: Atomic positions of the crystallographic sites of the unit cell of NaCaCo₂F₇. The displacement parameters are listed in J. W. Krizan *et al.* [28] and are not shown.

disorder plays an important role because it can lift the degeneracy of the ground states and may lead to unconventional states by the order-by-disorder mechanism [52].

4.2 Order-by-disorder and XY cluster-spin glassiness

NaCaCo₂F₇ is no conventional spin glass in which the spins freeze into a random pattern and a magnetic LRO state is excluded as well. Experimentally, both is described in the next subsection. The initial motivation was the study of the order-by-disorder mechanism. The absence of magnetic LRO was rather surprising. Nowadays, NaCaCo₂F₇ is proposed to be a XY cluster spin glass, which means naively something between a magnetic LRO XY state and a spin glass involving probably quantum fluctuations. One purpose of this subsection is to emphasize how many scientific questions are still open regarding this compound and also the quantum-order-by-disorder candidate Er₂Ti₂O₇ from a theoretical point of view.

It is predicted that quenched disorder (bond-disorder or vacancies) of the pyrochlore Heisenberg antiferromagnet favors locally collinear antiferromagnetic correlations in the limit of weak disorder with the variation of the exchange interaction $\Delta \ll J$, where J is the mean value of exchange interactions $J \pm \Delta$ and freezes around $T_f \approx \Delta$ [59, 60, 61].

Order-by-disorder means a magnetic LRO is selected by disorder, e.g., by structural disorder. Is the source of disorder attributed to quantum fluctuations, it is called quantum order-by-disorder considering quantum fluctuations as the predominant mechanism relieving spin frustration. The lift of the degeneracy is discussed for the structural disorder-free XY pyrochlore antiferromagnet Er₂Ti₂O₇ by quantum fluctuations, a order-by-quantum-disorder candidate which is stabilized in the noncoplanar groundstate $\psi_2(m_{3z^2-r^2})$ [32, 33, 34]. Figure 4.4 visualizes the XY states of Γ_5 of irreducible representations of one tetrahedron. $\psi_2(m_{3z^2-r^2})$ is shown in red in different directions. The Er³⁺ ions show a Kramers doublet with $3.8\mu_B$ parallel and $0.12\mu_B$ perpendicular to the local [111]-axis reflecting the XY nature [52] and, therefore, a planar nature perpendicular to the local [111]-axis. Furthermore, for Er₂Ti₂O₇ this is shown analytically and numerically that structural disorder competes with thermal and quantum fluctuations and can lead to the coplanar groundstate $\psi_3(m_{x^2-y^2})$ [31]. Figure 4.4

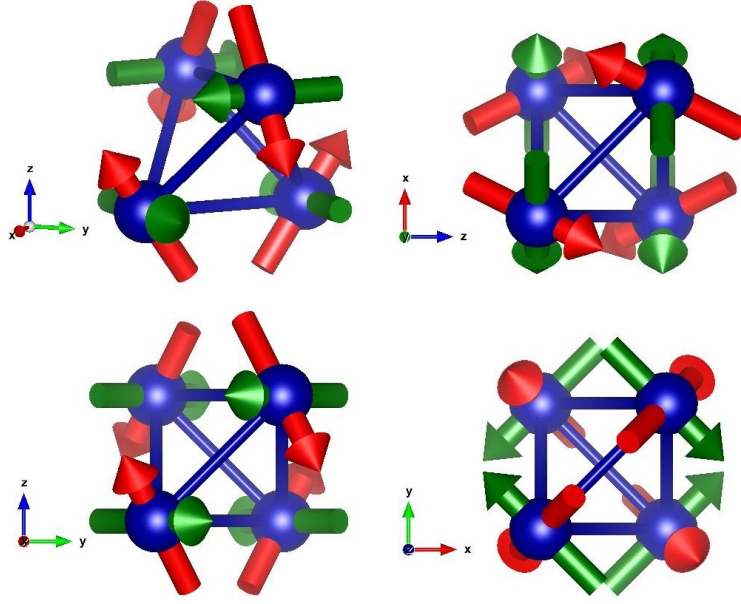


Figure 4.4: The proposed XY states $\psi_2(m_{3z^2-r^2})$ (red) and $\psi_3(m_{x^2-y^2})$ (green) of $\text{Er}_2\text{Ti}_2\text{O}_7$ and used by K. Ross *et al.* to describe the continuous short-range-ordered manifold of states in $\text{NaCaCo}_2\text{F}_7$ by a superposition of $\psi_2(m_{3z^2-r^2})$ and $\psi_3(m_{x^2-r^2})$ [35]. The Co^{2+} ions are blue.

shows the coplanar groundstate $\psi_3(m_{x^2-y^2})$ in green. Adding to the Heisenberg exchange model $\hat{\mathcal{H}} = -\sum_{i,j} J_{ij} \mathbf{S}_i \cdot \mathbf{S}_j$ with classical pseudospins \mathbf{S}_i an easy-plane anisotropy term,

$$\hat{\mathcal{H}}_{xy} = -D \sum_i \mathbf{S}_i \cdot \mathbf{d}_i \quad (4.7)$$

with an anisotropy $D < 0$ to confine the spins to easy XY planes, given by a perpendicular local axis $\mathbf{d}_i = (111)$ is consistent with the classical XY pyrochlore antiferromagnet model ($J_{ij} < 0$) [34, 62]. There are experimental contradictions to this model in $\text{Er}_2\text{Ti}_2\text{O}_7$:

1. The transition is continuous and not first order as theoretically predicted.
2. The predicted constant density of states is inconsistent with the observed T^3 dependence of the heat capacity below 1 K.
3. The classical model does not predict a gap in the quasielastic excitation spectrum.
4. Calculations on isostructural $\text{Er}_2\text{GaSbO}_7$ and $\text{Er}_2\text{Sn}_2\text{O}_7$ are inconsistent with the observed specific heat and susceptibility results.

All this points strongly suggest a non-classical nature, see J. Lago *et al.* [62] and therein. μSR low-energy experiments have shown effective magnetic SRO in $\text{Er}_2\text{Ti}_2\text{O}_7$ [62]. A proposed coexistence of magnetic SRO and LRO confirms the ambiguity in an extensive study of $\text{Er}_2\text{Ti}_2\text{O}_7$ performed by D. Dalmas de Réotier *et al.* [63].

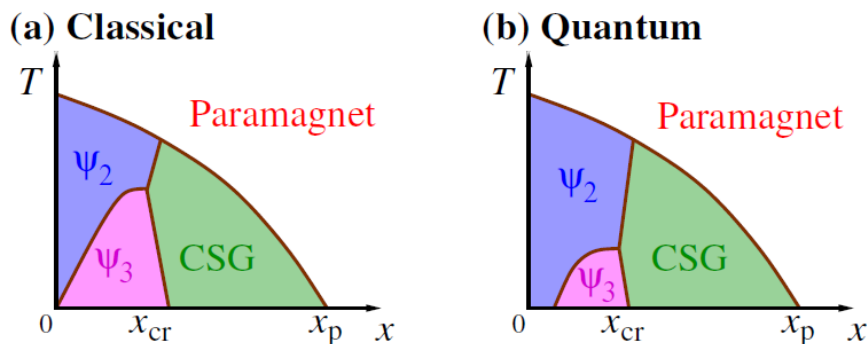


Figure 4.5: (a) Schematic phase diagram of ordering temperature T as a function of the dilution x taken from M. Vojta *et al* [36]. The proposed XY states $\psi_2(m_{3z^2-r^2})$ and $\psi_3(m_{x^2-r^2})$ are destroyed beyond a critical level of randomness x_{cr} . (b) Including quantum fluctuations $\psi_3(m_{x^2-r^2})$ may disappear completely [36].

NaCaCo₂F₇ has a higher frustration index and is believed to be more sensitive for quantum fluctuations, quantum disordered phase boundaries because of the stronger magnetic correlation [64]. Motivated by studies of NaCaCo₂F₇ and NaSrCo₂F₇ it is argued that every LRO state like $\psi_2(m_{3z^2-r^2})$ or $\psi_3(m_{x^2-r^2})$, is destroyed beyond a critical level of bond randomness and leads to a glass of spin clusters assuming a pyrochlore XY antiferromagnetic model by M. Vojta *et al* [36]. Quantum fluctuations may lead to a domination of the cluster-spin-glass phase and to a reduction of $\psi_3(m_{x^2-r^2})$ [36]. Figure 4.5 shows the schematic phase diagram proposed for NaCaCo₂F₇ which lies in the cluster-spin-glass (CSG) phase. The area of the magnetic phase $\psi_3(m_{x^2-r^2})$ is decreased after the inclusion of quantum fluctuations.

4.3 Previous experimental studies on NaCaCo₂F₇

This subsection summarizes published experimental studies on NaCaCo₂F₇, bulk-studies are shown and the results of the pulsed high-field magnetization measurements on NaCaCo₂F₇ measured by the author of this work in Dresden-Rossendorf, see S. A. Bräuninger *et al.* [65]. Neutron-scattering studies of the spin dynamics in the meV range was performed [35]. One part of this work is a μ^+ SR study to allow us to draw conclusions regarding the role of fluctuations, quantum effects and the low-energy spin dynamics in the (neV- μ eV) range in NaCaCo₂F₇ down to 20 mK. NMR is here powerful as well, but sometimes the magnetic field can change the magnetic properties or the ground state. For example, in Er₂Ti₂O₇ an external magnetic field aligned along [110] tunes the ground state continuously through a variety of noncollinear phases below 1.5 T, above 1.75 T a broadening of the transition in the heat capacity was found [66]. This emphasizes the advantage of μ SR to perform experiments without magnetic fields or with very small magnetic fields using the muon as a sensitive probe for even very small magnetic field down to a few Gauss.

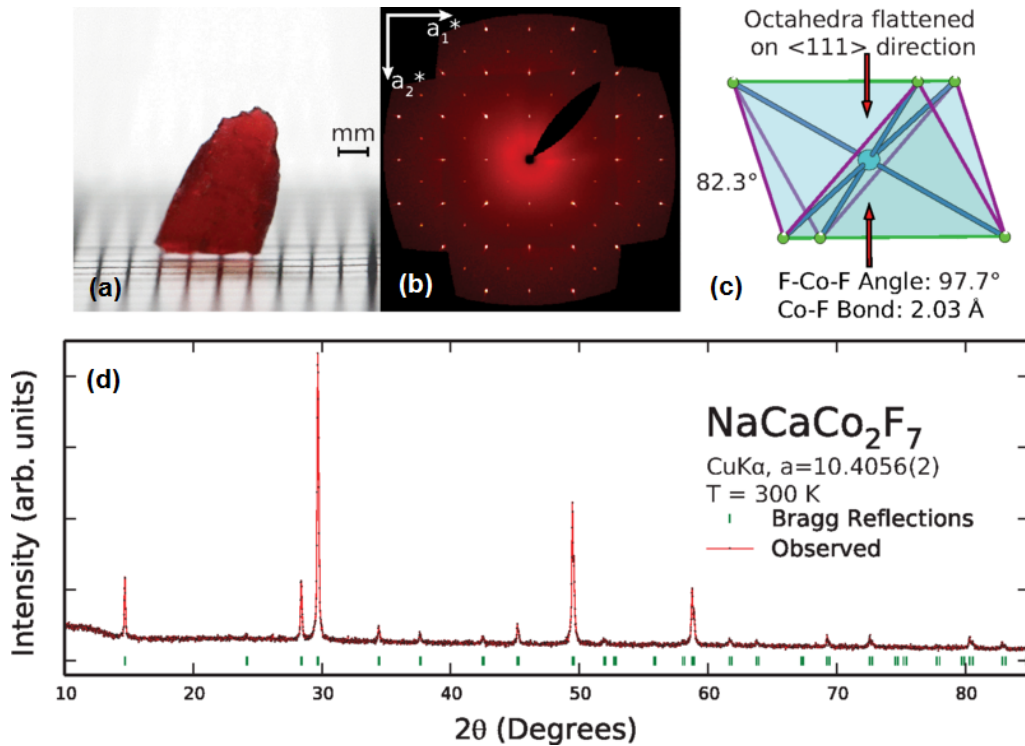


Figure 4.6: Original figure taken from J. Krizan *et al.* [28]: (a) shows a red crystal cut of $\text{NaCaCo}_2\text{F}_7$, (b) shows a single-crystal diffraction image of the $(0kl)$ plane, (c) shows the compression of the octahedra, (d) is an X-ray powder pattern of $\text{NaCaCo}_2\text{F}_7$ confirming the crystal structure of a $\text{A}_2\text{B}_2\text{F}_7$ pyrochlore.

4.3.1 Spin glass-like freezing, bond-disorder and XY cluster-spin glassiness

Figure 4.6 (a) shows a piece of a $\text{NaCaCo}_2\text{F}_7$ crystal which is a colorful red crystal. This is expected for a crystal containing a transition-metal element, e.g. Co^{2+} , which are well known for their colorful compounds because of the partial filled d -orbital and electronic transitions in the energy range of visible light. $\text{NaCaCo}_2\text{F}_7$ is an insulator. $\text{NaCaCo}_2\text{F}_7$ was grown in a floating-zone furnace obtaining rather large single crystals of the size of more than 1 cm, as shown. Interestingly, the first crystal of $\text{NaCaCo}_2\text{F}_7$ was grown already in 1970 in Tübingen, Germany [54]. However, the detailed study of the magnetic properties of this pyrochlore fluoride group and the extension of the crystal synthesis to $\text{NaSrCo}_2\text{F}_7$ and related compounds has started in 2014, as presented in table 4.2.

Figure 4.6 (d) shows the powder X-ray diffraction (PXRD) measurement on synthesized $\text{NaCaCo}_2\text{F}_7$ confirming the crystal structure of a $\text{A}_2\text{B}_2\text{F}_7$ pyrochlore using the Cu K- α line with an X-ray energy of ≈ 8.04 keV. Here, the intensity (arbitrary units) is given as a function of the scattering angle 2θ and Bragg reflections are given by green lines. Bragg reflections occur when the Bragg law

$$2d \sin \theta = n\lambda, \quad (4.8)$$

is satisfied leading to constructive interference. Here, d is the lattice constant, n an integer and λ the wavelength of the Cu K- α line of $\lambda \approx 1.5 \text{ \AA}$. A single crystal X-ray diffraction (SXRD) pattern is presented in figure 4.6 (b) using the Mo K- α line (≈ 17.45 keV) [28]. The result is presented in

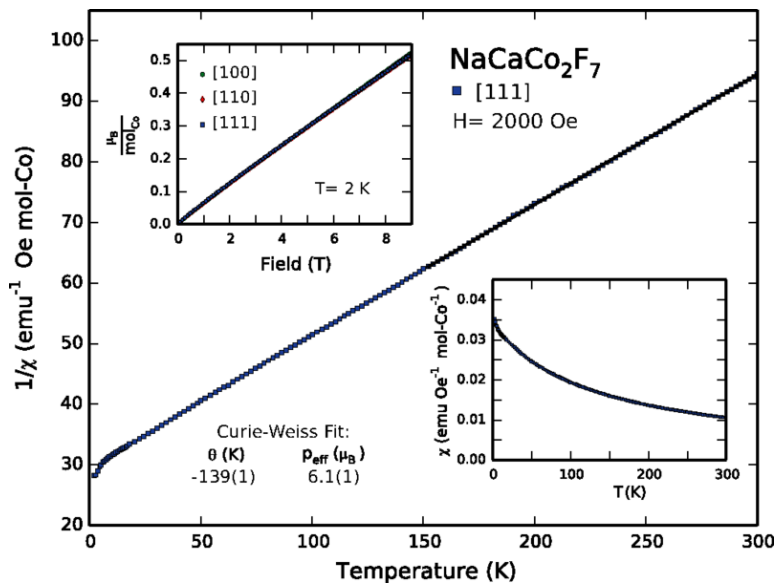


Figure 4.7: Original figure taken from J. Krizan *et al.* [28]. The main panel shows the inverse d.c. susceptibility $1/\chi$ as a function of temperature T in the crystallographic direction [111] of NaCaCo₂F₇ and the bottom panel the raw $\chi(t)$ -data. The top panel presents the magnetization as a function of the applied magnetic field in the three directions [100], [110] and [111] at $T = 2$ K. Here, in our notation is $\Theta_{CW} \equiv \theta$ and $p_{\text{eff}} \equiv \mu_{\text{eff}}$.

table 4.3 showing the atomic positions of the crystallographic sites⁵ of the unit cell of NaCaCo₂F₇ together with visualization of the unit cell in figure 4.3. Figure 4.6 (c) visualizes the compressed CoF₆ octahedra mentioning the obtained angles of the F-Co-F bond.

Figure 4.7 shows the inverse static magnetic susceptibility $1/\chi$ as a function of temperature T (main plot). NaCaCo₂F₇ shows dominantly antiferromagnetic interactions. For low applied magnetic fields B the magnetic susceptibility χ is given by

$$\chi = \frac{M}{H} \approx \frac{\mu_0 M}{B} = \frac{n\mu_0\mu_{\text{eff}}^2}{3k_B(T - \Theta_{CW})}, \quad (4.9)$$

where n denotes the number of magnetic moments per unit volume and μ_0 the vacuum permeability⁶. This temperature dependence with $\chi = C/(T - \theta)$ is known as Curie-Weiss law where C is the Curie constant and Θ_{CW} the Curie-Weiss temperature⁷. The effective moment estimated from the Curie-Weiss analysis at high temperature is $\mu_{\text{eff}} = 6.1(1)\mu_B$ per Cobalt ion obtained in an applied field of 2000 Oe along the [111]-direction [28]. This value is larger than the spin-only value of $S = 3/2$ of Co²⁺ of $3.87\mu_B$ reflecting a considerable orbital contribution. NaCaCo₂F₇ possesses a large Curie-Weiss temperature $\Theta_{CW} \approx -139(1)$ K. This yields a frustration index of $f = |\Theta_{CW}/T_f| \approx 56$ with $T_f \approx 2.4$ K as presented in table 4.2. $T_f \ll \Theta_{CW}$ shows a considerable suppression of the magnetic freezing temperature and, therefore, competing interactions. The bottom inset of figure 4.7 shows the noninverse data $\chi(T)$ and the top panel presents the magnetization in μ_B per mol of Co as a

⁵The crystal structure was discussed in the last section in detail.

⁶See *Magnetism in Condensed Matter* by S. Blundell [67].

⁷as mentioned in the section *Frustration in Fluorides and NaCaCo₂F₇*

function of the applied magnetic field at 2 K. The temperature-behavior is linear and equal for all three direction [100], [110] and [111] up to 9 T. Therefore, the saturation magnetization is not reached in NaCaCo₂F₇ up to 9 T.

NaCaCo₂F₇ is not magnetically long-range ordered down to 0.6 K. Instead, a.c. (alternating current) and d.c. (direct current) susceptibility experiments exhibit a spin freezing temperature of $T_f \approx 2.4$ K as presented in figure 4.8 (a) [28]. In general, the a.c. susceptibility is a complex quantity,

$$\chi_{ac} = \chi' - i\chi'', \quad (4.10)$$

and the real part χ' is associated with reversible magnetization processes which stays in-phase with applied oscillating driving field, $H(t) = H_0 + h \cos(2\pi\nu t)$, with a frequency ν and amplitude h . χ'' is associated with irreversible magnetization processes leading to a phase shift in magnetization by an energy absorption from the field, e.g., because of irreversible relaxation in domain walls [68]. However, the real part χ' of the a.c. magnetic susceptibility shows a strong frequency dependence of χ' which is consistent with a spin glassiness. Magnetic LRO systems like ferromagnets show frequency dependence in the range of MHz and spin glasses shows it in the kHz range [68]. An initial rough estimation to categorize the nature of the spin freezing is the expression

$$\frac{\Delta T_f}{T_f \Delta \log \nu} \approx 0.029, \quad (4.11)$$

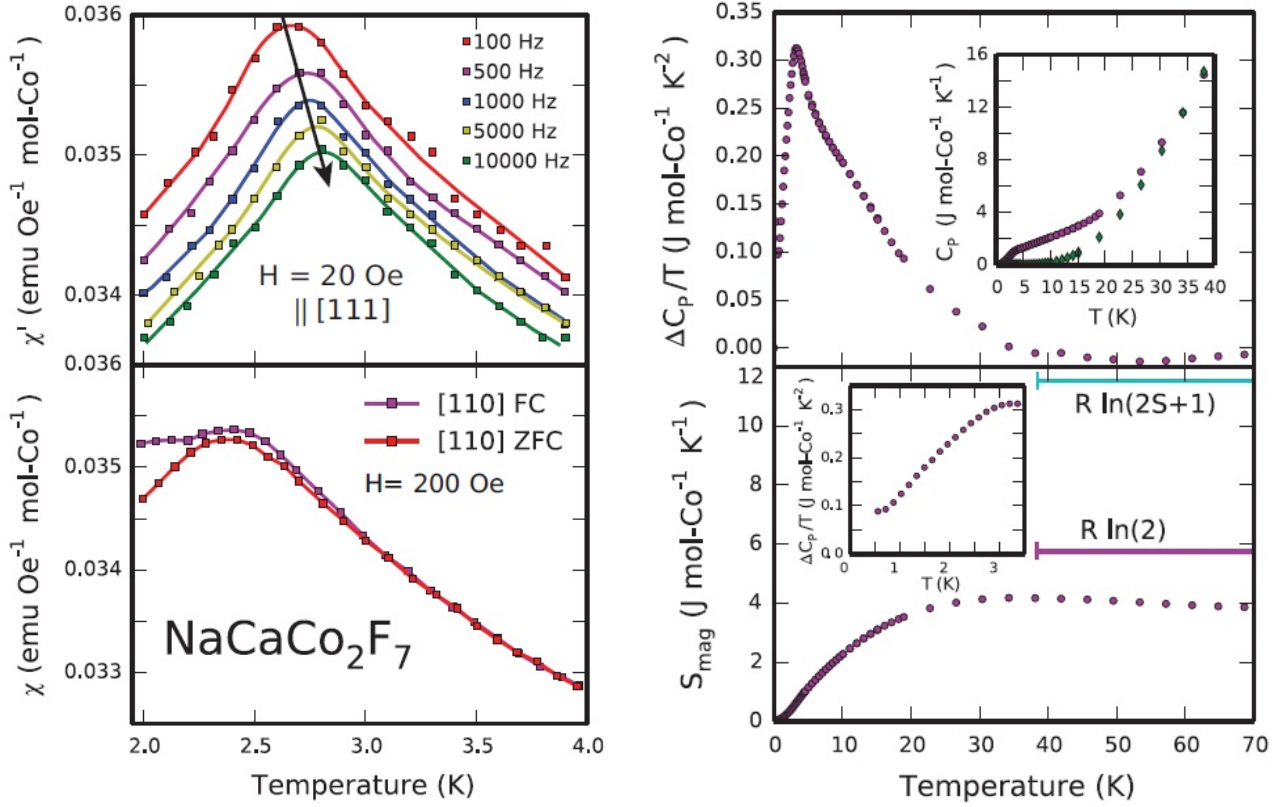
which is in the range of an insulating spin glass and, interestingly, one order of magnitude higher as expected for a cluster spin glass [28]. However, the Volger-Fulcher law takes into account interaction between spin centers/clusters and is given by

$$T_f = T_0 - \frac{E_a}{k_B \ln(\tau_0 \nu)}. \quad (4.12)$$

Here, τ_0 is the intrinsic relaxation time, E_a is the so-called activation energy and T_0 the *ideal glass temperature*⁸. As already mentioned in the last subsection and as will be discussed in more details below, NaCaCo₂F₇ is a cluster spin glass shown by neutron scattering [35]. Fixing $\tau_0 \approx 10^{-11}$ s as usually observed intrinsic relaxation time of cluster spin glasses yields $E_a \approx 7.9 \cdot 10^{-4}$ eV and $T_0 \approx 2.24$ K. T_0 can be interpreted as strength between the spin clusters. Additionally, d.c. magnetic susceptibility shows a difference between ZFC (Zero Field Cooled) and FC (Field Cooled) measurements in $H = 200$ Oe applied along [110]-direction below T_f . The presented difference of the temperature dependence between ZFC and FC is consistent with a spin-glass-like behavior (figure 4.8) (a). Similar behaviors are observed in the [100]- and [111]-directions [28].

Figure 4.8 (b) shows the heat capacity $\Delta C_p/T$ after subtraction of the specific of the nonmagnetic NaCaZn₂F₇ (circles). A peak around T_f is observed which is quiet broad for a conventional spin-glass freezing. The inset of the top panel shows C_p per Co for NaCaCo₂F₇ (circles) and for NaCaZn₂F₇

⁸For details, see e.g. *Understanding the spin glass transition as a dynamic phenomenon* by K. Trachenko [69] which discusses the interpretation of a spin glass transition from a dynamical perspective.



(a) Top panel: Real part χ' of the a.c. susceptibility $\chi_{ac} = \chi' - i\chi''$ in an applied field of 20 Oe as a function of different frequencies. Bottom panel: D.c. susceptibility $\chi_{dc} = \chi$ at 200 Oe; both for the mentioned different crystal directions.

(b) Top panel: Magnetic heat capacity $\Delta C_p/T$ (the inset shows C_p after subtraction of the nonmagnetic NaCaZn₂F₇). Bottom panel: Integration of the magnetic heat capacity yields the magnetic entropy which saturates below 50 K (inset shows a close-up of $\Delta C_p/T$ around T_f).

Figure 4.8: Bulk investigations (d.c., a.c. susceptibility and heat capacity) of NaCaCo₂F₇ published by Krizan *et al.* [28].

(diamonds). The magnetic entropy S_{mag} is calculated by the integration of the heat capacity up to the temperature T_i ,

$$S_{mag}(T_i) = \int_0^{T_i} \Delta C_p \frac{dT}{T}, \quad (4.13)$$

to estimate the magnetic entropy which is frozen out. This entropy has a magnetic origin because of the subtraction of the nonmagnetic part using NaCaZn₂F₇. The bottom panel of figure 4.8 shows that the magnetic entropy is saturated between 20 K and 70 K (inset panel shows a close-up of $\Delta C_p/T$ below T_f). The two horizontal lines in figure 4.8 (b) represent the values of the Heisenberg entropy $R \ln(2S+1)$ (aquamarine) and the Ising entropy $R \ln 2$ (purple) with the molar gas constant R . The released entropy is below the Ising level $R \ln 2$. The observed entropy loss at the freezing transition is low, suggesting that magnetic entropy remains present in the system down to 0.6 K. All these points let conclude that NaCaCo₂F₇ is a highly frustrated pyrochlore antiferromagnet with bond-disorder since a clear distinction by the upper data between a conventional spin glass and cluster spin glass is not possible.

However, elastic diffuse neutron scattering experiments of NaCaCo₂F₇ suggest a continuous de-

formable manifold of XY states spanned by $\psi_2(m_{3z^2-r^2})$ and $\psi_3(m_{x^2-r^2})$ which suggests a magnetic SRO XY antiferromagnetic states⁹ [35]. Figure 4.4 visualizes the two XY states of Γ_5 of irreducible representations on one tetrahedron in different views. The spins are restricted to planes with the normal vector parallel to the local [111]-direction. This cluster-like short-range-ordered state is estimated to have a correlation length of 16 Å with a Kramers doublet Co²⁺ ground state confirming a $S_{\text{eff}} = \frac{1}{2}$ model [64]. Inelastic neutron scattering shows XY-like cluster excitations at energies below 5.5 meV and collinear fluctuations above this energy threshold [35]. An intermediate spin-orbit coupling model yielded an XY-like g tensor with $g_{xy}/g_z \approx 3$ and polarized neutron data observed nearest-neighbor short-range correlation up to 200 K [70].

In-house NMR investigations prove a broad quasi-static field distribution and freezing below 3.6 K measured at 0.88 T (¹⁹F) and 3.0 T (²³Na). Locally, the crystal structure is confirmed by the probed nuclei. Nevertheless, at low temperature a strong-wipe out effect of the NMR signal puts forward certain limitations for the reliable estimation of the true ground state [71]. M. Vojta *et al.* complement the experimental NMR results by large-scale Monte-Carlo simulations of a pyrochlore XY model with bond-disorder. While the simulation results are qualitatively consistent with a glass-like spatial mixture of $\psi_2(m_{3z^2-r^2})$ and $\psi_3(m_{x^2-r^2})$ states, reported by K. Ross *et al.* [35], quantitatively the magnetic correlation length and the freezing temperature are overestimated proposing the nonclassical nature of NaCaCo₂F₇ below T_f .

4.3.2 XY planar anisotropy versus isotropy in NaCaCo₂F₇

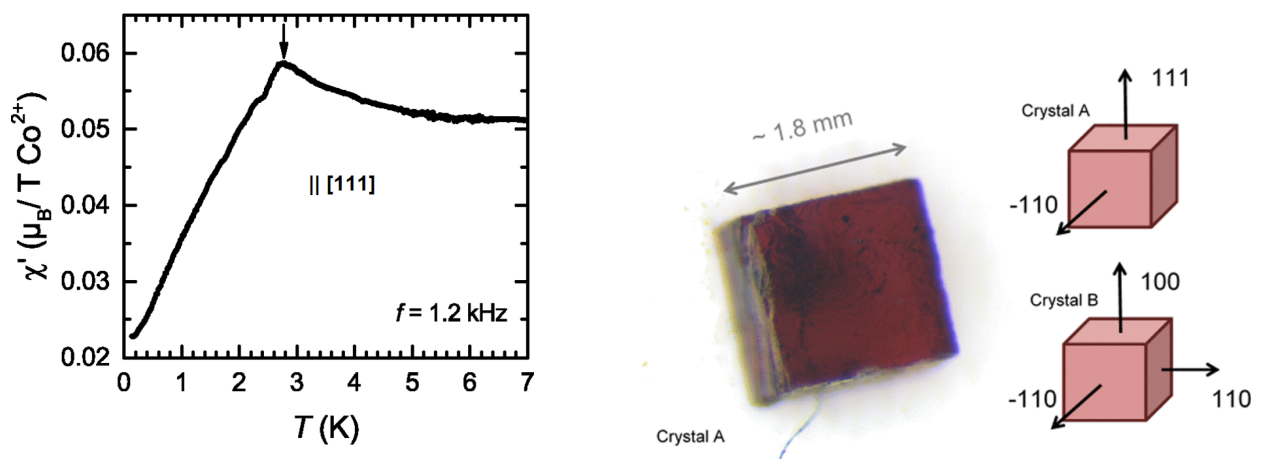
To investigate the bulk-averaged planar XY nature in detail, we have performed pulsed high-field magnetization measurements in Dresden-Rossendorf up to 58 T in three different crystal directions¹⁰. In parallel, we have motivated Vadim Kataev and Julian Zeisner from the IFW in Dresden to start ESR (Electron Spin Resonance) spectroscopy experiments to obtain the effective g -values improving complementary the understanding anisotropic behavior of this compound. For details, see *Magnetic interaction and spin dynamics in the bond-disordered pyrochlore fluoride NaCaCo₂F₇* by J. Zeisner, S. A. Bräuninger *et al.* [65].

NaCaCo₂F₇ has shown an isotropic magnetic behavior up to 9 T below T_f as shown in figure 4.7 (inset top). ESR (Electron Spin Resonance) spectroscopy experiments obtained the effective g -values to improve the understanding of the anisotropic behavior of this compound [65]. The results are the averaged projections in the direction of the applied fields over the four sites on the tetrahedron of Co²⁺. The ESR experiment showed g -values close to 2 which is in contrast to a strongly XY-like g -tensor of a single-ion model with $g_{xy}/g_z \approx 3$ proposed by inelastic neutron scattering [70].

Additionally, the real part of the magnetic susceptibility $\chi'(T)$ was measured down to 150 mK at 1.2 kHz on a single crystal in [111]-direction as shown in figure 4.9 (a) to extend the temperature

⁹As mentioned, the further investigations (Neutron scattering studies, NMR, ESR) are not that extensively discussed and summarized, for details, please see corresponding citations.

¹⁰Nicely supported by the Rossendorf team, especially Thomas Herrmannsdörfer and Lars Opherden extended the experimental findings by enhanced phenomenological considerations. Special thanks to Christian Blume (IFW Dresden) for the close collaboration to help me with the crystal cut and Denis Gorbunov for experimental support during the magnet time.



(a) Real part χ' of the a.c. susceptibility $\chi_{ac} = \chi' - i\chi''$ per Co in ZF static magnetic field down to 150 mK at 1.2 kHz on a single crystal, taken from [65]. The measurement is discussed in the PhD thesis by L. Opherden [72] as well. The imaginary part χ'' had a too high signal-to-noise ratio and is not unshown.

(b) Left: Photo of one of the two measured single crystals cut for pulsed-high field magnetization measurements (here crystal A). The length is 1.8 mm. Right: My schematic drawn of the cubic crystals and corresponding crystal directions. The figure is taken from [65].

Figure 4.9: Low- T a.c. susceptibility data down to 150 mK of $\text{NaCaCo}_2\text{F}_7$ and one of the used single crystals together with a schematic visualization of the cubic single crystals [65].

range below 2 K supporting the μ^+ SR study. Here, the freezing temperature is shifted to 2.77 K consistent with the a.c. study performed by J. Krizan *et al.*, as shown by the black arrow. There is no additional transition observed, e.g., to a LRO state, down to 150 mK as, we will see, is consistent with our μ^+ SR study.

The crystals were cut in the directions as presented in figure 4.9 (b) forming two cubes. Therefore, the mass and geometry was comparable and the [110]-direction was measured two times for a consistency check. The direction-dependent different shape or cross section of a crystal may sometimes play a role, which is avoided here with the cube shape reducing anisotropy shape effects.

The pulsed high-field magnetization measurements were performed in the Dresden High Magnetic Field Laboratory measured by integrating the voltage induced in a compensated coil system¹¹ surrounding the sample normalized using static low-field data ($B < 9$ T) which confirmed the data shown in figure 4.7. Figure 4.10 (a) shows the magnetization m in μ_B per Co as a function of the magnetic field up to 58 T for different temperatures as indicated for the crystallographic direction [110]. Here, the full saturation is not reached even at 2 T and 58 T. For a comparison, for noninteracting XY spins on the pyrochlore lattice the saturation is already reached at 3 T, such as for $\text{Er}_2\text{Ti}_2\text{O}_7$ [65]. Therefore, it reflects the strong antiferromagnetic interaction. Figure 4.10 (b) shows the crystallographic direction dependence of the magnetization m in μ_B per Co as a function of the magnetic field up to 58 T at $T = 2$ K. The magnetization is isotropic up to 58 T and a splitting cannot be specified. To describe the interaction, a phenomenological model is introduced replacing the real temperature T by $T \rightarrow T_{\text{eff}} = T + T_0$ leading to a modified Brillouin function using the spin projection along the field

¹¹For experimental details, see Skourski *et al.* [73].

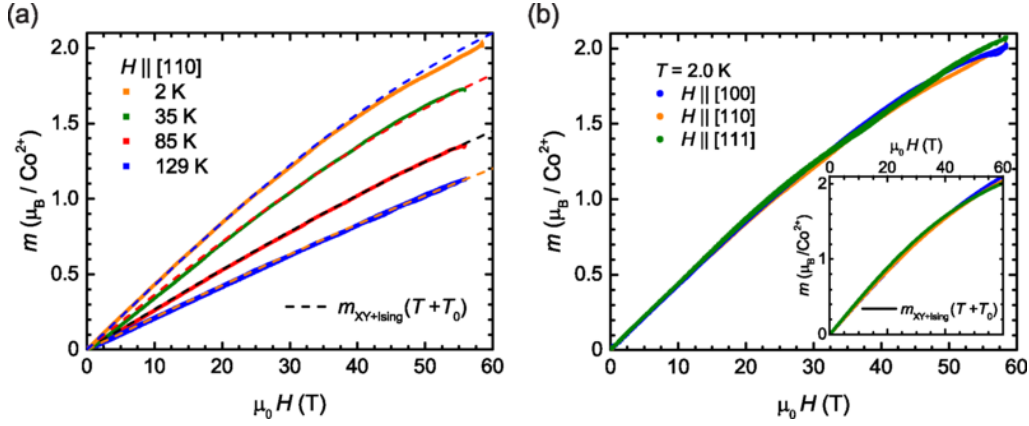


Figure 4.10: Left panel: (a) Magnetization m in μ_B per Co as a function of the magnetic field for different temperatures as indicated, all for the crystallographic direction $[110]$. Right panel: (b) Magnetization m in μ_B per Co as a function of the magnetic field for the directions $[111]$, $[110]$, $[100]$ at $T = 2$ K. The dashed lines in (a) and solid line in the inset in (b) represent the model taking an effective temperature $T_{\text{eff}} = T + T_0$ assuming a small Ising contribution of $\mu_{\text{Ising}} = 0.935\mu_B$ and a dominant XY moment of $\mu_{\text{XY}} = 3.040\mu_B$ as proposed by neutron studies. The figure is taken from J. Zeisner *et al.* [65].

direction. In this approach $k_B T_0$ is the energy scale of the frustrated interaction. This model uses the proposed Ising contribution of $\mu_{\text{Ising}} = 0.935\mu_B$ and a dominant XY moment of $\mu_{\text{XY}} = 3.040\mu_B$ by neutron studies. The results are shown in (a) and (b) by the dashed and solid lines (inset in (b)), respectively. T_0 is of the order of the Curie-Weiss temperature. It is argued, that the strong antiferromagnetic interactions leads to an effective *masking* of the XY anisotropy and the field range of 0-58 T corresponds, therefore, only to a magnetic field of 0-1.15 T [65]. However, the isotropy in ESR and NMR is not explained with this ansatz.

To conclude, ESR spectroscopy, pulsed high-field magnetization measurements up to 58 T and NMR studies have shown an isotropic behavior from a magnetic point of view. Neutron-scattering studies proposed mainly a local XY nature perpendicular to the local $[111]$ -axis of the corner of the tetrahedra containing Co. To gain an understanding of this combined observations motivates further experimental and theoretical studies [65].

5 Quenched Disorder and Persistent μ^+ Spin Dynamics in $\text{BaTi}_{0.5}\text{Mn}_{0.5}\text{O}_3$

In this chapter, the μSR results of $\text{BaTi}_{0.5}\text{Mn}_{0.5}\text{O}_3$ are presented. One purpose is to show an example of a disordered oxide system probed by $\mu^+\text{SR}$. $\text{NaCaCo}_2\text{F}_7$ and $\text{BaTi}_{0.5}\text{Mn}_{0.5}\text{O}_3$ contain a 50% : 50% disorder of one site: Na^+ and Ca^{2+} or Ti^{4+} and Mn^{4+} , respectively. Quantitatively, most μSR spectra of disordered oxides are analyzed by a stretched exponential polarization function reflecting a considerable amount of magnetic disorder making the data analysis quite straightforward, in contrast to the observed behavior in $\text{NaCaCo}_2\text{F}_7$. The related double perovskite $\text{SrTi}_{0.5}\text{Mn}_{0.5}\text{O}_3$ is proposed to be a cluster spin glass which shows a clear experimental difference as probed by $\mu^+\text{SR}$ compared to $\text{BaTi}_{0.5}\text{Mn}_{0.5}\text{O}_3$. $\text{BaTi}_{0.5}\text{Mn}_{0.5}\text{O}_3$ is an example of a disordered frustrated compound probed by μSR showing persistent spin dynamics (PSD). CaF_2 probed by μSR exhibits a $\text{F}-\mu^+-\text{F}$ state and the final chapter of the first main part of this work combines all: Bond-disorder, $\text{F}-\mu^+-\text{F}$ state physics and PSD in $\text{NaCaCo}_2\text{F}_7$, see figure 1.2. The following two points are emphasized:

1. I have observed a clear difference between $\text{BaTi}_{0.5}\text{Mn}_{0.5}\text{O}_3$ [37] and $\text{SrTi}_{0.5}\text{Mn}_{0.5}\text{O}_3$ [74]. $\text{BaTi}_{0.5}\text{Mn}_{0.5}\text{O}_3$ shows mainly a dynamical relaxation rate down to 20 mK and this rate increases for $T \rightarrow 0$. $\text{SrTi}_{0.5}\text{Mn}_{0.5}\text{O}_3$ shows a clear peak around the freezing temperature $T_f \approx 14$ K and the dynamical relaxation rate decreases for $T \rightarrow 0$ close to zero. This temperature dependence is expected for a common spin glass or cluster spin glass as observed in $\text{SrTi}_{0.5}\text{Mn}_{0.5}\text{O}_3$ [74].
2. I have done a successful DFT estimation of the possible muon site in $\text{BaTi}_{0.5}\text{Mn}_{0.5}\text{O}_3$ which is already published [37].

For details, see *Dynamic magnetism in the disordered hexagonal double perovskite $\text{BaTi}_{1/2}\text{Mn}_{1/2}\text{O}_3$* by M. R. Cantarino, S. A. Bräuninger *et al.*¹ [37].

5.1 Motivation

Oxides with a perovskite structure have shown a rich variety of ground states and properties like multiferroicity, high-temperature superconductivity, and colossal magnetoresistance [75]. A disordered double perovskite is given by the structure $AB_{0.5}B'_{0.5}O_3$ where B and B' are $3d$, $4d$, and/or $5d$ transition-metals. A is a rare-earth or alkaline-earth cation. $\text{BaTi}_{0.5}\text{Mn}_{0.5}\text{O}_3$ contains a mixing

¹In the following, the notation $\text{BaTi}_{0.5}\text{Mn}_{0.5}\text{O}_3$ is used rather than $\text{BaTi}_{1/2}\text{Mn}_{1/2}\text{O}_3$.

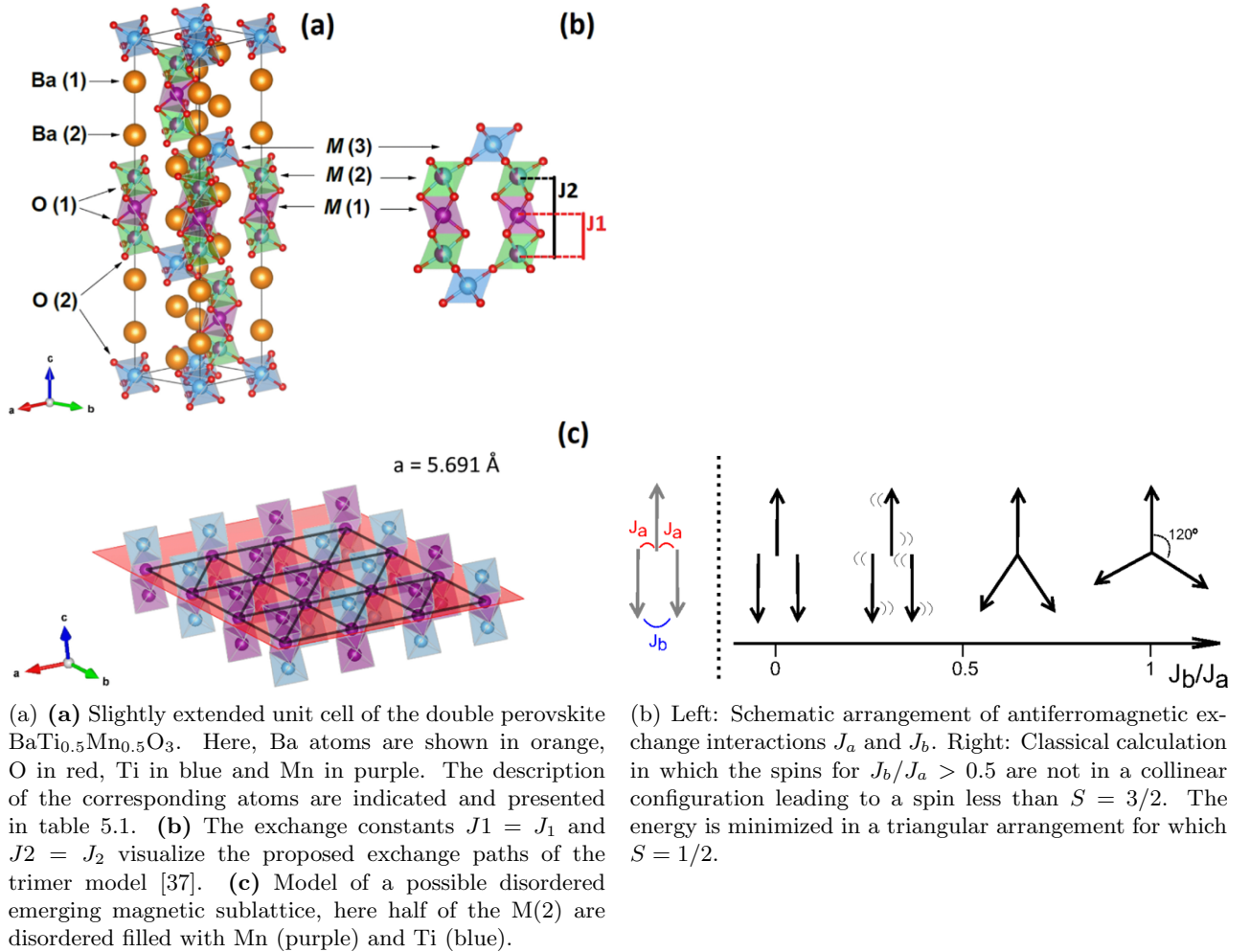


Figure 5.1: (a) Structural models after M. R. Cantarino, S. A. Bräuninger *et al.* [37] and (b) the corresponding qualitative scenario of magnetic trimers taken from F. A. Garcia *et al.* [29].

of nonmagnetic Ti^{4+} and magnetic Mn^{4+} on the B and B' sites leading to structural disorder. The possible magnetic interaction of the transition metal elements, here Mn^{4+} , is provided by superexchange interaction. The nonmagnetic ions of Ti^{4+} locally *interrupt* possible antiferromagnetic or competitive interaction paths leading to short-range magnetically weakly-coupled structural trimers with three (magnetic trimer) or less (dimers, orphans) magnetic Mn^{4+} forming a possible spin-gap system [29]. In spin-gap systems there is an energy gap in the spin excitation, e.g., between a singlet ($S = 0$) groundstate and an excited state with ($S = 1$) as discussed in the pioneering work of the Bose-Einstein condensation of magnons in TlCuCl_3 [76] and therein.

However, in $\text{BaTi}_{0.5}\text{Mn}_{0.5}\text{O}_3$ there is the possibility given to study the less-investigated $S = \frac{3}{2}$ spin-gap systems because of the valance of Mn of 4+ combined with the interplay of structural disorder and frustration which can give rise to exotic ground states like spin liquids.

5.2 Crystallographic and magnetic properties of $\text{BaTi}_{0.5}\text{Mn}_{0.5}\text{O}_3$

Figure 5.1 (a) (a) shows the lattice structure of the hexagonal double perovskite $\text{BaTi}_{0.5}\text{Mn}_{0.5}\text{O}_3$. The crystallographic data are taken from F. A. Garcia *et al.* [29] and shown in table 5.1. The angles of the unit cell are

$$\angle(a, b) = 120^\circ \quad (5.1)$$

and

$$\angle(a, c) = \angle(b, c) = 90^\circ. \quad (5.2)$$

The compound $\text{BaTi}_{0.5}\text{Mn}_{0.5}\text{O}_3$ is a 12R-type double perovskite with space group $R\bar{3}m$ (space group number 166). Trimers of face-sharing octahedra lying in the direction of the c-axis are shown in figure 5.1 (a) (b). Here, the crystallographic site M(2) is mixed occupied by Mn^{4+} and Ti^{4+} . The site M(1) is occupied by Mn^{4+} and M(3) by Ti^{4+} according to table 5.1. It is proposed that the properties of $\text{BaTi}_{0.5}\text{Mn}_{0.5}\text{O}_3$ depend on the local occupation of the structural trimer² configuration, presented in figure 5.1 (a) (b), that leads to magnetically frustrated trimers and, additionally, to dimers and orphan spins. The exchange pathways $J1 = J_1$ and $J2 = J_2$ visualize the proposed exchange paths of the magnetically frustrated trimer model which is suggested for three Mn^{4+} ions in figure 5.1 (a) (b), after F. A. Garcia *et al.* [37]. A structural trimer with one Ti^{4+} and two Mn^{4+} leads to a magnetic dimer configuration and a structural trimer of two Ti^{4+} and one Mn^{4+} to an orphan spin, respectively. Figure 5.1 (b) shows a qualitative scenario for the magnetic properties of the magnetic trimer containing three Mn^{4+} . A schematic arrangement of antiferromagnetic exchange interactions J_a and J_b is shown. The right panel shows the result of the classical calculation in which the spins for $J_b/J_a > 0.5$ are not in a collinear configuration leading to a spin less than $S = 3/2$. The energy is minimized in a triangular arrangement ($J_b/J_a = 1$) for which $S = 1/2$. The detailed relation between J_1 , J_2 and J_a , J_b may exceed this classical treatment.

Experimentally, there is no sign for magnetic LRO found down to 20 mK [37]. Heat-capacity measure-

²In the following, one should distinguish between a *structural* trimer which contain all possible permutations of Mn^{4+} and Ti^{4+} and the *magnetic* trimer which contains three Mn^{4+} .

Element	Site	x	y	z	Occupancy
Ba(1)	6c	0	0	0.2856(2)	1
Ba(2)	6c	0	0	0.1290(2)	1
M(1)(Mn)	3b	0	0	0.5	1
M(2)(Ti/Mn)	6c	0	0	0.4091(2)	0.5/0.5
M(3)(Ti)	3a	0	0	0	1
O(1)	18f	0.1513(2)	0.8487(2)	0.45656(8)	1
O(2)	18f	0.1673(3)	0.8327(3)	0.62700(9)	1

Table 5.1: Refined structural parameters of $\text{BaTi}_{0.5}\text{Mn}_{0.5}\text{O}_3$ at room temperature according to F. A. Garcia *et al.* [29]. The space group is $R\bar{3}m$ (space-group number 166) with $a = 5.6910(3)$ Å, $b = 5.6910(3)$ Å and $c = 27.915(1)$ Å. M(1-3) are the transition-metal sites.

ments (C_p) show a broad anomaly around 3 K which seems more like a crossover. D.c. susceptibility $\chi(T)$ tends towards saturation below 10 K and cannot be described by a simple Curie-Weiss law in the entire T -range and is described by a phenomenological model of contributions for the correlated (dimer, trimer) and orphan spins (close to be negligible) and a contribution for the frustrated system (interacting structural trimers) below 150 K. A rough estimation of the effective high-temperature magnetic moment is obtained by d.c. susceptibility measurements yielding $\mu_{\text{eff}} \approx 3.9\mu_B$ which is close to the full moment of Mn^{4+} . The data indicate the presence of a highly correlated spin state below 10 K. Here, the arrangement of layers play a role forming a triangular lattice with possible antiferromagnetic in-plane exchange interactions. The formation of the magnetic dimers and trimers occur at a temperature around 150 K consistent with a large energy scale and extracted exchange constants $J_a/k_B = 200(2)$ K and $J_b/k_B = 130(10)$ K. The frustrated subsystem containing orphan spins, dimers and trimers of Mn^{4+} at lower temperature yielded an effective Curie-Weiss temperature of $\Theta_{\text{CW}} = -7.5(5)$ K. Quantitatively, $f = |\Theta_{\text{CW}}/T_f| \gg 1$ is a sign for frustration and competitive interactions and a lower bound of the frustration index is around 75 because of the missing freezing temperature down to 0.1 K³ [37]. Interestingly, a.c. susceptibility has not shown any frequency dependence of $\chi'(T)$ as expected for a spin glass [29].

The lattice is arranged in layers of triangular substructures with a lattice constant of around 5.69 Å occupied with Mn^{4+} and Ti^{4+} with the normal vector parallel to the c -axis. Figure 5.1 (a) (c) presents a layer of a possible disordered emerging magnetic sublattice, here half of the M(2) sites are randomly filled with Mn^{4+} and Ti^{4+} . An antiferromagnetic intralayer exchange interaction is proposed between $S = 3/2$ orphan spins and effective $S = 1/2$ magnetic trimers to explain the second low-energy scale and effective exchange coupling of around 10 K. An interlayer interaction cannot be excluded but should be much weaker because of a layer separation of around 9.8 Å.

Therefore, $\text{BaTi}_{0.5}\text{Mn}_{0.5}\text{O}_3$ is proposed to be an intrinsically disordered $S = \frac{3}{2}$ spin-gap system which has a frustrated magnetic ground state [29]. The lack of a clear magnetic phase transition, on one hand, and the evidence of a correlated spin state at low T together with the absence of a glassy frequency dependence of $\chi'(T)$ on the other hand open the question and discussion for a spin-liquid-like ground state.

³One could argue to take the anomaly around 3 K which appears in $\chi(T)$. This would lead to a much lower value.

5.3 μ^+ SR study on $\text{BaTi}_{0.5}\text{Mn}_{0.5}\text{O}_3$

We have performed a μ^+ SR experiment on a powder sample of $\text{BaTi}_{0.5}\text{Mn}_{0.5}\text{O}_3$ at the Paul-Scherrer Institute (PSI) in Villigen in Switzerland using the spectrometers LTF (Low Temperature Facility) and GPS (General Purpose Spectrometer). For experimental details see M. R. Cantarino *et al.* [37]. The spectra were analyzed using the asymmetry function described by a stretched exponential

$$A(t) = a \exp \left[-(\lambda t)^\beta \right] + b. \quad (5.3)$$

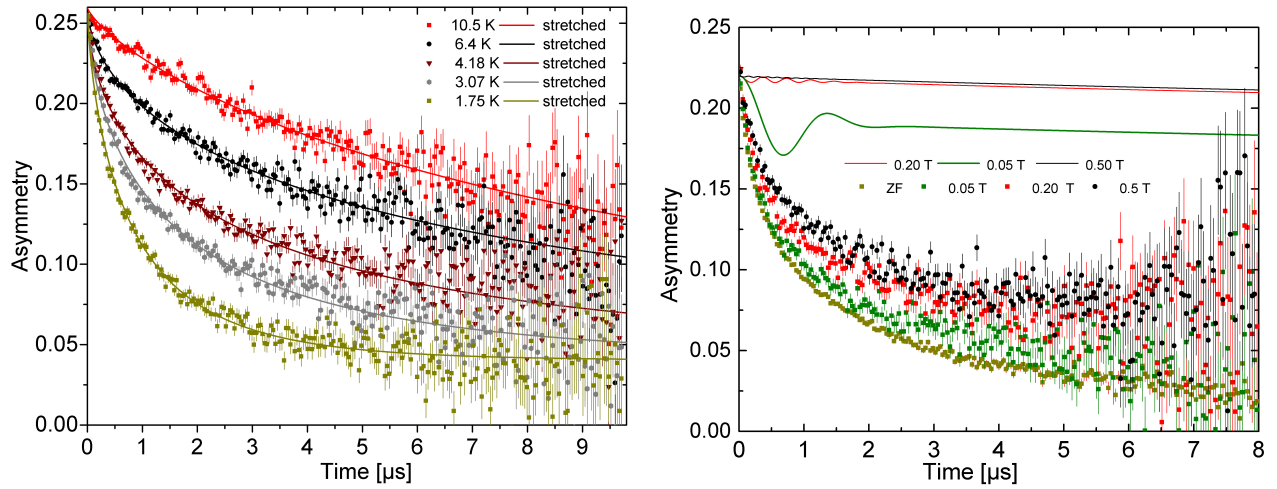
Here, λ is the μ^+ relaxation rate of the muon spin polarization which can be a static or dynamical relaxation or a combination of both and the positive β is the so-called stretched exponent. This behavior is known as Kohlrausch law and is discussed in the chapter *Methods*. b is the fraction of muons not stopped in the sample, e.g., in the sample holder (silver plate) depending on the spectrometer. a is the fraction of muons stopping in the sample. In detail, the second term is given by $be^{\lambda_b t}$ including a possible relaxation of the background material. In this study the background is set to be time independent, since $\lambda_b \ll \lambda$. The stretched exponential model reflects for $\beta \approx 0.5$ a huge amount of relaxation channels and has a phenomenological nature⁴. The relaxation channel or frequency distribution is a consequence of the intrinsic disorder reflecting the microscopic magnetic disorder, e.g., because of structural disorder which is magnetoelastically coupled, here because of the Ti^{4+} and Mn^{4+} randomness. μ SR time spectra of selected temperatures of $\text{BaTi}_{0.5}\text{Mn}_{0.5}\text{O}_3$ are presented in figure 5.2 (a) and the corresponding stretched exponential fits are given by the lines and are in full agreement with the obtained data. Figure 5.3 (a) and (b) show the results of the stretched exponential fits for the measured temperature range down to 19 mK. The data were taken with an overlap of spectra measured in the spectrometers GPS and LTF. Figure 5.3 (a) shows the relaxation rate λ as a function of temperature. The relaxation rate λ converges to around $1.2 \mu\text{s}^{-1}$ and $\beta \approx 0.55$ down to 19 mK. Figure 5.3 (b) shows the stretched exponent β as a function of temperature. At high temperature β is close to 1 and β converges close to $\beta \approx \frac{1}{2}$ at low T . At 100 K, the system is in the fast paramagnetic limit. The yellow background shows a shift in the overlap of the GPS and LTF data, probably because of experimental restrictions of the LTF and GPS spectrometers.

In a decoupling experiment it had turned out that the main part ($> 80\%$) of the muon spin relaxation λ has a dynamical nature as shown in figure 5.2 (b). The solid lines show the comparison to a dynamical Kubo-Toyabe fit according to the applied longitudinal magnetic field. This means the main part of the muons probe fluctuating magnetic fields and no static magnetic SRO even at 19 mK.

5.4 DFT of $\text{BaTi}_{0.5}\text{Mn}_{0.5}\text{O}_3$

I have performed DFT calculations of an unperturbed unit cell to obtain the electrostatic potential using the all-electron full-potential linearized augmented-plane-wave (FP-LAPW) code Elk 4.3.6 [26] using Broyden mixing [24] and the Perdew-Burke-Ernzerhof-GGA (Generalized gradient approxima-

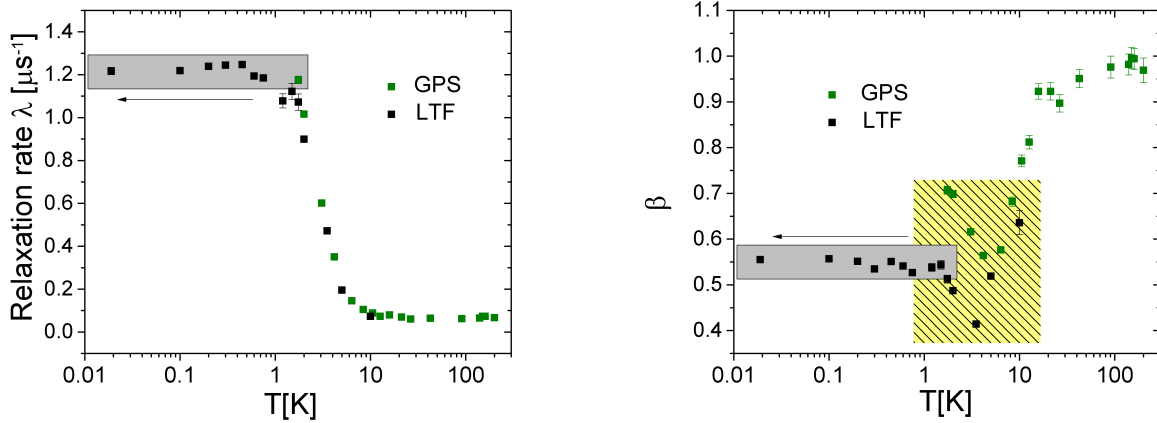
⁴A similar model is sometimes taken for the depolarization, means relaxation of the population difference of the nuclei in NMR [13] or in magnetization-relaxation experiments.



(a) μSR spectra as a function of temperature measured using the GPS spectrometer at PSI, Switzerland and fit of the stretched exponential model.

(b) Spectra of LF-decoupling experiment using LTF spectrometer for different external magnetic fields and the comparison with a dynamical Kubo-Toyabe theory (solid lines).

Figure 5.2: $\mu^+\text{SR}$ spectra of the double perovskite compound $\text{BaTi}_{0.5}\text{Mn}_{0.5}\text{O}_3$ (powder) as published in [37].



(a) Relaxation rate λ as a function of temperature using the spectrometers GPS (green) and LTF (black) measured at PSI, Switzerland.

(b) Stretched exponent β as a function of temperature.

Figure 5.3: Results of the stretched exponential model, $A(t) = a \exp[-(\lambda t)^\beta] + b$, of the polarization function of the double perovskite $\text{BaTi}_{0.5}\text{Mn}_{0.5}\text{O}_3$ [37].

Element	Site	x	y	z	Occupancy
Ba(1)	6c	0.2856(2)	0.2856(2)	0.2856(2)	1
Ba(2)	6c	0.1290(2)	0.1290(2)	0.1290(2)	1
M(1)(Mn)	3b	0.5	0.5	0.5	1
M(2)(Ti/Mn)	6c	0.4091(2)	0.4091(2)	0.4091(2)	0.5/0.5
M(3)(Ti)	3a	0	0	0	1
O(1)	18f	0.60786(2)	1.15396(2)	-0.39214(1)	1
O(2)	18f	0.7943(2)	1.2924(2)	-0.62057(1)	1

Table 5.2: Structural parameters of $\text{BaTi}_{0.5}\text{Mn}_{0.5}\text{O}_3$ of the space group $R\bar{3}m:\text{R}$ at room temperature. The calculation is based on the values from F. A. Garcia *et al.* [29]. The space group is $R\bar{3}m:\text{R}$ (space-group number 166) with $a = b = c = 9.86807(9)$ Å. M(1-3) are the transition-metal sites.

tion) functional [25]. For details see chapter *Methods*.

The unit cell of $\text{BaTi}_{0.5}\text{Mn}_{0.5}\text{O}_3$ contains 88 atoms as presented above. This assumes the hexagonal space group $R\bar{3}m:\text{H}$ (No.1) in the Hermann-Mauguin notation. The crystal system, the Bravais lattice is trigonal of $R\bar{3}m:\text{H}$. The symmetry is D_{3d} in Schönflies notation. The second representation, $R\bar{3}m:\text{R}$ (No.2), takes a rhombohedral axis and contains 27 atoms. This means the number of atoms is considerable reduced. Therefore, I have chosen the space group $R\bar{3}m:\text{R}$ (No.2) for the DFT calculations to reduce the calculation time significantly. Table 5.2 shows the calculated values of $R\bar{3}m:\text{R}$ (No.2) starting from the values measured by F. A. Garcia *et al.* [29]. Here, the cell is rhombohedral with

$$\angle(a, b) = \angle(a, c) = \angle(b, c) = 33.5189^\circ. \quad (5.4)$$

The used length of the unit cell is taken to be $18.64794971 a_0$ ignoring the experimental error bar⁵. The unit cell of the space group $R\bar{3}m:\text{R}$ is visualized in figure 5.4-5.7. The diagonal line of the unit cell of $R\bar{3}m:\text{R}$ corresponds to the c -axis of $R\bar{3}m:\text{H}$. The disordered Ba^{4+} and Ti^{4+} ions are close to the sharp edges. The contained disorder of Mn^{4+} and Ti^{4+} is handled in the following way: The primitive $R\bar{3}m:\text{R}$ cell contains two disordered ions and one is chosen to be Mn and the second one Ti. Statistically, this is assumed to be the most represented case. The muon carries a positive charge and should be located close to the O^{2-} ion. The electrostatic energy minimum of the undistorted unit cell is located insight the yellow structures of figure 5.4, 5.6, and 5.7. The lowest total energy minima are insight the flower structures of figure 5.7. The isosurface structures are slightly asymmetric because of the mentioned assumption of one Ti and one Mn of the 6c site leading to an asymmetric unit cell. Therefore, a muon site closer to a disordered Mn is slightly preferred. However, this result proposes that the muon is located close to O close to the Ba plane ignoring a possible muon-induced local lattice displacement.

⁵The digits are more than given by F. A. Garcia *et al.* [29]. This is because the Spacegroup package requires so many digits since it is based on atomic units.

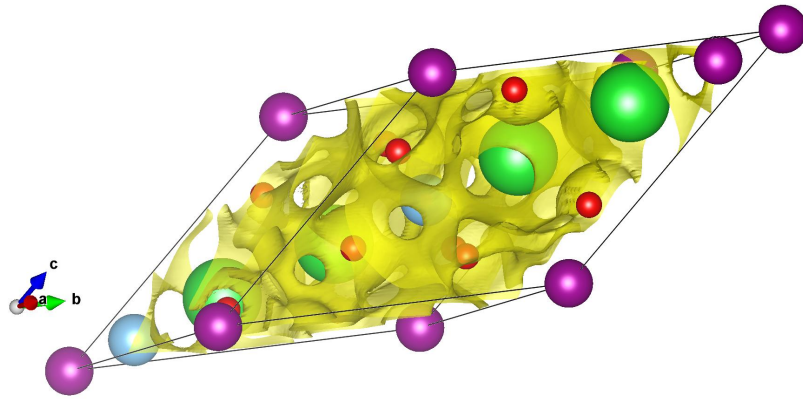


Figure 5.4: Unit cell of $\text{BaTi}_{0.5}\text{Mn}_{0.5}\text{O}_3$ of the space group $R\bar{3}m:\text{R}$ visualized by the atomic radii. Ba atoms are shown in green, O in red, Ti in blue and Mn in purple. The yellow surface shows the isosurface of the potential φ of $0.41 \frac{E_h}{e}$.

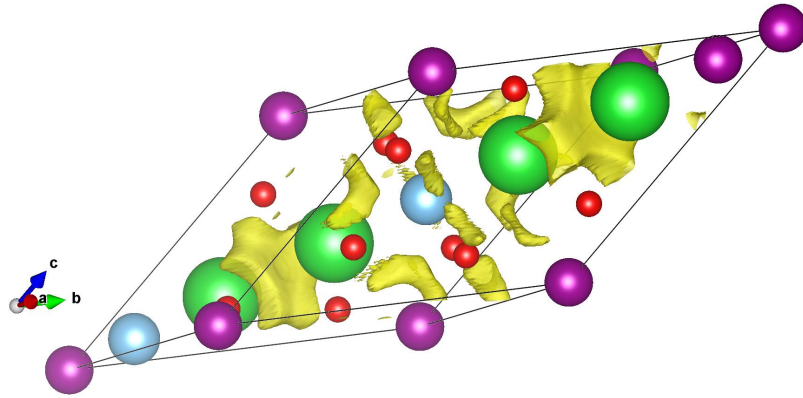


Figure 5.5: Unit cell of $\text{BaTi}_{0.5}\text{Mn}_{0.5}\text{O}_3$ of the space group $R\bar{3}m:\text{R}$ and the yellow isosurface of the potential φ of $0.45 \frac{E_h}{e}$. Two flower-like structures between Ba atoms and banana-like structures are observed in the middle of the unit cell.

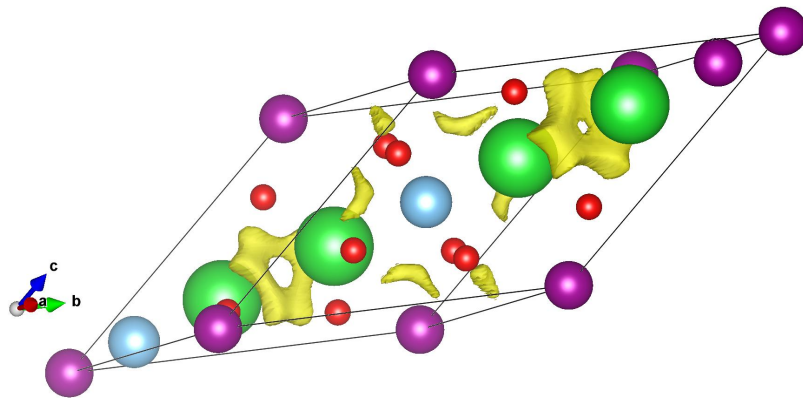


Figure 5.6: Unit cell of $\text{BaTi}_{0.5}\text{Mn}_{0.5}\text{O}_3$ of the space group $R\bar{3}m:\text{R}$ and the yellow isosurface of the potential φ of $0.46 \frac{E_h}{e}$. Two flower-like structures with holes between Ba and the banana-like structures are observed in the middle of the unit cell. Compared to $\varphi = 0.45 \frac{E_h}{e}$ the bananas are smaller.

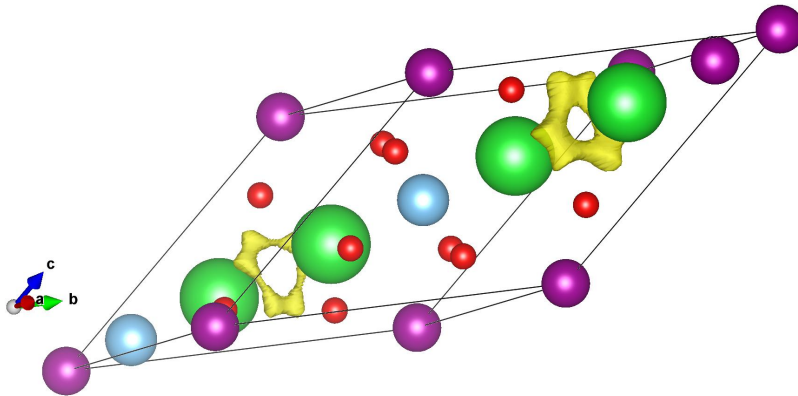


Figure 5.7: Unit cell of $\text{BaTi}_{0.5}\text{Mn}_{0.5}\text{O}_3$ of the space group $R\bar{3}m:\text{R}$ and the yellow isosurface of the potential φ of $0.468 \frac{E_h}{e}$. The two flower structures are remained. The isosurface structures are slightly asymmetric because of the mentioned assumption of one Ti and one Mn of the $6c$ site leading to an asymmetric unit cell.

5.5 Discussion

The muon spin relaxation rate λ is nearly temperature independent for $T > 10\text{ K}$ consistent with a paramagnetic behavior, see figure 5.3 (a). The increase of λ from $0.06 \mu\text{s}^{-1}$ up to $1.2 \mu\text{s}^{-1}$ occurs below around 3 K which is the crossover region observed by heat-capacity measurements. The polarization function $A(t)$ goes for $t \rightarrow 8 \mu\text{s}$ significantly below the expected $1/3$ -part which implies mainly dynamical magnetic fields at the muon site down to 0.019 K [37]. The static part ($< 20\%$) shows magnetic SRO rather than a coherent oscillation in $\text{BaTi}_{0.5}\text{Mn}_{0.5}\text{O}_3$. The main part is given by fluctuating magnetic fields at the muon site. Quantitatively, the spin-fluctuation rates can be roughly estimated using mean field approximation which is discussed in the supplement of Refs. [37] in detail. The results of the frequency estimations are $\nu(T > 10\text{ K}) = 7.4(1) \cdot 10^{10}\text{ Hz}$ and $\nu(T < 1.5\text{ K}) = 3.7(6) \cdot 10^6\text{ Hz}$ and, therefore, a decrease of four orders of magnitude. In the insulating double perovskite $\text{Sr}_2\text{FeOsO}_6$ which exhibits magnetic order around 135 K , the muon site is calculated using DFT and confirmed to be close to O^{2-} [77, 78, 79, 80]. The estimated muon site in $\text{BaTi}_{0.5}\text{Mn}_{0.5}\text{O}_3$ is close to O^{2-} . However, because of a missing value of the static magnetic field at the muon site a confirmation by dipole-dipole estimations is not possible.

The observation of PSD down to $T \rightarrow 0$ is often associated with a non-classical, quantum-like, or unconventional ground state. Conventional spin glasses and cluster spin glasses show a peak-like dependence of $\lambda(T)$ as observed in the cubic double perovskite $\text{SrTi}_{0.5}\text{Mn}_{0.5}\text{O}_3$ [74] rather than a saturated muon-spin dynamics. Therefore, PSD is believed to exclude the observation of a classical spin glass or cluster-spin glass state. The true microscopic reason of PSD is still in discussion. PSD is observed in different material classes probed by μ^+ SR, see table 5.3⁶. The table shows a selection of frustrated systems showing PSD at low temperatures. Interestingly, PSD appears not exclusively. A coexistence of PSD and partial frozen states or even magnetic LRO is observed. One should emphasize that PSD is observed in some molecular magnets and superconductors as well. Possible low- T

⁶Special thanks to Dr. Rajib Sarkar who shared this table for discussions.

System	Crystal properties	Groundstate by μ^+ SR
$\text{Cu}_2\text{Cl}(\text{OH})_3$	corner sharing tetrahedra	partial long-range order and PSD [81]
$\text{Gd}_2\text{Ti}_2\text{O}_7$	corner sharing tetrahedra	long-range order and PSD [82]
$\text{Zn}_x\text{Cu}_{4-x}(\text{OH})_6\text{Cl}_2$	kagome lattice	partial frozen state and PSD [83]
FeGa_2S_4	triangular lattice	partial frozen state and PSD [84]
$\text{Er}_2\text{Ti}_2\text{O}_7$	corner sharing tetrahedra	long range order and PSD [85]
$\text{Er}_2\text{Sn}_2\text{O}_7$	corner sharing tetrahedra	PSD [85]
$\text{Tb}_2\text{Ti}_2\text{O}_7$	corner sharing tetrahedra	PSD [86]
$\text{Tb}_2\text{Sn}_2\text{O}_7$	corner sharing tetrahedra	long range order and PSD [87, 88]
$\text{SrCr}_8\text{Ga}_4\text{O}_{19}$	kagome lattice	partial spin frozen and PSD [89]
CdHo_2S_4	corner sharing tetrahedra	ordered state and PSD [90]
$\text{Nd}_3\text{Ga}_5\text{SiO}_{14}$	anisotropic kagome lattice	PSD [91]
$\text{Gd}_3\text{Ga}_5\text{O}_{12}$	crossing triangular sublattices	PSD [92]
ZnCr_2O_4	spinel structure	PSD-like [93]
$\text{Y}_2\text{Mo}_2\text{O}_7, \text{Tb}_2\text{Mo}_2\text{O}_7$	corner sharing tetrahedra	PSD [94]
$\text{Dy}_2\text{Ti}_2\text{O}_7, \text{Tb}_2\text{Mo}_2\text{O}_7$	corner sharing tetrahedra	PSD [94]

Table 5.3: Selection of frustrated systems showing PSD at low temperature. For details see the corresponding references. Interestingly, PSD appears not exclusively. A coexistence of PSD and partially frozen states or even LRO is observed.

excitations are gapless spin-wave and spinon excitations.

$\text{Tb}_2\text{Ti}_2\text{O}_7$ is a frustrated pyrochlore and has shown PSD as observed in $\text{BaTi}_{0.5}\text{Mn}_{0.5}\text{O}_3$. The substitution series $\text{Tb}_p\text{Y}_{1-p}\text{Ti}_2\text{O}_7$ in which Tb is substituted by nonmagnetic Y was investigated [53]. The result was a mainly concentration-independent relaxation rate showing a local excitation rather than a collective magnetic origin. It is argued that magnetoelastic coupling plays an important role in pyrochlore and kagome systems leading to a lattice deformation relieving frustration [53]. Magnetoelastic coupling or exchange is the dependence of the exchange integral as a function of the atomic positions. A detailed discussion of possible explanations and candidate theories to explain PSD can be found in the chapter on $\text{NaCaCo}_2\text{F}_7$.

5.6 Conclusion

The μ^+ SR experiment on $\text{BaTi}_{0.5}\text{Mn}_{0.5}\text{O}_3$ shows an increase of the dynamical muon spin relaxation rate around the crossover region $T_C \approx 3\text{ K}$ which saturates down to 0.019 K coexisting with residual short-range magnetic order ($< 20\%$ of the signal). In $\text{BaTi}_{0.5}\text{Mn}_{0.5}\text{O}_3$, a clear difference is observed with respect to the proposed cluster spin glass $\text{SrTi}_{0.5}\text{Mn}_{0.5}\text{O}_3$ which shows a peak of the zero-field muon spin relaxation rate. DFT calculations propose a muon site insight the Ba plane close to O atom. Here, a slight preference of the muon site close to Mn^{4+} is possible which could position the muon close the orphan spins, dimers, and magnetic trimers, respectively, avoiding the nonmagnetic Ti^{4+} face-sharing octahedra.

The missing frequency dependence of χ' and the missing peak probed by μ^+ SR exclude the classical cluster-spin-glass scenario. The saturation of $\chi(T \rightarrow 0)$ suggests a spin-liquid ground state with a spinon Fermi surface and another groundstate candidate is a $U(1)$ Dirac spin liquid. Both ground

state candidates are excluded because of the dependence $C_{\text{mag}} \approx T^{1.4-1.5}$ of the magnetic heat capacity [37]. Therefore, additional theoretical treatments are required and the appearance of spin-liquid by disorder is not excluded.

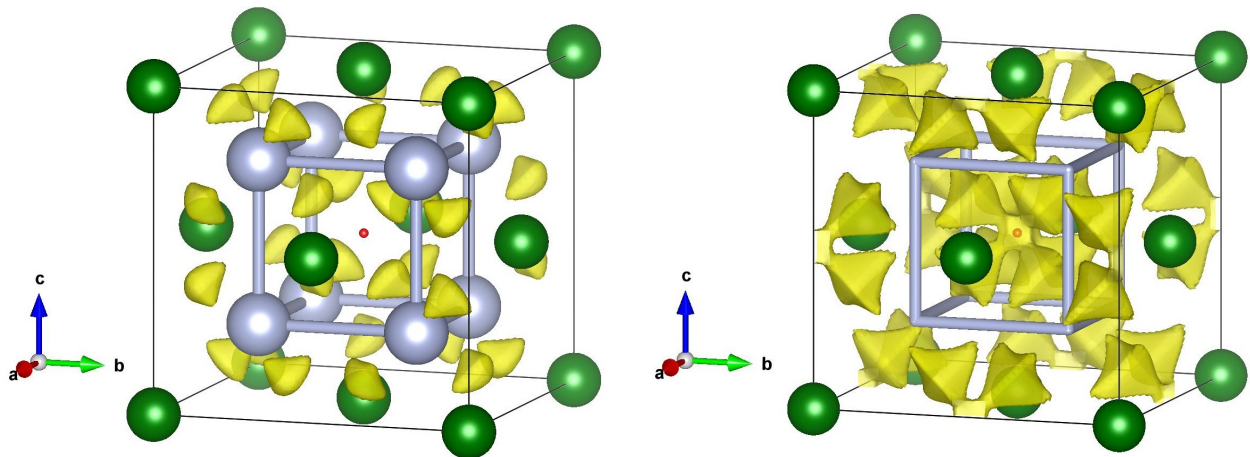
6 μ^+ SR Study on CaF_2 and the F- μ^+ -F state

The focus of this section is the nonmagnetic CaF_2 compound and, as we will see, the magnetic entanglement of the muon spin with the F nuclei is revealed at temperatures as high as 200 K. A F- μ -F bound state is observed in CaF_2 and in $\text{NaCaCo}_2\text{F}_7$ which is presented in the next chapter. There are different reasons why I have conducted the CaF_2 experiments:

1. The possibility to reveal fundamental differences or at least a comparison of the formation of the F- μ -F bound state in CaF_2 and $\text{NaCaCo}_2\text{F}_7$ above 250 K. As we will see, even the room-temperature measurements of $\text{NaCaCo}_2\text{F}_7$ show fundamental different behavior compared to the 200 K μ SR time spectra which leads to the second point:
2. A detailed temperature dependence is missing and unpublished of F- μ -F bound states even of a nonmagnetic analogon like CaF_2 . The μ SR time spectra are temperature dependent above 200 K.
3. I have observed two muon sites in $\text{NaCaCo}_2\text{F}_7$. One site corresponds to a F- μ -F site (muon site **I**) and the second site (called muon site **II**) has an unclear nature. Brewer *et al.* proposed a fast relaxing contribution of μ SR time spectra of CaF_2 which are presumably associated with a muonium site [95]. The purpose was to compare a possible similarity of this site and the muon site **II** in $\text{NaCaCo}_2\text{F}_7$.
4. Additionally, I have performed a DFT calculation of CaF_2 to compare it with a reported study to confirm the used DFT code and my procedure.

6.1 Structure and DFT calculations

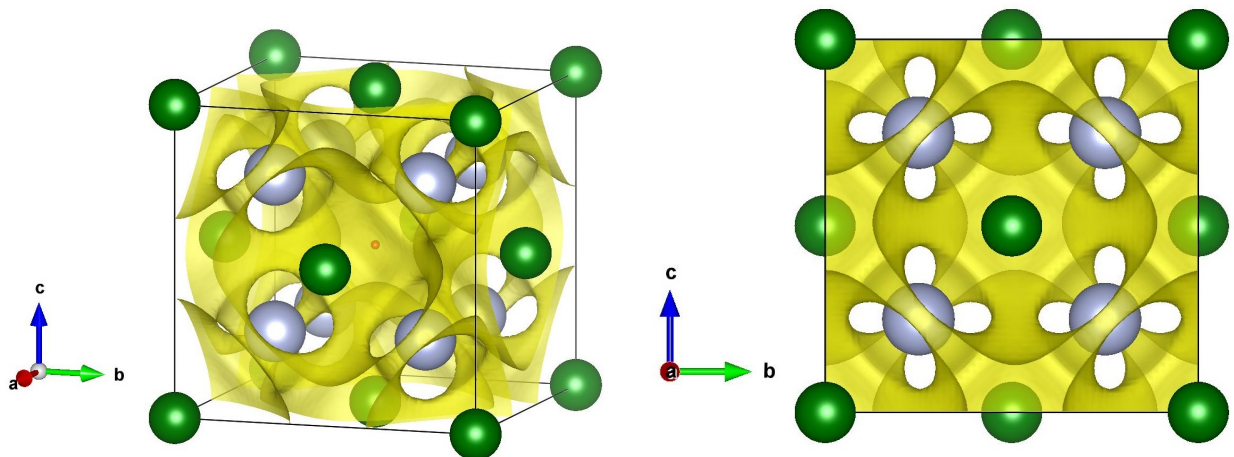
This subsection discusses the CaF_2 lattice and my DFT calculations of CaF_2 performed within the scope of this thesis. The initial idea was to deduce muon sites and to calculate the electrostatic potential and charge density. Quantitatively, point charge models are often inadequate to estimate the EFG tensor since DFT treatments are taking into account the spatial extension of the electronic charge distribution. It turned out that these calculations are useful also for NMR. I have used the all-electron FP-LAPW code Elk 4.3.6 to obtain the crystal data file based on the crystal structure, see *Methods*. I have calculated and compared the Ca^{2+} EFG of CaF_2 with the experimental expectation according to the symmetry.



(a) Unit cell of CaF_2 and the isosurface of $0.245 \frac{E_h}{e}$ in yellow showing crab chips structures. The sticks show the manifold of smallest distances between two F^- insight the unit cell.

(b) Unit cell of CaF_2 and the isosurface of $0.24 \frac{E_h}{e}$. The gray ions of F^- are not shown and the discussed muonium site in red is just weakly visible behind the isosurface.

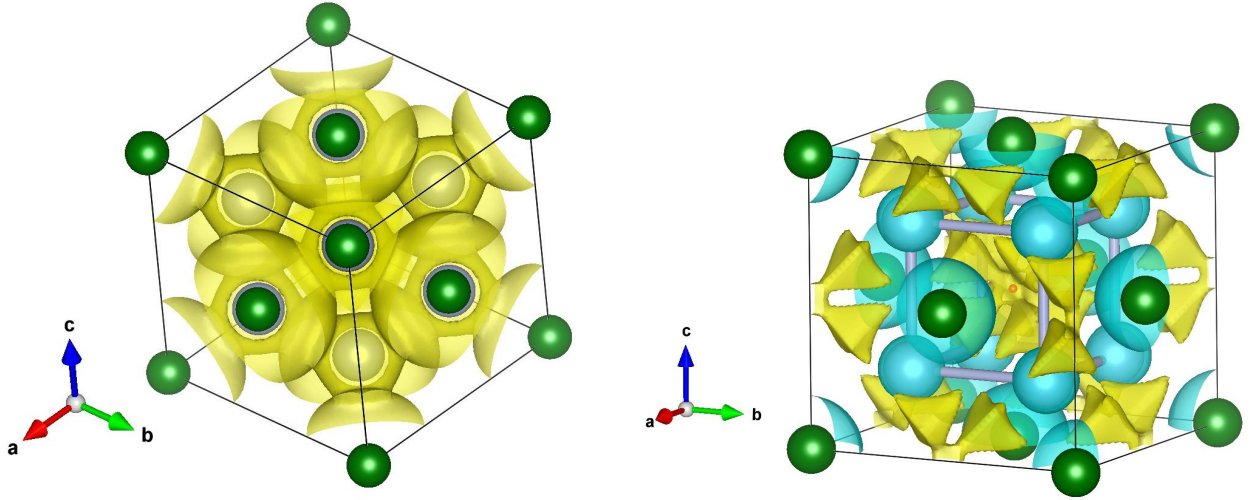
Figure 6.1: Unit cell of CaF_2 and corresponding DFT calculation of the electrostatic potential φ of the unperturbed lattice by the Elk package 4.3.6, here isosurfaces are shown in yellow. Ca^{2+} is shown in green and F^- in gray, each with their ionic radii. The gray sticks show the smallest distances between two F^- of 2.732 \AA . The red point shows the position of the proposed muonium site by J. S. Möller *et al.* [96].



(a) Unit cell of CaF_2 and the isosurface of $0.23 \frac{E_h}{e}$. The red point shows the position of the proposed muonium site by J. S. Möller *et al.* [96].

(b) Unit cell of CaF_2 and the isosurface of $0.23 \frac{E_h}{e}$. One can clearly identify the flower structures.

Figure 6.2: Unit cell of CaF_2 and corresponding DFT calculation of the electrostatic potential of the unperturbed lattice with the isosurfaces in yellow. Ca^{2+} is shown in green and F^- in gray.



(a) Unit cell of the cubic CaF_2 shown in $[111]$ -direction (normal vector) and the isosurface of $0.2 \frac{E_h}{e}$. (b) Unit cell of CaF_2 and corresponding DFT calculation of the electrostatic potential with the isosurfaces of positive (yellow) and negative (blue) potential of $0.24 \frac{E_h}{e}$.

Figure 6.3: Unit cell of CaF_2 and corresponding DFT calculation. Estimation of possible $\text{F}-\mu^+-\text{F}$ bound-state positions assuming the smallest distance between two F is selected by μ^+ , grey sticks.

CaF_2 crystallizes in the cubic fluorite-type structure exhibiting the space-group $Fm\bar{3}m$ (Nr. 225) which is a well known ccp (cubic close-packed) structure. The Ca^{2+} ions are surrounded by six fluoride ions F^- since the F^- is tetrahedrally coordinated and surrounded by four Ca^{2+} . The lattice constant at ambient pressure is determined to be $a_0 = 5.466(3) \text{ \AA}$ by L. Gerward *et al.* [97]. CaF_2 is nonmagnetic.

The used crystal data were taken from L. Gerward *et al.* [97] and a meshing of $10 \times 10 \times 10$ was used. Figure 6.1 (a) shows the unit cell of CaF_2 and the DFT calculation of the electrostatic potential φ of the unperturbed lattice including the isosurfaces (equivalent potential surface) of $0.245 \frac{E_h}{e}$ in yellow¹. The total lattice energy converged to around $-3521.82 E_h$ with an energy difference of the last loop of $< 5 \cdot 10^{-5} E_h$. The units of Elk are atomic units with the elementary charge $e = 1$, the length unit is the Bohr radius $a_0 = 1$ and the electron mass $m = 1$. The energy is given in Hartree energy E_h , for details see table 2.4. To avoid confusion one should keep in mind, the electron charge is positive and the atomic numbers Z are negative in the Elk DFT package.

Just a rough check of consistency: The Ca^{2+} site should not have a considerable electric field gradient (EFG) because of the cubic symmetry. For CaF_2 at position (000) the calculation yielded the calculated EFG tensor

$$\hat{V} = \begin{pmatrix} -0.3414389124 \cdot 10^{-16} & -0.8978314109 \cdot 10^{-17} & -0.6991688699 \cdot 10^{-17} \\ -0.8978314109 \cdot 10^{-17} & -0.4295814680 \cdot 10^{-17} & 0.3450421183 \cdot 10^{-17} \\ -0.6991688699 \cdot 10^{-17} & 0.3450421183 \cdot 10^{-17} & 0.3843970592 \cdot 10^{-16} \end{pmatrix} \frac{E_h}{ea_0^2}, \quad (6.1)$$

¹The discussed muonium site in red and the shown grey sticks which are not chemical bonds will be explained in the subsection *Discussion of CaF_2* .

with the eigenvector

$$\vec{u} = \begin{pmatrix} -0.3708853988 \cdot 10^{-16} \\ -0.2447741889 \cdot 10^{-17} \\ 0.3953628177 \cdot 10^{-16} \end{pmatrix} \frac{E_h}{ea_0^2}. \quad (6.2)$$

The trace is

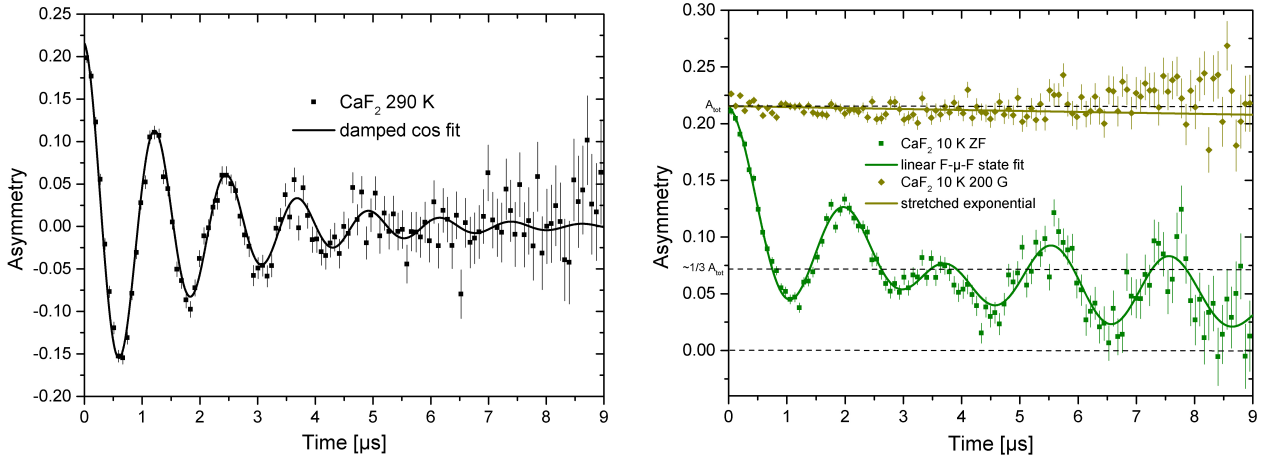
$$\sum_{i=1}^3 \frac{\partial^2 \varphi}{\partial x_i^2} = 0.1232595164 \cdot 10^{-31} \frac{E_h}{ea_0^2} \approx 0 \text{V}/\text{\AA}^2, \quad (6.3)$$

which is expected because of the Laplace equation $\Delta\varphi = \nabla \cdot \nabla\varphi = 0$ describing the electrostatic conditions and $\varphi = \varphi(x_1, x_2, x_3)$ the electrostatic potential. One should keep in mind the trace is invariant under base transformation and the same for the diagonal shape. One can see that the components of the EFG tensor are very close to zero. To have an idea regarding V_{zz} values of ^{57}Fe -Mössbauer spectroscopy, V_{zz} (largest principle axis) can reach $200 \text{V}/\text{\AA}^2$ and $\frac{E_h}{ea_0^2} \approx 9.7 \cdot 10^{21} \text{V}/\text{m}^2$. Effectively, this means $V_{ij} \approx 0 \text{V}/\text{\AA}^2$. This is expected. For the isomorphic SrF_2 it is discussed as well that the uniformly symmetric arrangement of eight F^- around Sr^{2+} in the center of the cube leads to a vanishing EFG [98]. Theoretically, point defects and dislocations are ignored which are discussed as source for an experimental deviation in NMR of SrF_2 [98].

Figure 6.1 (b) shows the isosurface of $0.24 \frac{E_h}{e}$ of the unit cell. Figure 6.2 shows the unit cell of the atomic-ball model and the isosurface of $0.23 \frac{E_h}{e}$ in two different views. The view in figure 6.2 (b) emphasize the complexity and corresponding flower structures. Figure 6.3 (a) represents the isosurface of $0.2 \frac{E_h}{e}$ of the unit cell of cubic CaF_2 shown along the $[111]$ -direction (normal vector). Figure 6.3 (b) shows the isosurfaces of the positive and negative potential of $\pm 0.24 \frac{E_h}{e}$ together. As mentioned, the electron has a positive charge in Elk. In this notation a positive muon would have a negative sign leading to the counter intuitive signs of φ . One should keep it mind, the electrostatic potential is visualized and the blue sphere would repel a positive charge around Ca^{2+} even in a far distance to the center of the ion. On the other hand, a positive charge is only repelled in a much closer distance to the F center because here is the force generated by the electronic shell which is more attractive. The comparison with J. S. Möller *et al.* [96] of the electrostatic potential φ is consistent. The crap-chips structures and the space of the crap structures shown in figure 6.1 (a) correspond to the lowest energy minima of the unperturbated lattice according to J. S. Möller *et al.* [96]. As we will see in the next subsections, the real muon site is far away from the crab chips. The muon forms a bound state leading to a strong local lattice distortion.

6.2 Experimental details

A high-quality powder sample of CaF_2 from Sigma Aldrich (sample number 01223) was mounted in the spectrometer GPS in a He cryostat at the $\pi\text{M}3$ beam line at the Paul-Scherrer-Institute in Switzerland. The powder was wrapped in a thin foil. Positive spin-polarized muons are implanted into the sample and the initial muon spin polarization was in longitudinal mode. The time evolution of the muon-spin polarization, $P(t)$, was monitored by detecting the asymmetric spatial distribution of positrons emitted from the muon decay [5, 4, 6, 7, 8]. Zero magnetic field (ZF) and longitudinal magnetic field (LF) geometry with respect to the initial muon-beam direction were used. The μSR



(a) Calibration run of a CaF_2 powder sample using a transverse magnetic field of 60 G at 290 K. The line shows the damped cosine fit $A(t) = A_{\text{tot}} \cos(\gamma_{\mu} B t) e^{-\lambda t}$ which yielded $\alpha = 0.6965(18)$, $A_{\text{tot}} = 0.2156(66)$, $B = 59.77(18)$ G and $\lambda = 0.520(24) \mu\text{s}^{-1}$.

(b) μ^+ SR measurements at 10 K. The ZF μ^+ SR of CaF_2 and the fit of the linear F- μ -F bound-state model is shown in green. The decoupling experiment in a LF of 400 G is shown in dark yellow supplemented by a stretched exponential fit describing the remained weak relaxation. The dotted lines are guides for the eyes showing the total asymmetry A_{tot} , the 1/3-part of A_{tot} and the zero-line.

Figure 6.4: μ^+ SR spectra of a CaF_2 powder sample obtained using GPS, PSI, Switzerland.

time spectra were analyzed using the software package MUSRFIT [99]. The total asymmetry, A_{tot} , was obtained by a calibration run in 60 G at 290 K and used for the following spectra. The asymmetry α was fitted according to the 290 K measurement in ZF. The asymmetry α is slightly corrected at 10 K to keep the total asymmetry constant².

6.3 μ SR Results of CaF_2 and the F- μ -F state

This subsection discusses the observed bound state in CaF_2 , the so called F- μ^+ -F state and the used fit model. Brewer *et al.* have reported the archetype publication in 1985 of the observation of muon-fluorine hydrogen-like bonding in ionic crystals [95]. It shows just one μ^+ SR spectra of CaF_2 at 80 K. Open questions are remaining as remarked in the discussion.

Figure 6.4 (a) shows the μ SR time spectra of the calibration run³ at 290 K. The applied transverse magnetic-field value of 60 G is consistent within the error bars with the result of the damped cosine fit $A(t) = A_{\text{tot}} \cos(\gamma_{\mu} B t) e^{-\lambda t}$ with $B = 59.77(18)$ G. Figure 6.4 (b) shows the μ SR time spectra at 10 K. The time-dependent polarization exhibits a coherent muon-spin precession which is associated with a homogenous quasi-static magnetic-field distribution. The origin of this static field is not a static electronic spin order. Instead, it reflects the magnetic field of nuclear moments and the formation of a diamagnetic F- μ^+ -F bound state and the entanglement of the muon with fluorine nuclear spins.

²A second calibration run was not possible because of time restrictions.

³The calibration run is discussed once in my thesis for completeness. The discussion is skipped in the sections of $\text{NaCaCo}_2\text{F}_7$ and $\text{BaTi}_{0.5}\text{Mn}_{0.5}\text{O}_3$, however, the procedure is equivalent.

The notation as $\text{F-}\mu^+\text{-F}$ state is often used in the literature although the observed molecular state is, from a chemical point of view, close to $(\text{F-H}^+\text{-F})^-$ and $(\text{F-}\mu^+\text{-F})^-$ would be more correct [96]. A $\text{F-}\mu^+\text{-F}$ state is often observed in F systems for three reasons:

1. F is the most electronegative element which leads to a very attractive electrostatic interaction with the muon [15].
2. F occurs only with the single isotope ^{19}F in nature which leads to a coherent hyperfine interaction.
3. ^{19}F with $I = 1/2$ has one of the largest nuclear moments and leads to a strong dipole-dipole interaction described by the dipole coupling Hamiltonian,

$$\hat{\mathcal{H}} = \sum_{i>j} \frac{\mu_0 \gamma_i \gamma_j \hbar}{4\pi r^3} [\mathbf{I}_i \cdot \mathbf{I}_j - 3(\mathbf{I}_i \cdot \hat{\mathbf{r}})(\mathbf{I}_j \cdot \hat{\mathbf{r}})], \quad (6.4)$$

between the muon and the ^{19}F nuclei. Here, $\hat{\mathbf{r}}$ is the normalized vector connecting the spins \mathbf{I}_i and \mathbf{I}_j and $\gamma_{i,j}$ the gyromagnetic ratios [100, 101, 102, 103]. A $\text{F-}\mu^+\text{-F}$ state is often considered as a strong distortion of the lattice and is treated as a molecule-in-crystal defect [96]. The muon sits between two F ions and pulls these ions close to the muon [95]. The F-F distance is approximately twice the F ionic radius: 2.38 Å [15]. This bond is one of the strongest hydrogen bonds in nature [96, 104, 105]. In general, the time evolution of the muon spin polarization $G_z(t)$ along the quantization axis z is given by

$$G_z(t) = \frac{1}{N} \sum_{m,n} |\langle m | \sigma_z | n \rangle|^2 \cos(\omega_{mn}t). \quad (6.5)$$

Here, N is the number of spins, $|m\rangle$ and $|m\rangle$ are the eigenstates of the dipole Hamiltonian $\hat{\mathcal{H}}$ and σ_z the Pauli spin matrix corresponding to the axis z .

In our case, the ZF muon spin relaxation function for a $\text{F-}\mu^+\text{-F}$ state is modeled by the three-spin model which assumes a static collinear geometry with a bond angle between $\text{F-}\mu^+\text{-F}$ of 180° [95]. $G_z(t)$ considers only $\mu^+\text{-F}$ dipole-dipole interaction and a three-frequency polarization function $G_z(t)$ for the muon was achieved averaged over equivalent directions for the cubic lattice:

$$G(t) = \langle G_\xi(t) \rangle_{\text{cub}} = \frac{1}{6} \left\{ 3 + \cos(\sqrt{3}\omega_d t) + \left(1 - \frac{1}{\sqrt{3}}\right) \cos\left[\left(\frac{3-\sqrt{3}}{2}\right)\omega_d t\right] + \left(1 + \frac{1}{\sqrt{3}}\right) \cos\left[\left(\frac{3+\sqrt{3}}{2}\right)\omega_d t\right] \right\}. \quad (6.6)$$

This model is sometimes called Brewer's function [106]. Effectively, $G(t)$ is modulated by a static relaxation term, yielding the quasi-static model $G(t)e^{-(\lambda_c t)^{\beta_c}}$ [95]. The term $e^{-(\lambda_c t)^{\beta_c}}$ is taking into account a phenomenological static broadening. $G(t)$ assumes a sideband splitting quantified by the dipole frequency ν_d with

$$\omega_d = 2\pi\nu_d = \frac{\mu_0 \gamma_\mu \gamma_F \hbar}{8\pi^2 r^3}. \quad (6.7)$$

Here, r is the μ^+ - ^{19}F distance reflecting the dipole-dipole interaction of the muon and the ^{19}F nucleus, $\gamma_F = 2\pi \cdot 2.518 \cdot 10^8 \text{ MHz T}^{-1}$ the gyromagnetic ratio of the ^{19}F nucleus [107, 95, 101].

The following model was used to describe the polarization function in ZF in figure 6.4 (b):

$$A(t) = a_{F\mu F} G(t) e^{-(\lambda_c t)^{\beta_c}} + a_B e^{-\lambda_B t}. \quad (6.8)$$

The first term describes the F- μ^+ -F state and the corresponding muon site. The second term, $a_B e^{-\lambda_B t}$, describes the background of muons not stopped in the sample. λ_B is expected to be close to zero. Table 6.1 shows the obtained parameters by the convergence of the ZF model. The introduced dipole-coupling field B_d corresponds to $\nu_D = \gamma_\mu B_d$, with

$$\gamma_\mu = \frac{\gamma}{2\pi} \approx 0.0135538817 \text{ MHz/G}, \quad (6.9)$$

and yields $\nu_D = 0.224(1) \text{ MHz}$, for a comparison with the literature see *Discussion*.

Figure 6.5 (a) shows ZF μ^+ SR spectra at the representative temperatures of 200 250 and 290 K. The used fit model is the polarization function $A(t)$ of the F- μ^+ -F state. The term $e^{-(\lambda_c t)^{\beta_c}}$ is a function of temperature and, therefore, the λ_c and β_c values and the frequency ν_d as well. The oscillation given by the F- μ^+ -F state disappears at 290 K and the fit is converged to a stretched exponential function with $\nu_d = 0.0(0) \mu\text{s}^{-1}$.

Figure 6.6 (a) and (b) show the obtained parameters λ_c , β_c , and B_d as a function of temperature using the proposed model applied to all measured data in ZF. The temperature dependence of λ_c and β_c converged to constant values below 200 K. The converged values of λ_c and β_c vary slightly depending on α . The magnetic dipole-coupling field B_d as a function of temperature converged to a value around 16.5 G at lowest temperatures.

Figure 6.5 (b) shows the ZF μ^+ SR spectra at 100 K of CaF_2 and the fit of the linear F- μ -F bound-state model. Additionally, data points and fits are shown of the decoupling experiment in 200 G LF at 100 and 290 K. The fits are exponential relaxation polarization functions

$$A_{\text{LF}}(t) = a_R e^{-(\lambda t)^\beta} + a_B e^{-\lambda_B t}. \quad (6.10)$$

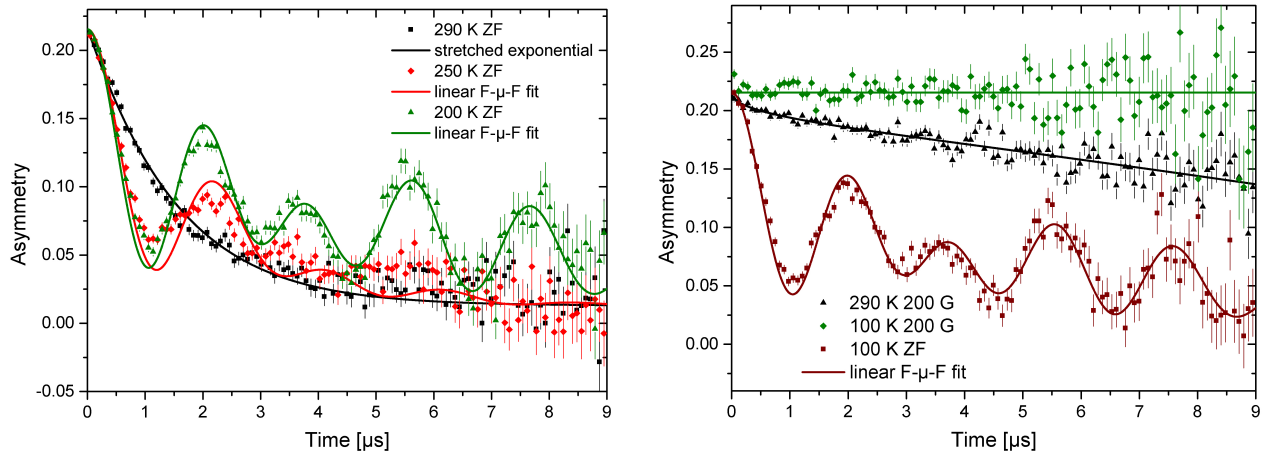
The fit yielded $\lambda = 0.0(0) \mu\text{s}^{-1}$ with $\beta = 0.0(0)$ at 100 K. The fit at 290 K yielded $\lambda = 0.022(3) \mu\text{s}^{-1}$ with $\beta = 0.57(3)$. This shows a residual dynamical relaxation rate is preserved at 290 K after decoupling and the time dependence of the polarization function at 290 K has not only a static nature regarding the probed field by the muon.

6.4 Discussion of CaF_2

It is well known that the positive muon μ^+ is preferably implanted in an interstitial site rather than a substitutional site consistent with the character of a light proton. This statement is correct if no vacancies are present excluding exotic exceptions. The general starting point is the lowest energy minimum of the unperturbed unit cell for the search of the positive muon site in a crystal. Neglecting a possible muon-induced lattice distortion because of the charge of the muon the lowest

Parameter	Value
λ_B	$0.01(2) \mu\text{s}^{-1}$
a_B	0.06(1)
λ_c	$0.138(1) \mu\text{s}^{-1}$
β_c	0.88(8)
B_d	16.51(7) G
$a_{\text{F}\mu\text{F}}$	0.94(1)

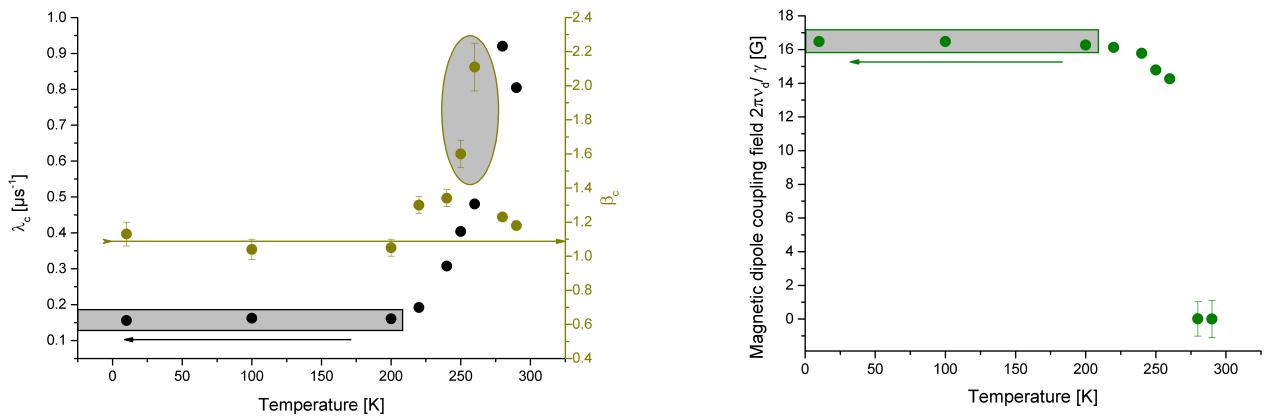
Table 6.1: Extracted values of the 10 K measurement in ZF of CaF_2 fitted by the linear F- μ^+ -F state model. B_d is the dipole-coupling field. Because of a small experimental increase of the asymmetry, α is slightly corrected to $\alpha = 0.7086(40)$.



(a) ZF μ^+ SR spectra at the representative temperatures showing the fit in which the term $e^{-(\lambda_c t)^{\beta_c}}$ is changed as a function of temperature, means the λ_c and β_c values up to 290 K and decreased values of B_d . Effectively, B_d is zero at 290 K leading to a stretched exponential relaxation.

(b) ZF μ^+ SR measurement of CaF_2 at 100 K and the fit of the linear F- μ -F bound state model in brown. The black and green data points show the decoupling experiment in 200 G LF, respectively at 100 and 290 K. The fits are stretched exponential relaxation models $A_{\text{LF}}(t) = a_R e^{-(\lambda t)^\beta} + a_B e^{-\lambda_B t}$.

Figure 6.5: μ^+ SR spectra of a CaF_2 powder sample obtained using GPS, PSI, Switzerland.



(a) Temperature dependence of λ_c (left scale) and β_c (right scale). λ_c and β_c converge to constant values below 200 K. The spectra are not described accurately in the temperature range between 240 and 280 K leading to a large error of β_c around 250 K, see gray-oval shadow.

(b) The magnetic dipole-coupling field as a function of temperature converge to a value around 16.5 G at to low temperatures.

Figure 6.6: Extracted values out of the ZF μ^+ SR spectra of CaF_2 between 10 K and 290 K.

energy minimum is often consistent with the observed muon site. CaF_2 is an ionic crystal and it is expected that the μ^+ lattice interaction should be stronger compared to most metals in which the charge of the muon is partially screened by the conduction electrons. However, the general combination of screening effects, the muon-lattice interaction and the exceptional large zero-point energy of the muon may lead to very exotic muon sites [96, 6, 5, 4]. This is the case in CaF_2 .

The muon probes a clear temperature-independent F- μ -F signal with a dipole frequency of $\nu_D = 0.224(1)$ MHz at 10 K consistent with a local distortion pulling two F^- close together. This frequency is fully consistent with the frequency of $\nu_D = 0.226(2)$ MHz measured by Brewer *et al.* at 80 K [95]. The shortest distances insight the unperturbed unit cell of CaF_2 are given by the gray sticks of 2.732 Å in figure 6.1. The effective distance between the two F^- of the F- μ -F is reduced to 2.34(2) Å calculated from the side-band splitting frequency ν_d . The discussed crap-chip structures containing the electrostatic energy minima for the muon site in the DFT calculations above are not consistent with the observed F- μ -F sites. This shows the important role of the local lattice distortion and the failure of the muon-site search by the unperturbed unit cell of CaF_2 . This conclusion is consistent with the DFT study done by J. S. Möller *et al.* [96]. The model of the polarization function assuming a linear F- μ -F state is consistent with the experimental data.

The observed exponent $\beta_c \approx 0.5$ by Brewer *et al.* is not fully consistent with $\beta_c = 0.88(8)$ deduced in my experiment. This deviation may be caused by the difference of the sample, eventually the sample quality. The λ_c -value is not given by Brewer *et al.* [95].

As shown by the data and fit in figure 6.5 (a) at 250 K, the muon spin relaxation rate λ_c changes drastically above 200 K. Brewer *et al.* [95] have discussed:

For CaF_2 and BaF_2 , $\beta_c \approx 0.5$; values of $\beta < 1$ indicate the presence of fast-relaxing components in the μSR signal. One may speculate that such components are due to the products of heterofore undetected reaction pathway involving muonium. [95]

CaF_2 and BaF_2 have the same crystal structure. Here, a Gaussian relaxation below $0.5 \mu\text{s}^{-1}$ is not observed which was found in LiF and NaF which are exhibiting a rocksalt structure [95]. A calculated muonium site in CaF_2 is presented by J. S. Möller *et al.* [96]. This proposed muonium site is shown in figure 6.1 (a) and (b) by the red point in the middle of the unit cell. My entire study of CaF_2 , especially the TF and LF experiments, do not show a strong hint for the discussed muonium site.

6.5 Conclusions of CaF_2

The observation of the linear F- μ -F bound state is consistent with the report by Brewer *et al.* [95]. The experimentally observed muon site is not given by the energy minima of the unperturbed unit cell represented by DFT calculation results rather it is located between two F ions. The μSR spectra are invariant between 10 and 200 K. The spectra below 200 K are quantitatively very close to the single crystal measurement at 80 K by Brewer *et al.* [95]. The high- temperature behavior of the nonmagnetic CaF_2 probed by $\mu\text{SR} > 200$ K shows a clear dynamical relaxation and a continuous disappearance of the F- μ -F signal up to 290 K. The decoupling experiment shows no second muon site⁴. The muon spin is decoupled in a LF of 200 G below 100 K reflecting the quasi-static nature, meaning a quasi-static nuclear field is probed by the muon.

A more non-phenomenological model of the temperature dependence above 200 K is missing requiring a detailed understanding the high-temperature process, probably a muon hopping or diffusion process.

⁴... as observed in $\text{NaCaCo}_2\text{F}_7$ by muon site **II**, see next chapter. The experimentally observed value of $\beta < 1$ was proposed initially as hint for a second fast relaxing site [95]. This is not confirmed by my LF experiments on CaF_2 .

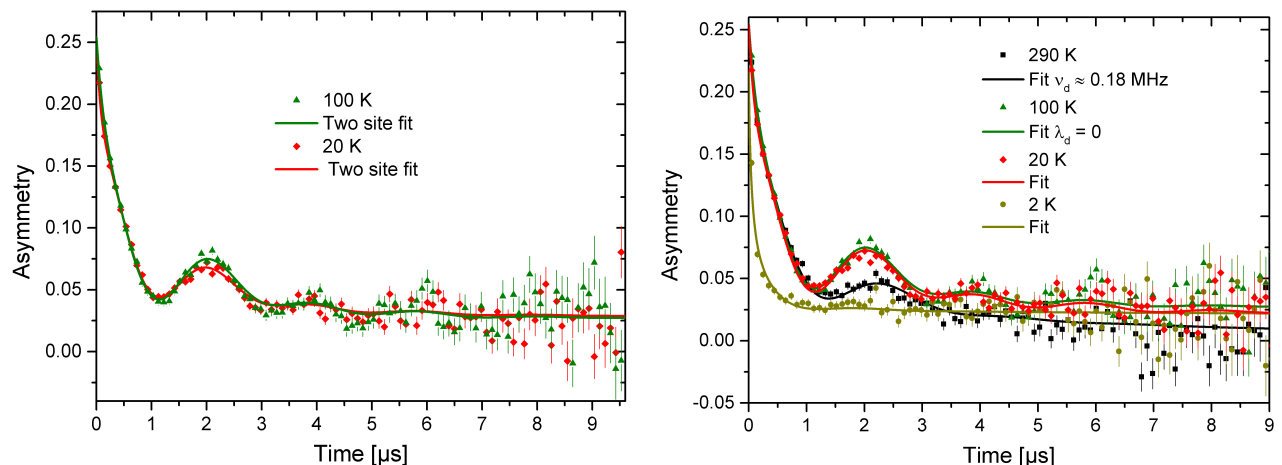
7 Persistent μ^+ Spin Dynamics, F- μ^+ -F State Relaxation and Local μ^+ -Induced Lattice Distortion in NaCaCo₂F₇

This chapter presents one core part of my thesis: The μ SR results of NaCaCo₂F₇. A F- μ -F state is observed which is muon site **I**. Interestingly, I have observed a second muon site (muon site **II**) which has an unclear nature. However, the main site of interest is the first muon site **I** which is the observed F- μ -F site. The nuclear F moments of the F- μ -F state are dominated by the magnetic Co²⁺ moments below 20 K.

NaCaCo₂F₇ shows PSD down to 20 mK, see S. A. Bräuninger *et al.* [108]. The F- μ -F state physics was described in detail in the last chapter.

7.1 Experimental description

Single crystals of NaCaCo₂F₇ were prepared in an optical floating-zone furnace, for details see J. Krizan *et al.* [28]. All experiments were carried out at the π M3 beam-line at the GPS (longitudinal muon spin polarization mode) and LTF (transverse polarization mode) at the Swiss Muon Source at the Paul-Scherrer-Institute, Switzerland. To achieve thermal contact in LTF, the samples were glued on an Ag plate giving rise to a background of 54.70(2)% due to muons stopped in the Ag plate. Positive spin-polarized muons are implanted into the sample parallel to the [111]-crystal axis. The time evolution of the muon-spin polarization, $P(t)$, was monitored by detecting the asymmetric spatial distribution of positrons emitted from the muon decay [5, 4, 6, 7, 8]. Zero magnetic field (ZF) and longitudinal magnetic fields (LF) with respect to the initial muon beam direction were used. The μ SR time spectra were analyzed using the software package MUSRFIT [99]. The NMR spin freezing temperature $T_f \approx 2.4$ K of NaCaCo₂F₇ is situated near the lowest temperature of the GPS and the highest temperature of the LTF cryostat. To overcome this difficulty spectra with overlapping temperatures were recorded at both the GPS and LTF spectrometer, and the relaxation-rate values were determined from the GPS spectra. These values were used as input parameters and the comparison to analyze and continue the LTF data. The α values are corrected for high LF > 1000 G according to the GPS manual [109] because of the Lorentz force and non-perfectly aligned longitudinal geometry.



(a) NaCaCo₂F₇ in ZF at 100 and 20 K (GPS). The fit shows the two-site model with a free convergence of the site ratio.

(b) Selected time spectra at different temperatures in ZF (GPS). The lines show the fits assuming a temperature-independent relative ratio of the muon sites with respect to 100 K.

Figure 7.1: Selected μ^+ SR time spectra of NaCaCo₂F₇.

7.2 μ^+ SR results of NaCaCo₂F₇

7.2.1 Muon sites

Two muon sites are found in NaCaCo₂F₇. Muon site **I** is a diamagnetic F- μ^+ -F bound state and a second muon site is observed, called muon site **II**. The introduction of muon site **II** is needed because of a dynamical relaxation rate λ_f (approximately 38% of the total asymmetry) revealed by LF experiments which exceeds conventional relaxation frequencies of frustrated magnets by one order of magnitude. The dynamical relaxation rate λ_f is observed even at temperatures $290 \text{ K} \geq T \gg T_f$ above the freezing temperature $T_f \approx 2.4 \text{ K}$. The analysis of muon site **I** reveals a lattice distortion by the muon and could be called NaCaCo₂(μ^+ F₂⁻)F₅ site. The notation as F- μ^+ -F state is often used in the literature although the observed molecule state is from a chemical point of view close to (F-H⁺-F)⁻ and (F- μ^+ -F)⁻ would be more correct [96].

The assumption of a temperature-independent relative occupancy of muon site **I** and **II** is important for the interpretation of the low-temperature behavior $T < 2 \text{ K}$.

Figure 7.1 (a) shows two selected μ SR time spectra at 100 K and 20 K measured with the initial muon spin polarization $P_\mu(0)$ parallel to the [111]-crystal axis. The time-dependent polarization is a coherent muon spin precession which is associated with a homogenous static magnetic field distribution. The origin of this static field is not a static electronic spin state. Instead, it reflects the magnetic field of nuclear moments and the formation of a diamagnetic F- μ^+ -F bound state and the entanglement of the muon and F spins as observed in CaF₂. The ZF muon spin relaxation function for a F- μ^+ -F state is modeled by the three-spin model which assumes a static collinear geometry with a bond angle between F- μ^+ -F of 180° [95]. $G_z(t)$ considers only μ^+ -F dipole-dipole interaction and a

three-frequency polarization function $G_z(t)$ for the muon is used, averaged over equivalent direction for the cubic lattice¹:

$$G(t) = \langle G_\xi(t) \rangle_{\text{cub}} = \frac{1}{6} \left\{ 3 + \cos(\sqrt{3}\omega_d t) + \left(1 - \frac{1}{\sqrt{3}}\right) \cos\left[\left(\frac{3-\sqrt{3}}{2}\right)\omega_d t\right] + \left(1 + \frac{1}{\sqrt{3}}\right) \cos\left[\left(\frac{3+\sqrt{3}}{2}\right)\omega_d t\right] \right\} \quad (7.1)$$

This model is the Brewer's function [106]. Effectively, $G(t)$ is modulated by a static relaxation term, in detail the quasi-static model $G(t)e^{-(\lambda_c t)^{\beta_c}}$ [95]. The term $e^{-(\lambda_c t)^{\beta_c}}$ is taking into account a phenomenological static broadening. I have used for the fits in figure 7.1 the following model to describe the polarization function:

$$A(t) = a_{\text{F}\mu\text{F}}G(t)e^{-(\lambda_c t)^{\beta_c}}e^{-(\lambda_d t)^{\beta_d}} + a_f e^{-\lambda_f t} + a_B e^{-\lambda_B t}. \quad (7.2)$$

The first term describes the F- μ^+ -F state and the corresponding muon site **I**. The second term $a_f e^{-\lambda_f t}$ describes an observed fast dynamical relaxation channel λ_f associated with muon site **II**. The last term is the background of muons not stopped in the sample. $a_B = 0.106(2)$ is the fraction of the background signal with $\lambda_B = 0.11(3) \mu\text{s}^{-1}$ taken from the 1.6 K spectrum in which the muon spin relaxation is fully dynamic and probes fluctuating magnetic fields, see below. The fit at 100 K was used to determine the static relaxation term $e^{-(\lambda_c t)^{\beta_c}}$ assuming the dynamical relaxation rate $\lambda_d = 0$. This yielded $\lambda_c = 0.381(21) \mu\text{s}^{-1}$ and $\beta_c = 1.37(20)$. $e^{-(\lambda_c t)^{\beta_c}}$ is considered temperature-independent and shows a more Gaussian behavior ($\beta_c > 1$). $G(t)$ assumes a sideband splitting quantified by the dipole frequency ν_d with

$$\omega_d = 2\pi\nu_d = \frac{\mu_0\gamma_\mu\gamma_F\hbar}{8\pi^2r^3}. \quad (7.3)$$

Here, r is the μ^+ -¹⁹F distance reflecting the dipole-dipole interaction of the muon and the ¹⁹F nucleus, $\gamma_F = 2\pi \cdot 2.518 \cdot 10^8 \text{ MHz T}^{-1}$ the gyromagnetic ratio of the ¹⁹F nucleus [107, 95, 101]. The two-site model yielded $\nu_d = 0.2081(17) \text{ MHz}$ at 100 K.

The above ansatz was used to extract the dynamical relaxation rate λ_d and to describe the fluctuating Co²⁺ moments in the presence of the static F- μ^+ -F state below 100 K. For the fit at 20 K only the relative site occupancies, $a_{\text{F}\mu\text{F}}$ and, a_f , and λ_d were varied. Table 7.1 lists the results of the free convergence, e.g., $a_{\text{F}\mu\text{F}} = 0.5110(37)$ for the F- μ^+ -F state and $a_f = 0.3830(34)$ for muon site **II** at 100 K. The occupancy of muon site **II** at 20 K is comparable or slightly less and probably a result of the restriction of the used model, see *Discussion*. However, the site occupancy is roughly temperature-independent between 100 and 20 K and, as I will present in the next subsection using

¹This equation is cited once again because of its importance and completeness for the reader who had skipped the CaF₂ section. This is done to emphasize that the same equation is used in the powder case of CaF₂ and the single-crystal case of NaCaCo₂F₇.

Temperature [K]	Occupancy of muon site II [%]	λ_d [μs^{-1}]
290	38.30(-)	0
100	38.30(34)	0
20	33.32(91)	0.200(15)

Table 7.1: The extracted values with the σ -confidence interval errors assuming $\lambda_d = 0$ at 100 K.

a phenomenological model, the spectrum at 290 K is consistent with the discussed muon-site signal ratio.

7.2.2 Temperature-independent model of the muon-site occupancy

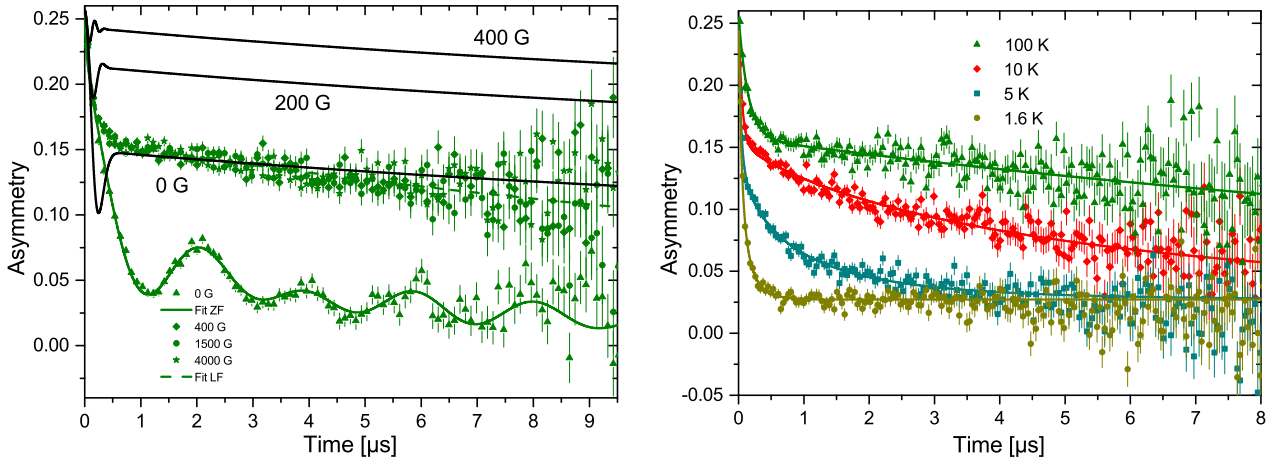
To determine the muon spin relaxation rates, I have used a temperature-independent muon-site ratio down to 20 mK. The fit at 100 K in ZF was used to calibrate the relative muon site occupancy assuming the obtained values of table 7.1. Figure 7.1 (b) shows the fit results. Close to the freezing temperature and below, the fluctuating electronic Co²⁺ moments dominate the muon spin relaxation. The electronic dipole-dipole interaction to the muon exceeds the interaction of the muon to the nuclear F moments. This is shown by the strong increase of the muon spin relaxation rate from 290 K down to 2 K. The oscillations of the polarization function produced by the quasi-static magnetic field at the muon site generated by the F- μ^+ -F state is masked by the electronic relaxation at 2 K. Therefore, it is not possible to distinguish clearly between the two muon sites **I** and **II** below T_f , especially when the relaxation rates λ_f and λ_d are of similar values. The spectrum at 290 K deviates strongly from those at 100 and 20 K. I have used a phenomenological model to describe the 290 K spectrum assuming the same muon-site ratio. Qualitatively, the time dependence is the same below 1 μs (at early times) reflecting the validity of the static muon site model at 290 K. However, the late time polarization function ($t > 5 \mu\text{s}$) is reduced, probably due to the onset of a diffusion as observed also in CaF₂. The frequency ν_d is clearly lower, $\nu_d = 0.1815(30)$ MHz.

7.2.3 LF experiments above T_f

We have performed LF experiments to decouple the static nuclear F moments as in CaF₂ to examine the dynamic nature of the muon spin relaxation rate λ_d at low temperature. The main results are depicted in figure 7.2 (a). The static contribution of the F- μ^+ -F state is fully decoupled at 400 G. In the paramagnetic state at 400 G μSR time spectra are well described by using a two-site model in LF:

$$A_{\text{LF}}(t) = a_s e^{-\lambda_s t} + a_f e^{-\lambda_f t} + a_B e^{-\lambda_B t}. \quad (7.4)$$

The first term $a_s e^{-\lambda_s t}$ replaces the F- μ^+ -F term in ZF. The relaxation rate λ_B of the background is smaller in LF and is set to 0, $\lambda_s, \lambda_f \gg \lambda_B$. In the following the slow relaxation rate λ_s is identified with the dynamical relaxation rate λ_d after decoupling of the static F- μ^+ -F state and represents the diamagnetic F- μ^+ -F state contribution which is sensitive to the fluctuating Co²⁺ moments. The fast relaxation term $a_f e^{-\lambda_f t}$ represents muon site **II** and the temperature-dependent rate λ_f includes a possible coupling to fluctuating Co²⁺ moments. The fits converged to the same values of the muon-site occupation in ZF and LF at 100 K. In a free fit at 100 K in LF one gets $a_f = 0.385(6)$. The black



(a) μ SR time spectra using GPS at 100 K at different LFs as indicated. The black lines show the fast relaxation term replaced by a Gaussian Kubo-Tayabe model for $< 0.1 \mu s^{-1}$ in LF.

(b) μ SR time spectra using GPS at four temperatures at 400 G. The lines indicate the two-site fit with $\approx 51.1\%$ F- μ^+ -F states and $\approx 38.3\%$ fast relaxation channel.

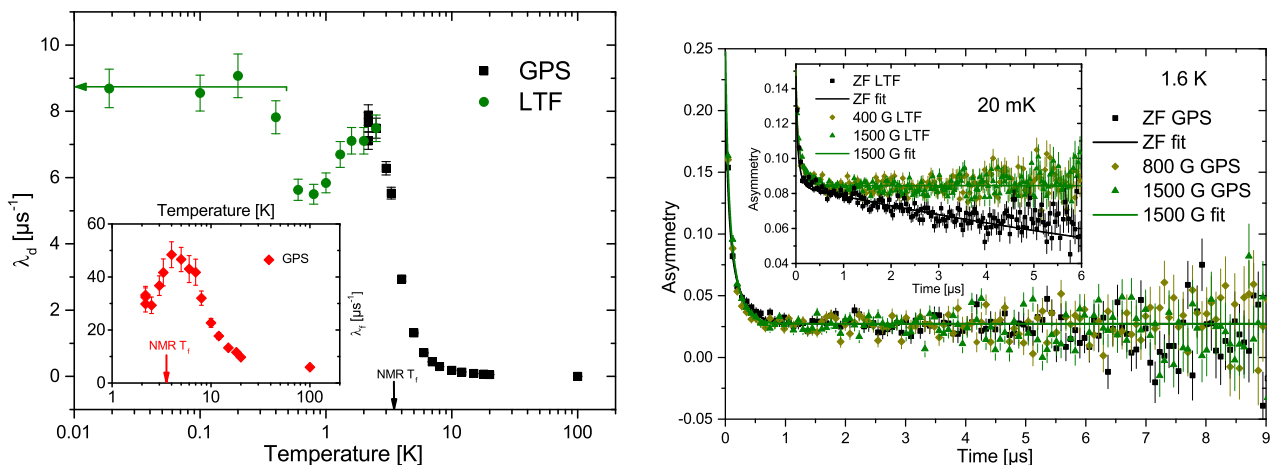
Figure 7.2: Longitudinal field (LF) μ^+ SR time spectra obtained using GPS to decouple the positive muons.

lines in figure 7.2 (a) show a Gaussian Kubo-Toyabe function fitted for the first $0.1 \mu s^{-1}$ yielding $\sigma = 6.99(41) \mu s^{-1}$ [6, 12]. A static muon spin relaxation with $\sigma = 6.99(41) \mu s^{-1}$ should be decoupled nearly completely in 400 G static external magnetic field. This is not observed. This justifies that the muon spin relaxation of muon site **II**, given by $a_f e^{-\lambda_f t}$ as reflected in figure 7.2, is caused by purely dynamic local fields at this muon sites [4, 5].

Figure 7.2 (b) shows four μ SR time spectra at representative temperatures at 400 G in LF. The relaxation rate increases gradually and smoothly with decreasing temperature. At 100 K, $\lambda_f = 6.85(37) \mu s^{-1}$ was estimated from the fit. The extension of the term $a_s e^{-\lambda_s t}$ by the stretched exponential $a_s e^{-(\lambda_s t)^{\beta_s}}$ yields $\beta_s = 0.623(18)$ at 5 K which reflects a relaxation-rate distribution often observed in disordered systems [110, 111].

7.2.4 Low-temperature decoupling $T < T_f$ and persistent μ^+ spin dynamics

Figure 7.3 (a) shows the relaxation rates, λ_d , and λ_f as a function of temperature in a LF of 400 G. These values are extracted using the single-channel approximation of muon site **I** assuming $\beta_d = 1$ to restrict the parameter space. With lowering the temperature, λ_d and λ_f increases at least one order of magnitude down to 3 K. Below 3 K, the dynamical relaxation rate λ_d of muon site **I** firstly decreases, then increases and finally remains constant in a broad temperature range. This implies the slowing down of the Co²⁺ spin fluctuations consistent with NMR and neutron-scattering data. The freezing temperature of the diamagnetic F- μ^+ -F state muon spin relaxation λ_d is shifted to a lower temperature compared to the NMR freezing temperature T_f . Below 20 K, NaCaCo₂F₇ enters into a correlated paramagnetic state, before settling down in a spin frozen state [35, 71] indicated by a maximum in λ_d and λ_f . Clearly, λ_d enters a low-temperature plateau below 500 mK indicating persistent spin dynamics being present in NaCaCo₂F₇. Figure 7.3 (b) shows the decoupling at 1.6 K



(a) Results for λ_d and λ_f extracted in applied 400 G. The arrows show the NMR freezing temperature T_f and the spectrometer values λ_d of GPS and LTF have a clear overlap.

(b) The decoupling experiment is shown using GPS in applied longitudinal magnetic fields. The inset shows the decoupling of the LTF spectrometer at 20 mK.

Figure 7.3: μ^+ SR data reflecting persistent μ^+ spin dynamics.

and 20 mK. These results rule out the presence of dominant static relaxation contributions. The decoupled contribution at 20 mK in ZF is consistent with the silver relaxation rate $\lambda_B = 0.072(2) \mu\text{s}^{-1}$ of the sample holder. The relaxation rate λ_d is a dynamical relaxation rate at 20 mK concluded by the unchanged rate in low-LF experiments. Muon site **I** shows persistent μ^+ spin dynamics down to 20 mK with high relaxation rates assuming the presented temperature-independent muon-site occupancy.

7.2.5 DFT calculations

I have performed DFT calculations to examine the plausibility and identify the experimentally observed two-muon-sites. A μ^+ SR study was done on $\text{NaCaNi}_2\text{F}_7$ [112]. In that study, only one muon site is observed which shows coherent F- μ^+ -F state oscillation as observed in $\text{NaCaCo}_2\text{F}_7$ for muon site **I**. The early time range < 1 is described by a Gaussian relaxation showing the pure nuclear nature. Therefore, I have performed DFT calculations on $\text{NaCaNi}_2\text{F}_7$ and $\text{NaCaCo}_2\text{F}_7$ for a direct comparison.

The DFT calculations were done for the unperturbed unit cell calculating the electrostatic potential using the all-electron FP-LAPW code Elk 4.3.6 [26] which includes the Spacegroup package using Broyden mixing [24] and the Perdew-Burke-Ernzerhof GGA (Generalized gradient approximation) functional [25], for details see chapter *Methods*. The crystallographic data are presented in table 4.3 and taken from J. W. Krizan *et al.* [28, 56]. The length of the cubic unit cell of $\text{NaCaCo}_2\text{F}_7$ is $a = 19.68886733 a_0$, a_0 being the Bohr radius, see table 2.4 for the definition of atomic units. The length of the unit cell of $\text{NaCaNi}_2\text{F}_7$ is $a = 19.42638459 a_0$ [56].

To perform the calculation in the presence of disorder on the A site, I have chosen a configuration assuming a homogenous distribution of Na^+ and Ca^{2+} . This configuration is visualized in three directions, each parallel to the axis of the unit cell as shown in figure 7.4. The unit cell of $\text{NaCaCo}_2\text{F}_7$ for

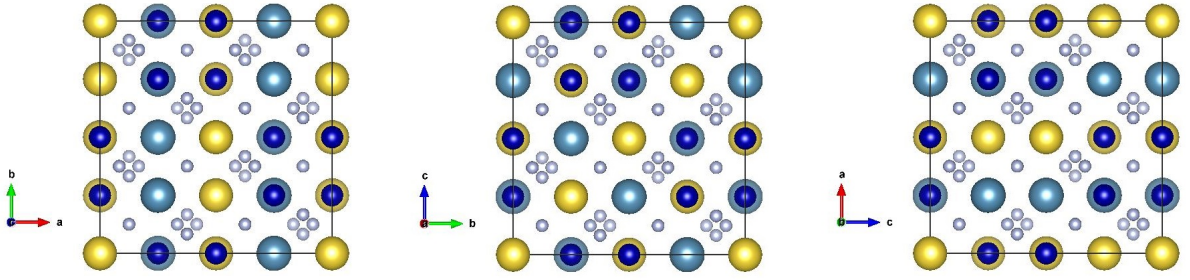


Figure 7.4: Used unit cell for NaCaCo₂F₇ of the DFT calculation and the corresponding disordered ion configuration for an alternating diagonal or vertical arrangement of Na⁺ and Ca²⁺, respectively. The *c*-axis (left), *a*-axis (middle), or *b*-axis (right) are out of plane. The atoms are visualized using an atomic sphere with the corresponding atomic radii. Grey: F⁻, small blue atoms: Co²⁺, yellow: Na⁺, big aquamarine atoms: Ca²⁺. The unit cell contains eight Na⁺ and eight Ca²⁺ to guarantee charge neutrality.

Isosurface	NaCaNi ₂ F ₇	NaCaCo ₂ F ₇
Banana	0.281705	0.272646
Snail	0.285872	0.271777
Difference	-0.004167	+0.000869

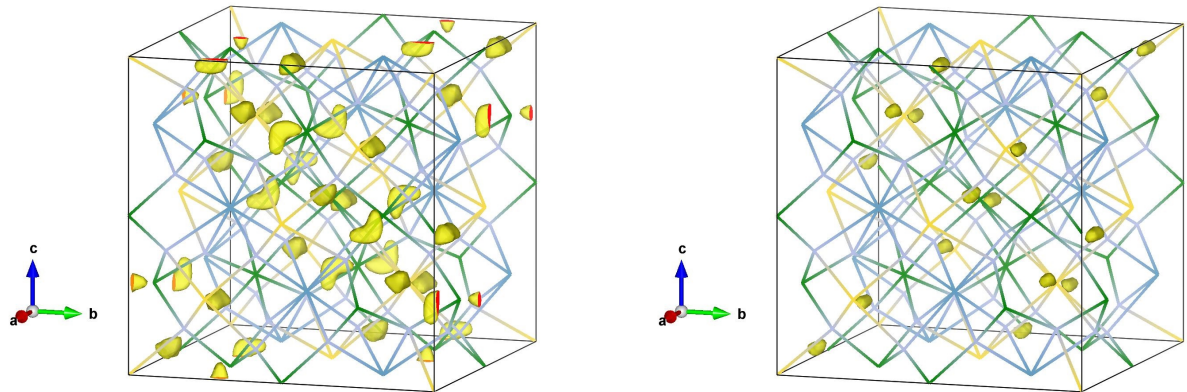
Table 7.2: Comparison of peak values (positive values correspond to energy minima) of the electrostatic potential φ in E_h/e of the DFT result of NaCaCo₂F₇ and NaCaNi₂F₇ of the presented configuration shown in figure 7.4.

the DFT calculation and the corresponding disordered ion configuration has an alternating diagonal or vertical arrangement of Na⁺ and Ca²⁺, respectively. The unit cell contains eight Na⁺ and eight Ca²⁺ to guarantee charge neutrality. The used unit cell configuration of NaCaNi₂F₇ has the identical Na⁺-Ca²⁺-configuration as presented in figure 7.4 and is just varied by the lattice parameters published in J. W. Krizan *et al.* [56]. For clarity not all atoms in the unit cell are shown.

Additionally to the calculation of the electrostatic potential, I have calculated the EFG of NaCaCo₂F₇ at the Na⁺ site yielding a largest principle axis of $V_{zz} = 0.097E_h/ea_0^2$. A comparison with NMR results is discussed below.

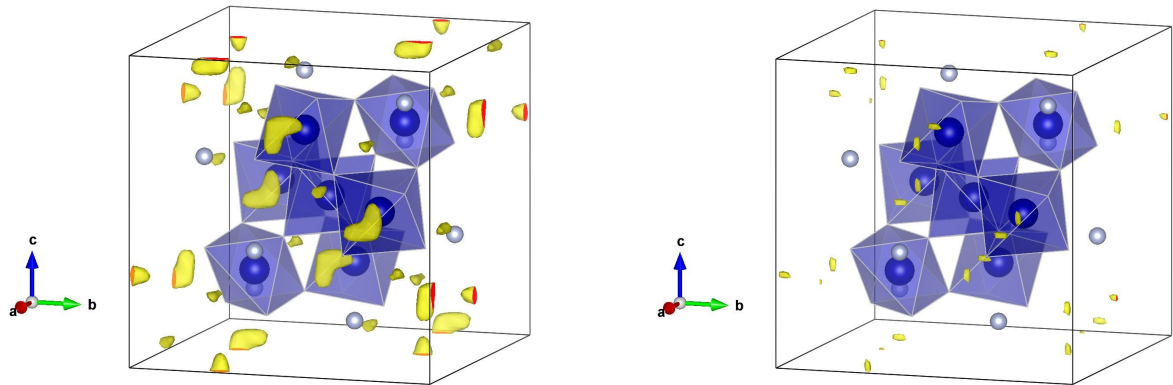
Figures 7.5-7.7 show isosurfaces of the electrostatic potentials φ of the unit cells of NaCaNi₂F₇ and NaCaCo₂F₇. Table 7.2 shows the comparison of peak values of the electrostatic potential φ of the DFT results for NaCaCo₂F₇ and NaCaNi₂F₇ of the configuration shown in figure 7.4. For NaCaNi₂F₇, the absolute energy maxima are insight the snail-structure-like isosurfaces with 0.285872 E_h/e and the second highest energy maxima are insight the banana-like isosurfaces with a potential of 0.281705 E_h/e , see figure 7.5. This calculated energy sequence is reversed in NaCaCo₂F₇ and the total energy maxima are located within the banana structures shown in figures 7.6 and 7.7. This is emphasized by the calculated energy difference as shown by a change of sign in table 7.2.

The energy differences of the two manifolds of equivalent maxima are $\Delta E_{Ni} \approx -0.11$ eV in NaCaNi₂F₇ and $\Delta E_{Co} \approx 0.02$ eV in NaCaCo₂F₇. Therefore, the energy difference between the discussed maxima is reduced by one order of magnitude and is inverted.



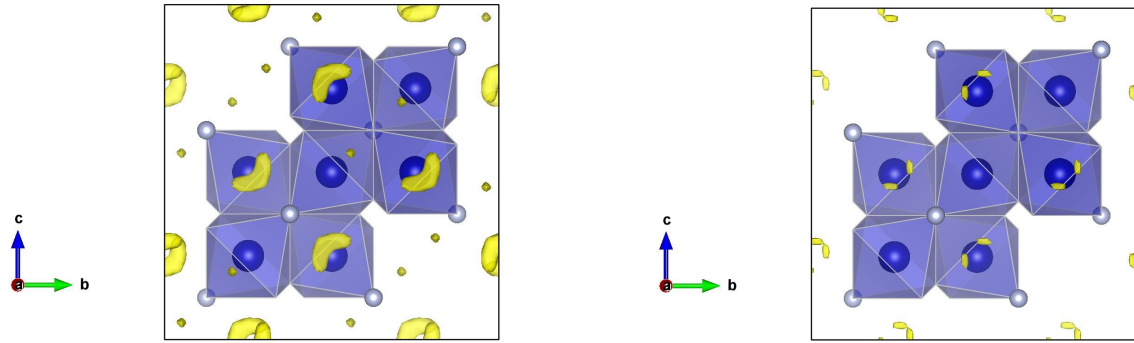
(a) Unit cell of NaCaNi₂F₇ and the isosurface of $\varphi = 0.279 \frac{E_h}{e}$ in yellow showing banana and snail isosurfaces. (b) Unit cell of NaCaNi₂F₇ and the isosurface of $\varphi = 0.2819 \frac{E_h}{e}$ in yellow. The snail structures are preserved.

Figure 7.5: Unit cell of NaCaNi₂F₇ (stick model for better perceptibility) and calculated isosurface (yellow) of the electrostatic potential φ of the unperturbed lattice. Grey sticks: F⁻, green: Ni²⁺, yellow: Na⁺, aquamarine: Ca²⁺. With increased energy from $0.279 \frac{E_h}{e}$ to $0.2819 \frac{E_h}{e}$, the bananas vanish.



(a) Unit cell of NaCaCo₂F₇ and the isosurface of $\varphi = 0.269 \frac{E_h}{e}$ in yellow showing banana- and snail-isosurfaces like in NaCaNi₂F₇ as presented in figure 7.5. (b) Unit cell of NaCaCo₂F₇ and the isosurface of $\varphi = 0.272 \frac{E_h}{e}$ in yellow. The banana-structures are preserved.

Figure 7.6: Unit cell of NaCaCo₂F₇ showing selected atoms for better perceptibility and calculated isosurface (yellow) of the electrostatic potential φ of the unperturbed lattice. Grey atoms: F⁻-8*b* sites, blue atoms: selected Co²⁺, Na⁺ and Ca²⁺ are unshown, blue octahedra are the distorted octahedra formed by F⁻ (unshown). The bananas remain with increasing energy from $0.269 \frac{E_h}{e}$ to $0.272 \frac{E_h}{e}$.



(a) Unit cell of NaCaCo₂F₇ and the isosurface of $\varphi = 0.269 \frac{E_h}{e}$ in yellow showing banana and snail isosurfaces such as for NaCaNi₂F₇ as presented in figure 7.5. (b) Unit cell of NaCaCo₂F₇ and the isosurface of $\varphi = 0.272 \frac{E_h}{e}$ in yellow. The banana structures are remained.

Figure 7.7: Unit cell of NaCaCo₂F₇ (here, parallel to the a -axis) showing selected atoms for better perceptibility and calculated isosurface (yellow) of the electrostatic potential φ of the unperturbed lattice. Grey atoms: F⁻- $8b$ sites, blue atoms: selected Co²⁺, Na⁺ and Ca²⁺ are not shown, blue octahedra are the distorted octahedra formed by F⁻ (not shown). With increased energy from $0.269 \frac{E_h}{e}$ to $0.272 \frac{E_h}{e}$, the bananas are preserved.

7.3 Discussion

7.3.1 Muon site I

The F- μ^+ -F state (muon site **I**) can be regarded as a bound, negatively charged molecule state (F- μ -F)⁻. The molecule orbital configuration is assumed to be comparable to (F-H-F)⁻ which is often interpreted as a three-center four-electron bound state with a symmetrically shared proton in the center [113].

The static relaxation term, $e^{-(\lambda_c t)^{\beta_c}}$, to modulate $G(t)$ has yielded $\beta_c = 1.37(20)$. This reflects a Gaussian-like magnetic-field distribution ($\beta_c > 1$) which is expected for nuclear moments and similar to other compounds containing F- μ^+ -F states [15, 101, 106, 114, 115, 116]. The notable exceptions are BaF₂ and CaF₂ [95]. The Na⁺-Ca²⁺-disorder is not probed considerably by the F- μ^+ -F state above T_f .

The two-site model yielded a dipole frequency of $\nu_d = 0.2081(17)$ MHz at 100 K which is in the same range as in the high- T_c superconductor Cs₂AgF₄ [114]. The frequency ν_d at 290 K is lower with $\nu_d = 0.1815(30)$ MHz since vibrational modes like a stretching mode may lead to an increased averaged distance of the muon and the F nuclei or a change of the bond angle of the F- μ^+ -F state [96]. The frequency of vibration modes is orders of magnitudes higher and not observable in μ SR experiments and thermal fluctuations are time averaged [101]. Such a time-averaged fluctuation can cause the observed static decrease in ν_d . It is shown that the muon spin oscillation intensity decreases with higher temperature in F- μ^+ -F states in Teflon and F- μ states in perfluorotripropylamine [117]. The decrease is probably caused by an onset of muon diffusion as discussed in the last chapter of CaF₂. Interestingly, in bifluorides, a decomposition to fluoride salts and hydrogen fluoride is ob-

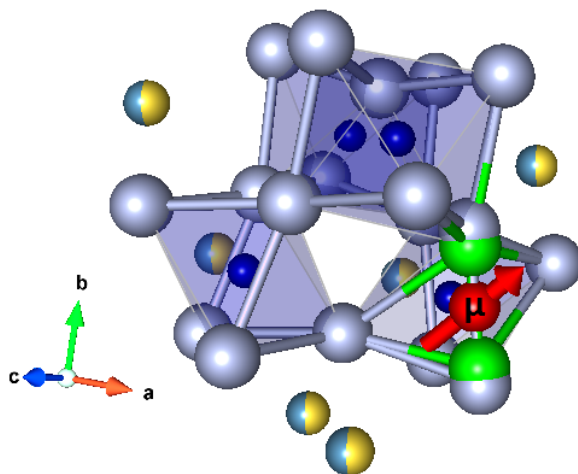


Figure 7.8: Possible muon sites between two F⁻ assuming the smallest F-F distance. Co²⁺ tetrahedron of the structural unit cell of NaCaCo₂F₇: Co²⁺ blue, F⁻ grey balls, disordered Na⁺ and Ca²⁺ aquamarine and yellow, grey sticks: shortest distance between two F⁻ of 2.678(1) Å, possible muon site red, displacement distortion of the F-μ⁺-F state in green. Visualized with VESTA with the crystallographic data taken from [28].

served, $[\text{HF}_2]^- \rightleftharpoons \text{HF} + \text{F}^-$, creating the question if a decay $[\mu\text{F}_2]^- \rightleftharpoons \mu\text{F} + \text{F}^-$ occurs or even an autodissociation process like $\mu\text{F} \rightleftharpoons \mu^+ + \text{F}^-$, e.g., at the $8b$ site, which supports a muon diffusion scenario [104, 118, 113].

The μSR measurements are performed on single crystals in $[111]$ -direction. The Brewer's function $\langle G_z(t) \rangle_{\text{cub}}$ used for the time evolution of the polarization function of the muon spin contains an effective powder average. The single crystal in $[111]$ -direction of a cubic pyrochlore behaves like an effective powder due to the considerable manifold of orientations of possible F-μ⁺-F positions per unit cell. The intrinsic disorder in NaCaCo₂F₇ is not considered.

The number of possible F-μ⁺-F sites per unit cell of NaCaCo₂F₇ is considerable, the shortest distance is 2.678(1) Å between two F⁻ inside the unit cell and there are 64 possibilities per unit cell in three inequivalent geometries. These are located at the small edges of the compressed CoF₆ octahedra. The next shorter distance between two F⁻ is much larger (3.044(1) Å) with 48 possibilities per unit cell. Let us assume that the smallest F-F distance of 2.678(1) Å is selected by μ⁺ just for the purpose of discussion. Figure 7.8 shows the muon located between the two F ions assuming the smallest distance of 2.678(1) Å of the unit cell. The resulting displacement distortion is visualized in green. All bonds below 3 Å are shown by grey and grey-green sticks. The F-μ⁺-F state displacement distortion leads to the appearance of two sticks in grey-green because of the fall below the 3 Å threshold. The long edge of the compressed octahedra is 3.063(1) Å which means that the displacement of the F-μ⁺-F state out of the equilibrium position of the crystal for NaCaCo₂F₇ is smaller than the intrinsic difference between the long and small edges of the compressed octahedra which is shown in figure 7.8. The possible muon site is given by a complex interplay of the (total) energy minimum of the system which is close to the formed F-μ⁺-F state and the effort of deformation energy for pulling the (rigid) F ions together. The electrostatic energy is lower in the proximity of Na⁺ compared to Ca²⁺ which can lead to a preferred Na⁺ next-next-nearest neighbor site environment for the positive muon.

Compound	$2\Delta d$ [Å]	$2\Delta d$ [%]	Refs.
LiHo _{0.045} Y _{0.955} F ₄	0.22(1)	8.5(4)	[120]
NaCaCo ₂ F ₇	0.29(1)	12.2(5)	
CaF ₂	0.39(2)	14.3(7)	[95]
LiF	0.49(2)	17.2(7)	[95]
BaF ₂	0.73(2)	24.5(6)	[95]
Cs ₂ AgF ₄	0.80(2)	25.2(6)	[114]
NaF	0.89(1)	27.2(3)	[95]

Table 7.3: The displacement $2\Delta d$ for both F atoms with a linear diamagnetic F- μ^+ -F state configuration of different compounds in Ångstrom and the relative displacement compared to the initial F-F distance.

It was shown in DFT calculation that for model systems the F- μ^+ -F state possesses, in general, the lowest energy minimum [100]. For complicated systems this assumption is not necessarily true. For instance, in the kagome antiferromagnet [NH₄]₂[C₇H₁₄N][V₇O₆F₁₈] only 10% F- μ^+ -F state occupancy was found [119]. Therefore, the observed muon-site ambivalence is supported by the large unit cell of NaCaCo₂F₇ together with the special conditions of the local energy minima.

In the following, I give an overview on the F- μ^+ -F state displacement distortion of different compounds compared to the unperturbed lattice. The goal is a comparison with model systems containing F- μ^+ -F states to discuss the lower boundary of the displacement distortion in NaCaCo₂F₇. The shortest unperturbed F-F distance in NaCaCo₂F₇ is the mentioned 2.678(1) Å. This yields with a reduction to around 2.38 Å a displacement of $2\Delta d = 0.29(1)$ Å. Here, Δd is the length displacement per F. In NaCaCo₂F₇, the minimum displacement is approximately $2\Delta d \approx 12\%$ which is smaller compared to other often discussed model systems, see table 7.3. LiHo_{0.045}Y_{0.955}F₄ has a smaller crystal structure displacement $2\Delta d$. The minimal relative lattice displacement by the F- μ^+ -F state formation has a lower boundary value of 12.2(5)%.

The minimal distance of Co²⁺ to the next corresponding F⁻ is around 2.034 Å. A rough estimation of the distance of the muon to the next Co²⁺ yields:

$$d_{\text{Co}} \approx \sqrt{(2.03 \text{ Å})^2 - \left(\frac{2.38 \text{ Å}}{2}\right)^2} \approx 1.65 \text{ Å}. \quad (7.5)$$

This estimation assumes that the smallest F-F distance of 2.678(1) Å is μ^+ -selected and can be understood as lower threshold for the distance to Co²⁺ as well.

7.3.2 DFT treatment

In the following, I discuss the results of the DFT calculation of the components of the EFG tensor,

$$V_{ij} = \frac{\partial^2 V}{\partial x_i \partial x_j}, \quad (7.6)$$

of the ²³Na site in which V is the potential of the charge distribution generated by the electrons and the nucleus. In contrast to ¹⁹F NMR with a spin of the nucleus of $I = \frac{1}{2}$ which was studied by R.

Parameter	DFT	NMR [71]	Point charge model
V_{zz} (E_h/ea_0^2)	0.097	0.092 (large peak) 0.117 (small peak)	-
η	0.216	-	0.066, 0.0 as set in Ref. [71]

Table 7.4: Comparison of the DFT result of the EFG for the Na⁺ site of the configuration shown in figure 7.4 and experimentally obtained values. See table 2.4 for the definition of atomic units. The value of the point-charge model contains the averaging over all possible configurations [71].

Sarkar *et al.* [71], ²³Na NMR with $I = \frac{3}{2}$ makes the electric quadrupole interaction accessible. As we will see below, the calculated results for a unit cell with an alteration of Na⁺ and Ca²⁺ are consistent with the experimental mean values of the largest principle tensor component V_{zz} , denoted as usually,

$$|V_{zz}| \geq |V_{xx}| \geq |V_{yy}| \quad (7.7)$$

and the introduced asymmetry parameter

$$\eta = \frac{|V_{xx}| - |V_{yy}|}{|V_{zz}|} \leq 1. \quad (7.8)$$

This leads to the deduced quadrupole Hamiltonian

$$\hat{\mathcal{H}}_Q = \frac{eQV_{zz}}{4I(2I-1)} \left[3\hat{I}_z^2 - \hat{I}^2 + \frac{1}{2}\eta(\hat{I}_+^2 + \hat{I}_-^2) \right], \quad (7.9)$$

with the quadrupole moment $Q \approx 0.1 \cdot 10^{-28} \text{ m}^2$ for ²³Na and the raising and lowering spin operators $\hat{I}_+^2 = \hat{I}_x^2 + i\hat{I}_y$ and $\hat{I}_-^2 = \hat{I}_x^2 - i\hat{I}_y$. The energy eigenvalues are given by

$$E_Q = \frac{eQV_{zz}}{4I(2I-1)} [3m^2 - I(I+1)] \sqrt{1 + \frac{\eta^2}{3}}, \quad (7.10)$$

with $I = \frac{3}{2}$ for ²³Na NMR with $m = I, I-1, \dots -I$. Therefore, this yields a quadrupole splitting and two lines in zero magnetic field in the ²³Na case. The calculation of the EFG of NaCaCo₂F₇ at the Na⁺ site yielded the largest principle axis of $V_{zz} = 0.097E_h/ea_0^2$ and an asymmetry parameter $\eta = 0.216$. Table 7.4 shows the comparison with experimental results obtained by R. Sarkar *et al.* [71]. Here, the published value of the quadrupole frequency is related by

$$\nu_q = \frac{3eQV_{zz}}{2I(2I-1)\hbar}. \quad (7.11)$$

The value of V_{zz} of the homogenous Na⁺-Ca²⁺ distribution on the A site (see figure 7.4) is consistent with the experimentally obtained value or very close to the peak with 80% intensity of the ²³Na NMR study [71]. The calculated asymmetry of $\eta = 0.216$ should be understood as maximal possible asymmetry. The reason is that three Na⁺ appear in the assumed homogenous Na⁺-Ca²⁺ arrangement in line with the hour-glass structure shown in Ref. [71]. Therefore, all other η values of all config-

urations are smaller including other homogenous arrangements, i.e., alternating-like distributions of Na⁺-Ca²⁺. The charge disorder was averaged by fractionalized charges $0.5e$ [71] which results in $\eta \approx 0$. η could not be extracted from the spectrum because of a limited experimental resolution due to magnetic line broadening.

The presented DFT calculations could identify two muon sites and the change between NaCaNi₂F₇ and NaCaCo₂F₇ assuming the formation of the F- μ^+ -F state as a constant energy shift between these minima. One of the most important limitation of the performed DFT calculations is the fact that the local lattice perturbation of the F- μ^+ -F state is not considered by a local lattice relaxation. The final result of the decreased energy difference is consistent with the experimental observation of two muon sites NaCaCo₂F₇. The sequence of the energy minima of the snail and banana isosurfaces is reversed. The energy minima in NaCaCo₂F₇ are closer to each other than in NaCaNi₂F₇ [112]. It is proposed that the muon occupies the off-centre site close to a four Na⁺ cluster of the $8b$ site in NaCaNi₂F₇. A more detailed DFT study including the local lattice distortion and local Na⁺-Ca²⁺ disorder can reveal the influence of the next-next-neighbor environment for the muon site occupancy in NaCaCo₂F₇. Nevertheless, the experimental observation of two muon sites may propose that the local next-next-neighbor Na⁺-Ca²⁺ environments and configurations play no important role for the muon-site selection.

7.3.3 Muon site II

NaCaCo₂F₇ is an insulator and, therefore, the Fermi contact field \mathbf{B}_{con} by conduction electrons and the Rudermann-Kittel-Kasyua-Yosida field \mathbf{B}_{RKKY} observed in metals is assumed to be zero. The Lorentz field \mathbf{B}_{L} is negligible because the magnetization vanishes and the diamagnetic contribution \mathbf{B}_{dia} plays only an important role in superconductors. Therefore, the local magnetic field at the muon site should be composed by the dipole field \mathbf{B}'_{dip} and the transferred hyperfine field $\mathbf{B}_{\text{trans}}$. The latter arises from a possible overlap of the wave function of the spin polarized Co $3d$ -electrons with the muon.

Muon site **II** shows a strong dynamical relaxation rate λ_f of the order of a few μs^{-1} which increases from room temperature down to base temperature by more than one order of magnitude. However, the true nature and origin is unclear so far. The relative muon-site ratio between muon site **I** and muon site **II** is temperature-independent between 290 and 20 K. This is a strong indication for independent muon sites and an electrostatic origin. The reason is not a thermally activated muonium state like probably in BaF₂ [121]. One could argue, the implanted muon is able to provide a much stronger lattice distortion for muon site **II** which leads to this dynamical relaxation effect. Large dynamical muon spin relaxation rates up to $10 \mu\text{s}^{-1}$ are uncommon in magnets and more known from muonium sites [122]. In KCuF₃ and K₂CuF₄ compounds, a decrease of the F- μ^+ -F-state signal and, therefore, of the site occupancy was found [106]. However, in our study, a loss of the signal in magnetic field is not observed as expected for muonium, e.g., a muonium atom in vacuum has a hyperfine frequency around 4.4 GHz, see *Appendix*. In Teflon and Flourinert, the spectrum was described by multiple relaxation functions argued by a dynamical motion or muon diffusion leading to a damping in the later time region. The added Gaussian component has probably a nuclear origin, this is not comparable to our case and should be able to be decoupled in a small LF, e.g. 400 G [117].

The large value of the dynamical relaxation rate λ_f speaks for an electronic origin rather than for a nuclear one. In semiconductors with low electron mobility weakly bound muonium states were found with an ineffective auger process [123]. Those are highly excited states with a weak hyperfine coupling between the electron and the muon which seems not to be the case here. Such states exceed the muon lifetime. A charge transfer model like in Si cannot be excluded [124]. A coexistence of around 75% F- μ^+ -F-state site occupancy and muonium radicals is found in saturated polymers such as polyethylene and polytetrafluoroethylene [125]. This shows the experimental possibility of the formation of the second site in parallel, even in the presence of a F- μ^+ -F state which is located in a very deep energy minimum. This is similar to the kagome antiferromagnet [NH₄]₂[C₇H₁₄N][V₇O₆F₁₈] where only 10% F- μ^+ -F state was found [119]. Muon site **II** may be a F- μ^+ -F-like state as well. However, this can not be concluded because of the missing coherent precession frequencies of ¹⁹F. The F- μ^+ -F state is one of the strongest local lattice displacement distortions which can be produced by the implanted muon. The tuning from spin glass to quantum spin liquid was investigated in molybdate pyrochlores substituting Lu₂Mo₂O₇ to Lu₂Mo₂N₂O₅ [126]. Locally, maybe the F- μ^+ -F state chemically expressed as NaCaCo₂(μ^+ F₂⁻)F₅ acts as an effective NaCaCo₂O₂F₅ defect and tunes the system more to a spin liquid. The importance of spin-lattice coupling in frustrated antiferromagnets, especially pyrochlores depending of the magnitude of distortion in frustrated cluster units has already been discussed in [53], see below.

7.3.4 Persistent μ^+ spin dynamics

Table 4.2 shows the synthesized series of cubic pyrochlore fluorides in 2014-2017. In this series NaCaCo₂F₇ has the highest frustration index. The highly-frustrated pyrochlore antiferromagnet CsNiCrF₆ has shown magnetic SRO and neutron-scattering results which are qualitatively consistent with a nearest-neighbor Heisenberg model [127, 128]. Antiferromagnetic SRO was also found in the compound CsMnFeF₆ exhibiting a modified pyrochlore structure isomorphic to RbNiCrF₆, but the magnetization results are more consistent with a magnetic cluster model. It is proposed that CsMnFeF₆ shows clusters of antiferromagnetically coupled spins even at 300 K [129, 130, 131, 132]. Low-field a.c. and d.c. susceptibility measurements revealed fundamental differences compared to classical spin glass states found in CsNiCrF₆ and CsMnFeF₆ emphasizing the controversial role of pyrochlore fluorides [133].

In NaCaCo₂F₇, the relaxation rate increases gradually and smoothly with decreasing temperature, see figure 7.3 (a). This behavior is inconsistent with a sharp transition to a magnetic LRO state. Similar behavior was found in Er₂Ti₂O₇ and Er₂Sn₂O₇. Although magnetic LRO is proposed in the order-by-disorder candidate Er₂Ti₂O₇, a magnetic SRO was deduced from μ SR [62]. The wide temperature range of the slowing down reflects the large ratio of the frustration index $f \approx 56$ in NaCaCo₂F₇. In usual spin glasses with $J \sim kT_g$ the slowing down of λ_d occurs in a much narrower region $T_g \leq T \leq 2T_g$ [134]. PSD is present down to 20 mK and, therefore, it cannot be considered as a canonical spin-glass state. For LRO or frozen moments as in spin glasses, the dynamical relaxation rate should tend to zero as $T \rightarrow 0$. Similar results, although of different magnitude, were also observed in Tb₂Ti₂O₇ [86].

The effect of PSD reflected by a mainly constant and saturated dynamic relaxation is not understood

in detail as discussed in the chapter of BaTi_{0.5}Mn_{0.5}O₃. PSD is observed in different material classes probed by μ^+ SR, see table 5.3. The table shows a selection of frustrated systems showing PSD at low temperatures, for details see corresponding references. Interestingly, PSD appears not exclusively. A coexistence of PSD and partial frozen states or magnetic LRO is observed. Unidimensional low-energy excitations are proposed as a motor in CdHo₂S₄ [135]. In the spin-ice stuffed metallic pyrochlore Pr_{2+x}Ir_{2-x}O_{7- δ} a muon-induced Pr³⁺ crystal electric field ground state splitting and a hyperfine-enhanced ¹⁴¹Pr nuclear magnetization are strongly discussed as possible origin [136]. This shows the possibility of the induced change of the crystal field by the muon, the spin-lattice coupling in pyrochlores plays an important role. Additionally, spin-driven Jahn-Teller distortions are proposed to lead to a cubic or tetragonal structural transition in spinel compounds [137].

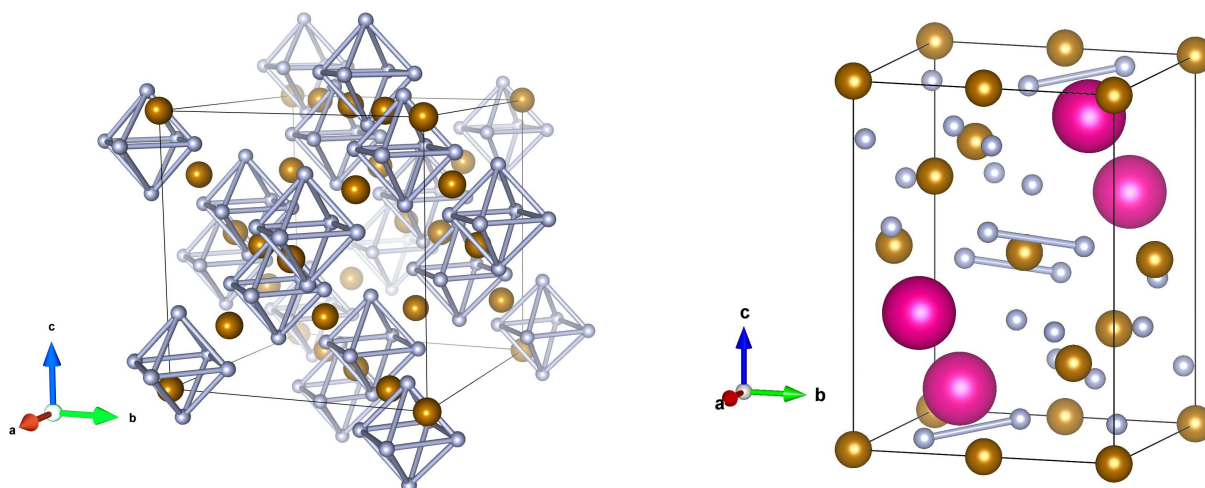
7.4 Conclusions

No evidence for dominant static magnetic order is found in NaCaCo₂F₇ as it is the case in NaCaNi₂F₇ probed by μ^+ SR [112]. The presence of persistent low-energy spin dynamics down to 20 mK locates NaCaCo₂F₇ in close proximity of a quantum spin-liquid regime. Our observations are qualitatively consistent with the possible quantum cluster spin glassiness² as proposed and discussed by E. C. Andrade *et al.* [36]. The quantitative analysis of the F- μ^+ -F dipole frequency ν_d results in a minimal F-F distance shortening by 12.2(5)% due to the presence of the muon.

A second muon site **II** is found. Qualitatively, muon site **II** shows PSD with higher dynamical relaxation rates of one order of magnitude compared to muon site **I**. Here, the effective crossover temperature is shifted to $T_C \approx 10$ K compared to muon site **I** with $T_C \approx T_f \approx 3$ K, which is close to the freezing temperature measured by heat capacity and a.c. susceptibility by J. W. Krizan *et al.* [28].

DFT calculations of the unperturbed unit cells of NaCaCo₂F₇ and NaCaNi₂F₇ are consistent with a decrease of the energy differences of energy minima of the electrostatic potential that support the experimental observed two muon sites. The calculated largest main axis V_{zz} of the EFG tensor for the Na⁺ site is consistent with the experimentally observed ²³Na-NMR value.

²Special thanks to Prof. M. Vojta for discussions of the description.



(a) Enhanced unit cell of the cubic pyrochlore magnet FeF₃: Fe in brown and F in grey, the sticks show the manifold of smallest distances between two F of 2.707(2) Å.

(b) Unit cell of RbFe²⁺Fe³⁺F₆: Fe in brown, F in grey and Rb in pink, the sticks show the manifold of smallest distances of 2.673(1) Å between two F.

Figure 7.9: Estimation of possible F- μ -F bound state positions assuming the smallest distance between two F is μ^+ -selected. The FeF₃ estimation leads to cage structures.

7.5 Outlook

This section discusses possibilities for future work to improve the physical understanding of NaCaCo₂F₇. Additionally, I suggest to study other geometrically frustrated fluoride systems. The observation of well-defined F- μ^+ bound states offers the possibility to analyze the muon spin relaxation with a well-defined muon site in the lattice which is often difficult to identify in oxides. I propose two systems: The cubic pyrochlore magnet FeF₃ and the magnetically frustrated pyrochlore-related mixed-metal fluoride RbFe²⁺Fe³⁺F₆. Both systems contain Fe and make a supplemented ⁵⁷Fe-Mössbauer study possible by our group.

7.5.1 NaCaCo₂F₇

Interestingly, the tuning from spin glass to quantum spin liquid was investigated in molybdate pyrochlores substituting Lu₂Mo₂O₇ to Lu₂Mo₂O₅N₂ [126]. Since the Co³⁺ oxidation state is less stable³ to grow NaCaCo₂F₅O₂, one could try if the perhaps more stable compound NaCaFe₂F₅O₂ exists from an experimental and chemical point of view. Maybe this tunes the spin glass more to a quantum spin liquid phase.

The second observed muon site **II** is not fully understood. A deeper investigation is necessary. One should keep in mind that the reason for the occurrence of the second muon site is more of interest for scientists working with μ SR.

³Concerning this, I had a discussion with Prof. Dr. T. Doert. He has mentioned the unfortunate chemical stability of the Co³⁺ oxidation state. A synthesis of NaCaFe₂F₅O₂ could be more promising.

Element	Site	x	y	z	Occupancy
-	16 <i>d</i>	-	-	-	-
Fe	16 <i>c</i>	0	0	0	1
-	8 <i>a</i>	-	-	-	-
F	48 <i>f</i>	0.3104(5)	0.125	0.125	1

Table 7.5: Atomic positions of the crystallographic sites of the unit cell of the pyrochlore FeF₃ with $a = 10.325(2)$ Å. The data are taken from R. De Pape *et al.* [49]

Additionally, a DFT study including the muon distortion should be done in the framework of the NaSrCo₂F₇ publication extending the microscopic understanding.

7.5.2 Highly frustrated pyrochlore FeF₃

The highly frustrated pyrochlore FeF₃ exhibits magnetic LRO at $T_N = 15.5$ K. Neutron-diffraction studies have shown clear evidence for short-range correlations above T_N [50]. Strong antiferromagnetic correlations are observed between nearest neighbors below 160 K. Ferromagnetic correlations develop between second and third neighbors below 80 K. The pyrochlore FeF₃ exhibits an unconventional form of magnetic noncoplanar order [138]. Table 7.5 shows the crystal data taken from R. De Pape *et al.* [49]. The short formula of the cubic pyrochlore FeF₃ arises from the missing occupancy of the crystallographic 16*d* and 8*a* sites. Figure 4.2 shows the unit cell of FeF₃ visualized by VESTA by the ionic radii as presented in the introduction. One should keep in mind, the calculated F_c and θ_c values with Monte-Carlo simulations of FeF₃ assuming only antiferromagnetic next nearest neighbor interactions in table 4.1 taken from P. Lacorre [46].

Depending on the crystal structure and on the F distances, one can expect different geometries of possible manifolds of F- μ -F states assuming the smallest F-F distance will be selected. This is just a rough estimation, but fortunately it is mostly experimental consistent with the really observed F- μ -F site. For instance, for FeF₃ one gets cage structures, see figure 7.9 (a). The minimal lattice distortion displacement is around 12.1% which is very close to the NaCaCo₂F₇ value of the minimal possible displacement. The FeF₃ is proposed because of the simplified unit cell compared to other pyrochlore compounds. The absence of the 16*d* and 8*a* sites making this compound an excellent candidate combining a distortion study of possible F- μ -F sites in a highly frustrated compound containing less atomic species and especially no disorder as in the NaCaCo₂F₇ family reducing the possible complexity.

7.5.3 Mixed-metal β -pyrochlore RbFe²⁺Fe³⁺F₆

Figure 7.9 (b) shows the unit cell of the magnetically frustrated pyrochlore-related mixed-metal fluoride RbFe²⁺Fe³⁺F₆. RbFe²⁺Fe³⁺F₆ shows a Curie-Weiss temperature of $\Theta \approx -270$ K and antiferromagnetic order around $T_N = 16$ K [139]. The crystal data are shown in table 7.6 taken from S. W. Kim *et al* [139]. RbFe²⁺Fe³⁺F₆ shows a three-dimensional related pyrochlore structure consisting of corner-sharing Fe²⁺F₆ and Fe³⁺F₆ octahedra. The unit cell has two ordered vacancies, different from the conventional α -pyrochlore structure, and is called β -pyrochlore. For instance, the

Atom	x	y	z
Rb	0.9942(3)	0.25(-)	0.3798(2)
Fe ²⁺	0.8014(2)	0.25(-)	0.7302
Fe ³⁺	0.5	0.0	0.5
F(1)	0.7413(2)	0.0644(2)	0.5784(2)
F(2)	0.3791(2)	0.0077(3)	0.6698(1)
F(3)	0.4322(3)	0.25	0.4672(2)
F(4)	0.5682(3)	0.25	0.8407(2)

Table 7.6: Atomic positions of RbFe²⁺Fe³⁺F₆ obtained by Rietfield refinement of powder neutron diffraction at 4K. The space group is *Pnma* (No.62) with $a = 6.96630(5) \text{ \AA}$, $b = 7.43903(5) \text{ \AA}$ and $c = 10.12164(7) \text{ \AA}$. The data are taken from taken from S. W. Kim *et al.* [139]

first cationic vacancy reverts the kagome network of Rb sites in the α -pyrochlore into a diamond lattice. Figure 7.9 (b) shows the smallest distance between two fluorine in grey and this is a distance of $2.673(1) \text{ \AA}$. This distance appears four times per unit cell. This means the number of equivalent F-F distances is here significantly reduced compared to the α -pyrochlore unit cell. RbFe²⁺Fe³⁺F₆ forms antiferromagnetic chains of Fe²⁺ and Fe³⁺ moments providing a well understood basis for a site-distortion study.

8 Magnetic Field Tuning of Low-Energy Spin Dynamics in the Single-Atomic Magnet $\text{Li}_2(\text{Li}_{1-x}\text{Fe}_x)\text{N}$ Probed by ^{57}Fe -Mössbauer Spectroscopy

This chapter discusses the second main part of my work. The first section introduces the preliminary state of the art on the $\text{Li}_2(\text{Li}_{1-x}\text{Fe}_x)\text{N}$ compound. The properties of the host crystal $\alpha\text{-Li}_3\text{N}$ are discussed in the context of new DFT calculations of this ionic crystal. $\text{Li}_2(\text{Li}_{1-x}\text{Fe}_x)\text{N}$ studies with $x > 0.15$ (high doping) and magnetization studies with $x \ll 1$ are discussed preparing the reader for my experimental results of $\text{Li}_2(\text{Li}_{1-x}\text{Fe}_x)\text{N}$ ($x \ll 1$), see S. A. Bräuninger et al. [140]. The temperature and external magnetic field dependence of the single-ion spin dynamics is probed by ^{57}Fe Mössbauer spectroscopy. The homogenous distribution of Fe centers is shown over the $\alpha\text{-Li}_3\text{N}$ matrix. Our observed transverse magnetic field sensitivity is qualitatively reproduced and explained by a single-ion spin Hamiltonian analysis done by Prof. Andre Zvyagin. A recent study reports a slow paramagnetic relaxation stressing the proposed ferromagnetic nature of nondiluted $\text{Li}_2(\text{Li}_{1-x}\text{Fe}_x)\text{N}$ ($x \approx 0.30$) by M. Fix, S. A. Bräuninger *et al.* [141].

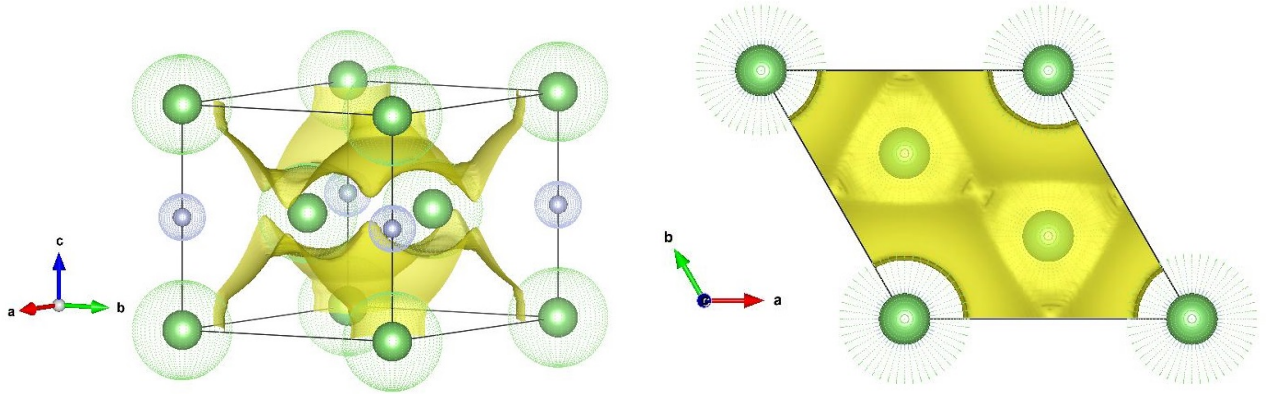
8.1 Introduction

8.1.1 Single-molecule and single-atomic magnets

Single-molecule magnets (SMMs) and single-atomic magnets (SAMs) are model systems to study magnetic relaxation at elevated temperatures as well as quantum tunneling of magnetization and quantum coherence in nanoscale systems at low temperatures [142, 143]. Moreover, SMMs and SAMs are proposed for novel data storage devices in spintronics or possible applications for quantum computing [144, 145, 146].

In the paramagnetic state isolated magnetic moments with a strong axial anisotropy DS_z^2 and negative D can fluctuate between the degenerate $S_z = \pm S$ ground states due to spin-lattice relaxation or hyperfine coupling processes. For thermally activated fluctuations the spin autocorrelation time τ at a temperature T is described by the Neel-Arrhenius equation

$$\tau = \tau_0 \exp\left(\frac{E_A}{k_B T}\right), \quad (8.1)$$



(a) View of the unit cell and isosurface of the charge density of $\alpha\text{-Li}_3\text{N}$ in tilted direction.

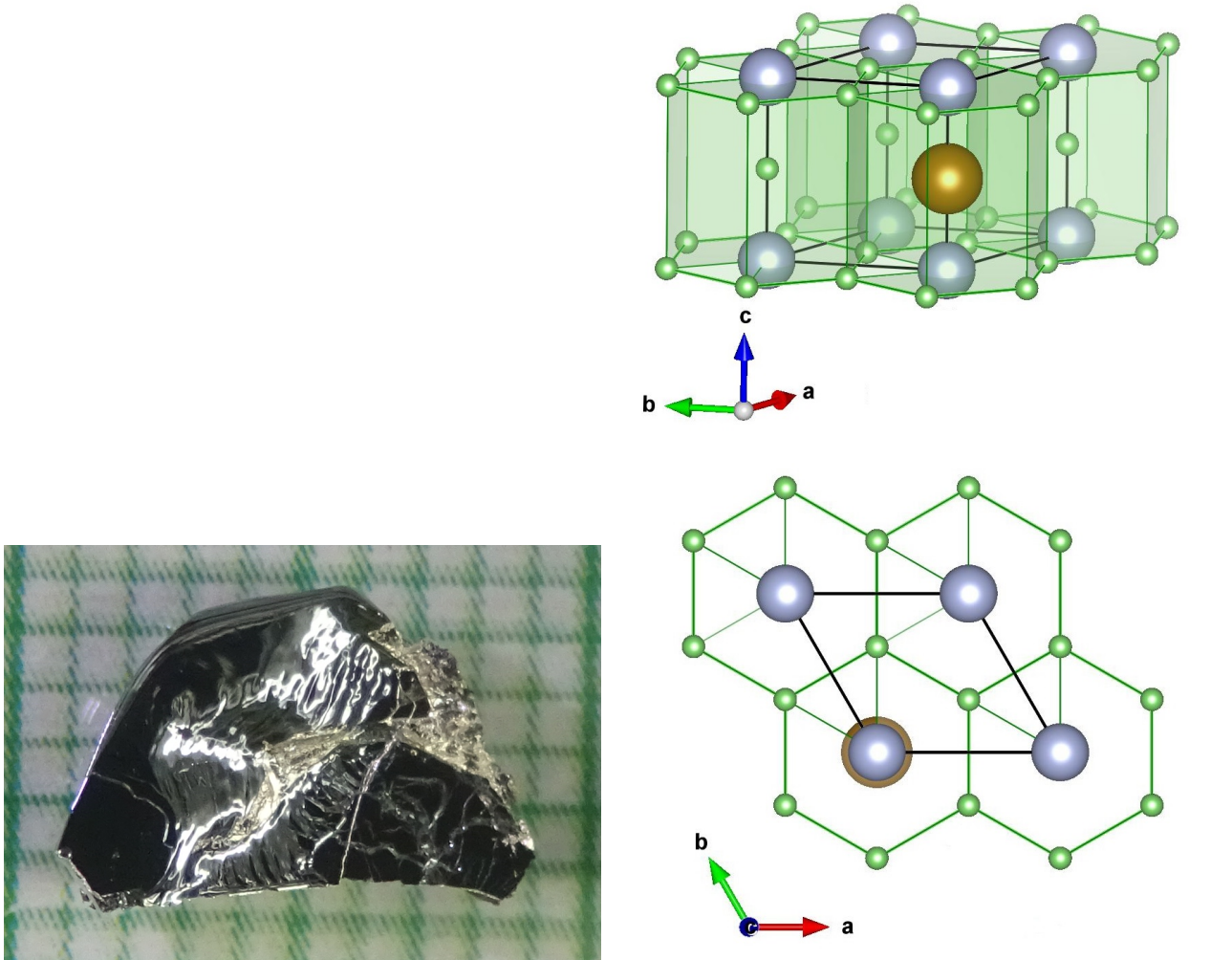
(b) View of the unit cell and isosurface of $\alpha\text{-Li}_3\text{N}$ along the c -axis.

Figure 8.1: Unit cell with the atomic radii of the host system $\alpha\text{-Li}_3\text{N}$, Li^+ is given in green and N^{3-} grey. The yellow surfaces show the isosurfaces of the charge density of 0.012 a_0^{-3} .

controlled by an effective energy barrier E_A with the Boltzmann constant k_B . The experimentally observed energy barrier E_A can be very different from the magnetic anisotropy energy $E_m = DS^2$. Magnetic quantum tunneling processes via degenerate S_z states at or above the $\pm S$ ground state can considerably reduce E_A . External magnetic fields applied longitudinal to the magnetic anisotropy axis can be used to tune the magnetic system through the level crossing condition for specific S_z states via Zeeman interaction. However, quantum tunneling can only occur if off-diagonal elements in the spin Hamiltonian cause a mixing of these S_z eigenstates and an avoided level-crossing with a finite minimum energy gap $\Delta_{m,m'}$ is generated. The Landau-Zener model is applied to describe the magnetic quantum tunneling observed via magnetization steps in low temperature magnetization experiments, e.g. in nanomagnets such as $\text{Mn}_{12}\text{-ac}$ [147] or $[\text{Fe}_8\text{O}_2(\text{OH})_{12}(\text{tacn})_6]^{8+}$, briefly Fe_8 [148]. In an external magnetic field applied transverse to the anisotropy axis the quantum tunneling can be modulated by quantum interference [149]. This topological quantum phase interference described by a Berry phase is experimentally observed [150]. A topological theory of diabolical points of quantum magnets is discussed and topological sum rules are derived which characterize diabolical points by their diabolicity index [151]. Interestingly, a new perspective of the Landau-Zener model is obtained by the description in terms of the Kibble-Zurek theory of topological defect production in nonequilibrium phase transitions [152].

8.1.2 The host crystal $\alpha\text{-Li}_3\text{N}$

The host crystal is a $\text{Li}^+\text{-N}^{3-}$ compound with a lithiumnitrid $\alpha\text{-Li}_3\text{N}$ structure. $\alpha\text{-Li}_3\text{N}$ is an ionic conductor with a strong anisotropy [153]. The compound is proposed for applications of hydrogen storages due to the high H_2 capacity, a component in the synthesis of GaN nanophases and even as an electrode material in Li -batteries [154, 155]. Every N^{3-} ion is surrounded by eight Li^+ ions. Six Li^+ are located in-plane in a hexagonal geometry. The other two Li^+ are located above and below N leading to a hexagonal-bipyramidal geometry. The crystal data are presented in the next subsection. The root of this compound can be understood as linear chains of N and Li along the c -axis. So far,



(a) Single crystal of $\text{Li}_2(\text{Li}_{1-x}\text{Fe}_x)\text{N}$ with $x \approx 2.5\%$ on a millimeter grid. Here, one square corresponds to 1 mm^2 .

(b) Two views of the extended unit cells of $\text{Li}_2(\text{Li}_{1-x}\text{Fe}_x)\text{N}$ according to the crystal data presented in table 8.1. The host system is a $\alpha\text{-Li}_3\text{N}$ matrix, here Li^+ shown in green ($2c$ -site in-plane), N^{3-} in gray ($1a$ -site) and the green-brown site between N^{3-} is mainly occupied by Li^+ and by Fe ($1b$ -site). The ionic radius of Fe is overestimated for better perceptibility. The black lines show the primitive unit cell according to figure 8.1.

Figure 8.2: Photo of a crystal of Fe-diluted $\text{Li}_2(\text{Li}_{1-x}\text{Fe}_x)\text{N}$ and the emphasized hexagonal symmetry of the crystal structure. The structure is unstable for high Fe concentration $x > 0.34(2)$ and the synthesis fails because of phase separation.

α - Li_3N and the corresponding high pressure derivatives provide the only known example for a stable N^{3-} ion [154]. Figure 8.1 (a) and (b) show the unit cell of α - Li_3N and a corresponding isosurface of the charge density calculated by the DFT code Elk 4.3.6. The charge density is given in a_0^{-3} . Here, a_0 is the Bohr radius and the elemental charge is defined as $e = 1$. The shown unit cell is a parallelepiped in which the basis in the a-b-plane spans an angle of 60° or 120° , respectively. The dotted surfaces are the atomic ball models of the atomic radii. The highest electron charge densities are located around nitrogen. This result is qualitatively consistent with the DFT study done by Fister *et al.* [154], especially the two triangle structures in figure 8.1 (b). Fister *et al.* have shown the absence of a covalent bonding character. α - Li_3N was part of an extensive study and after some controversial chemical disputes the compound is now interpreted to be located near the extreme ionic endpoint of the continuum from covalent to ionic bond. A NMR study has shown that all of the diffusion processes take place in the Li_2N layers below 300 K. Above this temperature, the second Li site is also involved which leads to interplanar diffusion. Hydrogen doping increases the jump rates [153, 156].

8.1.3 $\text{Li}_2(\text{Li}_{1-x}\text{Fe}_x)\text{N}$

Figure 8.2 (a) shows a photo of a single crystal of Fe-diluted $\text{Li}_2(\text{Li}_{1-x}\text{Fe}_x)\text{N}$ right after the synthesis. $\text{Li}_2(\text{Li}_{1-x}\text{Fe}_x)\text{N}$ crystallizes in a hexagonal symmetry (space group $P6/mmm$, Nr. 191) and alternating planes of (Li_2N) and $(\text{Li}_{1-x}\text{Fe}_x)$ are oriented perpendicular to the hexagonal symmetry axis c [157]. Table 8.1 shows the used crystal structure data taken from A. Jesche *et al.* [157]. It is shown that the global crystal structure of $\text{Li}_2(\text{Li}_{1-x}\text{Fe}_x)\text{N}$ is invariant below $x = 0.26(1)$ since the error of 1% of the Fe occupancy excluded not a residual finite occupancy of Fe in the $2c$ or $1a$ sites, e.g. that at low $x < 0.02$ the dominant site changes from $1b$ to another site¹. The unit-cell parameters are $a = 3.6904(2)\text{\AA}$ and $c = 3.8164(2)\text{\AA}$ with the angles $\alpha = \beta = 90^\circ$ and $\gamma = 120^\circ$. Figure 8.2 (b) shows the enhanced unit cell (black lines) emphasizing the hexagonal symmetry of the Fe site and the corresponding linear N-Fe-N geometry. The Fe ions occupy only the Li $1b$ site out-of-plane of the hexagonal Li_2N planes present in this system.

Studies on polycrystalline samples of $\text{Li}_2(\text{Li}_{1-x}\text{Fe}_x)\text{N}$ with $x \approx 0.16$ and $x \approx 0.21$ by Mössbauer spectroscopy revealed a static hyperfine field below $T_C \approx 65$ K and long-range ferromagnetic ordering was proposed on the basis of magnetization studies [158, 159]. Recently, A. Jesche *et al.* performed magnetization studies on large single crystals of $\text{Li}_2(\text{Li}_{1-x}\text{Fe}_x)\text{N}$ with $x \ll 1$. Large magnetic moments exceeding the spin-only value with a strong axial anisotropy parallel to the c -axis are found. These magnetic moments can be associated with isolated Fe ions linearly coordinated with two nitrogen ions in covalent N-Fe-N bonds [160]. From low temperature magnetization experiments on single crystals a magnetic anisotropy field of $\mu_0 H \approx 88$ T ($x \approx 0.0032$) was estimated together with a large magnetic moment $\mu_{\text{eff}} = 6.5(4)\mu_B$ per Fe atom parallel to the c axis, mainly independent of the Fe concentration [157]. For $x \approx 0.28$ a considerable magnetic anisotropy field of $\mu_0 H \approx 220$ T was reported [157]. The deduced value of μ_{eff} is in agreement with the fully spin-orbit coupled Hund's rule value of a Fe^{1+} configuration [157, 158]. The observation of steps in magnetic hysteresis loops and relaxation

¹The invariance of the hyperfine parameters as I will show below as a function of x show that the assumption by A. Jesche *et al.* is valid at low x . The Fe site is restricted to the $1b$ site.

Atom	Wyckoff site	Occupation	x	y	z	U_e [\AA^2]
Fe 1	1b	0.26(1)	0	0	1/2	0.010(1)
Li 1	1b	0.74(1)	0	0	1/2	0.010(1)
Li 2	2c	1	1/3	2/3	0	0.031(1)
N 1	1a	1	0	0	0	0.010(1)

Table 8.1: Atomic coordinates and isotropic displacement parameters for $\text{Li}_2(\text{Li}_{1-x}\text{Fe}_x)\text{N}$ with $x = 0.26(1)$.

phenomena with an energy barrier $E_B \approx 430$ K indicate a SAM-like behavior. The relaxation time is only weakly temperature-dependent below 10 K indicating the importance of quantum tunneling in this temperature range. However, the microscopic process of the thermally excited relaxation is not known. A. Jesche *et al.* concluded that the spontaneous magnetization and hysteresis is eventually not caused by a collective magnetic ordering but rather due to the strong axial magnetic anisotropy in the linear N-Fe-N moiety. A recent study reports a slow paramagnetic relaxation stressing the proposed ferromagnetic nature of nondiluted $\text{Li}_2(\text{Li}_{1-x}\text{Fe}_x)\text{N}$ ($x \approx 0.30$) by M. Fix, S. A. Bräuninger² *et al.* [141].

8.1.4 Motivation

Xu *et al.* [161] performed electronic structure calculations for $\text{Li}_2(\text{Li}_{1-x}\text{Fe}_x)\text{N}$ which reveal large magnetic anisotropy energies of 305 K for an $\text{Fe}^{2+} d^6$ with $J = 4$ configuration and 360 K for an $\text{Fe}^{1+} d^7$ with $J = 7/2$ configuration. Moreover, the authors conclude that a Fe^{2+} state is expected to dominate at $x \ll 1$ whereas the Fe^{1+} state should play a dominant role at high x . However, it is not clear how such strong axial anisotropy energies around 300 K can be reconciled with the observation of electronic level crossings in the magnetic hysteresis experiments at very low magnetic fields³ of $B = 0.15, 0.55$ and 3 T [157, 162], i.e. energy scales $\mu_0 B/k_B$ of several Kelvin only.

To address these questions, in this thesis I report a detailed ^{57}Fe Mössbauer investigation on single crystals of highly diluted iron in $\text{Li}_2(\text{Li}_{1-x}\text{Fe}_x)\text{N}$ with $x \approx 0.025, 0.011, 0.01, 0.002$. The measurements were performed at temperatures $2 \text{ K} \leq T \leq 300 \text{ K}$ in magnetic fields $0 \text{ T} \leq B \leq 5 \text{ T}$ applied transverse and longitudinal to the magnetic anisotropy axis. Below 30 K the Fe centers exhibit a giant magnetic hyperfine field of $\bar{B}_A = 70.25(2) \text{ T}$ parallel to the axis of strongest electric field gradient $\bar{V}_{zz} = -154.0(1) \text{ V/\AA}^2$.

We demonstrate that the diluted iron ions in $\text{Li}_2(\text{Li}_{1-x}\text{Fe}_x)\text{N}$ indeed form isolated single-ion paramagnets consistent with a $\text{Fe}^{1+} d^7$ charge state and an unquenched orbital moment, i.e. total angular momentum $J = 7/2$. A continuous slowing down of the spin fluctuations is observed by Mössbauer spectroscopy below 300 K which can be described by a thermally activated Orbach process with an activation barrier of $\bar{E}_A = 570(6) \text{ K}$. The fluctuation rate is very sensitive to magnetic fields of the order a few Tesla applied transverse or longitudinal to the magnetic anisotropy axis. A quasistatic magnetic hyperfine field is observed below 50 K.

²The publication *Ferromagnetism versus slow paramagnetic relaxation in Fe-doped Li_3N* is not further discussed in this thesis because it deals with $x \approx 0.30$. For details, see Refs. [141].

³See also figure 8.3 which shows the isothermal magnetization data of a $\text{Li}_2(\text{Li}_{2.975}\text{Fe}_{0.025})\text{N}$ single crystal.

A clustering of nearest neighbor Fe ions is ruled out for $x \leq 0.025$. The experimental observations are qualitatively reproduced by a single-ion spin Hamiltonian analysis. It demonstrates that for dominant magnetic quantum tunneling relaxation processes a weak axial single-ion anisotropy D of the order of a few Kelvin can cause a two orders of magnitude larger energy barrier E_B for longitudinal spin fluctuations.

	MPMS [%]	ICP [%]	also denoted as
SC 1	2.526(126)	-	$\text{Li}_2(\text{Li}_{2.9747}\text{Fe}_{0.0253})\text{N}$
SC 2	-	1.087(40)	$\text{Li}_2(\text{Li}_{2.9891}\text{Fe}_{0.0109})\text{N}$
SC 3	-	0.989(39)	$\text{Li}_2(\text{Li}_{2.9901}\text{Fe}_{0.0099})\text{N}$
SC 4	0.139(7)	0.177(51)	$\text{Li}_2(\text{Li}_{2.9986}\text{Fe}_{0.0014})\text{N}$

Table 8.2: Doping concentrations x of the investigated single crystals (SCs) 1-4 measured using a MPMS or ICP. These measurements were performed by A. Jesche and M. Fix in Augsburg.

8.2 Results

Here, the main part of my results is presented. The preliminary work to understand the sample stability under air and the investigation of the concentration series was quite time consuming. Therefore, this should be appreciated in one sentences which is done at this place. After my initial temperature- and magnetic-field-dependent measurements of the sample $\text{Li}_2(\text{Li}_{2.9747}\text{Fe}_{0.0253})\text{N}$, my colleague S. Kamusella and our Bachelor student F. Seewald (bachelor thesis) supported me by extending the transverse field investigations. In total, we have measured eleven samples showing the effort of this study⁴.

8.2.1 Doping concentrations and magnetization studies of $\text{Li}_2(\text{Li}_{1-x}\text{Fe}_x)\text{N}$ with $x \ll 1$

The crystal growth of $\text{Li}_2(\text{Li}_{1-x}\text{Fe}_x)\text{N}$ and the magnetization measurements are described by A. Jesche, M. Fix *et al.* [141, 157]. Table 8.2 shows the four investigated single crystals (SCs) investigated by ^{57}Fe Mössbauer spectroscopy in this work and the corresponding Fe concentrations. The Fe-concentration for SC 4, $\text{Li}_2(\text{Li}_{2.9986}\text{Fe}_{0.0014})\text{N}$, is determined by magnetic susceptibility using a Quantum Design MPMS (Magnetic property measurement system 3 from Quantum Design, here, the estimation of the Fe concentration was done by the saturation magnetization at 2 K, with $\mu_0 H_c = 7\text{ T}$ assuming a magnetic moment of $5\mu_B$) and by ICP-OES (inductively-coupled-plasma optical-emission-spectroscopy) measurements, for SC 1 only MPMS measurements were performed, for SC 2 and SC 3 only ICP was used. SC 1-4 were plates. The diameter, thickness and mass of SC 1-4 were not uniform. Figure 8.3 shows the isothermal magnetization data of a $\text{Li}_2(\text{Li}_{2.975}\text{Fe}_{0.025})\text{N}$ single crystal, measured at different temperatures for magnetic fields applied parallel to the crystallographic c -axis, $H \parallel c$, for experimental details, see appendix. The effective sweep rate for the full loops was 2.9 mT/s with 10 mT/s between the measurements. For temperatures $T < 50\text{ K}$, magnetic hysteresis becomes apparent with magnetization steps visible at field of $\mu_0 H_c \approx 0, \pm 3.3\text{ T}$ at $T = 2\text{ K}$, for discussion, see below.

8.2.2 Experimental description: ^{57}Fe Mössbauer Spectroscopy

Mössbauer measurements were carried out in CryoVac and Oxford instruments helium flow cryostats in under-pressure mode or normal mode, respectively. We used a WissEl Moessbauer spectrometer. The detector was a proportional counter tube or a Si-PIN-detector from KETEK and the source a

⁴This number includes samples of higher concentration $x > 0.1$ which are not part of this thesis and discussed in the Bachelor thesis by F. Seewald [163].

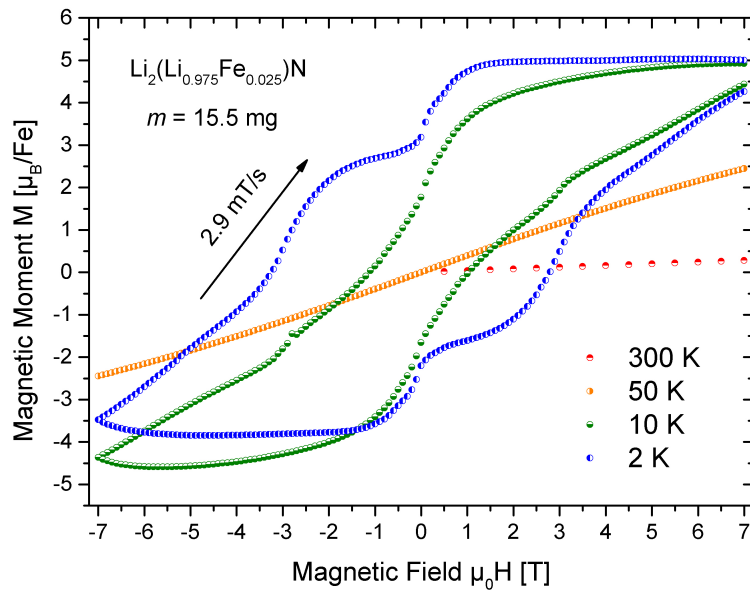


Figure 8.3: Hysteresis loops of $\text{Li}_2(\text{Li}_{1-x}\text{Fe}_x)\text{N}$ with $x = 0.025$ (crystal SC 1) at different temperatures measured by our colleagues in Augsburg, A. Jesche and M. Fix. For a detailed description, see text.

Rh/Co source with an initial activity of 1.4 GBq. The superconducting coil was powered by an Oxford instruments IPS 120-10 power supply with an applied magnetic field parallel or perpendicular to the γ -beam with an angle error of $< 5^\circ$. The absorber (sample) SC 1 exceeded the thin absorber limit requiring a transmission integral fit. The analysis was done using the Moessfit analysis software [1]. All measurements were performed with the normal vector of the largest surface of the crystals parallel to the γ -beam. The single crystals were protected by paraffin wax to avoid oxidation. An estimation of the effect of the ^{57}Co source splitting in longitudinal magnetic fields and more details can be found in the appendix.

8.2.3 Low temperature ^{57}Fe -Mössbauer spectroscopy at base temperature T_B

Mössbauer spectroscopy was performed at base temperature $T_B \leq 4\text{K}$ in zero-field (ZF) on the crystals SC 1-4. At this temperature the Fe spins are in the blocking state since the effective magnetic anisotropy energy barrier is much larger than the thermal energy. In this case the lifetime of the electronic states exceeds that of the nuclear states. The Mössbauer time window, determined by the mean Larmor precession time τ_M of the nuclear spin is on the order of nanoseconds and the electronic relaxation time $\tau \gg \tau_M$. The hyperfine interactions are effectively stationary [164].

Figure 8.4 shows the ^{57}Fe Mössbauer measurement at T_B in ZF of SC 1-4. For SC 1 two Fe sites A (green) and B (red) are observed. The dark black line is given by the total transmission integral fitting function

$$T(v) = \int_{-\infty}^{\infty} L(E, v) e^{-\sigma(E)t_a} dE \quad (8.2)$$

with the normalized Breit-Wigner resonance cross section $\sigma(E)$ depending on the energy E and an effective thickness $t_a = 2.39(10)$ reflecting a non-thin absorption limit. Therefore, the black line

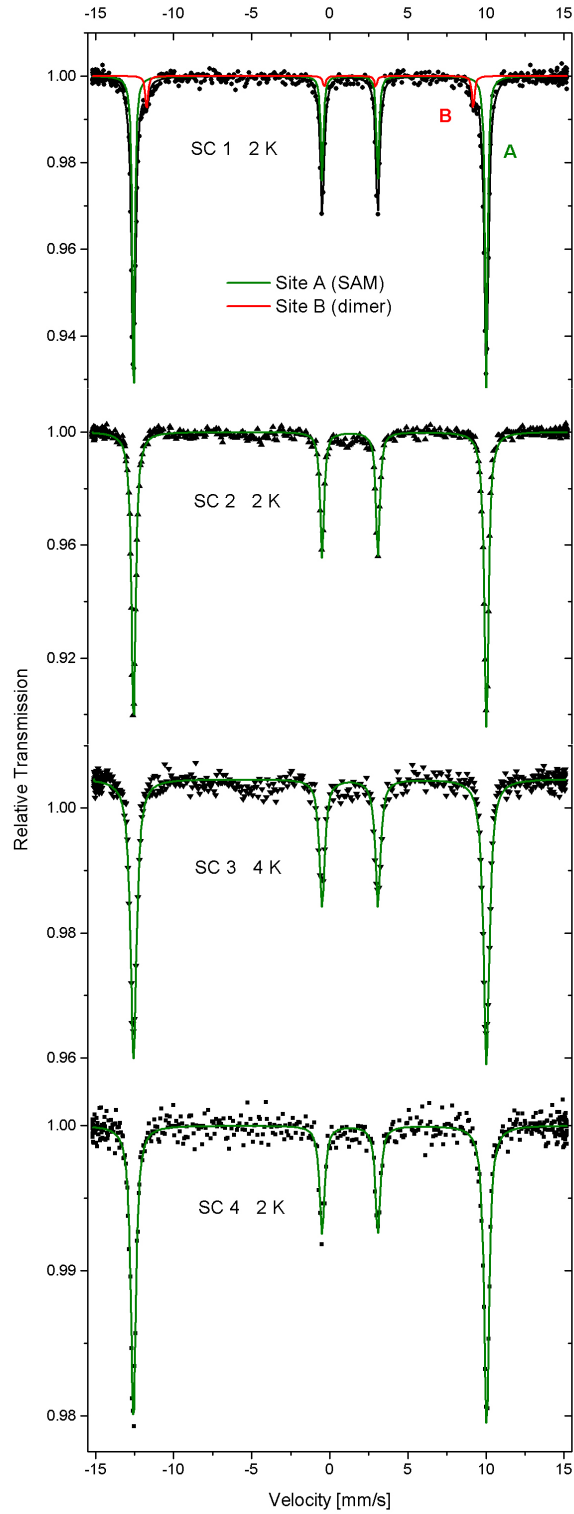


Figure 8.4: Static Mössbauer spectra of $\text{Li}_2(\text{Li}_{1-x}\text{Fe}_x)\text{N}$ of the single crystals SC 1-4 as specified in table 8.2 at base temperature $T_B \leq 4\text{ K}$ in ZF.

represents the transmission integral fit whereas the lines for the sites A and B show the natural line $L(E, v)$. $T(v)$ is proportional to the line intensity of the recoil-free γ -ray, a function of the absorber thickness, and v is the Doppler velocity. A thin absorber approximation is only valid for $t_a < 1$ and then the lines shape is described by a Lorentzian $L(E, v)$ [16]. For SC 2-4 the thin absorption limit is nearly indistinguishable from the black line is the green single Fe site A. The model used in figure 8.4 is the static crystal Hamiltonian

$$\hat{\mathcal{H}} = \hat{\mathcal{H}}_{\text{M}} + \hat{\mathcal{H}}_{\text{Q}} + \hat{\mathcal{H}}_{\text{Z}} \quad (8.3)$$

assuming the same electric monopole $\hat{\mathcal{H}}_{\text{M}}$ and quadrupole interaction $\hat{\mathcal{H}}_{\text{Q}}$ for the two Fe sites A and B. We deduced an isomer shift of $\delta = 0.100(21)$ mm/s with respect to α -Fe at room temperature assuming a negligible second-order Doppler shift $\delta_{\text{SOD}} \approx 0$ of the absorber at this temperature. The observed ^{57}Fe isomer shift δ is due to the shielding of the nuclear potential for core- s and valence- s electrons by the charge of the $3d$ electrons and the population of $4s$ orbitals as well. The electric monopole interaction of SC 1 is shifted to an energy of 4.8 neV relative to α -Fe. The electric monopole interaction between the nuclear charge $Ze = 26e$ of ^{57}Fe with the charge number Z and the s electron charge density $\rho_e(0) = -e|\psi(0)|_{\text{A/S}}^2$ at the nucleus is shifted by the energy E_{A} of the absorber material relative to the energy shift E_{S} of the source and leads to an effective energy shift

$$\delta = E_{\text{A}} - E_{\text{S}} = \frac{2\pi}{5} Ze^2 S(Z) \{ |\psi(0)|_{\text{A}}^2 - |\psi(0)|_{\text{S}}^2 \} \left(R_{(e)}^2 - R_{(g)}^2 \right). \quad (8.4)$$

Here, $R_{(g)}^2 = \langle r^2 \rangle_{(g)}$ and $R_{(e)}^2 = \langle r^2 \rangle_{(e)}$ are the mean square values of the radii of the ^{57}Fe nucleus of the excited state (e) with nuclear spin $\frac{3}{2}$ and groundstate (g) with nuclear spin $\frac{1}{2}$, respectively. $S(Z)$ is the dimensionless relativity factor which takes the spin-orbit coupling into account, e.g. for ^{57}Fe around $S(26) \approx 1.32$ or for neptunium $S(93) \approx 19.4$. This values varies slightly depending on the oxidation state. The coefficients of spin-orbit coupling scales with Z^4 which leads to an increase of $S(Z)$ for heavy elements.

The monopole interaction $\hat{\mathcal{H}}_{\text{M}}$ is given by a scalar $\hat{\mathcal{H}}_{\text{M}} \equiv \delta + \delta_{\text{SOD}}(T)$ as a function of the temperature. δ_{SOD} is the second-order Doppler shift and a direct consequence of the time dilation according to the relativity theory of the lattice dynamics. The γ -photon frequency ω_0 is shifted according to the transverse Doppler effect in the laboratory frame to

$$\omega = \omega_0 \frac{\sqrt{1 - v^2/c^2}}{1 - v \cos \alpha / c} \approx \omega_0 \left(1 + \frac{v}{c} \cos \alpha - \frac{v^2}{2c^2} \right) \quad (8.5)$$

where v is the velocity of the nucleus, α the angle between the movement of the nucleus and γ -photon absorption and c the speed of light. The last term assumes $v \ll c$. This yields in the Debye approximation the expression

$$\delta_{\text{SOD}} = -C \left[\Theta_{\text{D}} + 8T \left(\frac{T}{\Theta_{\text{D}}} \right)^3 \int_0^{\Theta_{\text{D}}/T} \frac{x^3 dx}{e^x - 1} \right] \quad (8.6)$$

with

$$C = \frac{9k_{\text{B}}E_{\gamma}}{16M_{\text{eff}}c^2}. \quad (8.7)$$

The temperature dependence of SC 1 yielded a Debye-temperature of $\Theta_D = 315(8)$ K. For details see appendix.

To describe the electric quadrupole interaction $\hat{\mathcal{H}}_Q$, e.g. SC 1 has a principle axis of the largest component of the EFG (electric field gradient) of $V_{zz} = -154.1(2)$ V/Å², denoted as usual,

$$|V_{zz}| \geq |V_{xx}| \geq |V_{yy}| \quad (8.8)$$

and the introduced asymmetry parameter

$$\eta = \frac{|V_{xx}| - |V_{yy}|}{|V_{zz}|} \leq 1. \quad (8.9)$$

This leads to the reduced quadrupole Hamiltonian

$$\hat{\mathcal{H}}_Q = \frac{eQV_{zz}}{4I(2I-1)} \left[3\hat{I}_z^2 - \hat{I}^2 + \frac{1}{2}\eta(\hat{I}_+^2 + \hat{I}_-^2) \right] \quad (8.10)$$

with the quadrupole moment Q and the raising and lowering spin operators $\hat{I}_+^2 = \hat{I}_x^2 + i\hat{I}_y$ and $\hat{I}_-^2 = \hat{I}_x^2 - i\hat{I}_y$. The pure quadrupole energy eigenvalues are given by

$$E_Q(m) = \frac{eQV_{zz}}{4I(2I-1)} [3m^2 - I(I+1)] \sqrt{1 + \frac{\eta^2}{3}} \quad (8.11)$$

with $I = \frac{3}{2}$. The negative sign of $V_{zz} < 0$ corresponds to an elongation of the EFG charge distribution and an excess of negative charges along the c-axis, the elongated case of the EFG ellipsoid [17]. An asymmetry parameter with $\eta = V_{zz}/(V_{xx} - V_{yy}) = 0$ was used assuming axial symmetry because of the hexagonal structure. Due to the Laplace equation the EFG tensor is traceless and yields $V_{zz} = -2V_{xx} = -2V_{yy}$.

The magnetic hyperfine or Zeeman term $\hat{\mathcal{H}}_Z$ of the Hamiltonian $\hat{\mathcal{H}}_{\text{hf}}$ is given by $\hat{\mathcal{H}}_Z = -g_N\mu_N\hat{\mathbf{I}} \cdot \hat{\mathbf{B}}$ with nuclear Landé factor g_N , the nuclear magneton $\mu_N = e\hbar/2m_p c$, the proton mass m_p and the magnetic field \mathbf{B} . Taking the scalar $|\mathbf{B}| = B$ and expressing $\hat{\mathcal{H}}_Z$ by the polar angle Θ and the azimuthal angle Φ of \mathbf{B} relative to the direction of V_{zz} yields

$$\hat{\mathcal{H}}_Z = -g_N\mu_N B \left(\frac{\hat{I}_+ e^{-i\Phi} + \hat{I}_- e^{+i\Phi}}{2} \sin \Theta + \hat{I}_z \cos \Theta \right). \quad (8.12)$$

The values of the magnetic hyperfine fields for the two Fe subspecies converged to $B_A = 70.21(1)$ T and $B_B = 65.0(2)$ T. Site A is the dominant Fe site and site B is the devote site with an area of 5.9(3)%. This site is only observed in SC 1 containing the highest Fe concentration. Two transitions

$$m = \pm \frac{1}{2} \rightarrow m = \pm \frac{1}{2} \quad (8.13)$$

with $\Delta m = 0$ are missing in the spectrum of figure 8.4. The relative line intensities $W(\beta)$, here $W(\beta)$ is the absorption probability of these lines, depend on the polar texture angle β describing the direction of the incident γ -ray with respect to the magnetic hyperfine field direction, $W(\beta) \propto \sin^2 \beta$.

	V_{zz} [$\text{V}/\text{\AA}^2$]	B_A [T]	E_A [K]	$\ln \nu_0$ [$\ln(\text{MHz})$]
SC 1	-154.1(2)	70.21(1)	552(26)	12.36(32)
SC 2	-154.2(4)	70.24(1)	563(12)	12.48(11)
SC 3	-154.0(2)	70.23(1)	581(12)	12.65(11)
SC 4	-154.0(6)	70.30(2)	552(44)	12.08(49)
Mean value	-154.0(1)	70.25(2)	570(6)	12.64(7)

Table 8.3: Hyperfine parameters V_{zz} , B_A and the Arrhenius parameters $\ln \nu_0$ and E_A for the samples SC 1-4 and the corresponding linear regression or extrapolation.

The angle Θ between the principle axis (largest component) V_{zz} of the EFG tensor and the magnetic hyperfine field was assumed to be an identical fit parameter for both sites A and B, $\Theta = 0$. For the analysis $\beta = 0$ was taken and a ratio of the spectral line intensities of 3:0:1:1:0:3. Therefore, I conclude that the magnetic hyperfine field and V_{zz} are parallel to the c -axis.

Figure 8.4 shows the measurements of SC 2-4 at T_B . It is not possible to identify Fe site B in SC 2 as well as in SC 3 and SC 4. The green line is the fit of the model using the static crystal Hamiltonian $\hat{\mathcal{H}}_{\text{hf}}$ with an isomer shift $\delta = 0.119(20)$ mm/s and a principle axis of the EFG of $V_{zz} = -154.2(4)$ $\text{V}/\text{\AA}^2$. The asymmetry parameter is assumed to be $\eta = 0$. The fit yielded a magnetic hyperfine field $B_A = 70.24(1)$ T parallel to V_{zz} of the EFG tensor and parallel to the γ -beam as well. Table 8.3 shows the obtained hyperfine parameters of SC 1-4 and the calculated mean values of \bar{V}_{zz} , \bar{B}_A , $\ln \bar{\nu}_0$ and \bar{E}_A . The hyperfine parameters are concentration-independent. The analysis to obtain the fluctuation rate parameters $\ln \bar{\nu}_0$ and \bar{E}_A of the Arrhenius temperature dependence are described below.

8.2.4 Zero field ^{57}Fe -Mössbauer spectroscopy for $T_B < T < 300$ K

Above 50 K the ^{57}Fe nucleus interacts with a fluctuating magnetic hyperfine field with $\tau \leq \tau_M$. Figure 8.5 shows representative spectra between 60 K and 200 K of SC 1 with $x = 2.5(1)\%$. In the following we will only consider Fe site A, site B is neglected in this analysis. The fit represents a Blume dynamic line shape model in the presence of quadrupole hyperfine interactions for two states, described by the absorption cross section

$$\sigma = -\frac{\sigma_a \Gamma_0}{2} \text{Im} \sum_{\alpha} \text{Sp} \left(\hat{V}_{\alpha} \langle W | \hat{\mathbf{A}}^{-1}(\omega, \Theta) | 1 \rangle \hat{V}_{\alpha}^+ \right). \quad (8.14)$$

Here, \hat{V}_{α} is the operator of hyperfine interactions of the γ -beam with polarization α and the nucleus, σ_a the effective absorber thickness and $\langle W |$ and $| 1 \rangle$ as described by Chuev and therein [165]. The superoperator

$$\hat{\mathbf{A}}(\omega, \Theta) = \tilde{\omega} + i\Gamma_0/2 - \hat{\mathbf{L}}(\Theta) + i\hat{\mathbf{P}}. \quad (8.15)$$

is defined by the Liouville operator of hyperfine interactions $\hat{\mathbf{L}}(\Theta)$, the resonance transition energy E_0 is given by the corresponding frequency $\tilde{\omega} = \omega - E_0/\hbar$, Γ_0 is the width of the excited nuclear level and $\hat{\mathbf{P}}$ the matrix of hyperfine transitions [166, 1, 165, 167].

The initial conditions of the analysis are identical to the static case at 2 K. A two level relaxation

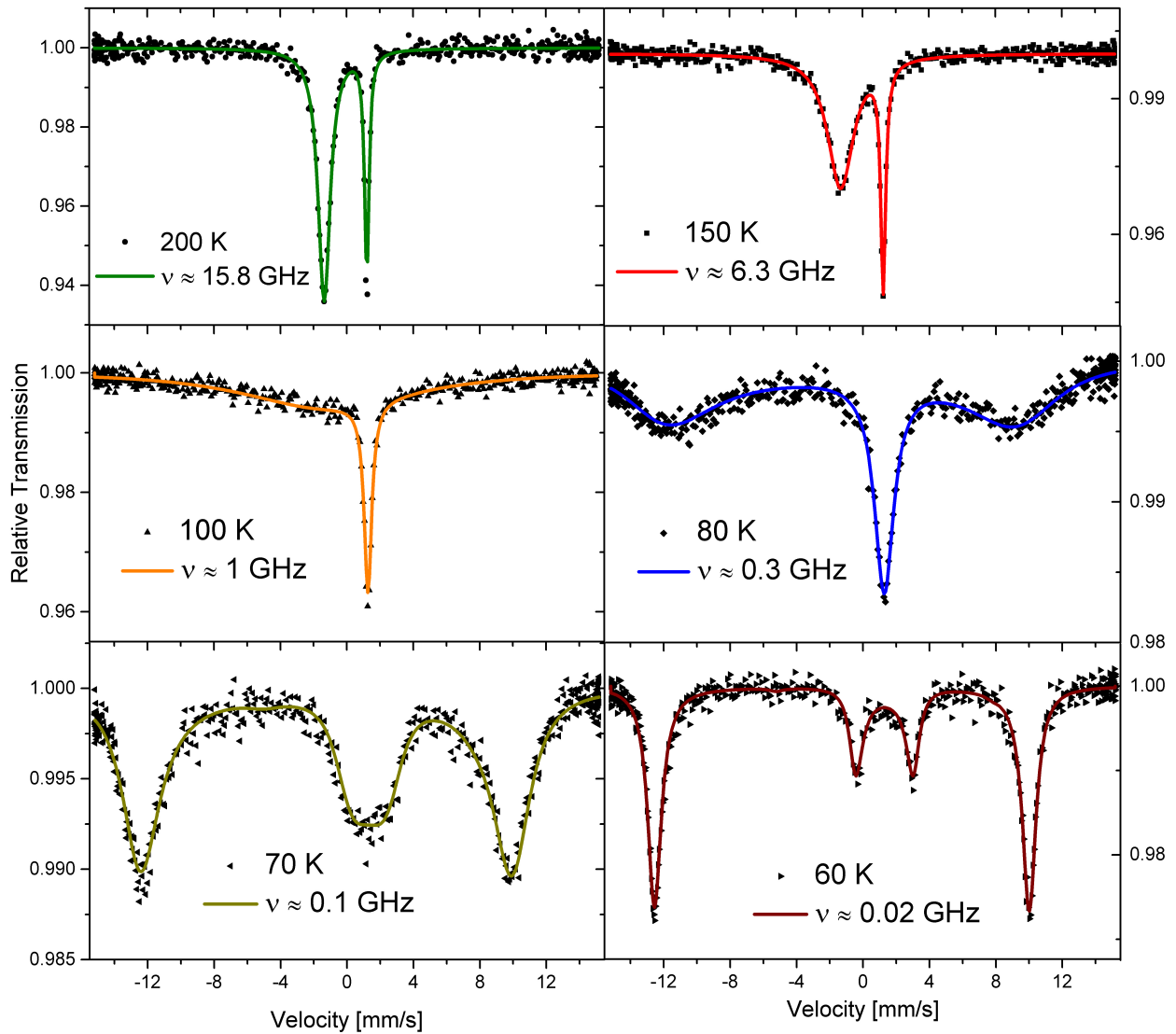


Figure 8.5: Spectra of SC 1, $\text{Li}_2(\text{Li}_{1-x}\text{Fe}_x)\text{N}$ with $x = 2.5(1)\%$. The lines show a two level Blume model fluctuation spectrum analysis. The magnetic hyperfine field fluctuates between $+B_A$ and $-B_A$ with the frequency ν . B_A in this model is assumed to be parallel to V_{zz} and to the γ -beam.

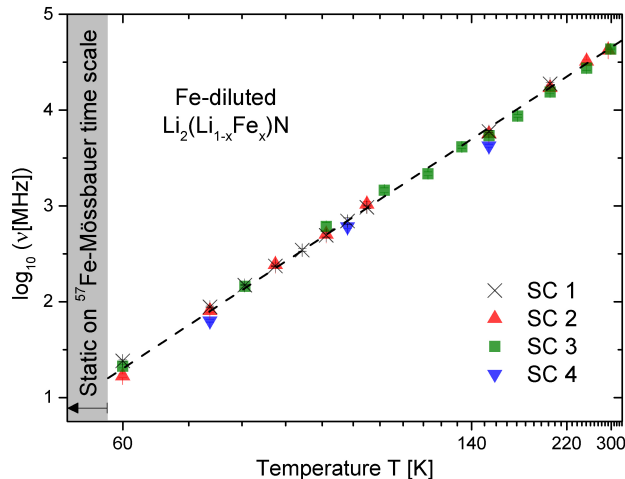


Figure 8.6: Logarithmic fluctuation frequencies $\log_{10} \nu$ of the Fe site A of SC 1-4 as a function of temperature.

model was used taking into account an electronic spin reversal process. The magnetic hyperfine field fluctuates with the fluctuation frequency ν between the two values $+B_A$ and $-B_A$. At 100 K the magnetic hyperfine structure collapsed into a singlet, see figure 8.5. Above 60 K, the spectral lines begin to broaden due to the fluctuations. With increasing ν at 70 K the two internal lines collapse first yielding a singlet at 100 K. At 150 K and above, the left resonance line of the quadrupole doublet, which is expected to appear in the fast relaxation limit $\nu \rightarrow \infty$, results from the collapse of the external lines [164]. The Arrhenius parameter E_A and $\ln \nu_0$ are obtained by an Arrhenius analysis

$$\ln \nu = \ln \nu_0 - \frac{E_A}{k_B} \left(\frac{1}{T} \right) \quad (8.16)$$

of the extracted fluctuation frequencies $\ln \nu$ of SC 1-4. In this analysis the values of ν for $T < 50$ K are not considered since these values reflect the lower bound of the fluctuation rate which the Mössbauer spectra analysis can resolve. This yielded a thermal activation barrier e.g. of $E_A = 552(26)$ K and $\ln \nu_0 = 12.36(32)$ for SC 1. The fluctuation frequency ν at the Fe site A is concentration-independent of SC 1-4. Table 8.3 shows the Arrhenius plot parameters for SC 1-4. Figure 8.6 shows the Arrhenius plot (reciprocal T -scaling) of the extracted fluctuation frequencies for SC 1-4 in MHz. For consistency with the transverse magnetic field part \log_{10} is used:

$$\log_{10} \nu = \log_{10} \nu_0 - \frac{E_A}{k_B} \left(\frac{1}{T} \right) \log_{10} e \quad (8.17)$$

with $\log_{10} e \approx 0.43$. The fluctuation frequency is concentration-independent as reflected by the parameter E_B and $\ln \nu_0$ in table 8.3.

8.2.5 ^{57}Fe -Mössbauer spectroscopy in transverse magnetic fields B_T

In the following, I present the results of systematic Mössbauer spectroscopy experiments under applied transverse magnet field B_T . These experiments were performed on sample SC 1. For eight

temperatures between 30 K and 247 K a magnetic field up to 5 T was applied perpendicular to the normal vector of the sample plate and therefore to the crystallographic c -axis and perpendicular to the γ -beam, see discussion. Therefore, the field was applied perpendicular to the quantization axis of the Fe spins which is identical to the low temperature orientation axis of the magnetic hyperfine field at the Fe nucleus. In this geometry an increasing field B_T leads to an increasing mixture of the S_z -eigenstates of the electronic spins and an increasing fluctuation rate of the magnetic hyperfine field is expected.

Figure 8.7 shows four typical Mössbauer spectra in different transverse magnetic fields (TF) up to 5 T. The experimental data clearly reveal an increase of the fluctuation frequency ν with increasing field strength. The temperature and field range for these experiments was chosen such that the slowly fluctuating magnetic hyperfine field of around 70 T can be regarded as the dominant hyperfine interaction with the ^{57}Fe nuclei and the Blume model of axial fluctuations of the magnetic hyperfine field described in the former subsection can be used for the quantitative analysis (solid lines in figure 8.7). For higher fields the vector sum of the external field and the internal magnetic hyperfine field must be considered.

At 70 K ν increased in 1 T by a factor 2 and in 5 T by a factor 8. This documents a strong transverse field sensitivity. The dependence of the fluctuation frequency ν on the transverse magnetic field B_T and temperature T is investigated in detail for SC 1. Figure 8.8 (a) shows the logarithmic frequency \log_{10} as a function of the inverse temperature $1/T$ for different transverse external fields and figure 8.8 (b) shows the logarithm of ν as a function of the transverse magnetic field for different temperatures. The data can be described with the phenomenological model function

$$\nu(T, B_T) = \nu_0 e^{-\frac{\Delta_1}{T}} + \xi B_T e^{-\frac{\Delta_2}{T}}. \quad (8.18)$$

The first term describes the field-independent temperature-activated Arrhenius-contribution observed in the zero field experiments using $\bar{\nu}_0$ and $\Delta_1 = \bar{E}_A/k_B$. The second term describes the increase of ν due to the transverse field scaling linear with B_T . In a global fit $\bar{\nu}_0$, ξ and Δ_i are constant parameters. The result is $\xi = 2332(995)$ MHz/T and $\Delta_2 = 251(20)$ K.

In figure 8.8 (a) at low temperatures $1/T > 0.01 \text{ K}^{-1}$ a pronounced field-induced non-linear deviation from the zero-field Arrhenius line is observed. For high temperatures $1/T < 0.01 \text{ K}^{-1}$ the data converge to the zero-field Arrhenius line, i.e. the temperature-induced fluctuations are dominant. This is also seen in figure 8.8 (b): the change of ν with increasing B_T is enhanced by lowering the temperature. Note that for the lowest temperatures (30 K and 40 K) the determined fluctuations rates are close to the lower bound of the frequency window of the Mössbauer method.

8.2.6 Mössbauer spectroscopy in longitudinal magnetic fields B_L

Mössbauer spectroscopy measurements were performed with applied longitudinal magnetic fields (LF) at 100 K up to 3 T with the γ -beam and parallel to the applied field parallel to the c -axis of the crystal. Figure 8.9 shows the ^{57}Fe -Mössbauer measurements at 100 K up to 2 T longitudinal magnetic field (LF). The measurements at 0.5 T and 1 T show an increase of the linewidth of the central absorption line compared to the ZF spectrum. The spectrum at 2 T clearly reveals a splitting

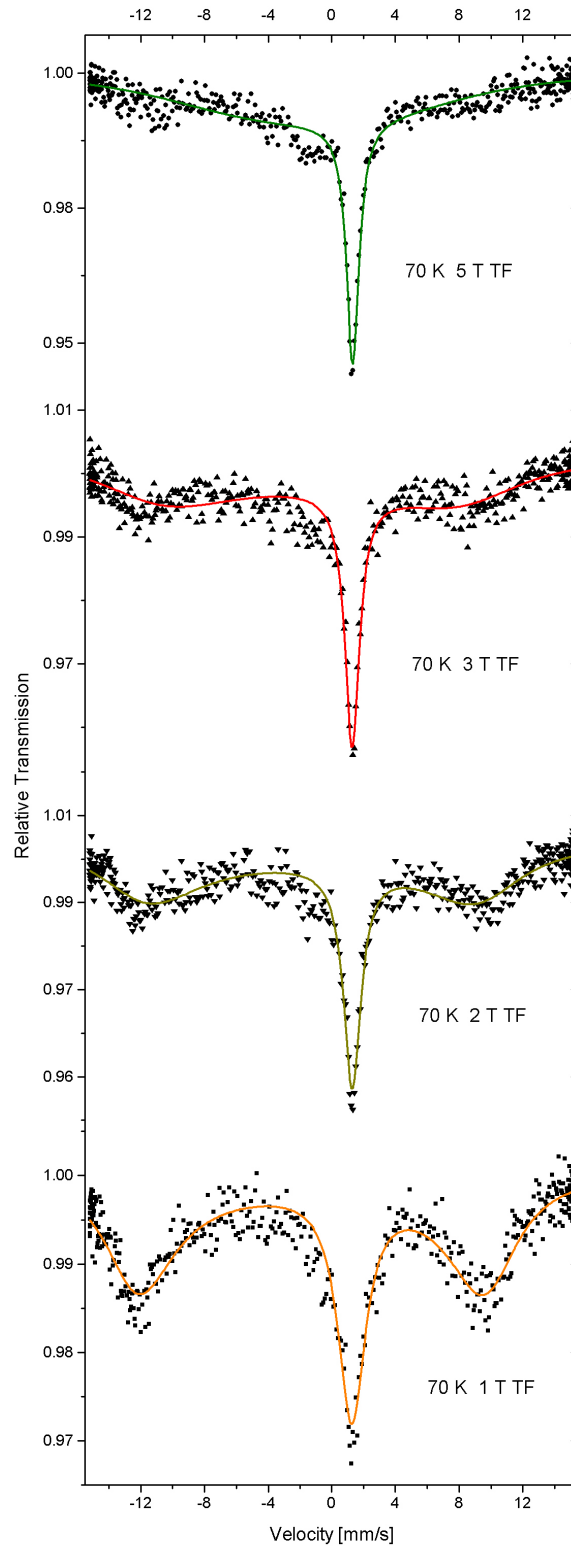
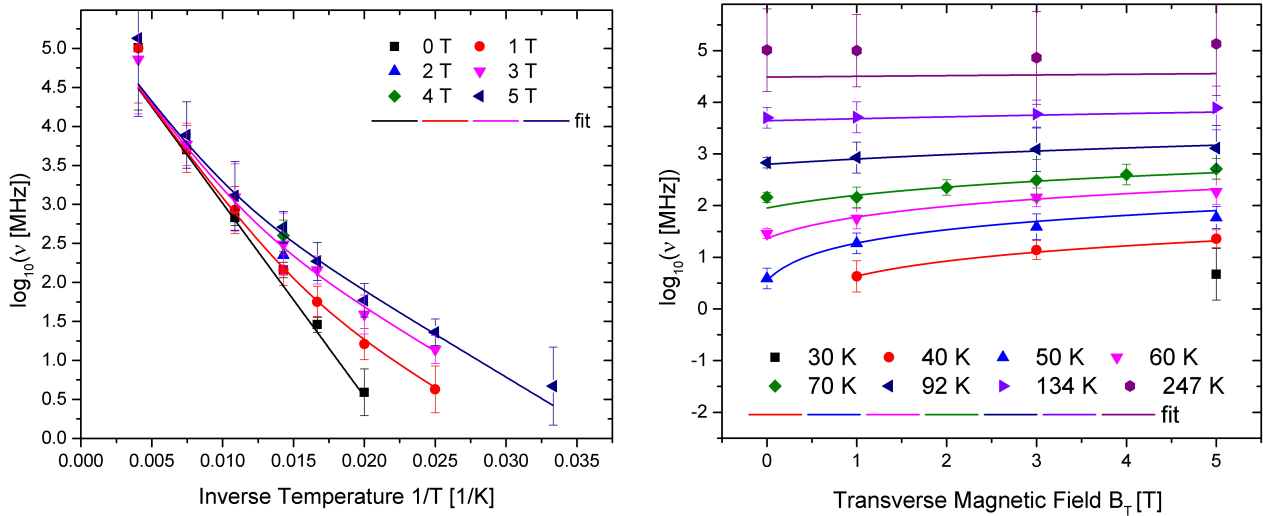


Figure 8.7: Mössbauer spectra of SC 1 in various transverse magnetic fields B_T at 70 K. The corresponding ZF measurement can be found in figure 8.5.



(a) Frequency dependence of the inverse temperature of $\text{Li}_2(\text{Li}_{1-x}\text{Fe}_x)\text{N}$ with $x = 2.5(1)\%$, SC 1, in different transverse magnetic fields B_T . The solid-line fit function is described in the text.

(b) Logarithmic frequency as a function of the transverse magnetic field for different temperatures. The solid-line fit function is described in the text.

Figure 8.8: Plots of the transverse magnetic field study of SC 1 as already presented in Ref. [163].

into two lines corresponding to two different fluctuation rates. The analysis model to describe the LF spectra is the Blume two-state spin reversal fluctuation model between the states with hyperfine fields $B_h = \bar{B}_A + B_L$ and $B_h = -\bar{B}_A + B_L$. Since the Zeeman interaction will lift the degeneracy between the "spin up" and "spin down" transitions two different fluctuation frequencies ν_{up} describing the frequency to flip the spin into the longitudinal magnetic field direction and ν_{down} to flip it against the applied field direction are considered. The population of the two states is assumed to be equal as shown by the equal line intensities at 2 T. A small static external field at the ^{57}Co -source position caused by the Helmholtz magnet leads to a slight increase of the linewidth (0.24(2) mm/s at 2 T). Figure 8.10 shows the deduced frequencies $\log_{10} \nu_{\text{up}}$ and $\log_{10} \nu_{\text{down}}$ as a function of the longitudinal magnetic field B_L . The observed change of the fluctuation rate is one order of magnitude smaller than in the case of applied transverse fields.

The data show a linear dependence of $\log_{10} \nu_{\text{up}}$ and $\log_{10} \nu_{\text{down}}$ as a function of B_L up to 3 T. An asymmetry of the observed positive and negative frequency change, i.e. a stronger increase of $\nu_{\text{up}}(B_L)$ than decrease of $\nu_{\text{down}}(B_L)$, is due to a general enhancement of the mixing in longitudinal fields, see next subsection. Even though the Zeeman-induced reduction of the energy differences for the allowed transition $J_z = -7/2 \rightarrow J_z = 5/2$ and increase of the energy difference for $J_z = 7/2 \rightarrow J_z = -5/2$ (see next section) are equal, the reduction leads to a stronger increase of the fluctuation rate for the former case than the decrease of the fluctuation rate for the latter. A detailed quantitative analysis is in progress.

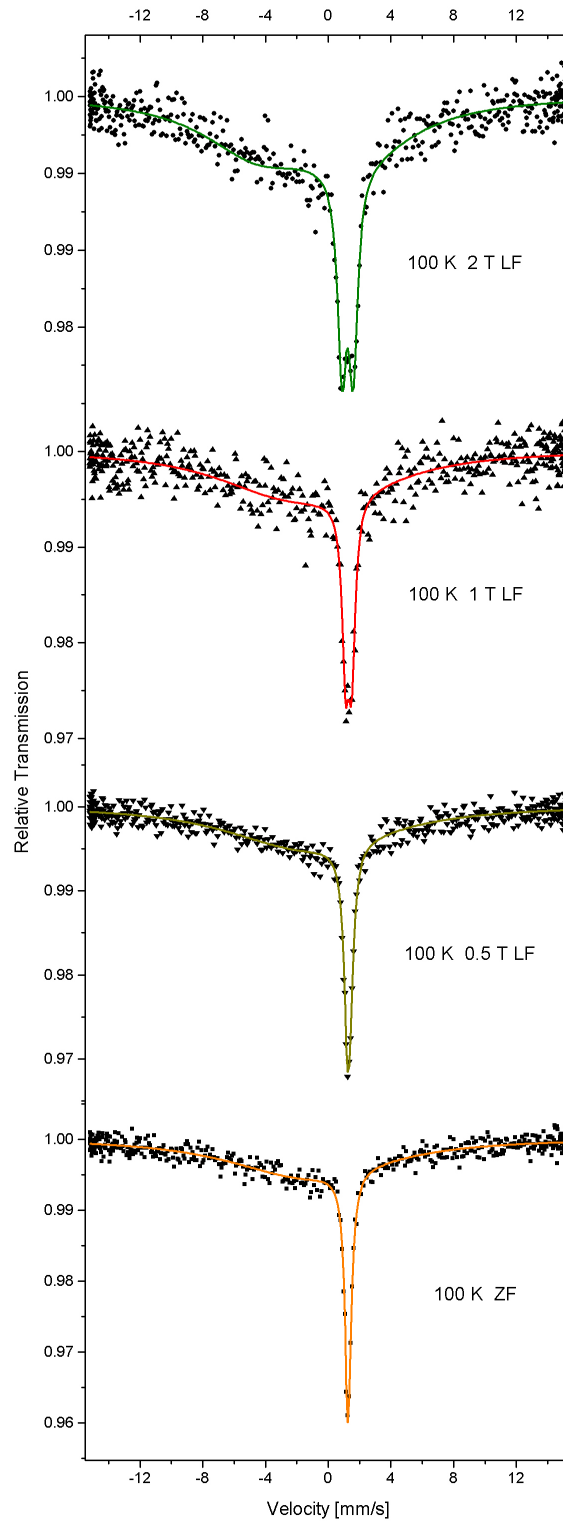


Figure 8.9: Comparison of the Mössbauer measurements of SC 1 at 100 K in ZF and in applied longitudinal magnetic fields B_L of 0.5 T, 1 T and 2 T.

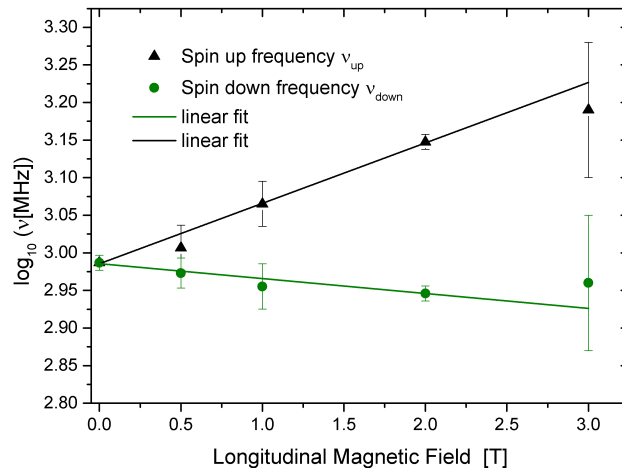


Figure 8.10: The fluctuation frequencies ν_{up} and ν_{down} as a function of the longitudinal magnetic field B_L . The solid lines are the linear regressions.

8.2.7 Single-ion spin Hamiltonian calculation of spin dynamics

This subsection describes a calculation performed and mainly formulated by A. A. Zvyagin (*B.I. Verkin Institute for Low Temperature Physics, Ukraine*). This text is adopted from a manuscript by S. A. Bräuninger *et al.* [140]. It shows that a magnetic anisotropy term D of the order of a few Kelvin can cause a much stronger effective energy barrier of the order of a few hundred Kelvin which is two orders of magnitude higher.

The striking result of the temperature and transverse magnetic field dependent Mössbauer spectroscopy is that the activation energy scale for thermal fluctuations of the individual electronic Fe spins of $E_A \approx 570$ K is two orders of magnitude larger than the Zeeman energy scale $g_p \mu_B B_x S_x \sim 5$ K of transverse magnetic fields inducing similar changes of the fluctuation rate. Moreover it is important to note, that the low temperature longitudinal magnetic field magnetization data of this system presented in figure 8.3, which are consistent with earlier reports by A. Jesche *et al.* [157], reveal an energy scale for longitudinal magnetic field induced system changes of the orders of 1 K to 5 K from the appearance of level crossing induced magnetization steps at $B_z = 0$ and 3 T. Therefore, for a qualitative understanding of the field and temperature dependence of the spin fluctuation frequency ν we present a calculation of the spin dynamics using a single-ion spin Hamiltonian model. We demonstrate that an axial anisotropy of energy scale $D \ll 570$ K consistent with the Zeeman response of the system can indeed give rise to an effectively two order of magnitude larger energy barrier for thermal fluctuations.

We consider the single-ion properties of Fe ions in $\text{Li}_2(\text{Li}_{1-x}\text{Fe}_x)\text{N}$. The crystal $\alpha\text{-Li}_3\text{N}$ has hexagonal symmetry. This is why the Fe impurity, which substitutes the Li ion in $\text{Li}_2(\text{Li}_{1-x}\text{Fe}_x)\text{N}$, is affected by the crystalline electric field of ligands with a hexagonal symmetry. Together with the spin-orbit interaction, the crystalline electric field yields the single-ion magnetic anisotropy for the $3d$ electronic state of such ions as

$$\hat{\mathcal{H}}_{\text{an}} = B_2^0 O_2^2 + B_4^0 O_4^0 + B_6^0 O_6^0 + B_6^6 O_6^6, \quad (8.19)$$

where O_n^m are Stevens' operators, and B_n^m are the parameters describing the magnetic anisotropy [168, 169, 170].

The ions of Fe in Li_3N can be either Fe^+ (which, according to Hund's rules have the lowest multiplet with $S = 3/2$, $L = 3$ and $J = 9/2$), or Fe^{2+} (it has $S = 2$, $L = 2$, and $J = 4$). Most of known facts support the Fe^+ state, see discussion. For transition metals it is commonly accepted that the Russel-Sounders scheme works well, and one can deal with S and L for electrons belonging to the $3d$ shell. Usually, L is quenched in transition metal compounds due to symmetry reasons. For the Fe impurity in $\alpha\text{-Li}_3\text{N}$, however, we can apply the arguments, used in Refs. [171] leading to the ground state $|M_L = -2, M_S = -3/2\rangle$. The arguments, namely, that the strong uniaxial anisotropy of the hexagonal lattice (due to O_2^0 , O_4^0 and O_6^0 operators, which distinguish only $z \parallel c$ axis) lifts the degeneracy, and only $L = 2$ states are coupled with $S = 3/2$ for Fe^+ in $\alpha\text{-Li}_3\text{N}$. It yields the effective total moment $J_{\text{eff}} = 7/2$. The splitting of the Mössbauer lines (see figure 8.9) also confirms that assumption: The splitting is too large for $S = 3/2$ or $S = 2$. In what follows we drop the index "eff" for simplicity. The most important part of the Hamiltonian \mathcal{H}_{an} is the first term, which can be written as $\mathcal{H}_{an} \approx -DJ_z^2$ (up to the operator-independent part), where $D = B_2^0$ is the parameter of the magnetic anisotropy. We can conclude from the magnetization experiments, that we deal with "easy-axis" magnetic anisotropy, $D > 0$. Consider the Hamiltonian of the Fe ion in the external magnetic field $B_z = B_L$, directed along the "easy" axis, namely $\mathcal{H}_0 = -DJ_z^2 - g_l\mu_B B_z J_z$, where μ_B is the Bohr magneton, and g_l is the z -component of the effective g -tensor. The levels of that Hamiltonian cross each other at several values of B_z , depending on the spin value. The only Stevens' operator from \mathcal{H}_{an} , which does not commute with J_z , and, hence, which can mix states with different values of J_z and lift the degeneracies at the crossover points, is $O_6^6 \equiv (J_+^6 - J_-^6)$, where $J_{\pm} = J_x \pm iJ_y$. Such a mixing is the crucial point for the quantum tunneling [172]. Note that according to standard quantum mechanics in the basis with diagonal action of the pure spin operator S_z the eigenstates of O_6^6 for $S = 3/2$ and $S = 2$ are zero. The operator O_6^6 corresponds to the processes with $\Delta J_z = 6$, hence connecting the states $J_z = -7/2$ with $J_z = 5/2$, and $J_z = -5/2$ with $J_z = 7/2$.

Unfortunately, explicit results for the relaxation rate due to quantum tunneling cannot be realized for O_6^6 . Therefore, to mimic the action of the operator O_6^6 we consider a more simplified perturbation related to the transverse magnetic field, for example, $J_x \equiv (J_+ + J_-)/2$. Such a term also can mix the states with different J_z , however with one difference from the O_6^6 processes, namely $\Delta J_z = 1$. Therefore, the substitution of J^x instead of O_6^6 , while giving the opportunity to obtain some qualitative agreement with the results of our experiments, still cannot give a quantitative description of $\text{Li}_2(\text{Li}_{1-x}\text{Fe}_x)\text{N}$.

Summarizing, we consider, an effective Hamiltonian, which permits quantum tunneling in Fe-diluted $\text{Li}_2(\text{Li}_{1-x}\text{Fe}_x)\text{N}$. It has the form

$$\hat{\mathcal{H}} = -DJ_z^2 - g_t\mu_B B_x J_x - g_l\mu_B B_z J_z, \quad (8.20)$$

where g_t is the value of the effective g -tensor in the plane, perpendicular to the easy axis. Note that B_x can include not only the effective field, introduced to mimic the action of the O_6^6 , but also the real transverse to the axis z external magnetic field. According to V. Ulyanov *et al.* [172] the

lowest $(2J+1)$ eigenvalues and eigenfunctions of that Hamiltonian coincide with those of the discrete spectrum of a quantum particle in the effective potential

$$U = \frac{DB^2}{4} \left[\sinh(x) - \frac{C}{B} \right]^2 - \frac{DB}{2}(2J+1) \cosh(x), \quad (8.21)$$

where $B = g_t \mu_B B_x / D$ and $C = g_l \mu_B B_z / D$. The spin quantum tunneling in that approach is totally equivalent to the tunneling of a quantum particle between the minima of the potential U . The tunneling rate can be calculated using the Euclidean version of dynamical equations, using dynamics of instantons of the Euclidean action, i.e., solitons, connecting two minima of the potential U with each other [173]. Consider the range of the field values, limited by the region $[B^{2/3} + C^{2/3}]^{3/2} < 2J+1$, in which the potential U has two minima (the lowest minimum is related to the stable state, and the highest one to the metastable state). The energy barrier between the minima is finite, hence there exists a probability for the metastable state to decay due to the quantum tunneling. It is possible to calculate the values of the relaxation rate due to the quantum tunneling [172], expanding the expression for U near the position of the metastable minimum. The decay rate is determined by the analytic continuation of the energy value to the complex plane. Analyzing the results obtained this way, we conclude that two regimes, $T_0 \leq T \leq T_1$, and $T \geq T_1$, where $T_0 = D\sqrt{a}/\pi k_B$, and $T_1 = 2D\sqrt{a}/\pi k_B$ can be related to the conditions of our experiments with $\text{Li}_2(\text{Li}_{1-x}\text{Fe}_x)\text{N}$. Here and below we use the notations

$$\begin{aligned} a &= \frac{3^{1/2}}{2^{3/2}} BC^{1/3} (2J+1)^{2/3} \delta^{1/2}, \\ b &= \frac{1}{12} B^{4/3} C^{1/3} (2J+1)^{1/3}, \\ \delta &= 1 - \frac{(B^{2/3} + C^{2/3})^{3/2}}{2J+1}. \end{aligned} \quad (8.22)$$

For $T_0 \leq T \leq T_1$, i.e., at low temperatures for our experiment, the relaxation rate can be approximated as, according to V. Ulyanov *et al.* [172],

$$\hbar\gamma_1 = D \frac{\sqrt{a} \sinh(D\sqrt{a}/k_B T)}{\pi \sin(D\sqrt{a}/k_B T)} \exp[-4Da^3/27b^2 k_B T]. \quad (8.23)$$

On the other hand, for higher temperatures $T \geq T_1$ the relaxation rate is

$$\hbar\gamma_2 = D \frac{\sqrt{a}}{\pi} \exp[-4Da^3/27b^2 k_B T], \quad (8.24)$$

see [172]. This higher temperature behavior of the relaxation rate caused by the quantum spin tunneling is similar to the Orbach relaxation as discussed by S. Mørup *et al.* [17], i.e., it has the Arrhenius form. Notice that the “true” quantum spin tunneling-induced relaxation rate exists at $T = 0$ [172].

Our estimates imply that the most essential regime for our experiments on $\text{Li}_2(\text{Li}_{1-x}\text{Fe}_x)\text{N}$ is the region with $T \geq T_1$. We see that the relaxation rate γ_2 follows an Arrhenius law in the temperature

dependence, $\gamma_2 = \nu_0 \exp(-E_A/k_B T)$, reminiscent of the Mössbauer studies of $\text{Li}_2(\text{Li}_{1-x}\text{Fe}_x)\text{N}$, with the prefactor ν_0 and the activation energy E_A determined as

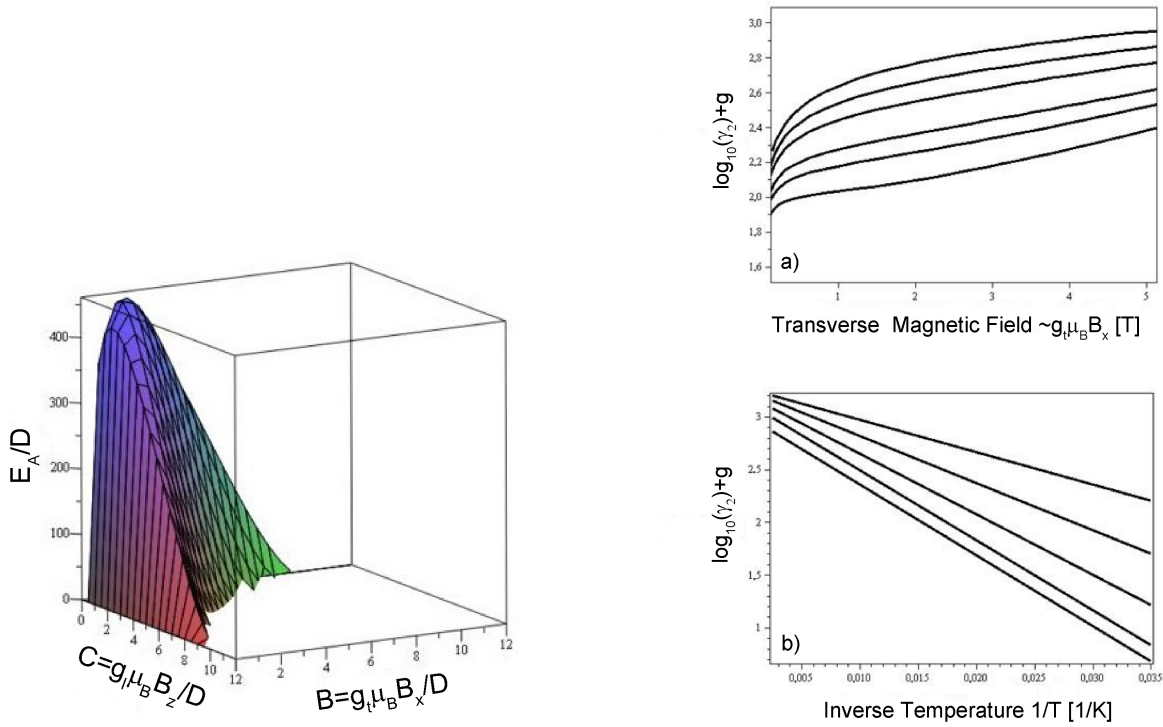
$$\begin{aligned}\nu_0 &= \frac{D\sqrt{a}}{\pi\hbar} \sim B_x^{1/2} B_z^{1/6} \delta^{1/4}, \\ E_A &= \frac{4Da^3}{27b^2} \sim (B_x B_z)^{1/3} \delta^{3/2}.\end{aligned}\quad (8.25)$$

Note that we cannot use the limits $B_x \rightarrow 0$, and $B_z \rightarrow 0$ in the expression for the relaxation rate caused by the spin tunneling, because the relaxation is absent there: Without B_z there is no crossover, and without B_x there is no lifting of the degeneracy of crossover points. However, we can evaluate the field dependence of the activation energy, not taking into account the limiting cases $B_x \rightarrow 0$ and $B_z \rightarrow 0$. A weak effective tilted magnetic field can be originated, e.g., from the long-range magnetic dipole-dipole interaction in the mean field approximation. We also suppose that the region of applicability of the results can be expanded to all $\delta < 1$, which implies the small difference between the potential U and its expansion near the position of the metastable state (that difference produces higher-order quantum corrections). The result is shown in figure 8.11 (a) for $J = 7/2$. We see that for very small (however finite, see above) values of the components of the external magnetic field the activation energy is much larger than the value of the magnetic anisotropy D . It explains the observation of the giant activation energy for the relaxation rate in our Mössbauer studies of $\text{Li}_2(\text{Li}_{1-x}\text{Fe}_x)\text{N}$. Also we see that the application of the external field of order of $(2J + 1)D$ reduces drastically the value of the activation energy. It is also similar to observed effect of the external transverse magnetic field on the relaxation rate in Mössbauer studies of $\text{Li}_2(\text{Li}_{1-x}\text{Fe}_x)\text{N}$.

Now we can compare the transverse field dependence of the relaxation rate, extracted from Mössbauer experiments in $\text{Li}_2(\text{Li}_{1-x}\text{Fe}_x)\text{N}$ with the calculated one. In figure 8.11 (b) a) the logarithm of the relaxation rate γ_2 is plotted as a function of the applied transverse field B_x at $g\mu_B B_z = 0.001$ for $J = 7/2$ and several values of the temperature. To have better agreement with experiment we had to add the constant $g = 5.5$ to $\ln(\gamma_2)$, which implies additional source of relaxation, which is temperature- and magnetic field-independent. In figure 8.11 (b) b) the logarithm of the relaxation rate γ_2 is plotted as a function of the inverse temperature, $1/T$ for several values of the transverse external magnetic field B_x .

We see that the general tendency is well described by our simplified theory, while there is no quantitative agreement. Nevertheless, we conclude that the single-ion theory, based on the spin properties of Fe impurities, which at low energies produce quantum spin tunneling, well reproduce the most dramatic feature of the dynamical experiments in $\text{Li}_2(\text{Li}_{1-x}\text{Fe}_x)\text{N}$: the giant value of the activation energy in the Arrhenius law for the temperature dependence of the relaxation rate, and much smaller values of the external magnetic field, which drastically change that relaxation rate. We think that it is one of the most spectacular manifestations of the macroscopic quantum spin tunneling observed in solid-state based single-spin magnet $\text{Li}_2(\text{Li}_{1-x}\text{Fe}_x)\text{N}$. Our approach can qualitatively explain the observed asymmetry in the relaxation processes in the longitudinal field.

For $B_z = 0$ the relaxation processes with $\Delta J_z = \pm 6$ are equivalent. However, a finite longitudinal field $B_z = B_L$ removes the degeneracy of the $J_z = \pm M_z$ energy levels. The values of the energy



(a) The dependence of the activation energy E_A/D for the relaxation rate γ_2 on the longitudinal $\sim B_z/D$ with respect to D and transverse $\sim B_x/D$.

(b) a) The dependence of the logarithm of the relaxation rate γ_2 on the transverse field B_x for several values of T . From top to bottom: $T = 247$ K, $T = 134$ K, $T = 92$ K, $T = 60$ K, $T = 50$ K and $T = 40$ K. b) The dependence of the logarithm of the relaxation rate γ_2 on the inverse temperature $1/T$ for several values of B_x . From bottom to top: $B_x = 1$ T, $B_x = 2$ T, $B_x = 3$ T, $B_x = 4$ T, $B_x = 5$ T.

Figure 8.11: Plots obtained by the discussed Hamiltonian to describe our experimentally observed data qualitatively.

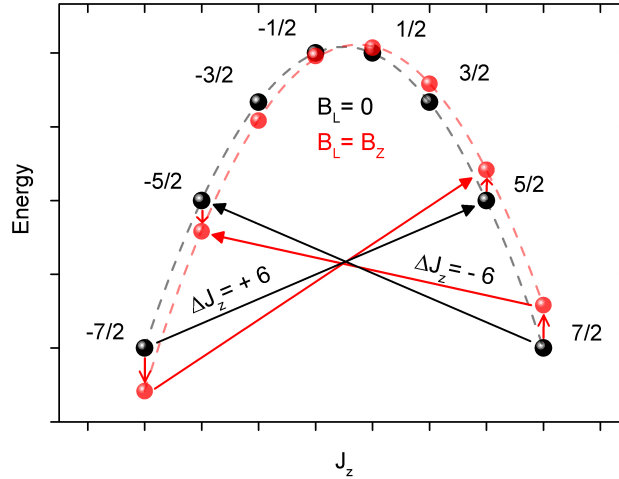


Figure 8.12: Possible schematic illustration of the transitions between $J_z = -7/2$ and $J_z = 5/2$ and $-7/2$ to $+5/2$, respectively. The energy levels $-DM_J^2$ are shifted in LF (red points) leading to different transition energies according to the Zeeman energy $\sim M_J B_Z$.

differences between the states $J_z = -7/2$ and $J_z = 5/2$, and between the states $J_z = -5/2$ and $J_z = 7/2$ become non-equal leading to a symmetric splitting (Zeeman splitting). The included higher order terms causes even in longitudinal fields a mixing and therefore the increase of the fluctuation rate ν_{up} for the $+7/2$ to $-5/2$ transition which is larger than the decrease of ν_{down} for the $-7/2$ to $+5/2$ transition as observed experimentally (see figures 8.10 (b) and 8.12). The result is an effective asymmetric shift of the two Zeeman branches.

8.3 Discussion

8.3.1 Magnetization steps in the hysteresis loop

The pronounced magnetization steps observed at $B_z = 0$ and ± 3 T at 2 K, shown in figure 8.3, are consistent with magnetization steps observed by A. Jesche et al. [157] and can be associated with a quantum tunneling of the magnetization at avoided level crossing field values. Quantitatively, the spin-flip probability of a resonance crossing is given by the Landau-Zener-Stückelberg formula

$$\delta P(\Delta_{mm'}, v_{mm'}) = 1 - \exp\left(-\frac{\pi \Delta_{mm'}^2}{2\hbar v_{mm'}}\right). \quad (8.26)$$

Here, $\Delta_{mm'} = 2\hbar|\omega_T^{(mm')}|$ depends on the resonance and

$$v_{mm'} = g\mu_B(m - m')\frac{dH_z}{dt} \quad (8.27)$$

is mainly given by the sweep rate dH_z/dt with the magnetic field H_z parallel to the quantization axis as it is done for SC 1, m and m' are the corresponding magnetic quantum numbers. $\delta P(\Delta_{mm'}, v_{mm'})$ interpolates between the adiabatic case, $\delta P = 0$ for small dH_z/dt and the fast sweeping case. In Fe_8 ,

this relation is confirmed for $dH_z/dt > 0.001$ T/s showing a ground state doublet with $m = -m' = 10$ [174].

8.3.2 Mössbauer sites and sample homogeneity

Two Fe sites A and B are observed in the low temperature Mössbauer spectra of sample SC 1. The main site A is associated with monomer Fe sites without relevant magnetic exchange with other Fe ions since it is observed also in the samples SC 2-4 which contain an up to one order of magnitude lower Fe concentration x . Site B is not observed in SC 2-4. We associate site B with a nearest neighbor in-plane or out-of-plane Fe-dimer site. The magnetic hyperfine field for the two Fe subspecies is determined to $B_A = 70.21(1)$ T and $B_B = 65.0(2)$ T at 2 K. These values are in agreement with Refs. [158, 159, 141]. Klatyk, Ksenofontov *et al.* have performed a powder study on $\text{Li}_2(\text{Li}_{1-x}\text{Fe}_x)\text{N}$ for $x > 0.15$ proposing ferromagnetic ordering for $T < 65$ K. Indications for a reentrant spin-glass transition is found by a.c. susceptibility which could reflect competitive interaction or diluted random moments in addition to the proposed ferromagnetic behavior [158].

The temperature-dependence of the Mössbauer spectrum shown in figure 8.5 is consistent with the expected behavior of a single atomic magnet (SAM). The observed spin fluctuations are consistently described by a thermal activation crossover rather than by a cooperative long-range order transition. However, this does not exclude by itself that Fe site A arises from small cluster-like SMM units like Fe_2 clusters in the Li_3N matrix with ferromagnetic interaction between the Fe ions. The deduced hyperfine parameters are within error bars identical for samples SC 1-4. The spin dynamics described by the fluctuation frequency $\nu(T)$, ν_0 and E_A are concentration-independent for Fe site A of SC 1-4. The spin dynamics depends strongly on the cluster size of a SMM. The size and spin flip probability of a possible ferromagnetic cluster should change with the doping concentration x . This would lead to a change of the frequency ν because of a change of the magnetic energy barrier. The invariance of ν as a function of x proves well isolated Fe sites like in a SAM. In the case of cluster-like SMMs one would expect that Fe site A shows a broad distribution of hyperfine parameters and frequencies because of different random clusters sizes and magnetic energy barriers.

A combinatorial expression to calculate the probability for n Li ions among six neighbors in the [001] plane for the Fe concentration x yields

$$W_n = 6![n!(6-n)!]^{-1}(1-x)^n x^{6-n} \approx 13\% \quad (8.28)$$

for $n=5$, i.e. an in-plane Fe-dimer [158]. This value is twice as large as the observed value. The area contribution of site B is overestimated in this statistical treatment in which every kind of Coulomb repulsion is neglected. Either due to Coulomb repulsion a more homogenous mononuclear SAM is preferred or the observed site B belongs to an out-of-plane Fe-N-Fe dimer configuration. Interestingly, the total contribution of the Fe-N-Fe in a binomial distribution is supposed to be $\approx 4.2\%$ which is closer to the experimentally determined value of $5.9(3)\%$ of Fe site B. A systematic Mössbauer study on a series of $\text{Li}_2(\text{Li}_{1-x}\text{Fe}_x)\text{N}$ with larger x is needed to identify the nearest neighbor Fe-cluster configurations in this system. However, this is beyond the scope of this work.

Compound	δ [mm/s]	ΔE_Q [mm/s]	B [T]
$[\text{Fe}(\text{C}(\text{SiMe}_3)_3)_2]^{1-}$	0.402(1)	-2.555(2)	63.68(2)
$[\text{Fe}(\text{C}(\text{SiMe}_3)_3)_2]$	0.460(3)	-1.275(5)	150.7(1)
$\text{Li}_2(\text{Li}_{1-x}\text{Fe}_x)\text{N}$ ($x \ll 1$)	0.100(2)	-2.572(2)	70.25(2)

Table 8.4: Comparison of selected Mössbauer parameters around 4 K assuming $\eta = 0$ with the results taken from Zadrozny *et al.* [175].

8.3.3 Oxidation and spin state of Fe ions in $\text{Li}_2(\text{Li}_{1-x}\text{Fe}_x)\text{N}$

The observed isomer shift value around 0.10 mm/s is unconventional for Fe oxidation states of Fe^{1+} $S = \frac{3}{2}$ or Fe^{2+} $S = 2$. It is observed due to the highly linear electronic structure of Fe in $\text{Li}_2(\text{Li}_{1-x}\text{Fe}_x)\text{N}$. Because of its magnetic behavior a Fe^{2+} low spin state $S = 0$ can be excluded. Interestingly, a ^{57}Fe -Mössbauer study was performed on the linear complexes $[\text{K}(\text{crypt-222})][\text{Fe}(\text{C}(\text{SiMe}_3)_3)_2]$ and $[\text{Fe}(\text{C}(\text{SiMe}_3)_3)_2]$ with a similar linear Fe coordination via carbon [175]. In these systems, a spin-reversal process was observed. The $[\text{Fe}(\text{C}(\text{SiMe}_3)_3)_2]^{1-}$ anion in $[\text{K}(\text{crypt-222})][\text{Fe}(\text{C}(\text{SiMe}_3)_3)_2]$ is proposed to have the oxidation state Fe^{+1} , since $[\text{Fe}(\text{C}(\text{SiMe}_3)_3)_2]$ has the oxidation state Fe^{2+} . The assumed asymmetry parameter $\eta = 0$ is according to the axial symmetric EFG tensor discussed by Lewis *et al.* and therein [176]. Table 8.4 shows the values of the isomer shift δ , the quadrupole splitting ΔE_Q and the magnetic hyperfine field B . For conversion [1] one can use

$$\Delta v_{QS} = \frac{ceQ}{2E_\gamma} V_{zz} \sqrt{1 + \frac{\eta^2}{3}} \quad (8.29)$$

with

$$\frac{ceQ}{2E_\gamma} \approx 0.0167 \frac{\text{mm/s}}{\text{V}/\text{\AA}^2}. \quad (8.30)$$

The smaller δ -value of Fe site A can be explained by the increase of s -electron density at the nucleus and the $4s$ -mixing, the electric monopole interaction is not comparable. The EFG value V_{zz} , here given by ΔE_Q of Fe-diluted $\text{Li}_2(\text{Li}_{1-x}\text{Fe}_x)\text{N}$ at site A and the Fe^{1+} -SMM, $[\text{Fe}(\text{C}(\text{SiMe}_3)_3)_2]^{1-}$, are very close to each other whereas the Fe^{2+} -SMM has only half of this value. Moreover, also the magnetic hyperfine fields of $[\text{Fe}(\text{C}(\text{SiMe}_3)_3)_2]^{1-}$ and Fe-diluted $\text{Li}_2(\text{Li}_{1-x}\text{Fe}_x)\text{N}$ are comparable as well. Therefore, we conclude an oxidation state Fe^{+1} for $\text{Li}_2(\text{Li}_{1-x}\text{Fe}_x)\text{N}$ for site A. In contrast, this state was concluded in the electronic structure calculations by Xu *et al.* [161] for high doping concentrations x . Electronic structure calculations of $\text{Li}_2(\text{Li}_{1-x}\text{Fe}_x)\text{N}$ were also reported for an Fe site with six Li and three Li neighbors in the (001) plane assuming a Fe^{1+} oxidation state [171]. Since we focus here on the low Fe substitution regime with $x \ll 1$ in the following we consider only the results for six Li neighbors in the (001) plane. The calculation showed that all majority spin $3d$ bands are occupied and the minority spin states are partially occupied. For isolated Fe centers one would expect that the antibonding d_{z^2} orbital forms the highest energy state in a $\text{Fe}(d_{z^2})\text{-N}(p_z)$ hybridization due to the strong Fe-N bond. In this case, the hybridization would dominate and determine the energy sequence of the orbitals. However, the electronic structure calculation yielded a counter intuitive orbital energy scheme in which d_{z^2} has the lowest energy. While the majority spin states are all occupied, the minority spin states are arranged as follow: $3d_{z^2}$ ($m_l = 0$) is occupied

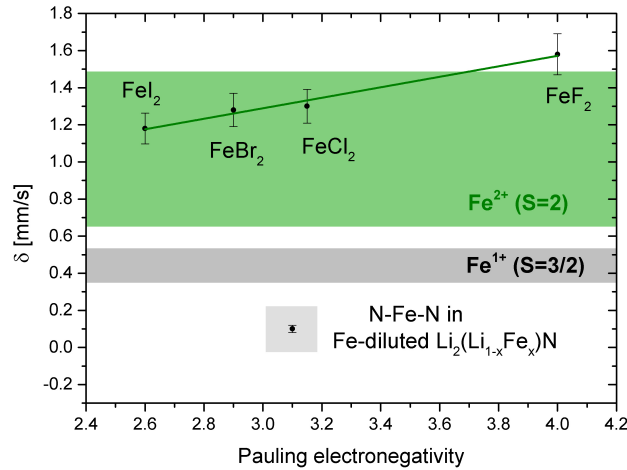


Figure 8.13: Isomer shift relative to α -iron as a function of the Pauling electronegativity of ferrous halides compared with SC 1. The errors are quiet large because the values were estimated by eyes taken from Axtmann *et al.* [78].

and has the lowest energy, the $3d_{xz}$, $3d_{yz}$ ($m_l = \pm 1$) lie 1-2 eV above the Fermi level E_F . The $3d_{x^2-y^2}$, $3d_{xy}$ ($m_l = \pm 2$) bands are only partially occupied and intersected by the Fermi energy E_F . A crystal field induced on-site mixing of the d_{z^2} states with the $4s$ states is the reason why the hybridization plays not the dominant role. This orbital sequence is consistent with the proposed sequence in $[\text{Fe}(\text{C}(\text{SiMe}_3)_3)_2]^{1-}$ of Fe^{1+} speaking for a reasonable comparison and analogy.

Such an energy sequence is also known from linear $3d$ metal dihalide molecules because of a σ -donating ligand induced $3d$ - $4s$ hybridization [177]. Interestingly, FeF_2 and FeCl_2 are discussed as Fe^{2+} (d^6) ($\delta^3\pi^2\sigma^1$) $^5\Delta_g$ states from an experimental and theoretical point of view and a spin reversal energy barrier of 305 K is proposed [161]. Axtmann *et al.* have found a linear relationship of the Pauling electronegativity and the isomer shift δ of ferrous halides discussed as Fe^{2+} compounds [78]. The difference of the ligand electronegativity is related to the isomer shift. This is treated as direct evidence for the participation of $4s$ electrons in the formation of the chemical bonds [16]. Figure 8.13 shows the ferrous halides presented by Axtmann *et al.* and the isomer shift of SC 1. The observed isomer shift deviates strongly. In the ferrous halides the electronic configuration is $3d4s^x$ where x measures the ionicity. The ionicity increases with x [16]. The electric monopole hyperfine interaction in $\text{Li}_2(\text{Li}_{1-x}\text{Fe}_x)\text{N}$ is very different from the values of the Fe^{2+} ferrous halides. Therefore, the Fe^+ is the most probable state.

In general, the total magnetic hyperfine field B is the sum of different contributions

$$B_h = B_c + B_{\text{orb}} + B_{\text{dip}} + B_{\text{lat}}. \quad (8.31)$$

B_{lat} is the lattice contribution, which means magnetic field generated by other electronic moments of the lattice. This contribution can be neglected in the diluted system. The sign of the Fermi contact contribution B_c is negative and arises from the spin-polarization of the s -electrons by unpaired valence electrons. B_{orb} is the orbital contribution scaling with the orbital quantum number L which is expected to be important because of the exceeded spin only value of the magnetic moment. B_{dip}

Compound	Carry	E_B [K]	Reference
[Dy(bbpen)X]	Dy^{3+}	1025	[178]
TbBis(phthalocyaninate)	Tb^{3+}	940	[179]
$\text{Li}_2(\text{Li}_{1-x}\text{Fe}_x)\text{N}$	Fe^{1+}	570(6)	this work
$[\text{Fe}(\text{C}(\text{SiMe}_3)_3)_2]^{1-}$	Fe^{1+}	354	[175, 180]
$[\text{Sr}_{10}(\text{PO}_4)_6(\text{Cu}_x\text{OH}_{1-x-y})_2]$	Cu^{3+}	69	[181]

Table 8.5: Selected SAMs with large energy barrier E_A values and the corresponding superparamagnetic ion.

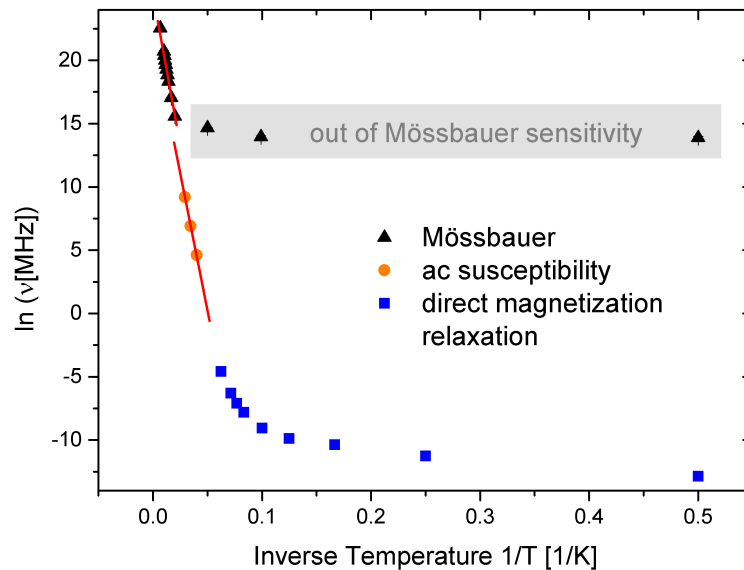


Figure 8.14: Electronic spin relaxation rate of SC 1 determined by Mössbauer spectroscopy (this work), a.c. susceptibility and magnetization relaxation measurements obtained by A. Jesche *et al.* [157].

is the dipolar contribution arising from a nonspherical electron spin density contribution which is approximately proportional to V_{zz} . The detailed values vary strongly on the used computational method and estimations, however, a tendency is given by

$$B_{\text{orb}} > B_{\text{dip}} \approx |B_c| > B_{\text{lat}} \approx 0, \quad (8.32)$$

or even $B_{\text{orb}} \gg B_{\text{dip}}, |B_c|$ which is based on the mentioned Fe^{1+} assumption [171].

8.3.4 Energy barrier and spin dynamics

Figure 8.14 shows the temperature dependence of the spin fluctuation rate of Fe in diluted $\text{Li}_2(\text{Li}_{1-x}\text{Fe}_x)\text{N}$, determined from Mössbauer spectroscopy, a.c. susceptibility and direct magnetization relaxation measurements. At three Mössbauer data points at $1/T \gg 0.05 \text{ K}^{-1}$ essentially static Mössbauer spectra are measured, i.e. the fluctuation rate becomes smaller than the lower bound of the frequency window of the method and these data points reflect this lower bound (see gray shadow). The obtained value of $\bar{E}_A = 570(6) \text{ K}$ is consistent with the value of 430 K obtained by A. Jesche *et al.* taking into

Compound	Θ_D [K]
$[\text{Fe}(\text{C}(\text{SiMe}_3)_3)_2]^{1-}$	313(16)
$[\text{Fe}(\text{C}(\text{SiMe}_3)_3)_2]$	125(1)
$\text{Li}_2(\text{Li}_{1-x}\text{Fe}_x)\text{N}$	315(8)

Table 8.6: Comparison of the Debye-temperature Θ_D for $\text{Li}_2(\text{Li}_{1-x}\text{Fe}_x)\text{N}$ with results for similar linear Fe^{1+} and Fe^{2+} complexes [175], for details of the fit see appendix.

account the different measurement techniques and respective frequency ranges. The pre-exponential factor of the Arrhenius law $\nu_0 \approx 3.6$ GHz fitted by A. Jesche *et al.* differs by two orders of magnitude from the Mössbauer value of $\bar{\nu}_0 = 309(10)$ GHz. Several reasons are possible: (i) The relaxation behavior of the magnetization is fitted by a stretched exponential $M(t) = M_0 \exp[-(t/\tau)^\beta]$ describing a distribution of fluctuation frequencies whereas the Mössbauer spectra analysis model uses one single frequency [157]. (ii) Magnetization measurements are more sensitive for the proposed dimer sites, orphan spins and surface clusters. (iii) The Mössbauer values are obtained in true ZF whereas the magnetization relaxation studies are performed in a finite external field. The β -value of $M(t)$ is temperature and magnetic field dependent which proposes this possibility [157]. In table 8.5 we compare the thermal activation energy barriers for several SAM systems with a large energy barrier E_B compared to Fe-diluted $\text{Li}_2(\text{Li}_{1-x}\text{Fe}_x)\text{N}$. In the literature the energy barrier is often identified with the zero-field splitting value D rather than considered as an effective experimental quantity, which depends on different microscopic quantities as discussed above. However, as demonstrated, the energy barrier is a function of the transverse magnetic field,

$$E_A = \frac{4Da^3}{27b^2} \sim (B_x B_z)^{1/3} \delta^{3/2}, \quad (8.33)$$

in which a and b contain the magnetic field components B_z and B_x . Here, one should keep in mind the limits of this formula as discussed. The thermal activation barrier E_B is often associated with a two-phonon Orbach process [17]. Above 50 K the dominant character of this process is plausible: the direct spin transition process in the Debye model accompanied by the creation or annihilation of a single phonon is dominant only for lower temperature $T < 50$ K with $\tau_S^{-1} \propto T$. An involved Raman process and pure quantum tunneling process of the magnetization above 50 K would lead to a deviation from the observed exponential dependence [175].

Finally, from the temperature dependence of the Mössbauer isomer shift the Debye-temperature Θ_D was calculated. The value is shown in table 8.6 in comparison with the aforementioned linear C-Fe-C compounds. Usually, organic systems exhibit values of Θ_D in the range of 100-300 K and inorganic compounds of 150-500 K. On the other hand, inorganic metals exhibit values of 1000 K and more which shows the nonmetallic character of $\text{Li}_2(\text{Li}_{1-x}\text{Fe}_x)\text{N}$ [17]. The values of $[\text{Fe}(\text{C}(\text{SiMe}_3)_3)_2]^{1-}$ and $\text{Li}_2(\text{Li}_{1-x}\text{Fe}_x)\text{N}$ are very close to each other as it was the case for the hyperfine field and quadrupole splitting as well.

8.4 Conclusions

In this chapter, I presented ^{57}Fe -Mössbauer studies on diluted Fe centers in a linear N-Fe-N configuration along the crystallographic c-axis in single crystalline specimens of hexagonal $\text{Li}_2(\text{Li}_{1-x}\text{Fe}_x)\text{N}$, i.e. Fe ions embedded in a hexagonal $\alpha\text{-Li}_3\text{N}$ crystal matrix. Homogeneously distributed isolated Fe centers are found and the single-atomic magnet nature confirmed.

Below 30 K, the magnetically isolated single-ion Fe centers exhibit a large quasistatic magnetic hyperfine field of $\bar{B}_A = 70.25(2)$ T parallel to the c-axis which is the strongest principle axis of the electric field gradient $\bar{V}_{zz} = -154.0(1)$ V/Å².

Fluctuations of the magnetic hyperfine field clearly observed in the Mössbauer spectra between 50 K and 300 K are described by a Blume two-level relaxation model.

The spin dynamics in $\text{Li}_2(\text{Li}_{1-x}\text{Fe}_x)\text{N}$ is concentration-independent for $x \leq 0.025$. From the temperature dependence an Orbach process is deduced as the dominant spin-lattice relaxation process. An Arrhenius analysis $\nu = \nu_0 e^{-E_A/k_B T}$ yields a thermal activation barrier of $\bar{E}_A = 570(6)$ K and an attempt frequency $\bar{\nu}_0 = 309(10)$ GHz.

Mössbauer spectroscopy studies with applied transverse magnetic fields up to 5 T reveal a huge increase of the fluctuation rate by two orders of magnitude. These experimental observations are qualitatively reproduced by a single-ion spin Hamiltonian analysis. This demonstrates that for dominant magnetic quantum tunneling a weak axial single-ion anisotropy D of the order of a few Kelvin can cause a two orders of magnitude larger energy barrier for temperature-induced longitudinal spin fluctuations. The experiments suggest $\text{Li}_2(\text{Li}_{1-x}\text{Fe}_x)\text{N}$ as a candidate for novel functional magnetic materials, e.g. for quantum computing or spintronic devices.

8.5 Outlook

8.5.1 Advantages of $\text{Li}_2(\text{Li}_{1-x}\text{Fe}_x)\text{N}$

Fe-diluted $\text{Li}_2(\text{Li}_{1-x}\text{Fe}_x)\text{N}$ is not only an ideal material for magnetic devices but also possesses many intriguing magnetic properties. In light of this discussion we anticipate many future applications of this material. The normal vector of the largest crystal surface was in our studies always parallel to the c-axis. This shows the simple handling and is important for magnetic or spintronic devices.

Fe-diluted $\text{Li}_2(\text{Li}_{1-x}\text{Fe}_x)\text{N}$ shows several advantages for an application in novel functional materials and devices:

1. The availability of large single crystals.
2. $\text{Li}_2(\text{Li}_{1-x}\text{Fe}_x)\text{N}$ contains only inexpensive elements.
3. These elements are nontoxic.

The last point is emphasized because, e.g. in contrast, the family $\text{LiY}_{0.998}\text{Ho}_{0.002}\text{F}_4$ is known for a macroscopic quantum tunneling in a solid state material [182, 183]. Also, examples to tune continuously a quasi-SMM or SAM behavior in a solid state material are rare. A slight increase of the Fe concentration beyond the SAM case leads to a complicated microscopic mixture of the investigated SAM and SMMs-like clusters. The above advantages confirm the possibility of spintronic applications in the future.

8.5.2 μSR on Fe-diluted $\text{Li}_2(\text{Li}_{1-x}\text{Fe}_x)\text{N}$

In the first part of this thesis, I demonstrated the investigation of low-energy spin dynamics probed by $\mu^+\text{SR}$. To discuss the usefulness and possibility of μSR on Fe-diluted $\text{Li}_2(\text{Li}_{1-x}\text{Fe}_x)\text{N}$ one should discuss two points:

1. The problem of the Fe-dilution for the positive muon
2. The question of the muon site in $\text{Li}_2(\text{Li}_{1-x}\text{Fe}_x)\text{N}$

A critical point is the high Fe-dilution. This means it can be that the positive muon will not be located close to Fe. It is argued that the muon finds the energy minimum described by a delocalized plane wave according to a Bloch treatment. Then the muon locates in the energy minimum being stronger localized. Of course, when the distribution of Fe centers is too low, this assumption has limitations. For $x = 0.30$ this seems rather unexpected because of the rather high concentration of quasi-magnetic centers. For $x > 0.04$ cluster sites can play an important role which leads to a manifold of possible muon sites. A distribution of relaxation rates is expected. The possibility that Fe-dilution is not the limiting factor assumes the energy minimum is close to Fe. To have a rough estimation of the muon site I have performed a supercell DFT calculation on $\text{Li}_2(\text{Li}_{1-x}\text{Fe}_x)\text{N}$. I have constructed a supercell of $2 \times 2 \times 2$ primitive unit cells. This supercell is shown in figure 8.15. The interplane between the cells does not contain any Fe (brown). Instead, the Fe is located at the edges of the supercell. Fe has no bond to another Fe via Nitrogen and there is no direct lateral Fe

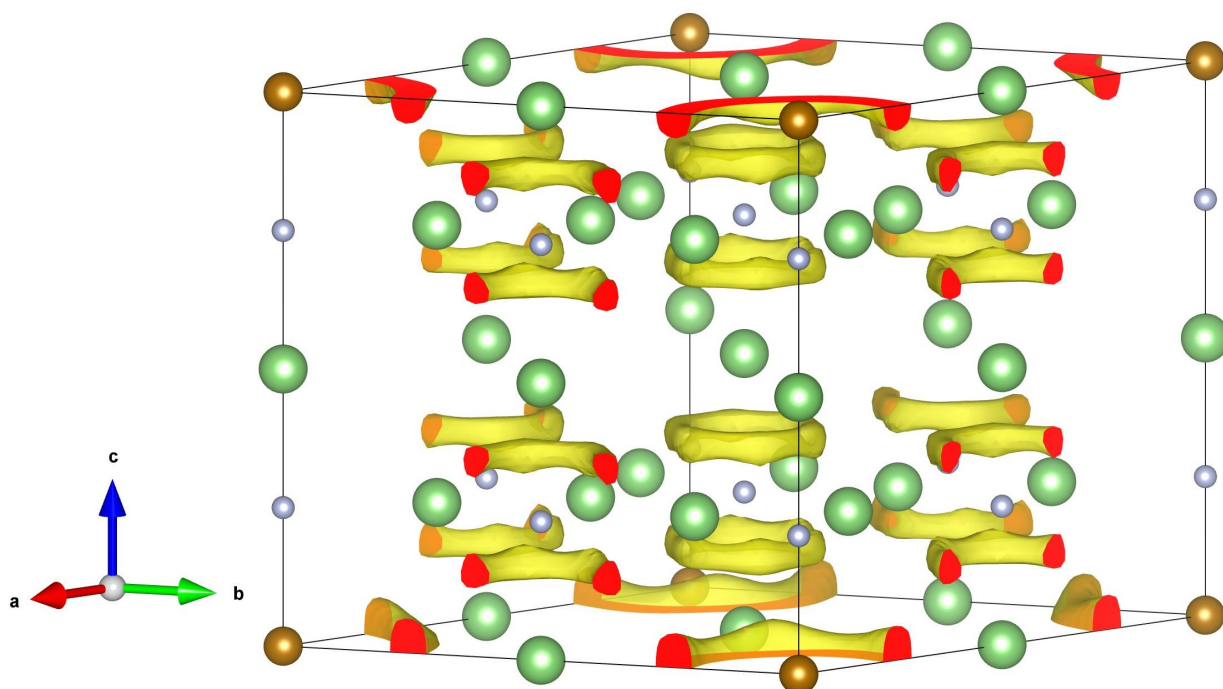


Figure 8.15: Supercell of $\text{Li}_2(\text{Li}_{1-x}\text{Fe}_x)\text{N}$ assuming an alternation of Fe (brown) and Li (green) in every direction of the $2c$ -sites, N is shown in grey. The isosurface of $0.19 \frac{E_h}{e}$ is shown in yellow. The red surfaces are the boundaries of the supercell. The isosurfaces are tori.

neighbor present as well. The isosurfaces are shown in yellow correspond to a potential of $0.19 \frac{E_h}{e}$. The isosurfaces are tori located around Li and close to Fe as well. Figure 8.16 shows the supercell with the isosurface of $0.2005 \frac{E_h}{e}$. The shape is contracted and the tori around Fe disappeared. The energy minimum of the shown calculation is therefore close a Li-N bond far away from the Fe ion. This is a very rough treatment which does not consider the special situation of the orbital sequence. However, together with the problem of the Fe-dilution it does not suggest to perform a μSR study of highly-diluted $\text{Li}_2(\text{Li}_{1-x}\text{Fe}_x)\text{N}$.

8.5.3 NMR

A. Jesche has grown ^{57}Fe -enriched single crystals for ^{57}Fe -NMR purposes. Li- and N-NMR studies have started already.

Our NMR laboratory requested a Mössbauer study on the ^{57}Fe -enriched $\text{Li}_2(\text{Li}_{1-x}\text{Fe}_x)\text{N}$ with $x \approx 4.3\%$. There are 3 reasons for a complementary study to support ^{57}Fe -NMR study by a Mössbauer investigation: (i) This study ensures the quality of the ^{57}Fe sample. (ii) The extracted value of the magnetic hyperfine field reduced the amount of work to find the ^{57}Fe -NMR signal. (iii) The possibility to improve the general understanding of the Fe sites neighbor treatment. So far, the detailed microscopic picture is still unclear, especially regarding the next(-next) nearest neighbor Fe-to-Fe interactions. The question of the existence of a Fe-N-Fe configuration out-of-plane is still open. Is this configuration present or even preferred? A statistical site treatment is needed for a deeper understanding.

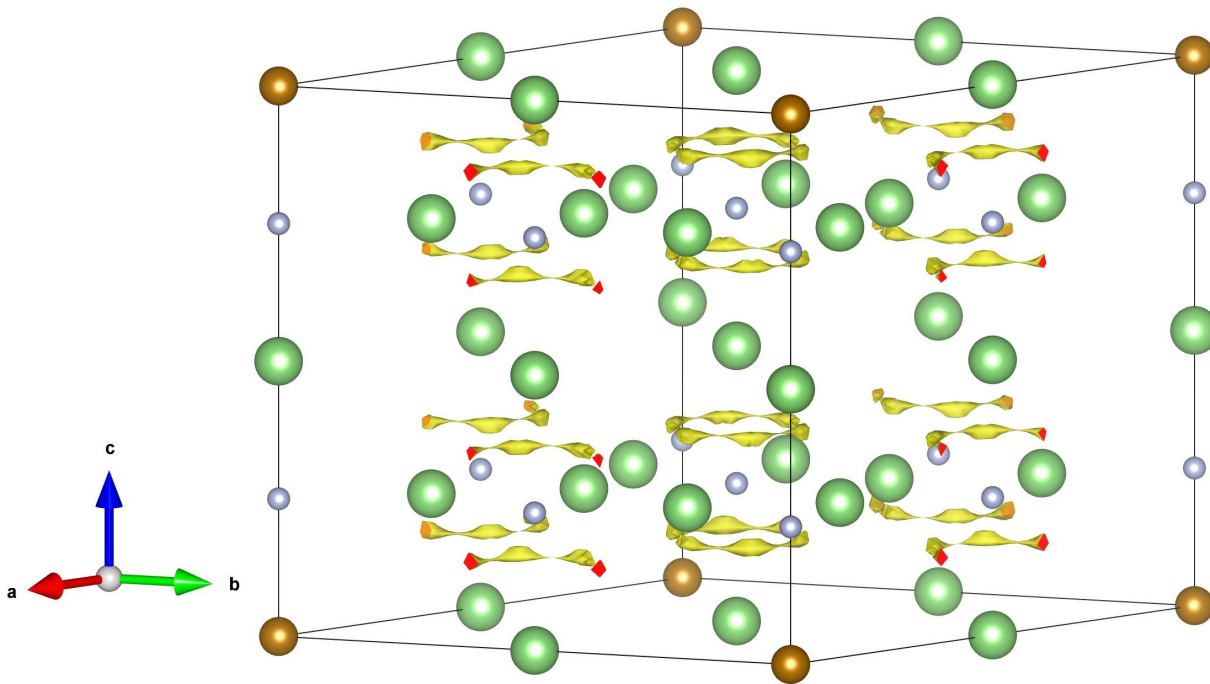


Figure 8.16: Supercell of $\text{Li}_2(\text{Li}_{1-x}\text{Fe}_x)\text{N}$ assuming an alternation of Fe (brown) and Li (green) in every direction of the $2c$ -sites. The isosurface of $0.2005 \frac{E_h}{e}$ is shown in yellow. The red surfaces are the boundaries of the supercell.

$\text{Li}_2(\text{Li}_{1-x}\text{Fe}_x)\text{N}$ provides an unique opportunity to investigate and to tune the interaction of molecular magnet-like centers in a solid material. Figure 8.4 shows my Mössbauer measurement at 9 K of a grown ^{57}Fe -enriched single crystal. Interestingly, the missing two transitions of the SAM site A is present. An additional site C is pronounced⁵.

The hope is to reveal more information of the low-energy spin dynamics probed by NMR which was done by ^{57}Fe -Mössbauer spectroscopy successfully in this work. Probably, the LF study will be continued for other temperatures and magnetic fields by ^{57}Fe -Mössbauer spectroscopy as well. However, the ^{57}Fe -NMR study is performed in the nuclear ground state with $I = 1/2$ and is not sensitive for quadrupole interactions. NMR can be performed at much higher external fields up to 20 T and probes the Fe site of interest.

8.5.4 Bridge up to $x = 0.30$

Locally, the discussed site A of the SAM shows a clear signature: Two Mössbauer transitions are suppressed. It is not possible to observe the suppression in a powder study as it was performed by Klatyk, Ksenofontov *et al.* [158, 159]. However, here the purpose of the studies by Klatyk, Ksenofontov *et al.* was mainly the characterization of the phase diagram.

The question of the existence of an antiferromagnetic coupling exists. This seems not impossible thinking on a superexchange path via nitrogen out-of-plane for a Fe-N-Fe dimer cluster. Furthermore,

⁵Here, the purpose is not to discuss the results in detail. The figure shows the status of the studies.

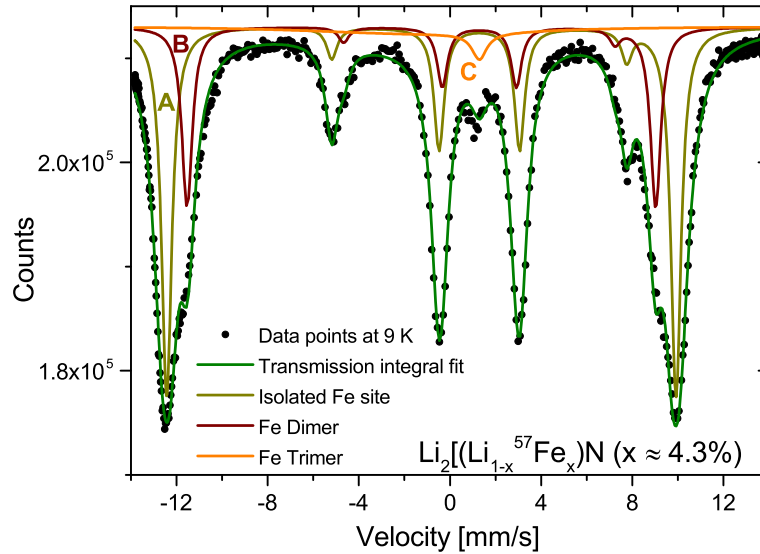


Figure 8.17: Mössbauer measurement of $\text{Li}_2(\text{Li}_{1-x}\text{Fe}_x)\text{N}$ at 9 K with $x \approx 4.3\%$. The dark green line is the transmission integral fit. The other lines show the natural lines of the Fe sites A, B and C, see main text.

the microscopic picture that the ^{57}Fe -Mössbauer studies reveal only lateral neighbors in the (001) plane and the ^{57}Fe -Mössbauer fast-relaxing subspectra of the Fe-rich environments are not clear at all. This model was taken by Klatyk, Ksenofontov *et al.*. The energy barrier should increase with an increasing number of ferromagnetic neighbors and not decrease as presented by relaxing subspectra even at 4 K.

To solve the discussed problem of the fluctuating subspectra one should investigate the Fe subspecies step by step. As presented and shown in this thesis, now the SAM case of $\text{Li}_2(\text{Li}_{1-x}\text{Fe}_x)\text{N}$ is well understood. The hyperfine parameter and the temperature dependence are well known using this knowledge as a basis. One can increase the concentration in steps of $\Delta x = 0.005$ starting from SC 1 to investigate the energy barrier and the fluctuation frequency of every Fe site iteratively. The single crystal provides additional information on a possible canting, e.g. possible for dimer or trimer clusters. A powder study cannot reveal this information. This procedure leads step by step to a microscopic picture of the entire system in the concentration phase diagram solving open questions⁶.

⁶This study started already and preliminary discussed by F. Seewald in his Bachelor thesis [163]. However, the microscopic understanding is still in progress and the understanding of the low- x SAM site A helps to fill the gap of the understanding between the low- x regime and the $x = 0.3$ regime.

9 Summary

In this thesis, I have presented selected experimental studies using μ^+ SR spectroscopy and ^{57}Fe -Mössbauer spectroscopy to investigate the low-energy spin dynamics in geometrically frustrated magnets with bond- and site-disorder and single-ion spin systems. In addition, I described a pulsed-high-field magnetization study which we have performed at the Helmholtz-Zentrum Dresden-Rossendorf. The experimental μ^+ SR studies are supplemented by my DFT calculations to estimate the muon sites in these systems.

One major topic is the examination of quenched disorder in highly frustrated $\text{BaTi}_{0.5}\text{Mn}_{0.5}\text{O}_3$ and $\text{NaCaCo}_2\text{F}_7$ probed by μ^+ SR spectroscopy. $\text{BaTi}_{0.5}\text{Mn}_{0.5}\text{O}_3$ contains disorder of its magnetic ions and $\text{NaCaCo}_2\text{F}_7$ contains structural disorder of nonmagnetic Na^+ and Ca^{2+} ions. Experimentally, $\text{BaTi}_{0.5}\text{Mn}_{0.5}\text{O}_3$ shows persistent muon spin dynamics together with the absence of a frequency dependence of a.c. susceptibility which suggests strongly a quantum spin-liquid-like ground state. Theoretically, the detailed quantum spin liquid-like state is still in discussion.

μ^+ SR spectroscopy studies on fluorides are different compared to other μ^+ SR studies due to the high electronegativity of F leading to a chemical bound state which is called F- μ^+ -F state. This is observed in $\text{NaCaCo}_2\text{F}_7$. It is discussed also in nonmagnetic CaF_2 revealing a static magnetic field probed by the muon of around 16 G. Here, the temperature-independence, below 200 K, of the characteristic F- μ^+ -F state oscillation is shown and some open questions could be answered, e.g., on the muon diffusion at room temperature. Additionally, I have shown that my DFT calculations are fully consistent with a DFT study of CaF_2 performed earlier.

The studies on $\text{BaTi}_{0.5}\text{Mn}_{0.5}\text{O}_3$ and CaF_2 have provided a bridge to the study on $\text{NaCaCo}_2\text{F}_7$ because of the observations of (i) disorder physics realized by structural disorder, (ii) the F- μ^+ -F state oscillation by the formed bound state of the muon and (iii) persistent spin dynamics given by a dynamical muon spin relaxation rate down to $T \rightarrow 0$. The main result - parallel to the interesting muon site ambivalence supported by my DFT calculations comparing $\text{NaCaCo}_2\text{F}_7$ and $\text{NaCaNi}_2\text{F}_7$ - proposes $\text{NaCaCo}_2\text{F}_7$ as a quantum cluster-spin glass candidate separating the compound from classical cluster-spin-glasses which show a clear peak of the muon spin relaxation rate.

In Fe-diluted $\text{Li}_2(\text{Li}_{1-x}\text{Fe}_x)\text{N}$ a rich temperature and field-dependent low-energy spin dynamics of ^{57}Fe is detected by Mössbauer spectroscopy. Here, an extensive study in ZF on a number of single-crystals have shown the single-atomic nature of Fe-diluted $\text{Li}_2(\text{Li}_{1-x}\text{Fe}_x)\text{N}$ by an Ising-like spin dynamics with the magnetic hyperfine field parallel to the main axis of the largest electric field gradient tensor component, parallel to the hexagonal c -axis.

The sensitivity to transverse magnetic fields is two orders of magnitude higher than the sensitivity to thermal energy. This is explained by an effective 7/2-spin-Hamiltonian. Here, a magnetic anisotropy constant D of a few Kelvin can cause an effective energy barrier of a few hundred Kelvin. Applied

longitudinal magnetic fields parallel to the c -axis show a Zeeman splitting into two frequency branches consistent with the Ising-like nature of the system.

Bibliography

- [1] Kamusella S and Klauss H H 2016 *Hyperfine Interactions* **237** 82
- [2] Kamusella S *PhD thesis: Electronic phase diagrams and competing groundstates of complex iron pnictides and chalcogenides*
- [3] Kamusella S *Moessfit manual*
- [4] Yaouanc A and de Réotier P 2011 *Muon Spin Rotation, Relaxation, and Resonance: Applications to Condensed Matter* International Series of Monographs on Physics (OUP Oxford) ISBN 9780199596478 URL <http://books.google.ch/books?id=nZyicQAACAAJ>
- [5] Schenck A 1985 *Muon spin rotation spectroscopy* ISBN 9780852745519 URL <http://books.google.de/books?id=b6dPAQAIAAJ>
- [6] Blundell S J 1999 *Contemporary Physics* **40** 175–192 (*Preprint cond-mat/0207699*) URL <http://adsabs.harvard.edu/abs/1999ConPh...40..175B>
- [7] de Réotier P D and Yaouanc A 1997 *Journal of Physics: Condensed Matter* **9** 9113 URL <http://stacks.iop.org/0953-8984/9/i=43/a=002>
- [8] Nuccio L, Schulz L and Drew A J 2014 *Journal of Physics D: Applied Physics* **47** 473001 URL <http://stacks.iop.org/0022-3727/47/i=47/a=473001>
- [9] Spehling J *PhD thesis: Magnetic Quantum Criticality in Heavy-Fermion Compounds*
- [10] Povh B, Rith K, Scholz C, Zetsche F and Rodejohann W 2015 *Particles and Nuclei Springer*
- [11] Klauss H H *Dissertation: μ SR-Untersuchungen der Seltenen-Erd-Monopnictide CeSb und DySb* 1st ed (Cuvillier) ISBN 978-3-89588-288-3 OCLC: 64527130
- [12] Hayano R S, Uemura Y J, Imazato J, Nishida N, Yamazaki T and Kubo R 1979 *Phys. Rev. B* **20**(3) 850–859 URL <http://link.aps.org/doi/10.1103/PhysRevB.20.850>
- [13] Slichter C P *Principles of Magnetic Resonance (Springer Series in Solid-State Sciences vol 1)* (Springer Berlin Heidelberg) ISBN 978-3-642-08069-2 978-3-662-09441-9 URL <http://link.springer.com/10.1007/978-3-662-09441-9>
- [14] Berberan-Santos M, Bodunov E and Valeur B 2005 *Chemical Physics* **315** 171 – 182 ISSN 0301-0104 URL <http://www.sciencedirect.com/science/article/pii/S0301010405001175>

- [15] Lancaster T, Blundell S J, Baker P J, Brooks M L, Hayes W, Pratt F L, Manson J L, Conner M M and Schlueter J A 2007 *Phys. Rev. Lett.* **99**(26) 267601 URL <http://link.aps.org/doi/10.1103/PhysRevLett.99.267601>
- [16] Chen Y and Yang D P *Mössbauer effect in lattice dynamics: experimental techniques and applications* (Wiley-VCH ; John Wiley, distributor) ISBN 978-3-527-40712-5 OCLC: ocm82672525
- [17] Gütlich P, Bill E and Trautwein A X 2011 *Moessbauer Spectroscopy and Transition Metal Chemistry* (Springer Berlin Heidelberg) ISBN 978-3-540-88427-9 978-3-540-88428-6 DOI: 10.1007/978-3-540-88428-6 URL <http://link.springer.com/10.1007/978-3-540-88428-6>
- [18] Rubinson W and Gopinathan K P 1968 *Phys. Rev.* **170**(4) 969–978 URL <https://link.aps.org/doi/10.1103/PhysRev.170.969>
- [19] Schünemann V and Winkler H 2000 *Reports on Progress in Physics* **63** 263 URL <http://stacks.iop.org/0034-4885/63/i=3/a=202>
- [20] Davey W P 1925 *Phys. Rev.* **25**(6) 753–761 URL <https://link.aps.org/doi/10.1103/PhysRev.25.753>
- [21] Bateman D S, Bose S K, Dutta-Roy B and Bhattacharyya M 1992 *American Journal of Physics* **60** 829–832
- [22] Kohn W and Sham L J 1965 *Phys. Rev.* **140**(4A) A1133–A1138 URL <https://link.aps.org/doi/10.1103/PhysRev.140.A1133>
- [23] Hohenberg P and Kohn W 1964 *Phys. Rev.* **136**(3B) B864–B871 URL <https://link.aps.org/doi/10.1103/PhysRev.136.B864>
- [24] Srivastava G P 1984 *Journal of Physics A: Mathematical and General* **17** 2737 URL <http://stacks.iop.org/0305-4470/17/i=13/a=525>
- [25] Perdew J P, Burke K and Ernzerhof M 1996 *Phys. Rev. Lett.* **77**(18) 3865–3868 URL <https://link.aps.org/doi/10.1103/PhysRevLett.77.3865>
- [26] URL <http://elk.sourceforge.net/>
- [27] Parr R G and Yang W *Density-functional theory of atoms and molecules* 1st ed (*International series of monographs on chemistry* no 16) (Oxford Univ. Press [u.a.]) ISBN 978-0-19-509276-9 978-0-19-504279-5 OCLC: 832732716
- [28] Krizan J W and Cava R J 2014 *Phys. Rev. B* **89**(21) 214401 URL <http://link.aps.org/doi/10.1103/PhysRevB.89.214401>
- [29] Garcia F A, Kaneko U F, Granado E, Sichelschmidt J, Hölzel M, Duque J G S, Nunes C A J, Amaral R P, Marques-Ferreira P and Lora-Serrano R 2015 *Phys. Rev. B* **91**(22) 224416 URL <https://link.aps.org/doi/10.1103/PhysRevB.91.224416>

- [30] Greedan J E 2001 *J. Mater. Chem.* **11**(1) 37–53 URL <http://dx.doi.org/10.1039/B003682J>
- [31] Maryasin V S and Zhitomirsky M E 2014 *Phys. Rev. B* **90**(9) 094412 URL <http://link.aps.org/doi/10.1103/PhysRevB.90.094412>
- [32] Zhitomirsky M E, Gvozdkova M V, Holdsworth P C W and Moessner R 2012 *Phys. Rev. Lett.* **109**(7) 077204 URL <http://link.aps.org/doi/10.1103/PhysRevLett.109.077204>
- [33] Savary L, Ross K A, Gaulin B D, Ruff J P C and Balents L 2012 *Phys. Rev. Lett.* **109**(16) 167201 URL <http://link.aps.org/doi/10.1103/PhysRevLett.109.167201>
- [34] Champion J D M, Harris M J, Holdsworth P C W, Wills A S, Balakrishnan G, Bramwell S T, Čížmár E, Fennell T, Gardner J S, Lago J, McMorro D F, Orendáč M, Orendáčová A, Paul D M, Smith R I, Telling M T F and Wildes A 2003 *Phys. Rev. B* **68**(2) 020401 URL <https://link.aps.org/doi/10.1103/PhysRevB.68.020401>
- [35] Ross K A, Krizan J W, Rodriguez-Rivera J A, Cava R J and Broholm C L 2016 *Phys. Rev. B* **93**(1) 014433 URL <http://link.aps.org/doi/10.1103/PhysRevB.93.014433>
- [36] Andrade E C, Hoyos J A, Rachel S and Vojta M 2017 *ArXiv e-prints (Preprint 1710.06658)*
- [37] Cantarino M R, Amaral R P, Freitas R S, Araújo J C R, Lora-Serrano R, Luetkens H, Baines C, Bräuninger S, Grinenko V, Sarkar R, Klauss H H, Andrade E C and Garcia F A 2019 *Phys. Rev. B* **99**(5) 054412 URL <https://link.aps.org/doi/10.1103/PhysRevB.99.054412>
- [38] Bilitewski T, Zhitomirsky M E and Moessner R 2017 *Phys. Rev. Lett.* **119**(24) 247201 URL <https://link.aps.org/doi/10.1103/PhysRevLett.119.247201>
- [39] Savary L and Balents L 2017 *Phys. Rev. Lett.* **118**(8) 087203 URL <https://link.aps.org/doi/10.1103/PhysRevLett.118.087203>
- [40] Wen J J, Koohpayeh S M, Ross K A, Trump B A, McQueen T M, Kimura K, Nakatsuji S, Qiu Y, Pajerowski D M, Copley J R D and Broholm C L 2017 *Phys. Rev. Lett.* **118**(10) 107206 URL <https://link.aps.org/doi/10.1103/PhysRevLett.118.107206>
- [41] Sibille R, Lhotel E, Ciomaga Hatnean M, Nilsen G J, Ehlers G, Cervellino A, Ressouche E, Frontzek M, Zaharko O, Pomjakushin V, Stuhr U, Walker H C, Adroja D T, Luetkens H, Baines C, Amato A, Balakrishnan G, Fennell T and Kenzelmann M **8** ISSN 2041-1723 URL <http://www.nature.com/articles/s41467-017-00905-w>
- [42] Lieb E H 1973 *Communications in Mathematical Physics* **31** 327–340 ISSN 1432-0916 URL <https://doi.org/10.1007/BF01646493>
- [43] Yan H, Benton O, Jaubert L and Shannon N 2017 *Phys. Rev. B* **95**(9) 094422 URL <https://link.aps.org/doi/10.1103/PhysRevB.95.094422>
- [44] Balents L **464** 199 URL <http://dx.doi.org/10.1038/nature08917>

- [45] Vannimenu J and Toulouse G 1977 *Journal of Physics C: Solid State Physics* **10** L537 URL <http://stacks.iop.org/0022-3719/10/i=18/a=008>
- [46] Lacorre P 1987 *Journal of Physics C: Solid State Physics* **20** L775 URL <http://stacks.iop.org/0022-3719/20/i=29/a=004>
- [47] Ross K A, Bordelon M M, Terho G and Neilson J R 2015 *Phys. Rev. B* **92**(13) 134419 URL <https://link.aps.org/doi/10.1103/PhysRevB.92.134419>
- [48] Pape R D and Ferey G 1986 *Materials Research Bulletin* **21** 971 – 978 ISSN 0025-5408 URL <http://www.sciencedirect.com/science/article/pii/0025540886901340>
- [49] Calage Y, Zemirli M, Greneche J, Varret F, Pape R D and Ferey G 1987 *Journal of Solid State Chemistry* **69** 197 – 201 ISSN 0022-4596 URL <http://www.sciencedirect.com/science/article/pii/0022459687900740>
- [50] Reimers J N, Greedan J E, Stager C V, Bjorgvinnsen M and Subramanian M A 1991 *Phys. Rev. B* **43**(7) 5692–5697 URL <https://link.aps.org/doi/10.1103/PhysRevB.43.5692>
- [51] Vojta M 2018 *Reports on Progress in Physics* **81** 064501 URL <http://stacks.iop.org/0034-4885/81/i=6/a=064501>
- [52] Gardner J S, Gingras M J P and Greedan J E 2010 *Rev. Mod. Phys.* **82**(1) 53–107 URL <http://link.aps.org/doi/10.1103/RevModPhys.82.53>
- [53] Lacroix C, Mendels P and Mila F Springer, Berlin, Heidelberg, 2011 *Introduction to Frustrated Magnetism: Materials, Experiments, Theory*, **Vol. 164**
- [54] Hänsler R and Rüdorff W 1970 **25** 1306 ISSN 18657117 URL <https://www.degruyter.com/view/j/znb.1970.25.issue-11/znb-1970-1121/znb-1970-1121.xml>
- [55] Krizan J W and Cava R J 2015 *Journal of Physics: Condensed Matter* **27** 296002 URL <http://stacks.iop.org/0953-8984/27/i=29/a=296002>
- [56] Krizan J W and Cava R J 2015 *Phys. Rev. B* **92**(1) 014406 URL <https://link.aps.org/doi/10.1103/PhysRevB.92.014406>
- [57] Sanders M B, Krizan J W, Plumb K W, McQueen T M and Cava R J 2017 *Journal of Physics: Condensed Matter* **29** 045801 URL <http://stacks.iop.org/0953-8984/29/i=4/a=045801>
- [58] Plumb K W, Changlani H J, Scheie A, Zhang S, Kriza J W, Rodriguez-Rivera J A, Qiu Y, Winn B, Cava R J and Broholm C L 2017 *ArXiv e-prints (Preprint 1711.07509)*
- [59] Saunders T E and Chalker J T 2007 *Phys. Rev. Lett.* **98**(15) 157201 URL <https://link.aps.org/doi/10.1103/PhysRevLett.98.157201>
- [60] Andreev A, Chalker J T, Saunders T E and Sherrington D 2010 *Phys. Rev. B* **81**(1) 014406 URL <https://link.aps.org/doi/10.1103/PhysRevB.81.014406>

- [61] Bellier-Castella L, Gingras M J, Holdsworth P C and Moessner R 2001 *Canadian Journal of Physics* **79** 1365–1371 (Preprint <https://doi.org/10.1139/p01-098>) URL <https://doi.org/10.1139/p01-098>
- [62] Lago J, Lancaster T, Blundell S J, Bramwell S T, Pratt F L, Shirai M and Baines C 2005 *Journal of Physics: Condensed Matter* **17** 979 URL <http://stacks.iop.org/0953-8984/17/i=6/a=015>
- [63] Dalmas de Réotier P, Yaouanc A, Chapuis Y, Curnoe S H, Grenier B, Ressouche E, Marin C, Lago J, Baines C and Gibling S R 2012 *Phys. Rev. B* **86**(10) 104424 URL <https://link.aps.org/doi/10.1103/PhysRevB.86.104424>
- [64] Ross K A, Brown J M, Cava R J, Krizan J W, Nagler S E, Rodriguez-Rivera J A and Stone M B 2017 *Phys. Rev. B* **95**(14) 144414 URL <https://link.aps.org/doi/10.1103/PhysRevB.95.144414>
- [65] Zeisner J, Bräuningner S A, Opherden L, Sarkar R, Gorbunov D I, Krizan J W, Herrmannsdörfer T, Cava R J, Wosnitza J, Büchner B, Klauss H H and Kataev V 2019 *Phys. Rev. B* **99**(15) 155104 URL <https://link.aps.org/doi/10.1103/PhysRevB.99.155104>
- [66] Ruff J P C, Clancy J P, Bourque A, White M A, Ramazanoglu M, Gardner J S, Qiu Y, Copley J R D, Johnson M B, Dabkowska H A and Gaulin B D 2008 *Phys. Rev. Lett.* **101**(14) 147205 URL <http://link.aps.org/doi/10.1103/PhysRevLett.101.147205>
- [67] Blundell S *Magnetism in condensed matter* reprint ed (*Oxford master series in condensed matter physics* no 4) (Oxford Univ. Press) ISBN 978-0-19-850591-4 OCLC: 898266646
- [68] Balanda M 2013 *ACTA Physica Polonica A* **124** 964
- [69] Trachenko K 2011 *Journal of Physics: Condensed Matter* **23** 366003 URL <https://doi.org/10.1088/0953-8984/23/36/03>
- [70] Frandsen B A, Ross K A, Krizan J W, Nilsen G J, Wildes A R, Cava R J, Birgeneau R J and Billinge S J L 2017 *Phys. Rev. Materials* **1**(7) 074412 URL <https://link.aps.org/doi/10.1103/PhysRevMaterials.1.074412>
- [71] Sarkar R, Krizan J W, Brückner F, Andrade E C, Rachel S, Vojta M, Cava R J and Klauss H H 2017 *Phys. Rev. B* **96**(23) 235117 URL <https://link.aps.org/doi/10.1103/PhysRevB.96.235117>
- [72] Opherden L *Doktorarbeit (2018): Untersuchung magnetischer Pyrochlor-Systeme, insbesondere der All-In-All-Out-Ordnung in $Nd_2T_2O_7$ ($T = Zr, Hf$)*
- [73] Skourski Y, Kuz'min M D, Skokov K P, Andreev A V and Wosnitza J 2011 *Phys. Rev. B* **83**(21) 214420 URL <https://link.aps.org/doi/10.1103/PhysRevB.83.214420>
- [74] Sharma S, Yadav P, Sau T, Yand a P, Baker P J, da Silva I, Sundaresan A and Lalla N P 2019 *arXiv e-prints* arXiv:1902.08961 (Preprint 1902.08961)

- [75] Dagotto E 2005 *Science* **309** 257–262 ISSN 0036-8075 (*Preprint* <https://science.sciencemag.org/content/309/5732/257.full.pdf>) URL <https://science.sciencemag.org/content/309/5732/257>
- [76] Nikuni T, Oshikawa M, Oosawa A and Tanaka H 2000 *Phys. Rev. Lett.* **84**(25) 5868–5871 URL <https://link.aps.org/doi/10.1103/PhysRevLett.84.5868>
- [77] Williams R C, Xiao F, Thomas I O, Clark S J, Lancaster T, Cornish G A, Blundell S J, Hayes W, Paul A K, Felser C and Jansen M 2016 *Journal of Physics: Condensed Matter* **28** 076001 URL <https://doi.org/10.1088%2F0953-8984%2F28%2F7%2F076001>
- [78] Axtmann R C, Hazony Y and Hurley Jr J W 1968 *Chemical Physics Letters* **2** 673–676
- [79] Yan B, Paul A K, Kanungo S, Reehuis M, Hoser A, Többens D M, Schnelle W, Williams R C, Lancaster T, Xiao F, Möller J S, Blundell S J, Hayes W, Felser C and Jansen M 2014 *Phys. Rev. Lett.* **112**(14) 147202 URL <https://link.aps.org/doi/10.1103/PhysRevLett.112.147202>
- [80] Feng H L, Adler P, Reehuis M, Schnelle W, Pattison P, Hoser A, Felser C and Jansen M 2017 *Chemistry of Materials* **29** 886–895 (*Preprint* <https://doi.org/10.1021/acs.chemmater.6b04983>) URL <https://doi.org/10.1021/acs.chemmater.6b04983>
- [81] Zheng X G, Kubozono H, Nishiyama K, Higemoto W, Kawae T, Koda A and Xu C N 2005 *Phys. Rev. Lett.* **95**(5) 057201 URL <http://link.aps.org/doi/10.1103/PhysRevLett.95.057201>
- [82] Yaouanc A, de Réotier P D, Glazkov V, Marin C, Bonville P, Hodges J A, Gubbens P C M, Sakarya S and Baines C 2005 *Phys. Rev. Lett.* **95**(4) 047203 URL <http://link.aps.org/doi/10.1103/PhysRevLett.95.047203>
- [83] Mendels P, Bert F, de Vries M A, Olariu A, Harrison A, Duc F, Trombe J C, Lord J S, Amato A and Baines C 2007 *Phys. Rev. Lett.* **98**(7) 077204 URL <http://link.aps.org/doi/10.1103/PhysRevLett.98.077204>
- [84] Dalmas de Réotier P, Yaouanc A, MacLaughlin D E, Zhao S, Higo T, Nakatsuji S, Nambu Y, Marin C, Lapertot G, Amato A and Baines C 2012 *Phys. Rev. B* **85**(14) 140407 URL <http://link.aps.org/doi/10.1103/PhysRevB.85.140407>
- [85] Lago J, Lancaster T, Blundell S J, Bramwell S T, Pratt F L, Shirai M and Baines C 2005 *Journal of Physics: Condensed Matter* **17** 979 URL <http://stacks.iop.org/0953-8984/17/i=6/a=015>
- [86] Gardner J S, Dunsiger S R, Gaulin B D, Gingras M J P, Greedan J E, Kiefl R F, Lumsden M D, MacFarlane W A, Raju N P, Sonier J E, Swainson I and Tun Z 1999 *Phys. Rev. Lett.* **82**(5) 1012–1015 URL <http://link.aps.org/doi/10.1103/PhysRevLett.82.1012>
- [87] Bert F, Mendels P, Olariu A, Blanchard N, Collin G, Amato A, Baines C and Hillier A D 2006 *Phys. Rev. Lett.* **97**(11) 117203 URL <http://link.aps.org/doi/10.1103/PhysRevLett.97.117203>

- [88] Dalmas de Réotier P, Yaouanc A, Keller L, Cervellino A, Roessli B, Baines C, Forget A, Vaju C, Gubbens P C M, Amato A and King P J C 2006 *Phys. Rev. Lett.* **96**(12) 127202 URL <http://link.aps.org/doi/10.1103/PhysRevLett.96.127202>
- [89] Uemura Y J, Keren A, Kojima K, Le L P, Luke G M, Wu W D, Ajiro Y, Asano T, Kuriyama Y, Mekata M, Kikuchi H and Kakurai K 1994 *Phys. Rev. Lett.* **73**(24) 3306–3309 URL <http://link.aps.org/doi/10.1103/PhysRevLett.73.3306>
- [90] Yaouanc A, Dalmas de Réotier P, Bertin A, Marin C, Lhotel E, Amato A and Baines C 2015 *Phys. Rev. B* **91**(10) 104427 URL <http://link.aps.org/doi/10.1103/PhysRevB.91.104427>
- [91] Zorko A, Bert F, Mendels P, Bordet P, Lejay P and Robert J 2008 *Phys. Rev. Lett.* **100**(14) 147201 URL <http://link.aps.org/doi/10.1103/PhysRevLett.100.147201>
- [92] Dunsiger S R, Gardner J S, Chakhalian J A, Cornelius A L, Jaime M, Kiefl R F, Movshovich R, MacFarlane W A, Miller R I, Sonier J E and Gaulin B D 2000 *Phys. Rev. Lett.* **85**(16) 3504–3507 URL <http://link.aps.org/doi/10.1103/PhysRevLett.85.3504>
- [93] Marshall I M, Blundell S J, Pratt F L, Husmann A, Steer C A, Coldea A I, Hayes W and Ward R C C 2002 *Journal of Physics: Condensed Matter* **14** L157 URL <http://stacks.iop.org/0953-8984/14/i=6/a=104>
- [94] Dunsiger S R, Kiefl R F, Chow K H, Gaulin B D, Gingras M J P, Greedan J E, Keren A, Kojima K, Luke G M, MacFarlane W A, Raju N P, Sonier J E, Uemura Y J and Wu W D 1996 *Phys. Rev. B* **54**(13) 9019–9022 URL <http://link.aps.org/doi/10.1103/PhysRevB.54.9019>
- [95] Brewer J H, Kreitzman S R, Noakes D R, Ansaldo E J, Harshman D R and Keitel R 1986 *Phys. Rev. B* **33**(11) 7813–7816 URL <http://link.aps.org/doi/10.1103/PhysRevB.33.7813>
- [96] Möller J S, Ceresoli D, Lancaster T, Marzari N and Blundell S J 2013 *Phys. Rev. B* **87**(12) 121108 URL <http://link.aps.org/doi/10.1103/PhysRevB.87.121108>
- [97] Gerward L, Olsen J S, Steenstrup S, Malinowski M, Åsbrink S and Waskowska A 1992 *Journal of Applied Crystallography* **25** 578–581 URL <https://doi.org/10.1107/S0021889892004096>
- [98] Bowers G M and Mueller K T 2005 *Phys. Rev. B* **71**(22) 224112 URL <https://link.aps.org/doi/10.1103/PhysRevB.71.224112>
- [99] Suter A and Wojek B 2012 *Physics Procedia* **30** 69 – 73 ISSN 1875-3892 12th International Conference on Muon Spin Rotation, Relaxation and Resonance (muSR2011) URL <http://www.sciencedirect.com/science/article/pii/S187538921201228X>
- [100] Möller J S, Bonfa P, Ceresoli D, Bernardini F, Blundell S J, Lancaster T, Renzi R D, Marzari N, Watanabe I, Sulaiman S and Mohamed-Ibrahim M I 2013 *Physica Scripta* **88** 068510 URL <http://stacks.iop.org/1402-4896/88/i=6/a=068510>

- [101] Steele A J, Lancaster T, Blundell S J, Baker P J, Pratt F L, Baines C, Conner M M, Southerland H I, Manson J L and Schlueter J A 2011 *Phys. Rev. B* **84**(6) 064412 URL <https://link.aps.org/doi/10.1103/PhysRevB.84.064412>
- [102] Meier P F 1984 *Hyperfine Interactions* **18** 427–433 ISSN 1572-9540 URL <https://doi.org/10.1007/BF02064848>
- [103] Celio M and Meier P F 1983 *Phys. Rev. B* **27** 1908–1910
- [104] Emsley J 1980 *Chem. Soc. Rev.* **9**(1) 91–124 URL <http://dx.doi.org/10.1039/CS9800900091>
- [105] Emsley J, Hoyte O P A and Overill R E 1977 *J. Chem. Soc., Chem. Commun.* (7) 225–226 URL <http://dx.doi.org/10.1039/C39770000225>
- [106] Mazzoli C, Allodi G, Guidi G, Renzi R D, Ghigna P and Baines C 2003 *Physica B: Condensed Matter* **326** 427 – 430 ISSN 0921-4526 URL <http://www.sciencedirect.com/science/article/pii/S0921452602016563>
- [107] Mansson M, Ikedo Y, Nozaki H, Sugiyama J, Russo P L, Andreica D, Shizuya M, Isobe M and Takayama-Muromachi E 2010 *Solid State Communications* **150** 307 – 310 ISSN 0038-1098 URL <http://www.sciencedirect.com/science/article/pii/S0038109809007832>
- [108] Bräuninger S A, Sarkar R, Krizan J W, Materne P, Baines C, de Réotier P D, Cava J C and Klauss H H 2019 *Persistent μ^+ Spin Dynamics, $F\text{-}\mu^+$ - F State Relaxation and local μ^+ -induced Lattice Distortion in $\text{NaCaCo}_2\text{F}_7$* (manuscript in progress)
- [109] 2015 URL https://www.psi.ch/sites/default/files/import/smus/InstrumentGpsEN/User_Guide_present_version.pdf
- [110] Dunsiger S R, Kiefl R F, Chow K H, Gaulin B D, Gingras M J P, Greedan J E, Keren A, Kojima K, Luke G M, MacFarlane W A, Raju N P, Sonier J E, Uemura Y J and Wu W D 1996 *Phys. Rev. B* **54**(13) 9019–9022 URL <http://link.aps.org/doi/10.1103/PhysRevB.54.9019>
- [111] Keren A, Mendels P, Campbell I A and Lord J 1996 *Phys. Rev. Lett.* **77**(7) 1386–1389 URL <https://link.aps.org/doi/10.1103/PhysRevLett.77.1386>
- [112] Cai Y, Wilson M N, Hallas A M, Liu L, Frandsen B A, Dunsiger S R, Krizan J W, Cava R J, Rubel O, Uemura Y J and Luke G M 2018 *Journal of Physics: Condensed Matter* **30** 385802 URL <https://doi.org/10.1088%2F1361-648x%2Faad91c>
- [113] Grabowski S J 2016 *Crystals* **6** ISSN 2073-4352 URL <http://www.mdpi.com/2073-4352/6/1/3>
- [114] Lancaster T, Blundell S J, Baker P J, Hayes W, Giblin S R, McLain S E, Pratt F L, Salman Z, Jacobs E A, Turner J F C and Barnes T 2007 *Physical Review B* **75**(22) 220408 URL <https://link.aps.org/doi/10.1103/PhysRevB.75.220408>
- [115] Johnson R, Chen K, Giblin S, Lord J, Amato A, Baines C, Barbara B, Malkin B and Graf M J 2011 *Physical Review B* **83** 174440

- [116] Bernardini F, Bonfa P, Massidda S and De Renzi R 2013 *Physical Review B* **87** 115148
- [117] Nishiyama K, Nishiyama S and Higemoto W 2003 *Physica B: Condensed Matter* **326** 41–45 ISSN 0921-4526 URL <http://www.sciencedirect.com/science/article/pii/S0921452602015739>
- [118] Shimizu K, Driver G W, Lucas M, Sparrman T, Shchukarev A and Boily J F 2016 *Dalton Trans.* **45**(22) 9045–9050 URL <http://dx.doi.org/10.1039/C5DT04425A>
- [119] Orain J C, Clark L, Bert F, Mendels P, Attfield P, Aidoudi F H, Morris R E, Lightfoot P, Amato A and Baines C 2014 *Journal of Physics: Conference Series* **551** 012004 URL <http://stacks.iop.org/1742-6596/551/i=1/a=012004>
- [120] Rodriguez J, Dunsiger S, Kycia J, MacDougall G, Quilliam J, Russo P, Savici A, Uemura Y, Wiebe C and Luke G 2006 *Physica B: Condensed Matter* **374-375** 13–16 ISSN 0921-4526 proceedings of the Tenth International Conference on Muon Spin Rotation, Relaxation and Resonance URL <http://www.sciencedirect.com/science/article/pii/S0921452605012032>
- [121] Kreitzman S R, Kiefl R F, Noakes D R, Brewer J H and Ansaldo E J 1986 *Hyperfine Interactions* **32** 521–526 ISSN 1572-9540 URL <http://dx.doi.org/10.1007/BF02394950>
- [122] Patterson B D 1988 *Rev. Mod. Phys.* **60**(1) 69–159 URL <https://link.aps.org/doi/10.1103/RevModPhys.60.69>
- [123] Storchak V G, Eshchenko D G and Brewer J H 2004 *Journal of Physics: Condensed Matter* **16** S4761 URL <http://stacks.iop.org/0953-8984/16/i=40/a=018>
- [124] Chow K H, Kiefl R F, Schneider J W, Estle T L, Hitti B, Lichti R L, Schwab C, Kreitzman S R, DuVarney R C, Senba M, Sonier J, Johnston T M S and MacFarlane W A 1994 *Hyperfine Interactions* **86** 693–698 ISSN 1572-9540 URL <http://dx.doi.org/10.1007/BF02068965>
- [125] Pratt F L, Blundell S J, Marshall I M, Lancaster T, Husmann A, Steer C, Hayes W, Fischmeister C, Martin R E and Holmes A B 2003 *Physica B Condensed Matter* **326** 34–40
- [126] Clark L, Nilsen G J, Kermarrec E, Ehlers G, Knight K S, Harrison A, Attfield J P and Gaulin B D 2014 *Phys. Rev. Lett.* **113**(11) 117201 URL <https://link.aps.org/doi/10.1103/PhysRevLett.113.117201>
- [127] Harris M J, Zinkin M P and Zeiske T 1995 *Phys. Rev. B* **52**(2) R707–R710 URL <https://link.aps.org/doi/10.1103/PhysRevB.52.R707>
- [128] Zinkin M P, Harris M J and Zeiske T 1997 *Phys. Rev. B* **56**(18) 11786–11790 URL <https://link.aps.org/doi/10.1103/PhysRevB.56.11786>
- [129] Bevaart L, Tegelaar P M H L, van Duynveldt A J and Steiner M 1982 *Phys. Rev. B* **26**(11) 6150–6158 URL <https://link.aps.org/doi/10.1103/PhysRevB.26.6150>

- [130] Steiner M 1985 *Phys. Rev. B* **32**(7) 4781–4781 URL <https://link.aps.org/doi/10.1103/PhysRevB.32.4781>
- [131] Kurtz W, Geller R, Dachs H and Convert P 1976 *Solid State Communications* **18** 1479 – 1483 ISSN 0038-1098 URL <http://www.sciencedirect.com/science/article/pii/0038109876903744>
- [132] Kurtz W and Roth S 1977 *Physica B+C* **86-88** 715 – 716 ISSN 0378-4363 URL <http://www.sciencedirect.com/science/article/pii/0378436377906581>
- [133] Alba M, Hammann J, Jacoboni C and Pappa C 1982 *Physics Letters A* **89** 423 – 426 ISSN 0375-9601 URL <http://www.sciencedirect.com/science/article/pii/0375960182903401>
- [134] Uemura Y J, Yamazaki T, Harshman D R, Senba M and Ansaldo E J 1985 *Phys. Rev. B* **31**(1) 546–563 URL <https://link.aps.org/doi/10.1103/PhysRevB.31.546>
- [135] Yaouanc A, Dalmas de Réotier P, Bertin A, Marin C, Lhotel E, Amato A and Baines C 2015 *Phys. Rev. B* **91**(10) 104427 URL <https://link.aps.org/doi/10.1103/PhysRevB.91.104427>
- [136] MacLaughlin D E, Bernal O O, Shu L, Ishikawa J, Matsumoto Y, Wen J J, Mourigal M, Stock C, Ehlers G, Broholm C L, Machida Y, Kimura K, Nakatsuji S, Shimura Y and Sakakibara T 2015 *Phys. Rev. B* **92**(5) 054432 URL <https://link.aps.org/doi/10.1103/PhysRevB.92.054432>
- [137] Yamashita Y and Ueda K 2000 *Phys. Rev. Lett.* **85**(23) 4960–4963 URL <https://link.aps.org/doi/10.1103/PhysRevLett.85.4960>
- [138] Reimers J N, Greedan J E and Björgvinsson M 1992 *Phys. Rev. B* **45**(13) 7295–7306 URL <https://link.aps.org/doi/10.1103/PhysRevB.45.7295>
- [139] Kim S W, Kim S H, Shiv Halasyamani P, Green M A, Preet Bhatti K, Leighton C, Das H and Fennie C J 2011 *ArXiv e-prints (Preprint 1111.5230)*
- [140] Bräuninger S A, Jesche A, Kamusella S, Seewald F, Sarkar R, Zvyagin A A and Klauss H H 2019 *Magnetic Field Tuning of low-Energy Spin Dynamics in the single-atomic Magnet $Li_2(Li_{1-x}Fe_x)N$ probed by ^{57}Fe -Mössbauer Spectroscopy* (manuscript in progress)
- [141] Fix M, Jesche A, Jantz S G, Bräuninger S A, Klauss H H, Manna R S, Pietsch I M, Höppe H A and Canfield P C 2018 *Phys. Rev. B* **97**(6) 064419 URL <https://link.aps.org/doi/10.1103/PhysRevB.97.064419>
- [142] Gatteschi D and Sessoli R 2003 *Angewandte Chemie International Edition* **42** 268–297 ISSN 1521-3773 URL <http://dx.doi.org/10.1002/anie.200390099>
- [143] Gatteschi D, Sessoli R and Villain J 2006 *Molecular Nanomagnets* (Oxford University Press) ISBN 978-0-19-856753-0 DOI: 10.1093/acprof:oso/9780198567530.001.0001 URL <http://www.oxfordscholarship.com/view/10.1093/acprof:oso/9780198567530.001.0001/acprof-9780198567530>

- [144] Bogani L and Wernsdorfer W 2008 **7** 179–186 ISSN 1476-1122, 1476-4660 URL <http://www.nature.com/doi/10.1038/nmat2133>
- [145] Strandberg T O, Canali C M and MacDonald A H 2007 **6** 648–651 ISSN 1476-1122, 1476-4660 URL <http://www.nature.com/doi/10.1038/nmat1968>
- [146] Leuenberger M N and Loss D 2001 **410** 789–793 ISSN 0028-0836 URL <http://dx.doi.org/10.1038/35071024>
- [147] Thomas L, Lioni F, Ballou R, Gatteschi D, Sessoli R and Barbara B 1996 **383** 145–147 ISSN 1476-4687 URL <https://doi.org/10.1038/383145a0>
- [148] Wernsdorfer W, Sessoli R, Caneschi A, Gatteschi D and Cornia A 2000 *EPL (Europhysics Letters)* **50** 552 URL <http://stacks.iop.org/0295-5075/50/i=4/a=552>
- [149] Loss D, DiVincenzo D P and Grinstein G 1992 *Phys. Rev. Lett.* **69**(22) 3232–3235 URL <https://link.aps.org/doi/10.1103/PhysRevLett.69.3232>
- [150] Wernsdorfer W 1999 **284** 133–135 ISSN 00368075, 10959203 URL <http://www.sciencemag.org/cgi/doi/10.1126/science.284.5411.133>
- [151] Bruno P 2006 *Phys. Rev. Lett.* **96**(11) 117208 URL <https://link.aps.org/doi/10.1103/PhysRevLett.96.117208>
- [152] Damski B 2005 *Phys. Rev. Lett.* **95**(3) 035701 URL <https://link.aps.org/doi/10.1103/PhysRevLett.95.035701>
- [153] Messer, R, Birli, H and Differt, K 1980 *J. Phys. Colloques* **41** C6–28–C6–31 URL <https://doi.org/10.1051/jphyscol:1980607>
- [154] Fister T T, Seidler G T, Shirley E L, Vila F D, Rehr J J, Nagle K P, Linehan J C and Cross J O 2008 *The Journal of Chemical Physics* **129** 044702 (Preprint <http://dx.doi.org/10.1063/1.2949550>) URL <http://dx.doi.org/10.1063/1.2949550>
- [155] Yamada A, Matsumoto S and Nakamura Y 2011 *J. Mater. Chem.* **21**(27) 10021–10025 URL <http://dx.doi.org/10.1039/C0JM03735D>
- [156] Wilkening M, Gebauer D and Heitjans P 2008 *Journal of Physics: Condensed Matter* **20** 022201 URL <http://stacks.iop.org/0953-8984/20/i=2/a=022201>
- [157] Jesche A, McCallum R W, Thimmaiah S, Jacobs J L, Taufour V, Kreyssig A, Houk R S, Bud’Ko S L and Canfield P C 2014 *Nature Communications* **5** 3333 (Preprint 1402.6626)
- [158] Klatyk J, Schnelle W, Wagner F R, Niewa R, Novák P, Kniep R, Waldeck M, Ksenofontov V and Gütlich P 2002 *Phys. Rev. Lett.* **88**(20) 207202 URL <http://link.aps.org/doi/10.1103/PhysRevLett.88.207202>

- [159] Ksenofontov V, Reiman S, Waldeck M, Niewa R, Kniep R and Gütlich P 2003 *Zeitschrift für anorganische und allgemeine Chemie* **629** 1787–1794 ISSN 1521-3749 URL <http://dx.doi.org/10.1002/zaac.200300135>
- [160] Jesche A, Ke L, Jacobs J L, Harmon B, Houk R S and Canfield P C 2015 *Phys. Rev. B* **91**(18) 180403 URL <https://link.aps.org/doi/10.1103/PhysRevB.91.180403>
- [161] Xu L, Zangeneh Z, Yadav R, Avdoshenko S, van den Brink J, Jesche A and Hozoi L 2017 *Nanoscale* **9**(30) 10596–10600 URL <http://dx.doi.org/10.1039/C7NR03041J>
- [162] Fix M, Atkinson J H, Canfield P C, del Barco E and Jesche A 2018 *Phys. Rev. Lett.* **120**(14) 147202 URL <https://link.aps.org/doi/10.1103/PhysRevLett.120.147202>
- [163] Seewald F *Bachelor thesis TU Dresden: Mössbauer spectroscopy in Fe(I) complexes in $Li_2[Fe_xLi_{1-x}]N$*
- [164] Carretta P and Lascialfari A (eds) *NMR-MRI, MSR and Moessbauer spectroscopies in molecular magnets* (Springer) ISBN 978-88-470-0531-0 OCLC: 255432892
- [165] Chuev M A 2011 *Journal of Physics: Condensed Matter* **23** 426003 URL <http://stacks.iop.org/0953-8984/23/i=42/a=426003>
- [166] Faid K and Fox R F 1986 *Phys. Rev. A* **34**(5) 4286–4302 URL <http://link.aps.org/doi/10.1103/PhysRevA.34.4286>
- [167] Blume M 1968 *Phys. Rev.* **174**(2) 351–358 URL <http://link.aps.org/doi/10.1103/PhysRev.174.351>
- [168] Segal E and Wallace W 1970 *Journal of Solid State Chemistry* **2** 347 – 365 ISSN 0022-4596 URL <http://www.sciencedirect.com/science/article/pii/0022459670900939>
- [169] Segal E and Wallace W 1973 *Journal of Solid State Chemistry* **6** 99 – 118 ISSN 0022-4596 URL <http://www.sciencedirect.com/science/article/pii/0022459673902107>
- [170] Segal E and Wallace W 1974 *Journal of Solid State Chemistry* **11** 203 – 213 ISSN 0022-4596 URL <http://www.sciencedirect.com/science/article/pii/S0022459674800058>
- [171] Novák P and Wagner F R 2002 *Phys. Rev. B* **66**(18) 184434 URL <http://link.aps.org/doi/10.1103/PhysRevB.66.184434>
- [172] Ulyanov V and Zaslavskii O 1992 *Physics Reports* **216** 179 – 251 ISSN 0370-1573 URL <http://www.sciencedirect.com/science/article/pii/037015739290158V>
- [173] Enz M and Schilling R 1986 *Journal of Physics C: Solid State Physics* **19** L711 URL <http://stacks.iop.org/0022-3719/19/i=30/a=005>
- [174] Wernsdorfer W, Sessoli R, Caneschi A, D, Cornia A and Maily D 2000 *Journal of Applied Physics* **87** 5481–5486 (*Preprint* <https://doi.org/10.1063/1.373379>) URL <https://doi.org/10.1063/1.373379>

- [175] Zadrozny J M, Xiao D J, Long J R, Atanasov M, Neese F, Grandjean F and Long G J **52** 13123–13131 ISSN 0020-1669, 1520-510X URL <http://pubs.acs.org/doi/abs/10.1021/ic402013n>
- [176] Lewis J and Schwarzenbach D 1981 *Acta Crystallographica Section A* **37** 507–510 URL <https://doi.org/10.1107/S0567739481001204>
- [177] Wang S G and Schwarz W H E 1998 *The Journal of Chemical Physics* **109** 7252–7262 (*Preprint* <http://dx.doi.org/10.1063/1.477359>) URL <http://dx.doi.org/10.1063/1.477359>
- [178] Liu J, Chen Y C, Liu J L, Vieru V, Ungur L, Jia J H, Chibotaru L F, Lan Y, Wernsdorfer W, Gao S, Chen X M and Tong M L 2016 *Journal of the American Chemical Society* **138** 5441–5450 pMID: 27054904 (*Preprint* <https://doi.org/10.1021/jacs.6b02638>) URL <https://doi.org/10.1021/jacs.6b02638>
- [179] R G C, Beatriz B, Gema T, M C J, Eugenio C and Tomas T 2013 *Chemistry-A European Journal* **19** 1457–1465 URL <https://onlinelibrary.wiley.com/doi/abs/10.1002/chem.201202600>
- [180] Zadrozny J M, Xiao D J, Atanasov M, Long G J, Grandjean F, Neese F and Long J R 2013 **5** 577–581 ISSN 1755-4330, 1755-4349 URL <http://www.nature.com/articles/nchem.1630>
- [181] Pavel K, Mikhail Z, Yan Z, Oxana M, Robert D and Martin J 2014 *Chemistry-A European Journal* **20** 165–178 URL <https://onlinelibrary.wiley.com/doi/abs/10.1002/chem.201303136>
- [182] Giraud R, Tkachuk A M and Barbara B 2003 *Phys. Rev. Lett.* **91**(25) 257204 URL <http://link.aps.org/doi/10.1103/PhysRevLett.91.257204>
- [183] Giraud R, Wernsdorfer W, Tkachuk A M, Mailly D and Barbara B 2001 *Phys. Rev. Lett.* **87**(5) 057203 URL <http://link.aps.org/doi/10.1103/PhysRevLett.87.057203>
- [184] Banhart J, Ebert H, Voitländer J and Winter H 1986 *J. Magn. Magn. Mater.* **61** 221–224 ISSN 0304-8853
- [185] Höhn P, Hoffmann S, Hunger J, Leoni S, Nitsche F, Schnelle W and Kniep R 2009 *Chem. Eur. J.* **15** 3419–3425 ISSN 1521-3765 URL <http://onlinelibrary.wiley.com/doi/10.1002/chem.200801857/abstract>
- [186] Söhnle T, Böttcher P, Reichelt W and Wagner F E 1998 *Zeitschrift für anorganische und allgemeine Chemie* **624** 708–714 ISSN 1521-3749 URL [http://dx.doi.org/10.1002/\(SICI\)1521-3749\(199804\)624:4<708::AID-ZAAC708>3.0.CO;2-T](http://dx.doi.org/10.1002/(SICI)1521-3749(199804)624:4<708::AID-ZAAC708>3.0.CO;2-T)
- [187] Sarkar R, Kamusella S, Braeuninger S A, Holenstein S, Orain J C, Luetkens H, Grinenko V, Tarne M J, Neilson J R, Ross K A and Klauss H H 2017 *ArXiv e-prints* (*Preprint* 1707.07433)
- [188] Tarne M J, Bordelon M M, Calder S, Neilson J R and Ross K A 2017 *Phys. Rev. B* **96**(21) 214431 URL <https://link.aps.org/doi/10.1103/PhysRevB.96.214431>

A Appendix

A.1 NaCaCo₂F₇

A.1.1 μ^+ SR spectra in 30 G at 290 K

Figure A.1 shows two μ SR spectra at 30 G in LF and TF geometry. Here, the magnetic field of 30 G is about twice of the value of the static magnetic field of the nuclear moments provided by the F- μ^+ -F state of around 16 G. The fit at 30 G is described by the presented two site model, see main text. The transverse field experiment shows no signal loss below 1 μ s as well compared to ZF (not shown). This speaks against a strong hyperfine coupling as expected for a muonium site.

A.1.2 LTF data of λ_f

Figure A.2 shows the LTF and GPS data of the fast relaxation channel (muon site **II**). High relaxation rates $> 40 \mu\text{s}^{-1}$ are close to the experimental limit of the spectrometer LTF (long time mode) and, therefore, the error bars are large. However, a plateau-like saturation of the LF (400 G) muon spin relaxation rate λ_f is observed consistent with the observations for muon site **I**.

A.1.3 Low-field SQUID measurements of NaCaCo₂F₇

I have performed DC-SQUID measurements below a magnetic field of 1 T. This measurements were performed as a function of temperature and as a function of the applied magnetic field at the IFW in Dresden. One small cubic crystals was used which was taken for the pulsed-high-field magnetization

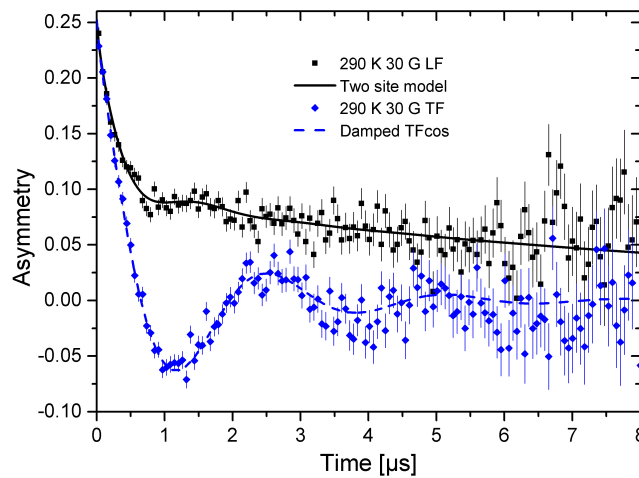


Figure A.1: μ SR spectra (GPS) at 290 K in 30 G LF (black points) and TF (blue points), respectively.

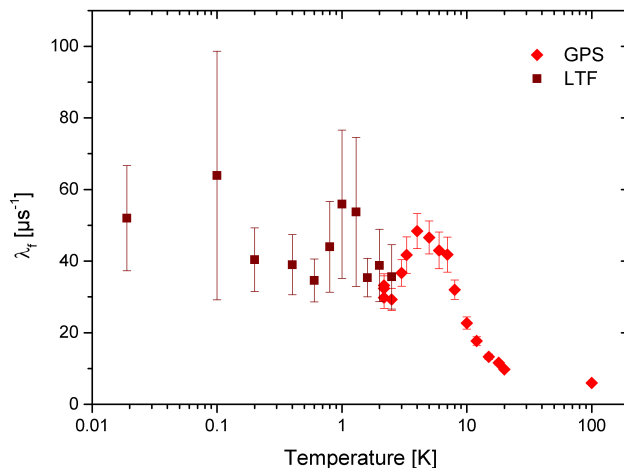
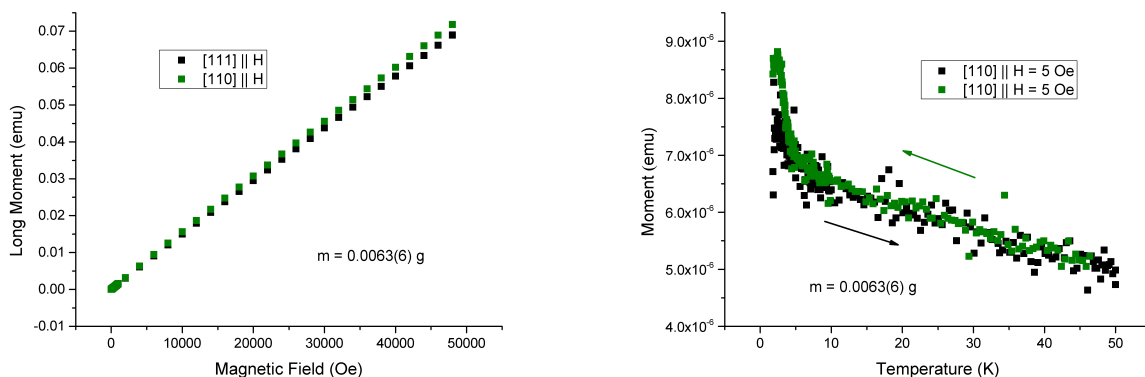


Figure A.2: Temperature dependence of the LTF (brown) and GPS (red) data, respectively, of the fast relaxation channel (muon site **II**). The relaxation rate converges to $\sim 50 \mu s^{-1}$.



(a) Absolute magnetic moment as a function of the applied field for two crystal directions.

(b) Absolute magnetic moment as a function of temperature in 5 Oe for increasing and decreasing temperature, see arrows.

Figure A.3: DC-SQUID measurements using a Quantum Design MPMS-5S.

studies in Dresden-Rossendorf, see *J. Zeisner et al.* [65]. The SQUID magnetometer was a Quantum Design MPMS-5S. The sample mass was $m = 0.0063(6)$ g measured with a Mettler Toledo AT 201 calculated by a difference method. The measurement results are shown in figure A.3. The difference between the data for field aligned along the [111] and [110] directions (figure A.3 (a)) occurs probably because of slightly different shapes of the not perfect cubic crystals. A dominant ferromagnetic contribution is excluded from the data shown in figure A.3 (b) showing no temperature-dependent hysteresis in 5 Oe. An observed intrinsic anomaly in my μ SR data around 200 G LF is excluded with this measurements.

Element	Atomic mass [u]	absorption coefficient [cm^2/g]
Li	3	0.277
N	7	1.4
Fe	26	64
Os	76	165

Table A.1: Mass absorption coefficients μ_a according to Chen *et al.* and references therein [16].

A.2 $\text{Li}_2(\text{Li}_{1-x}\text{Fe}_x)\text{N}$

A.2.1 Mass absorption coefficients

The Fe concentration of sample SC 4 is with less than 0.2% rather small, even for a ^{57}Fe Mössbauer experiment of a non- ^{57}Fe -enriched sample. Fortunately, $\text{Li}_2(\text{Li}_{1-x}\text{Fe}_x)\text{N}$ contains only light elements with small absorption coefficients of the 14.41 keV radiation, see table A.1. The mass absorption coefficient μ_a describes the exponential intensity reduction of the initial γ -ray intensity I_0 ,

$$I(d) = I_0(1 - f_s)e^{\mu_a d}, \quad (\text{A.1})$$

where d is the absorber thickness and f_s the recoil-free fraction of transitions. μ_a describes non-resonant atomic absorption, mainly by the photoelectric effect. For a comparison, the value of Os representing a heavy element in table A.1, shows the rather small mass absorption coefficient μ_a of Li and N since Fe is highly-diluted. We have used for this reason large crystals with a thickness of a few millimeter and the effective thickness $t_a = 2.39(10)$ of SC 1 reflects still absorption far away from the saturation limit. The Fe concentration of SC 4 is even below the concentration of Ho in $\text{LiY}_{0.998}\text{Ho}_{0.002}\text{F}_4$, or at least in the same order, which is a prominent example for a SAM in a solid crystal [182, 183].

A.2.2 Magnetization hysteresis loops

The magnetization hysteresis loops shown in figure 8.3 were measured at different temperatures for magnetic fields applied parallel to the crystallographic c -axis, $H \parallel c$. The effective sweep rate for the full loops was 2.9 mT/s with 10 mT/s between the measurements. The obtained data were corrected for the diamagnetic sample holder (sample sandwiched between two torlon discs and fixed inside a straw) for which the magnetization was determined separately using a similar setup. The Fe concentration x was inferred from the known saturation magnetization [157], cross checked on other samples by ICP measurements. The diamagnetic contribution of the α - Li_3N host was subsequently subtracted from the sample-holder-corrected data using $\rho(\text{Li}^{1+}) = 8.8 \cdot 10^{-12} \text{ m}^3 \text{ mol}^{-1}$ [184] and $\rho(\text{N}^{3-}) = 1.63 \cdot 10^{-10} \text{ m}^3 \text{ mol}^{-1}$ [185].

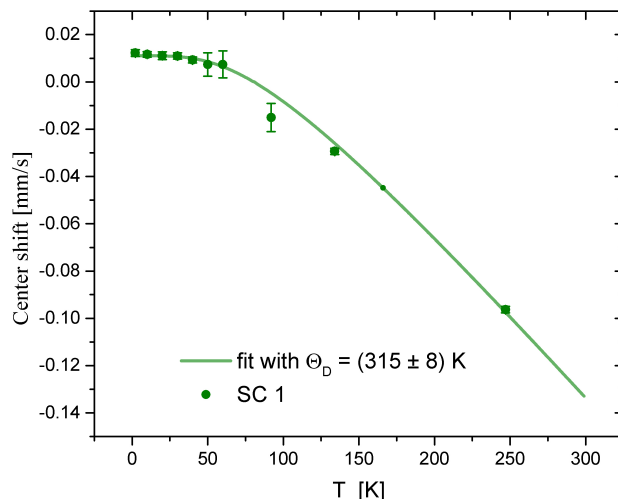


Figure A.4: Center shift as a function of temperature and the corresponding fit to determine the Debye-temperature Θ_D as used in [163].

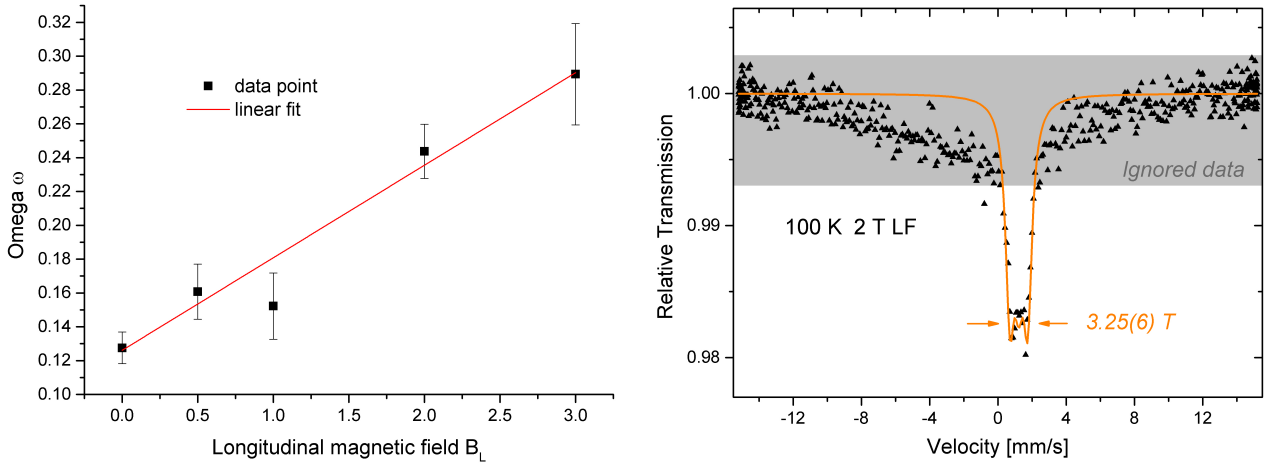
A.2.3 Debye-fit for Θ_D

Figure A.4 shows the center shift as a function of temperature obtained in ZF of sample SC 1. The center shift is here $\delta + \delta_{\text{SOD}}$ without α -iron correction, means relative to the ^{57}Co -source. The temperature dependence of SC 1 yielded a Debye-temperature of $\Theta_D = 315(8)$ K.

A.2.4 Discussion of the ^{57}Co -source splitting in longitudinal magnetic fields B_L

The purpose of this subsection is the exclusion of the observed splitting in our longitudinal magnetic field experiments as pure ^{57}Co -source splitting effect. In contrast to the transverse magnetic field setup, in the longitudinal measurement geometry the ^{57}Co -source is subjected to a finite but small magnetic field caused by the Helmholtz-magnet. This leads to an increase of the linewidth and for higher fields (> 3 T) to a considerable splitting effect because of the Zeeman splitting of the source. The increase of the linewidth in our experiment is shown in figure A.5 (a). The linewidth increase linearly as shown by the red fit. The error increases caused by broadening of the spectra and by the restriction of the used fit model. The source probes just a fraction B_{fr} of the applied longitudinal field $B_L > B_{\text{fr}}$ acting on the sample because of the decrease of the magnetic field outside of the superconducting coils.

The measurement at 100 K in ZF is given by a relaxing spectrum with a narrow line with $\nu_{\text{up}} = \nu_{\text{down}}$. Figure A.5 (b) shows the Mössbauer measurement at 100 K in 2 T LF using a wrong fit model for the purpose of discussion. To estimate the effect of a possible longitudinal magnetic field splitting a static single line ($V_{zz} = 0$), I estimated a hyperfine field which would yield the observed splitting ignoring the data in the grey shadowed area. The result is a hyperfine field of $B = 3.25(6)$ T. This field is too high to be a pure result of the ^{57}Co -source splitting which should not exceed a value of 0.5 T in the 2 T LF case presented in figure A.5 (b) since the sample shows Mössbauer spectra with intermediate relaxation times. Here, a relaxing Fe species between states with hyperfine fields of 72.25 T and -68.25 T leads to just one line and no splitting. The introduction of two frequencies is



(a) Linewidth ω as a function of the longitudinal magnetic field B_L caused by the ^{57}Co -source splitting effect with a linear fit.

(b) Mössbauer measurement at 100 K in an applied longitudinal field of 2 T. The orange line represents a static Hamiltonian fit to estimate the splitting and exclude pure source splitting as origin.

Figure A.5: Supplementary plots concerning the ^{57}Co -source splitting effect.

needed to describe the splitting. Therefore, the description of a ^{57}Co -source splitting by a slight increase of the linewidth is a reasonable approximation up to 3 T.

A.3 Additional DFT results

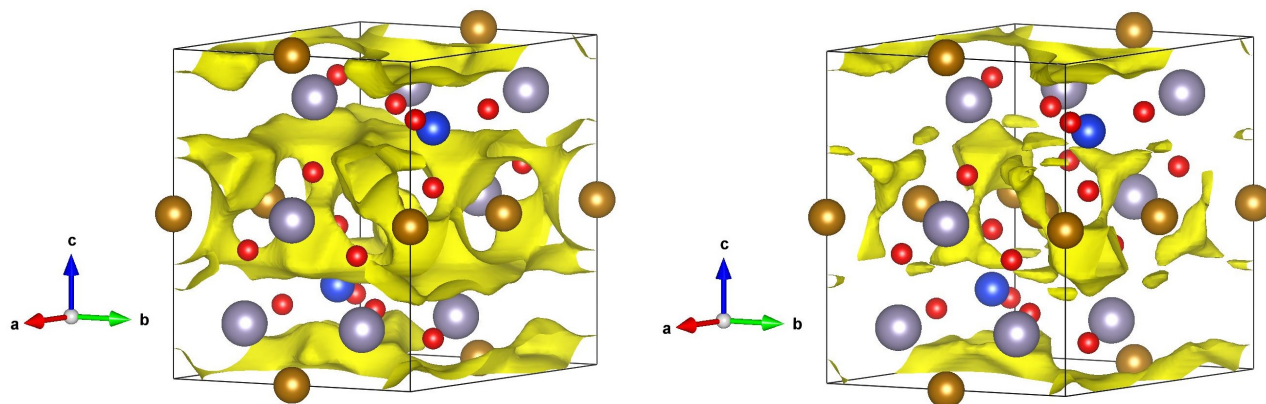
I have performed additional DFT calculations for other materials. This shows the universal application of the DFT routine introduced in our group as an estimation tool for the muon site.

A.3.1 DFT results of $\text{Fe}_4\text{Si}_2\text{Sn}_7\text{O}_{16}$

I have performed DFT calculations on $\text{Fe}_4\text{Si}_2\text{Sn}_7\text{O}_{16}$ to estimate the possible muon site. Here, the planes are separated by nonmagnetic Fe layers to avoid interplanar interaction. Figure A.6 and A.7 show the unit cell of $\text{Fe}_4\text{Si}_2\text{Sn}_7\text{O}_{16}$ and calculated isosurfaces of the electrostatic potential. The crystal structure data are taken from T. Söhnel *et al.* [186]. Figure A.6 (a) and (b) show that there are two distinct planes with volumes containing energy maxima with $0.37 \frac{E_h}{e}$ and $0.40 \frac{E_h}{e}$, respectively. Figure A.7 (a) restricts the possible space of highest energy close to O in both planes. A.7 (b) proposes that the muon site is close to the stannide layer (nonmagnetic layer) close to the p -orbitals of O. The calculated energy peaks have values of $0.437833 \frac{E_h}{e}$.

A.3.2 DFT results of $\text{Fe}_3\text{PO}_4\text{O}_3$

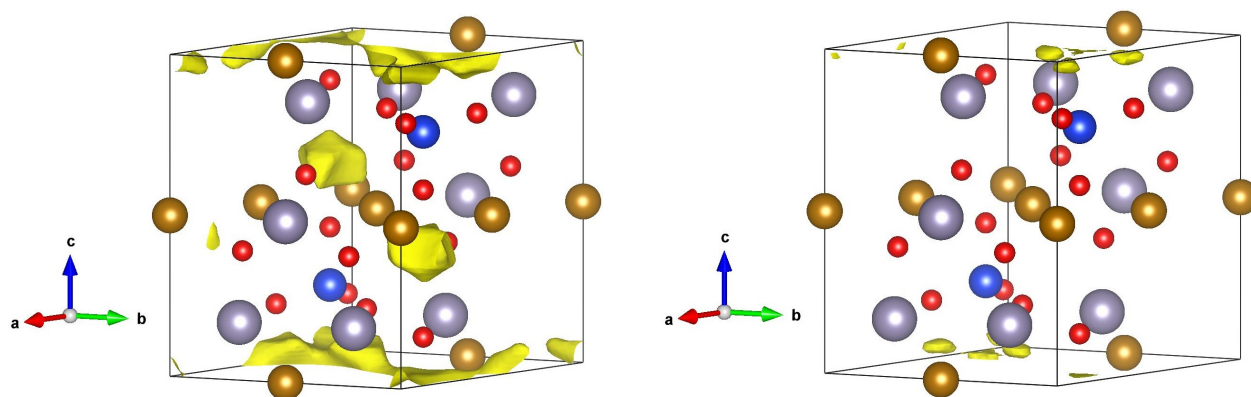
$\text{Fe}_3\text{PO}_4\text{O}_3$ is a frustrated helical magnet, for details see R. Sarkar, S. A. Bräuninger *et al.* [187]. Interestingly, the resolution of the Mössbauer measurements is improved compared to the study decades ago which shows one example for a reasonable reinvestigation and data improvements. The μSR spin-lattice relaxation rate exhibits two peaks: One at the magnetic ordering temperature related



(a) Unit cell of $\text{Fe}_4\text{Si}_2\text{Sn}_7\text{O}_{16}$ and corresponding DFT calculation of the electrostatic potential with the isosurfaces of the positive (yellow) potential of $0.37 \frac{E_h}{e}$.

(b) Unit cell of $\text{Fe}_4\text{Si}_2\text{Sn}_7\text{O}_{16}$ and corresponding DFT calculation of the electrostatic potential with the isosurfaces of the positive (yellow) potential of $0.40 \frac{E_h}{e}$.

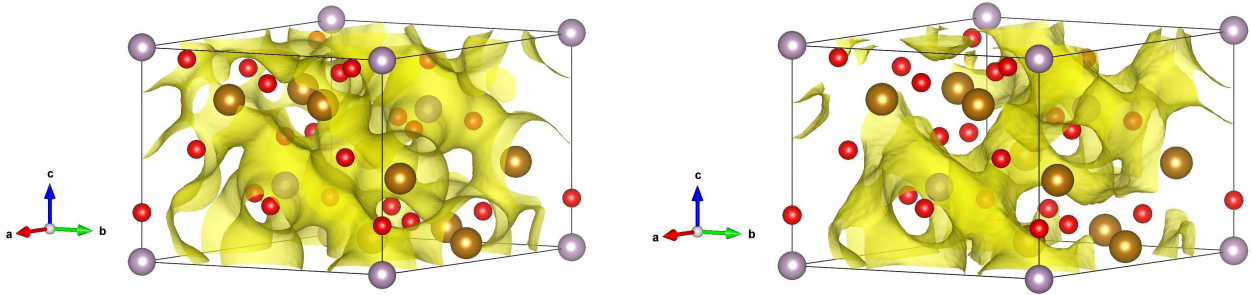
Figure A.6: Unit cell of $\text{Fe}_4\text{Si}_2\text{Sn}_7\text{O}_{16}$ and calculated isosurfaces of the electrostatic potential. Fe is shown in brown, O in red, Sn in gray and Si in blue.



(a) Unit cell of $\text{Fe}_4\text{Si}_2\text{Sn}_7\text{O}_{16}$ and corresponding DFT calculation of the electrostatic potential with the isosurfaces of the positive (yellow) potential of $0.41 \frac{E_h}{e}$.

(b) Unit cell of $\text{Fe}_4\text{Si}_2\text{Sn}_7\text{O}_{16}$ and corresponding DFT calculation of the electrostatic potential with the isosurfaces of the positive (yellow) potential of $0.431 \frac{E_h}{e}$.

Figure A.7: Unit cell of $\text{Fe}_4\text{Si}_2\text{Sn}_7\text{O}_{16}$ and calculated isosurfaces of the electrostatic potential. Fe is shown in brown, O in red, Sn in gray and Si in blue.



(a) Unit cell of $\text{Fe}_3\text{PO}_4\text{O}_3$ and the isosurfaces of $0.30 \frac{E_h}{e}$. (b) Unit cell of $\text{Fe}_3\text{PO}_4\text{O}_3$ and the isosurfaces of $0.35 \frac{E_h}{e}$.

Figure A.8: Unit cell of $\text{Fe}_3\text{PO}_4\text{O}_3$ shown and various isosurfaces in yellow. Fe is shown in brown, O in red and P in gray.

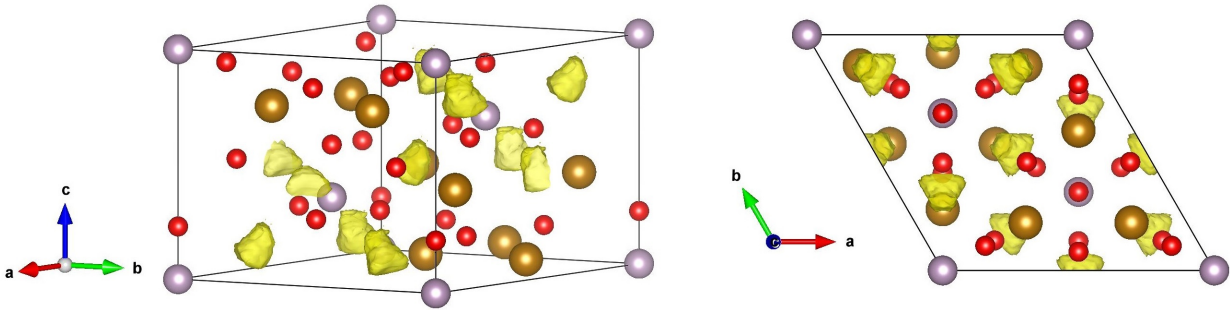


Figure A.9: Unit cell of $\text{Fe}_3\text{PO}_4\text{O}_3$ shown two different directions of the isosurface of $0.385 \frac{E_h}{e}$ (yellow). Fe is shown in brown, O in red and P in gray.

to critical magnetic fluctuations and another peak at 35 K (not shown) signaling the presence of a secondary low-energy scale in $\text{Fe}_3\text{PO}_4\text{O}_3$ which is not explained so far [187]. For further details, see K. Ross *et al.* describing the nanosized helical domains [188, 47].

I have performed DFT calculations to estimate roughly the possible muon site using the crystal structure data obtained by K. Ross *et al.* [47]. The procedure is the same as discussed in the main text. Figure A.8 (a) and (b) show the calculated isosurfaces in yellow of $0.30 \frac{E_h}{e}$ and $0.35 \frac{E_h}{e}$, respectively. Figure A.9 shows the calculated isosurface of $0.385 \frac{E_h}{e}$ inside the unit cell in two directions. The unit cell is shifted according to the DFT code compared to the one used by K. Ross *et al.* [47]. Here, the lowest energy minimum is located between eight O leading to a proposed octahedrally coordinated positive muon site near the p -orbitals of O, e.g. in the middle of the shown unit cell. This isosurface and the corresponding volume appears at a manifold of sites and occurs a few times per unit cell (see yellow surfaces) with the calculated energy maximum (peak) of $0.398368 \frac{E_h}{e}$ inside these volumes.

Danksagungen

Zunächst möchte ich mich herzlich bei meinen Eltern bedanken für ihre finanzielle und emotionale Unterstützung während meines Studiums.

Mein größter Dank gilt Professor Hans-Henning Klauß dafür, dass er immer eine offene Tür und ein offenes Ohr hatte, für die spannenden Promotionsthemen, dass er auf Entfaltungsvorschläge seiner Doktoranden gewissenhaft eingeht und durch wissenschaftliche Begeisterung sein Umfeld verzaubert. Die Tätigkeit und Möglichkeit der Fortbildung zum Strahlenschutzbeauftragten in Berlin war eine Bereicherung.

Ich danke Rajib Sarkar für die Organisation der Projekte und die Evaluation dieser. Manuel Richter danke ich für die unkomplizierte Durchsicht und Diskussion meiner DFT-Rechnungen, ebenso Mathias Dörr, welcher durch konstruktive Diskussionen und Durchsicht der Dissertation die Sicht eines Nicht-nuklearen-Sondenwissenschaftlers zu Protokoll gab. Seine Erfahrung war stets eine Bereicherung. Vadim Grinenko danke ich für seine allgemeinen Diskussionen. Er trägt mit seiner ruhigen Art zu einer entspannten Arbeitsatmosphäre bei.

Ich danke dem Hochschulsport, bei welchem ich durch Badmintonspiele den Stress vom Labor- und Arbeitsalltag wunderbar abbauen konnte. Die Tätigkeit als Kursleiter bereitete mir viel Freude und immernoch bereitet.

Aus unserer Arbeitsgruppe möchte ich insbesondere Sirko Kamusella und Felix Seewald für die Unterstützung am $\text{Li}_2(\text{Li}_{1-x}\text{Fe}_x)\text{N}$ -Projekt bedanken, ebenso Felix Brückner und Phillipp Materne für konstruktive Diskussionen wie auch Shanu Dengre und Shreenanda Ghosh.

Projektbezogen danke ich dem Rossendorf-Team, insbesondere Thomas Herrmannsdörfer und Lars Opherden, für die Unterstützung bei den gepulsten Hochfeldmagnetisierungsmessungen. Julian Zeisner spreche ich meine Dankbarkeit aus für seine ESR-Beiträge. Weiterhin danke ich Anton Jesche und Manuel Fix für die zahlreichen Telefonate zum $\text{Li}_2(\text{Li}_{1-x}\text{Fe}_x)\text{N}$ -Projekt und deren unermüdliche Neugier. Die finanzielle Unterstützung durch den SFB 1143 sei ebenfalls nicht unerwähnt.

Für den wissenschaftlichen Austausch danke ich vielen anderen nationalen und internationalen Kollegen, mit denen ich bisher zusammenarbeiten durfte.

Zuletzt danke ich unserer Sekretärin Elke Wachsmuth, welche uns immer viel Arbeit abnimmt. Richardt Schlitz für aufmunternde Sprüche und Professor Sebastian Gönnerwein für den Kaffeedienst und zuletzt natürlich Professor Joachim Wosnitza für das unkomplizierte Zweitgutachten.

Versicherung

Hiermit versichere ich, Sascha Albert Bräuninger, dass ich die vorliegende Arbeit ohne unzulässige Hilfe Dritter und ohne Benutzung anderer als der angegebenen Hilfsmittel angefertigt habe. Die aus fremden Quellen direkt oder indirekt übernommenen Gedanken sind als solche kenntlich gemacht.

Die Arbeit wurde bisher weder im Inland noch im Ausland in gleicher oder ähnlicher Form einer anderen Prüfungsbehörde vorgelegt.

Die vorliegende Dissertation wurde am Institut für Festkörper- und Materialphysik der Technischen Universität Dresden unter der wissenschaftlichen Betreuung von Herrn Professor Dr. Hans-Henning Klauß angefertigt.

Hiermit erkenne ich die Promotionsordnung der Technischen Universität Dresden in der Fassung vom 23.02.2011 an.

Dresden, den 25. September 2019

Sascha A. Bräuninger